The Pennsylvania State University

The Graduate School

Department of Materials Science and Engineering

LOCAL PIEZOELECTRIC BEHAVIOR IN PZT-BASED THIN FILMS FOR ULTRASOUND TRANSDUCERS

A Dissertation in

Materials Science and Engineering

by

Flavio Griggio

© 2011 Flavio Griggio

Submitted in Partial Fulfillment
of the Requirements
for the Degree of

Doctor of Philosophy

August 2011

The dissertation of Flavio Griggio was reviewed and approved* by the following:

Susan Trolier-McKinstry
Professor of Ceramic Science and Engineering
Dissertation Advisor
Chair of Committee

Clive A. Randall
Professor of Materials Science and Engineering

Thomas R. Shrout
Senior Scientist and Professor of Materials Science and Engineering

Thomas N. Jackson
Robert E. Kirby Chair Professor of Electrical Engineering

Gary L. Messing
Distinguished Professor of Ceramic Science and Engineering
Head of the Department of Materials Science and Engineering

*Signatures are on file in the Graduate School

ABSTRACT

Piezoelectric microelectromechanical systems (MEMS) are currently used in inkjet printers and precision resonators; numerous additional applications are being investigated for sensors, low-voltage actuators, and transducers. This work was aimed at improving piezoelectric MEMS by taking two approaches: 1) identifying factors affecting the piezoelectric response of ferroelectric thin films and 2) demonstrating integration of these films into a high frequency array transducer.

It was found that there are several key factors influencing the piezoelectric response of thin films for a given material composition. First, large grain size improves the piezoelectric response. This was demonstrated using chemical solution deposited lead nickel niobate – lead zirconate titanate $(0.3)Pb(Ni_{0.33}Nb_{0.67})O_3$ - $(0.7)Pb(Zr_{0.45}Ti_{0.55}O_3)$, (PNN-PZT) ferroelectric thin films. It was shown that this composition allows greater microstructural control than does PZT. Dielectric permittivities ranging from 1350 to 1520 and a transverse piezoelectric coefficient $e_{31,f}$ as high as – 9.7 C/m^2 were observed for films of about 0.25 μm in thickness. The permittivity and piezoelectric response as well as extrinsic contributions to the dielectric constant increased by 14 and 12 % respectively for samples with grain sizes ranging from 110 to 270 nm.

A second factor influencing the piezoelectric response is film composition with respect to the morphotropic phase boundary (MPB). The composition dependence of the dielectric and piezoelectric nonlinearities was characterized in epitaxially grown $(0.3)Pb(Ni_{0.33}Nb_{0.67})O_3$-$(0.7)Pb(Zr_xTi_{1-x}O_3)$ thin films deposited on $SrTiO_3$ to minimize the influence of large-angle grain boundaries. Tetragonal, MPB and rhombohedral films were prepared by changing the Zr/Ti ratio. The largest dielectric and piezoelectric nonlinearities were observed for the rhombohedral sample; this resulted from a higher domain wall mobility due to a smaller ferroelectric distortion and superior crystal quality.

Thirdly, changes in the mechanical boundary conditions experienced by a ferroelectric thin film were found to influence both the properties and the length scale for correlated motion of domain walls. Microfabrication was employed to release the PZT films from the Si substrate. Nonlinear piezoelectric maps, by band excitation piezoforce microscopy, showed formation of clusters of higher nonlinear activities of similar size for clamped PZT films with different microstructures. However PZT films that had been released from the Si substrate showed a distinct increase in the correlation length associated with coupled domain wall motion, suggesting that the *local* mechanical boundary conditions, more than microstructure or composition govern the domain wall dynamics. Release of both the local and the global stress states in films produced dielectric nonlinearities comparable to those of bulk ceramics.

The second research direction was targeted at demonstrating the functionality of a one dimensional transducer array. A diaphragm geometry was used for the transducer arrays in order to benefit from the unimorph-type displacement of the PZT-SiO_2 layers. For this purpose, the PZT and remaining films in the stack were patterned using reactive ion etching and partially released from the underlying silicon substrate by XeF_2 etching from the top. Admittance measurements on the fabricated structures showed resonance frequencies at ~40 MHz for a 80 μm diameter-wide diaphragms with a PZT thickness of 1.74 μm. In-water transmit and receive functionalities were demonstrated. A bandwidth on receive of 80 % centered at 40 MHz was determined during pitch-mode tests.

TABLE OF CONTENTS

LIST OF FIGURES

LIST OF TABLES

ACKNOWLEDGEMENTS

I must first express my gratitude for the support I received from my parents and family over the past four years. Their encouragement and love helped me to never lose motivation and optimism during my time at PennState.

I consider myself privileged in having encountered numerous exceptional people during the course of my studies. These people contributed to this work not only scientifically but also, and especially, at a human level.

My first thought goes to Prof. Susan Trolier-McKinstry, who gave me the opportunity and all the means necessary to explore the applied physics of ferroelectric thin films. Aside from being an excellent mentor, she infused into me her infinite enthusiasm for the field, which I now gladly share. I truly thank her for constant support and availability to discuss the results and suggest new directions.

I then wish to thank the other members of my committee for their participation, experienced advice, and useful comments. I particularly want to express my sincere appreciation to Prof. Thomas Jackson who constantly offered prompt and extremely valuable recommendations on sample processing and let me access his facility for part of the fabrication. I would then like to acknowledge Prof. Clive Randall and Prof. Thomas Shrout for helpful discussions on interpretation of ferroelectric phenomena.

I am very grateful to a National Security Science and Engineering Faculty Fellowship, the Center for Dielectric Studies at Penn State and Prof. Aldo Gini Fellowship for studies and research abroad for financial support.

I then must thank Prof. Sergei Kalinin, Dr. Stephen Jesse, Dr. Amit Kumar, Dr. Art Baddorf, Dr. Nina Balke, Dr. Maxim Nikiforov and Oleg Ovchinnikov at Oak Ridge National Laboratory for constant support on measurements and data analysis and at times for giving me access to multiple scanning probe microscopes at the same time. The extremely productive data acquisition at the Center for Nanophase Materials Science was also the result of invaluable help received from this young team of scientists.

I would like to extend my gratitude then to the MRL staff: Jeff Long and Paul Moses for helping with the dielectric and piezoelectric measurement setups; Bill Drawl and Tim Klinger for constantly monitoring the functionalities of the clean room at MRL; Nichole Wonderling and Maria Klimkiewicz for help with XRD and SEM characterization tools; Chris Jabco for machine shop assistance and Maria Di Cola. Thanks to Susie Sherlock, Kathy Gummo and Elaine Robinson.

Thanks to the MCL and MRI staff for very helpful interactions on sample processing and characterization. In particular, special thanks to: Chad Eichfeld, Kathy Gehoski, Guy Lavalle, Bangzhi Liu, Andrzej Mieckowski, Shane Miller, Josh Stapleton, Josh Maier, John Cantolina and Mark Angelone. Thanks to Dr. Weiguo Qu for TEM analysis.

I have to thank the whole STM group, past and present. I am glad I had the chance to meet you all: Aaron, Adarsh, Charley, Dan T. and Dan M., Derek, David, Eunki, Heidi, Hideki, Hong Goo, Ichiro, Jung In, Lauren, Mike, Nicolas, Pierre, Pum, Raegan, Raffi, Raja, Song Won, Sun Young, Tana, and Wanlin.

Last but not least I would like to thank my friends Insoo and Hyunsoo, Prof. Kyusun Choi, and Prof. Tutwiler, part of the MEMS ultrasound transducer team, Seyit Ural for performing finite element analysis and the students in the Jackson's Electronic Research Group that assisted me in the device fabrication: Devin, Hang-Beum, Myung-Yoon and Raymond.

Chapter 1

Introduction and Goals

1.1 Introduction

Piezoelectricity derives semantically from the Greek words for pressure and amber (which could be used to produce electrical charge). It describes either a linear variation of the dielectric displacement due to a stress (direct effect) or the development of a mechanical strain in response to an applied electric field (converse effect). Most commercially available piezoelectric ceramics are based on the PZT ($PbZr_{1-x}Ti_xO_3$) solid solution; for the past 60 years PZT has been the material of choice for transducer technology. PZT is one of many ferroelectric ceramics crystallizing with the perovskite structure. The second chapter provides a background on ferroelectricity to introduce concepts invoked in the rest of the thesis.

Interest in PZT-based piezoelectric microelectromechanical systems (MEMS) has seen a marked increase over the last few years. Several devices exploiting the large piezoelectric coefficients of PZT have been investigated, such as low-voltage radio frequency MEMS switches and resonators, actuators for millimeter-scale robotics, droplet sensors and medical transducers.[21] The key to all of these applications is to preserve large piezoelectric coefficients at small thicknesses and after the fabrication process. The second chapter will also provide an overview of how the dielectric and piezoelectric properties can be affected by microstructure and mechanical constraints.

The possibility of scaling down the size of resonating elements using MEMS motivated the development of a new fabrication approach for the next generation of medical ultrasound

devices.[21-23] The second chapter will conclude with a review of the state of the art in miniaturized ultrasound systems.

1.2 Statement of Problem

PZT thin films deposited on rigid substrates have not yet matched the property values of donor-doped "soft" PZT ceramics. Some of the factors that contribute to lowering the functional properties of thin films are submicron grain sizes, higher defect concentrations, compositional heterogeneity and substrate clamping experienced by thin films.

This motivated the study of $0.3Pb(Ni_{0.33}Nb_{0.67})O_3$ - $0.7PbZr_{0.45}Ti_{0.55}O_3$ films. A chemical solution deposition process was developed for this system. Of particular interest was whether large grained (>100 nm) films could be grown at comparable processing temperatures to those used for PZT piezoelectric films. The relative role of grain size on electrical properties is examined in chapter 3.

As devices continue to be miniaturized, the need for *local* characterization techniques with resolution on the order of 100 nm becomes more acute. With the advent of piezoresponse force microscopy (PFM), the investigation of nanoscale ferroelectric phenomena has become more accessible; considerable strides have been made to fully harness the potentials of this technique.[24,25] PFM can provide information on *local* surface potential and charge distributions, the domain structures, domain wall interaction with defects and domain dynamics.[26-28] In chapter 4, the implementation of an extension to conventional PFM is described; work was done to optimize the excitation signal containing a band of frequencies (band excitation PFM, BE-PFM) for characterization of the nonlinear properties of piezoelectric films. Chapters 5 and 6 describe use of this technique to perform *local* studies of the effect of composition and mechanical constraint on piezoelectric thin films.

Finally, the high quality piezoelectric thin films were exploited in high frequency 1D transducer arrays. For high-resolution images, high frequency is necessary, which in turn requires closely spaced transducer elements. Additionally close-coupled electronics are facilitated with low-voltage transducer operation, and electrically thin elements. Chapter 7 describes the fabrication of high-frequency piezoelectric transducer arrays using thin film processing techniques. Transducer arrays with PZT films were fabricated using micromachining techniques including thin-film deposition and dry etching techniques such as ion beam etching, reactive ion etching and xenon difluoride silicon etching. The resulting devices were characterized for their performance as ultrasound transducers in water.

In conclusion, a summary of the results of this research is reported in chapter 8, together with suggestions for future experiments to broaden the knowledge of domain wall dynamics and *local* defect structures.

Chapter 2

Background

This chapter provides an overview of the literature relevant to the current work. A general background on ferroelectricity and piezoelectricity is offered, followed by a description of the different contributions (intrinsic and extrinsic) to the dielectric and piezoelectric properties. A literature survey follows on the effect of microstructure and mechanical constraints on the extrinsic contributions to the properties. The chapter will conclude with a review of state-of-the-art micromachined ultrasound systems for imaging.

2.1 Ferroelectric Thin Films and Applications

Ferroelectricity is defined as the ability of a material to reorient permanently a spontaneous polarization between crystallographically defined directions at a sustainable electric field.[29]

Ferroelectric materials are suitable for many applications. In thin film form, ferroelectrics have been used for several years in nonvolatile memories. Components based on ferroelectric thin films are also being developed for various sensor and actuator applications and for tunable microwave circuits. Among ferroelectric films, the majority of the applications utilize materials with the perovskite crystal structure as depicted in Figure 2.1. These materials have the general formula ABX_3, where A and B are cations and X is an anion. Usually, ferroelectric perovskites transition from a cubic paraelectric high temperature state to a ferroelectric state with a lower symmetry where some of the atoms are slightly displaced, giving a net permanent dipole

moment. The transition point from the paraelectric to the ferroelectric phase is defined as the Curie temperature (T_c).[30]

One distinct feature of the ferroelectric character of a material is the polarization – electric field (P-E) hysteresis loop. The loop is generated by the nucleation and growth of domains of uniform polarization direction under the application of large AC voltage excitation.[30]

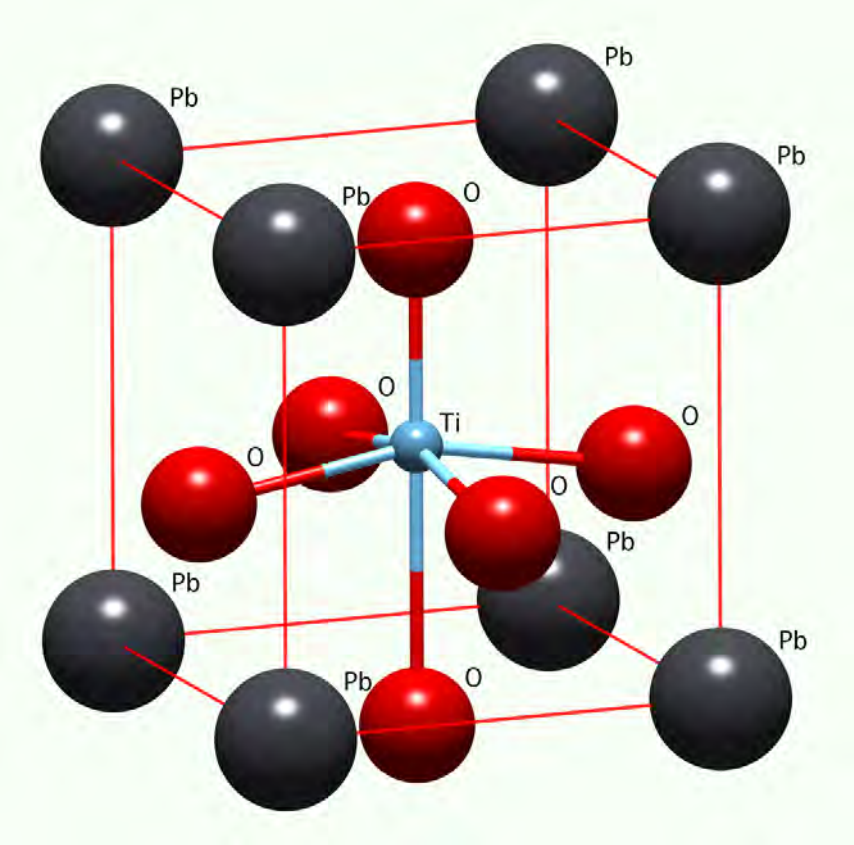

Figure **2-1**: Tetragonal $PbTiO_3$ crystal structure showing deformation of the unit cell along the *c* axis at temperatures below T_c. The labels indicate the Pb atoms sitting at the corners, the Ti atom in the center and the O atoms sitting on the faces of the unit cell.

Active research on ferroelectric thin films began in the late 1960s, with the advent of small- and medium-scale integration in Si devices and when new deposition techniques excited interest in the use of ferroelectric thin films to fabricate non-volatile memories.[31,32] Despite the initial research, issues related to the deposition of ferroelectric thin films slowed down progress in

memory and IR sensor devices until the end of the 1980s.[33-39] Soon after, with the intent of adding sensing and actuating functionalities exploiting the large piezoelectric coefficients of ferroelectric thin films to microelectronic devices, the first steps in the field of microelectromechanical systems (MEMS) were made using PZT.[40-44] Today ferroelectric films are used in a number of applications such as capacitors, non-volatile memories, ink-jet printers, RF switches, energy scavengers, actuators for mm-scale robotics, micropumps and sensors.[15,21,45]

Considerable research has been conducted worldwide to understand the physics and processing issues that determine the performance of the films in such applications.[46,47] Nonetheless, many open questions remain, including the origin of lower permittivity and piezoelectric properties of thin films when compared to bulk counterparts.

2.2 Piezoelectric Thin Films

Natural piezoelectric crystals, such as quartz and tourmaline, are rarely used in sensor and actuator applications because of their weak piezoelectric properties.[2] Polycrystalline ferroelectric materials such as lead zirconate titanate (PZT) are the most popular ceramics for piezoelectric applications. They offer large piezoelectric coefficients along the polarization axis at relatively lower costs compared to single crystals. The phase diagram of PZT (see Fig. 2-2) shows that the high temperature cubic unit cell undergoes a displacive phase transition into a tetragonally distorted structure on the Ti-rich side, while the structure is rhombohedral on much of the Zr-rich side.

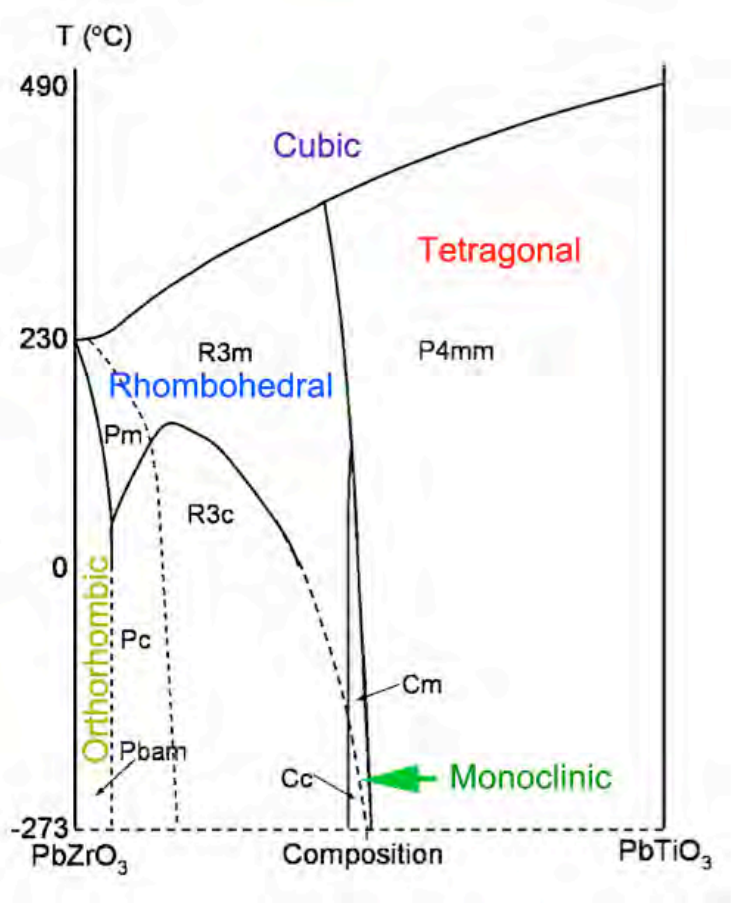

Figure **2-2**: PZT phase diagram (Pm, R3m, P4mm etc. are space group notations). Adapted from Woodward *et al.*[1]

The direct piezoelectric effect is the generation of a polarization that is linearly proportional to an external mechanical stress. The converse piezoelectric effect describes the linear coupling between mechanical strain and an applied electric field.[2]

$$D_i = d_{ijk}\sigma_{jk} \quad \text{or} \quad D_i = e_{ijk}x_{jk} \quad \text{(direct effect)} \qquad \text{Equation } \mathbf{2\text{-}1}$$

$$x_i = d_{ijk}E_{jk} \quad \text{or} \quad x_i = e_{ijk}E_{jk} \quad \text{(indirect effect)} \qquad \text{Equation } \mathbf{2\text{-}2}$$

With the development of piezoelectric microdevices,[14,48] a lot of effort has been spent on the optimization of processing conditions and properties of integrated PZT. PZT is the material of choice for piezoelectric film applications when force and output power are important. The high piezoelectric coefficients and the large electromechanical coupling factors make the

morphotropic phase boundary PZT composition useful.[2] A significant increase in properties can be obtained in bulk ceramics and single crystals by mixing relaxor ferroelectrics (such as $PbMg_{1/3}Nb_{2/3}O_3$, PMN; $PbYb_{1/2}Nb_{1/2}O_3$, PYbN; or $PbNi_{1/3}Nb_{2/3}O_3$, PNN) with normal ferroelectrics such as PT or PZT at the expenses of decreasing the ferroelectric to paraelectric transition temperatures.[49] Because of high intrinsic piezoelectric coefficients and low hysteresis in the strain vs. electric field behavior, a few research groups tried to grow these compositions as piezoelectric films.[5,50-52] However, the state of this field lags that of PZT films. Part of this thesis is dedicated to exploring the deposition conditions and properties of lead nickel niobate – PZT thin films.

The tensor coefficient utilized in many piezoelectric MEMS applications is $e_{31,f}$. This parameter relates the in-plane strain to the generated polarization (direct effect) and the piezoelectric stress used to bend a structure to the applied electric field (converse effect). The films are clamped by the substrates and thus cannot vibrate freely. The effective piezoelectric coefficients for clamped films are related to the bulk values by:[2]

$$d_{33,f} = d_{33} - \frac{2s_{13}^E}{s_{11}^E + s_{12}^E} d_{31} \qquad \text{Equation } \mathbf{2\text{-}3}$$

$$e_{31,f} = \frac{d_{13}^E}{s_{11}^E + s_{12}^E} = e_{31} - \frac{c_{13}^E}{c_{33}^E} e_{33} \qquad \text{Equation } \mathbf{2\text{-}4}$$

where s_{ij} and c_{ij} represent components of the elastic compliance and stiffness tensor. $d_{33,f}$ is always smaller than d_{33}, while the absolute value of $e_{31,f}$ is larger than e_{31}.

In PZT, it can be demonstrated that $e_{31,f}$ is at a maximum along the <001> crystallographic direction at compositions close to the MPB. This is shown in Fig. 2-3.

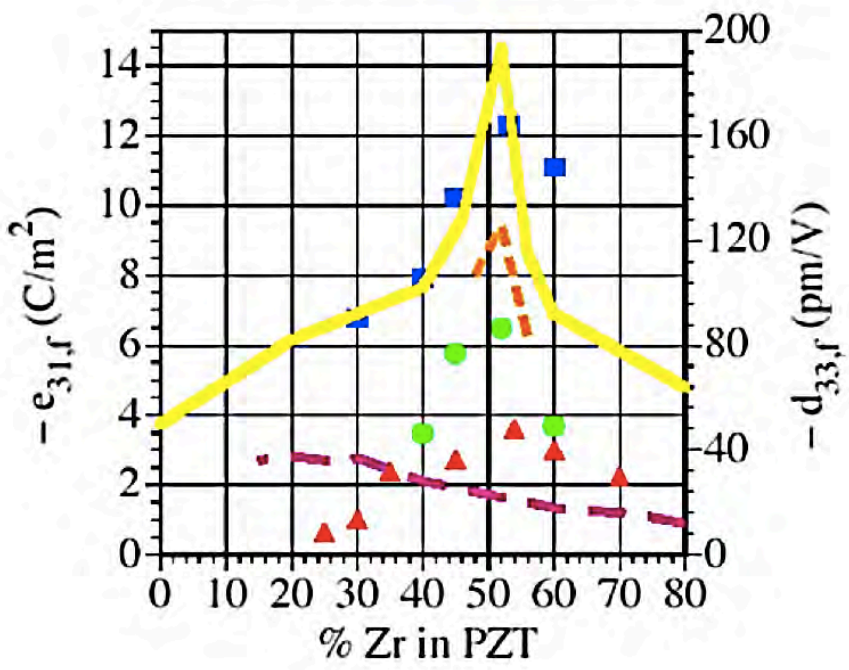

Figure **2-3**: Composition dependence of $e_{31,f}$ (symbols) and $d_{33,f}$ (lines) in PZT thin films.[2-6]

2.3 Ferroelectric Domain Structure

In order to minimize the free energy of the system by satisfying mechanical and electric boundary conditions, ferroelectric crystals often form complex ferroelectric domain patterns, where a domain is defined as a region with a uniform (or nearly uniform) direction of polarization.[29] The boundaries separating different domains are called *domain walls*. Depending on the crystal structure, different angles between the polarization directions of adjacent ferroelectric domains can be identified. In the case of rhombohedrally distorted perovskites, 180º, 109º and 71º domain boundaries exist. For tetragonally distorted perovskites, 180º and 90º domain walls can be found. The electric and elastic boundary conditions, crystal size, defect

structures, applied forces, temperature, and sample history all influence the number and size of the domains.[53]

2.4 Intrinsic and Extrinsic Contributions to the Properties

In general, the dielectric and piezoelectric properties of ferroelectric ceramics can be described in terms of intrinsic and extrinsic contributions. The intrinsic part is due to an average of the response of single domains present in the material. The extrinsic part is associated with the motion of domain walls and/or phase boundaries driven by the electric field.[54]

The Rayleigh law, first developed for ferromagnetic materials, [55] describes the field dependence of the dielectric and piezoelectric properties of many ferroelectric materials as well.[56-60] The physical model is that of mobile interfaces (i.e. domain walls and phase boundaries) interacting with a distribution of pinning centers; the interaction energy as a function of domain wall position can be represented with a potential energy landscape where each well is controlled by the *local* distribution of elastic and electric fields as shown in Figure 2-4. The assumption is that no correlation exists between the depth and shape of adjacent potential wells and that the probing field does not change the domain structure during the measurement.[61] The Rayleigh relations can be used to quantify the irreversible extrinsic contributions to the dielectric properties of ferroelectrics.[60]

$$\varepsilon_r = \varepsilon_{init} + \alpha_\varepsilon E_0 \qquad \text{Equation } \mathbf{2\text{-}5}$$

$$P(E) = (\varepsilon_{init} + \alpha_\varepsilon E_0) \pm \frac{\alpha_\varepsilon}{2}\left(E_0^2 - E^2\right) \qquad \text{Equation } \mathbf{2\text{-}6}$$

where ε_r is the real component of the dielectric permittivity, ε_{init} is the dielectric constant at the limit of zero applied field amplitude; it is the reversible Rayleigh coefficient. P is the measured

dielectric polarization, and α_ε describes the linear dependence of the dielectric constant ε_r on the amplitude of the applied field E_0.

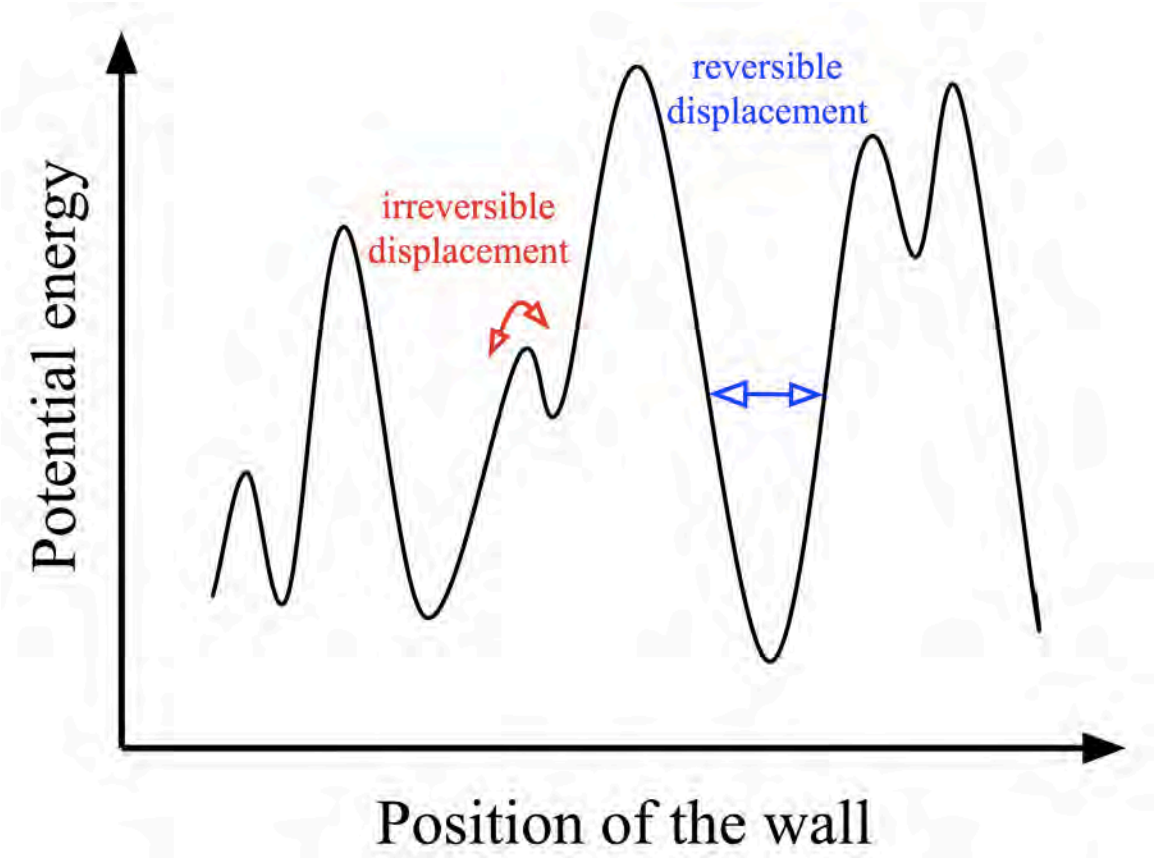

Figure **2-4**: Schematic of a potential landscape experienced by phase boundaries or domain walls. Irreversible motion occurs if the equilibrium position of the interface changes after applying an electric field.

When the extrinsic contributions of thin films are compared to those of bulk ceramics of the same composition, a smaller proportion of extrinsic contributions to the properties is observed. This may be due to the relatively small grain sizes, mediocre crystal quality, compositional heterogeneity, and substrate clamping experienced by thin films. Many of these factors are a result of thin film processing conditions, and are likely associated, at least in part, with the low annealing temperatures employed (significantly lower than ceramic sintering temperatures).

2.5 Impact of Grain Boundaries on Extrinsic Contributions to the Properties

As shown by Kim *et al.* submicron average grain sizes can limit the piezoelectric properties of PZT bulk ceramics; a decrease of 32% for the longitudinal piezoelectric coefficient d_{33} was observed going from average grain sizes of 3 μm to 160 nm, with a faster decay of the properties in the 160 -800 nm average grain size range.[7] This is shown in Figure 2.5. As reported in Kim's work and elsewhere, samples with smaller average grain sizes may present fewer domain variants, which may complicate domain wall rearrangements during polarization switching or poling.[7,62] Also, a denser network of small and large angle grain boundaries is expected to decrease the domain wall mobility, therefore reducing the extrinsic contribution to dielectric and piezoelectric properties.

Ihlefeld *et al.* showed that the properties of $BaTiO_3$ thin films are also dependent on grain size.[63,64] By varying the annealing temperature of $BaTiO_3$ thin films, mass transport was facilitated and larger grains were obtained. However, bulk ceramic processing temperatures cannot be used in most films on Si substrates. This is due both to the build up of large tensile stresses in the plane of ferroelectric films on Si substrates (which affect the reorientation of polarization under an applied electric field)[65] as well as degradation of the Pt electrodes on Si at high temperatures. For this reason, the average grain size of ferroelectric thin films on Pt-coated Si substrates are typically well below 1 micron.

Chapter 3 will describe how fluxing with lead nickel niobate can promote grain growth and increase the extrinsic contributions to the properties in PZT based piezoelectric thin films.

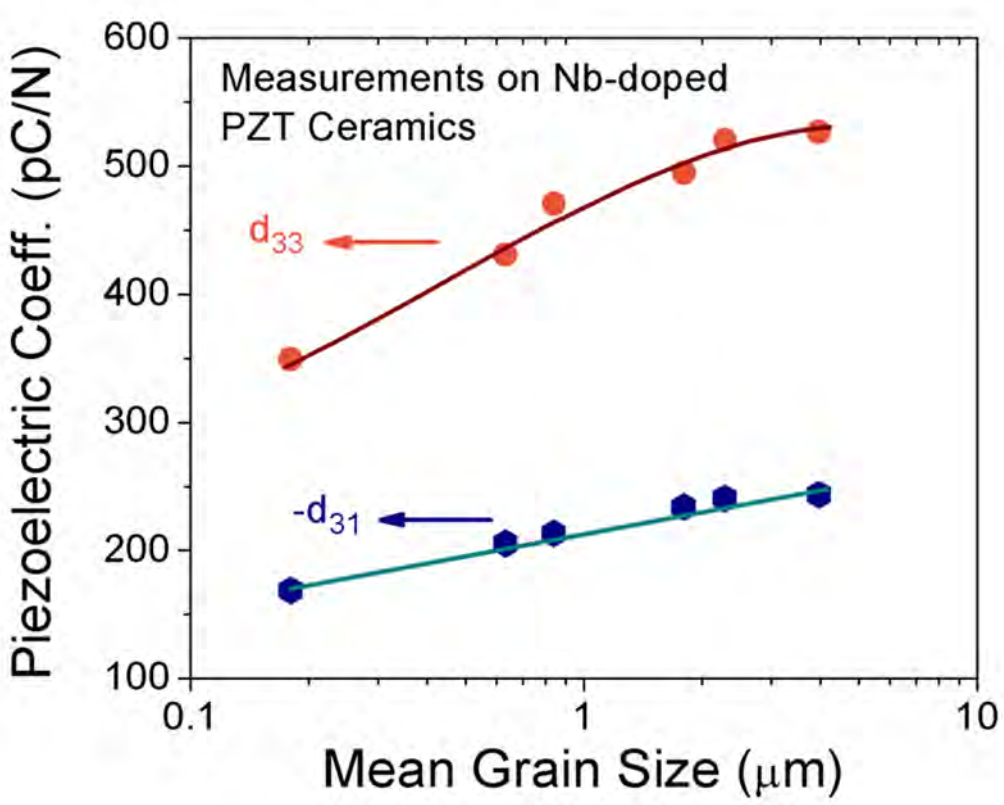

Figure **2-5**: Effect of grain size on the piezoelectric coefficients of Nb-doped PZT bulk ceramics.[7]

2.6 Impact of Composition on Extrinsic Contributions to the Properties

To date, there are comparatively few studies on the relationship between composition, crystallographic phase and extrinsic/intrinsic contributions to the dielectric and piezoelectric properties. A summary of the available literature is given in Table 2-1. Demartin and Damjanovic quantified the fraction of irreversible contribution to the direct piezoelectric effect for different bulk ceramic PZT compositions.[54] Percentages of 22.4, 13.8, and 7.3 % were calculated for the rhombohedral, MPB and tetragonal compositions respectively at 2 MPa ac

pressure; they suggested that the larger irreversible contributions for the rhombohedral composition are due to the smaller spontaneous strain, and hence higher domain wall mobilities.

Eitel *et al*. studied the nonlinear dielectric and piezoelectric response in (1-x) $BiScO_3$ - (x) $PbTiO_3$ (BS-PT) bulk ceramics; they observed the highest ratio of irreversible to reversible contributions in the $0.38BiScO_3$-$0.62PbTiO_3$ rhombohedral phase sample and the lowest for the $0.30BiScO_3$-$0.70PbTiO_3$ tetragonal sample.[57]

Pramanick *et al.* used X-ray data to directly link non-180° domain wall motion with the Rayleigh law for the converse piezoelectric effect in PZT ceramics.[66] The highest irreversible to reversible ratio was observed for the rhombohedral La-doped PZT series of samples (Table 2-1). The macroscopic strain depends on both the number of spontaneous ferroelastic distortions (4 and 3 for the rhombohedral and tetragonal samples, respectively) and the strain associated with each. Since the rhombohedral sample had the smallest spontaneous distortion[67] and showed the highest values of $\alpha_d / d_{33,init}$, they concluded that a high degree of non-180º domain wall motion must be associated with the Zr-rich sample.

Li *et al.* explored the reversible and irreversible contributions to the piezoelectric activity for a series of compositions in domain engineered PMN-PT single crystals across the rhombohedral, monoclinic and tetragonal phase fields.[68] They reported a sudden increase in the $\alpha_d / d_{33,init}$ ratio for compositions close to the rhombohedral-monoclinic and monoclinic-tetragonal phase boundaries (Table 2-1). The enhanced irreversible contributions were attributed to favored domain wall mobility for compositions close to a MPB.[69,70]

Chapter 5 will compare the extrinsic contributions to dielectric and piezoelectric properties in $Pb(Ni_{0.33}Nb_{0.67})O_3$-$Pb(Zr_xTi_{1-x})O_3$ thin films of different Zr/Ti ratios deposited on $SrTiO_3$ substrates to assess the influence of composition.

Table **2-1**: Literature survey of Rayleigh parameters as a function of composition. *Li et al. reported the errors based on 3 samples of the same composition, Eitel *et al.* and Pramanick *et al.* reported fitting errors. ** Bulk ceramic. *** Single crystal. **** Extrapolated values.

System and Composition	$\alpha_d / d_{33,init} x\ 10^3$ *(cm/kV)*	*Error**	*Reference*
BC,** 0.36 $BiScO_3$ - 0.64$PbTiO_3$ MPB	68.2	3.0	Eitel *et al.*[57]
BC, PZT MPB	57.7	0.8	Eitel *et al.*[57]
BC, 0.38 $BiScO_3$ - 0.62 $PbTiO_3$ Rhombohedral	77.4	2.5	Eitel *et al.*[57]
BC, 0.30 $BiScO_3$ - 0.70 $PbTiO_3$ Tetragonal	27.0	1.7	Eitel *et al.*[57]
BC, 2 at% La doped PZT MPB	93.1	2.3	Pramanick *et al.*[66]
BC, 2 at% La doped PZT Rhombohedral	173.7	6.1	Pramanick *et al.*[66]
BC, 2 at% La doped PZT Tetragonal	67.8	10.0	Pramanick *et al.*[66]
SC,*** 0.75 $PbMg_{1/3}Nb_{2/3}O_3$ - 0.25 $PbTiO_3$ Rhombohedral	25.9	6.2	Li *et al.*[68]
SC, 0.71 $PbMg_{1/3}Nb_{2/3}O_3$ - 0.29 $PbTiO_3$ Rhombohedral	53.8	9.1	Li *et al.*[68]
SC, 0.70 $PbMg_{1/3}Nb_{2/3}O_3$ - 0.30 $PbTiO_3$ Rhombohedral	49.8	9.0	Li *et al.*[68]
SC, 0.69 $PbMg_{1/3}Nb_{2/3}O_3$ - 0.31 $PbTiO_3$ Monoclinic	95.0	22.7	Li *et al.*[68]
SC, 0.67 $PbMg_{1/3}Nb_{2/3}O_3$ - 0.33 $PbTiO_3$ Monoclinic	32.1	6.1	Li *et al.*[68]
SC, 0.65 $PbMg_{1/3}Nb_{2/3}O_3$ - 0.35 $PbTiO_3$ Monoclinic	90.8	18.9	Li *et al.*[68]
SC, 0.63 $PbMg_{1/3}Nb_{2/3}O_3$ - 0.37 $PbTiO_3$ Tetragonal	47.9	20.4	Li *et al.*[68]
BC, Ferroperm PZ26****	39.0	1.0	Garcia *et al.*[71]
BC, 1 wt % Nb doped $PbZr_{0.58}Ti_{0.42}O_3$****	940.0	4.0	Morozov *et al.*[72]
BC, soft $PbZr_{0.52}Ti_{0.48}O_3$****	680.0	1.0	Li *et al.*[73]

2.7 Impact of Substrate Clamping on Extrinsic Contributions to the Properties

In most reported continuous films, the contributions to the piezoelectric response from domain wall motion are limited due to the presence of pinning sites and residual stresses.[74,75] For instance in tetragonal PZT thin films, the domain structure at room temperature is largely dictated by the thermal mismatch with the substrate;[76] Tuttle *et al.* demonstrated that the domain state, and hence the observed electrical properties of PZT thin films, are directly related to the sign of the film stress at the ferroelectric transition temperature (transformation stress model).[65] In particular, films under tensile in-plane stress tended to have the polarization predominantly in the film plane, with the result that the permittivity was high, and the relatively polarization comparatively low. In contrast, films with compressive in-plane stresses had the spontaneous polarization directed largely perpendicular to the substrate, producing large remanent polarizations and smaller permittivities. More recently Miyoshi *et al.* studied the effects of substrate clamping on MPB PZT films processed by aerosol deposition on yttria stabilized zirconia.[77] They reported a compressive in-plane stress as expected from the mismatch in thermal expansion coefficient between the film and the substrate. Because of the residual stress, 90º domain wall motion was severely limited. In agreement with the transformation stress model, they also observed a dominant c-domain distribution in their films. Yokoyama *et al.* and Utsugi *et al.* utilized control of the in-plane stress state to control domain state in epitaxial films.[78,79]

Several authors have investigated the role of substrate clamping on the electromechanical behavior of PZT thin films. Kholkin *et al.* derived electrostriction coefficients using double beam interferometry in a number of ferroelectric films, including PZT. They found that the electrostriction coefficients had a weak electric field dependence and were much smaller (52% for PZT at the MPB composition) than those of bulk ceramics. The origin of these phenomena was attributed to the substrate clamping.[80] Li *et al.* characterized the complex piezoelectric

response for PZT, La doped PZT and lead zirconate thin films on Si substrates as a function of frequency and DC bias.[81] Their work shows a decrease in the electromechanical coupling coefficient as a function of frequency, attributed to a clamping effect by the substrate. Lian and Sottos analyzed the piezoelectric response in sol-gel deposited $PbZr_{0.52}Ti_{0.48}O_3$ by laser interferometry as a function of externally applied mechanical strain.[82] They reported an increase in the field-induced strain with the application of a compressive strain opposing the residual tensile stress. These findings are in contrast with the work of Trolier-McKinstry *et al.*[83] In that work, no significant change in the properties was observed even when the films were brought through the zero global stress condition.

McIntyre *et al.* also observed modest changes in low field permittivity at increasing levels of tensile biaxial strain in tetragonal PZT thin films.[84] They suggested that the applied strains are relieved by 90º domain wall reconfiguration as observed from changes in the switching behavior of the films under tensile strain.

Roytburd *et al.* predicted that by laterally subdividing PZT thin films, such that the in-plane dimensions are smaller than the thickness of the film, the mechanical constraints and the internal stresses are also reduced.[85] This was confirmed experimentally by fabricating submicron epitaxial PZT capacitors. For example, Nagarajan *et al.* demonstrated using piezo-force microscopy (PFM) that it is possible to reach higher values of longitudinal piezoelectric coefficients when the in-plane constraints are removed.[86] Nagarajan *et al.* also reported a significant increase in the contribution of 90º domain wall motion to the dielectric and piezoelectric response of tetragonal PZT in 1 μm^2 islands.[87] Similarly, a significant increase of the remanent d_{33} in piezoelectric loops in PZT islands with lateral dimensions below 200 nm in diameter was shown by Bühlmann *et al*.[88] However, they attributed the increase in properties to a considerable reduction of *a* domains, rather than to increased mobility of domain walls.

Chapter 6 will show the effects of *local* mechanical boundary conditions on the extrinsic contributions to the dielectric and piezoelectric properties of PZT on Si substrates.

2.8 Band Excitation PFM as a Means to Study Local Nonlinearities

Measurements of the extrinsic contributions to the properties are generally macroscopic in character, where thousands to millions of domain walls are sampled collectively. Thus, the nanoscale phenomena governing the extrinsic contributions through domain wall or phase boundary motion remain largely unknown. It was recently demonstrated that the application of a band excitation technique to conventional piezo-force microscopy (BE-PFM) can successfully probe the converse nonlinear piezoelectric response at a *local* scale.[89]

However, when scanning probe methods are employed to probe nonlinearities, artifacts associated with a dynamic response of the cantilever in contact with the film surface need to be minimized. Chapter 4 describes an approach to reduce the dynamic nonlinearities and quantitatively collect *local* converse piezoelectric nonlinearity measurements.

2.9 Membrane Based Microfabricated Transducer Systems

The scientific endeavor of this work is aimed at the optimization of the piezoelectric properties of PZT-based thin films for a high frequency ultrasound transducer application. To set the work in context, this section provides a review of the state of the art of micromachined ultrasonic transducers (MUT).

Conventional piezoelectric transducers utilize bulk piezoelectric ceramics or single crystals diced into small resonating elements. The large thickness implies that the devices require

relatively large driving voltages. Furthermore, the large dimensions of the resonating elements limits the resolution for these devices.[90-92]

Two viable alternatives offering large bandwidth, ease of fabricating large arrays and potential for integration with supporting integrated circuitries are capacitive micromachined ultrasound transducers (CMUT) and piezoelectric micromachined ultrasound transducers (PMUT).

2.9.1 Capacitive Micromachined Ultrasound Transducers (CMUT)

CMUT have been investigated for a range of applications that includes medical imaging, therapeutics and sensor applications. The CMUT cell structures offer some advantages compared to piezo-based transducers, for instance, a larger bandwidth in immersion even at higher operational frequencies.[93] A CMUT can be thought of as a parallel plate capacitor with a fixed back plate and a flexible suspended electrode. Acoustic waves striking the surface cause the flexible electrode to oscillate, changing the inter-electrode distance and the capacitance of the structure. This gives rise to a small alternating current. Conversely, to generate acoustic waves, the plate is driven by superimposing an alternating voltage V_{AC} on a polarization voltage V_{DC}. An alternating voltage applied to the capacitor without the polarization voltage would cause the attraction to the top electrode to deflect twice in a cycle since the electrostatic force is only attractive.[94] The maximum amplitude for the polarization voltage is determined by the collapsing field, or the field at which the flexing plate collapses over the backplate. The large bandwidth, even higher than 100 % in immersion tests, and large coupling coefficients (defined as the ratio between the mechanical work performed by and the electrical energy delivered to the device) are related to the inherent good acoustic match between the compliant plate and the liquid medium.[93] In Figure 2-6, the V_{dc} dependence of the coupling coefficient is illustrated. Although the

operating conditions should not be too close to collapse, coupling coefficients higher than 70% have been demonstrated.[95,96]

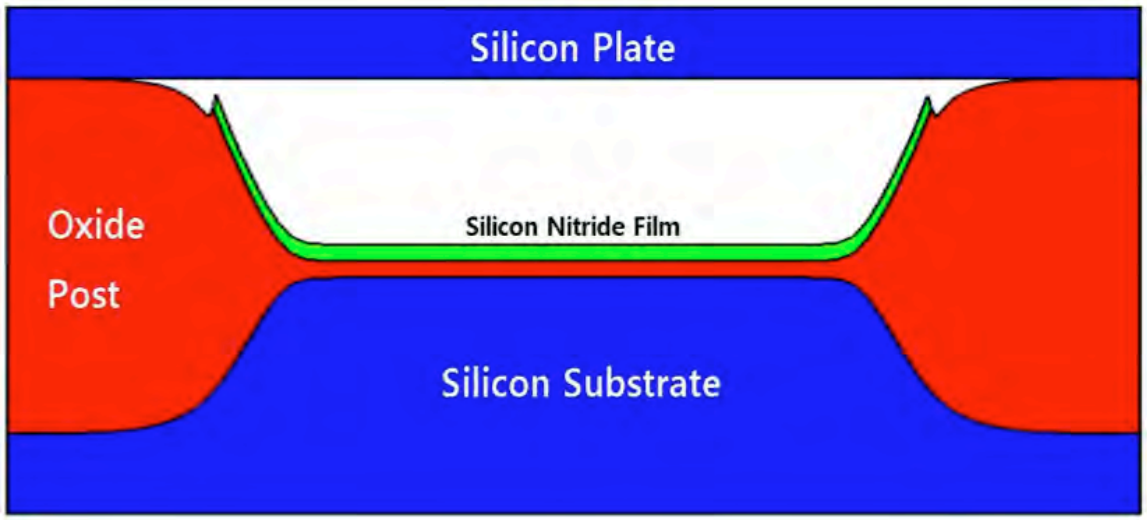

Figure **2-6**: Schematic cross-section of a CMUT cell.[8]

Despite the good electromechanical properties, with a calculated coupling coefficient k close to 100 % close to the collapse voltage, voltages as high as 100 V are required to drive CMUT devices.[97] In addition, stray capacitance and noise may be problematic due to the low capacitance of each CMUT element.

Also because of the relatively low capacitance C_0 of the air-gap, the emission power, P_{mech} as reported in 2-7[98] can be expected to be relatively low.

$$P_{mech} = k^2 P_{el} = k^2 \omega C_0 U_{rms}^2 \qquad \text{Equation } \mathbf{2\text{-}7}$$

where ω is the angular frequency and U_{rms} is the root mean square voltage applied to the capacitor.

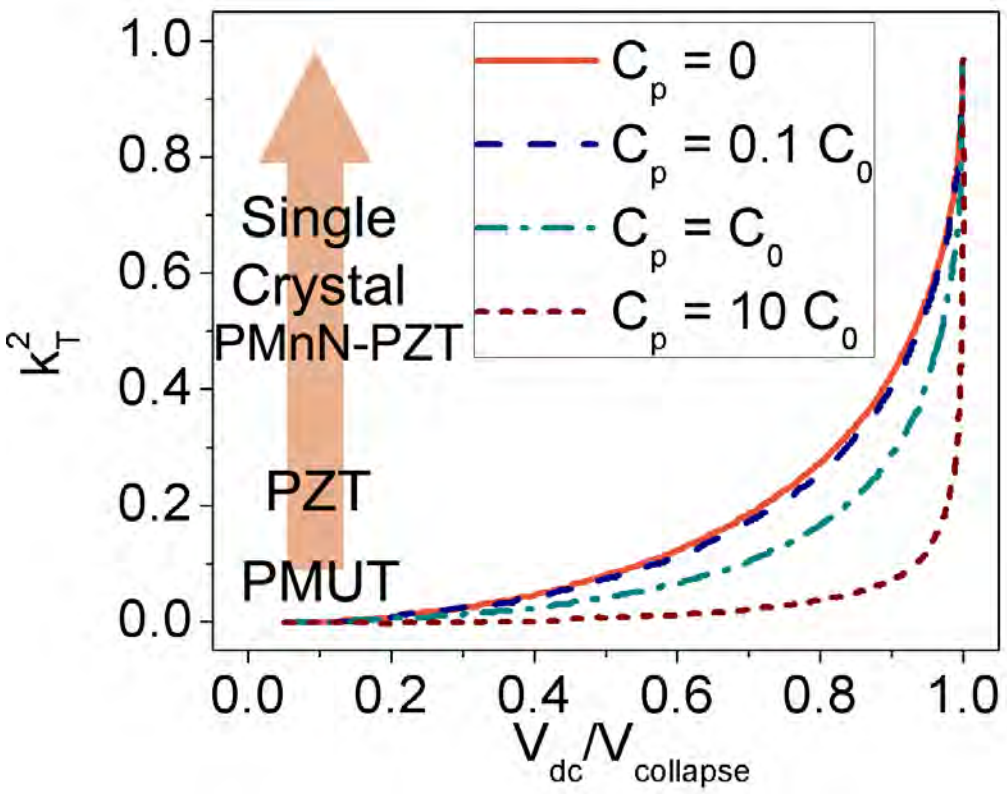

Figure **2-7**: Coupling coefficients for CMUT devices as a function of polarization voltage normalized by the collapse voltage for different levels of parasitic capacitance C_p. C_0 is the CMUT device capacitance at $V_{dc} = 0$. Data extracted from Yaralioglu *et al.*[9] The figure compares CMUT coupling coefficients with those of relaxor single crystals (Single Crystal), Mn and Nb doped PZT epitaxial thin films (PMnN-PZT), PZT bulk ceramics (PZT) and PMUT devices.[10-12]

2.9.2 Piezoelectric Micromachined Ultrasound Transducers (PMUT)

One alternative to CMUTs is piezoelectric micromachined ultrasound transducers (PMUT). The operating principle of this family of transducers entails flexural motion of a membrane as a result of piezoelectrically-induced stresses. Typically, these devices adopt either

a d_{33} approach by means of interdigitated electrodes or a d_{31} approach as shown in Figure 2-8.[11,13,99]

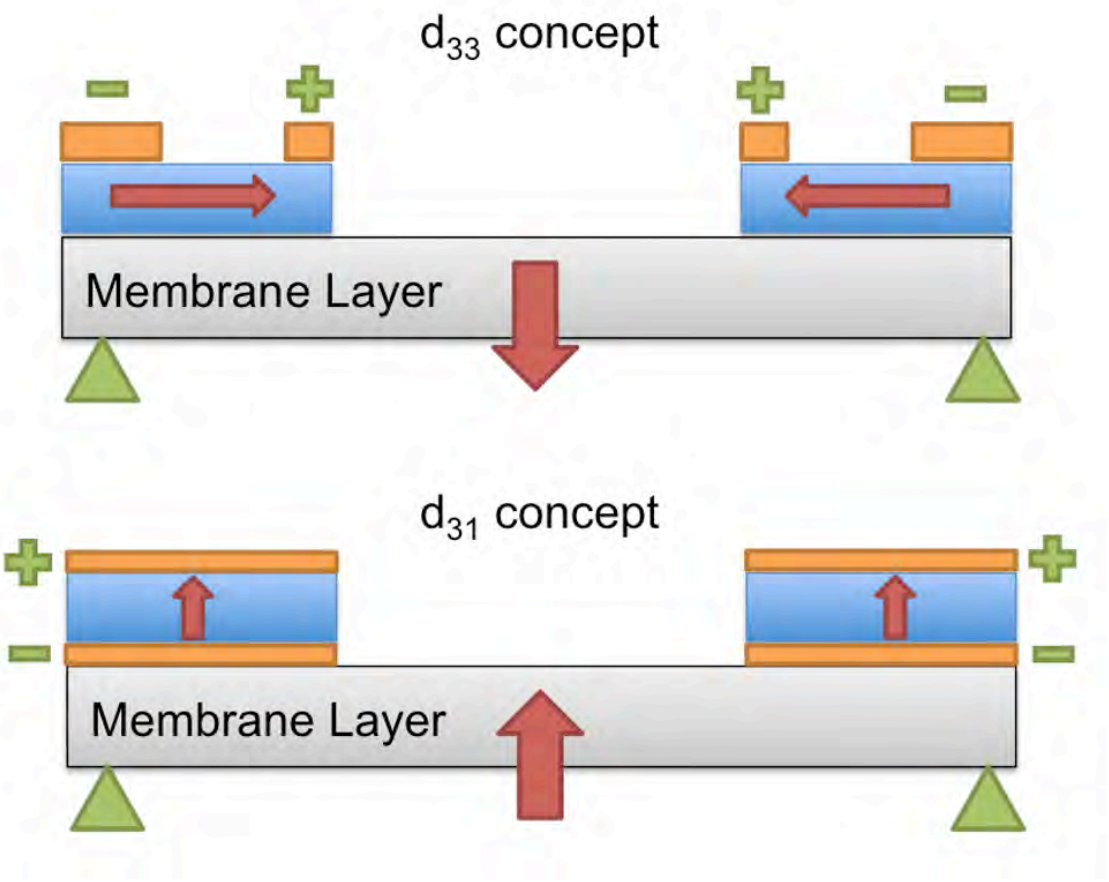

Figure **2-8**: Piezoelectric micromachined ultrasound transducer concepts operated in d_{33} and d_{31}. Adapted from Klee *et al.*[13]

Bandwidths larger than 100 % and coupling coefficients k_T as large as 40% have been demonstrated for PMUT operating in d_{33} mode.[13] In PMUT devices operated via d_{31}, the device operates as a unimorph, where the piezoelectric material layer is coupled with a passive layer (most often Si, SiO_2 or Si_3N_4).[15]

Calculations by Dubois and Muralt showed that the coupling coefficients in PMUT actuated in 31 mode reduces if the neutral plane is situated inside the PZT layer (Fig. 2-9).[14] Also the maximum coupling coefficient does not show a strong dependence on the PZT thickness,

saturating at around $k^2 \sim 3.5\%$; however the maximum becomes broader with increasing thickness.

The resonance frequency for PMUT plate structures increases as $f_0 \propto h / a^2$, where h is the thickness of the entire structure and a is the plate diameter. If the application defines the size of the plate and the frequency, the thickness of PZT and silicon can be determined from the condition of maximal coupling.

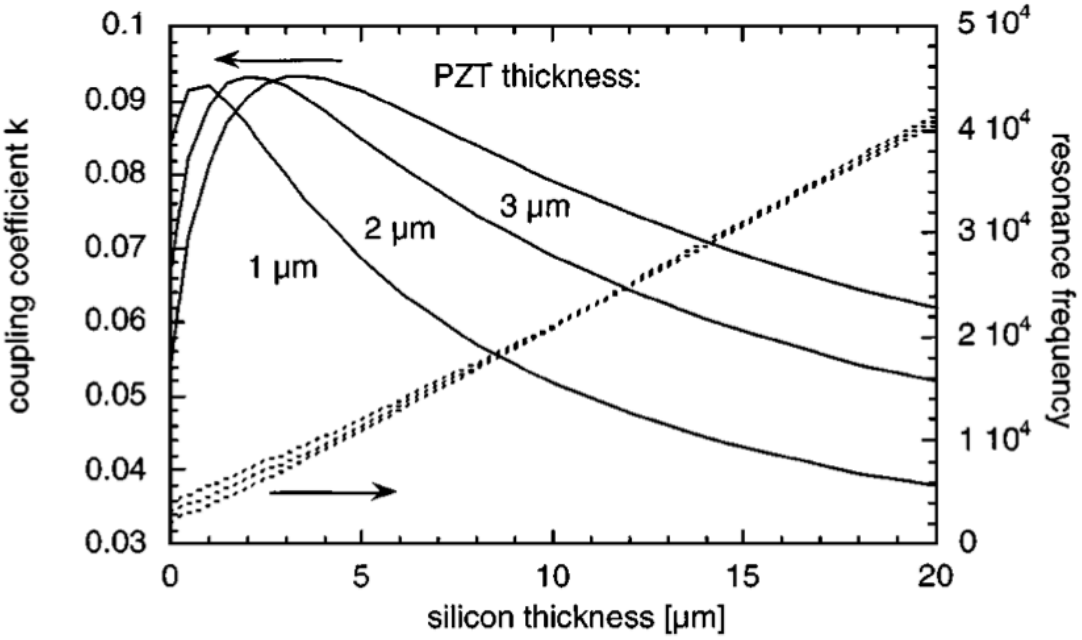

Figure **2-9**: Calculated values of k^2 for a stress free diaphragm of 300 μm diameter. The maximum k^2 value does not increase with the PZT thickness; the optimum silicon thickness and width depend upon it. From Dubois and Muralt.[14]

Advances in the deposition of piezoelectric thin films allow the fabrication of planar PMUT structures capable of large displacements at small actuation voltages.[21] By depositing piezoelectric thin films on larger compliant resonating elements to define the working frequency and obtain a better acoustical impedance match with the medium, further improvements in the sensitivity and power output of PMUT devices can be expected. Chapter 7 will describe the testing of a PMUT prototype using a diaphragm geometry.

Chapter 3

Synthesis and Properties of Lead Nickel Niobate – Lead Zirconate Titanate Films*

3.1 Abstract

A chemical solution deposition procedure was developed for lead nickel niobate – lead zirconate titanate (0.3)$Pb(Ni_{0.33}Nb_{0.67})O_3$ - (0.7)$Pb(Zr_{0.45}Ti_{0.55}O_3)$, (PNN-PZT) ferroelectric thin films. On increasing the crystallization temperatures from 650 to 800 °C, the average grain diameters grew from 110 to 270 nm. Dielectric permittivities ranging from 1350 to 1520 and a transverse piezoelectric coefficient $e_{31,f}$ as high as – 9.7 C/m^2 were observed. The permittivity and piezoelectric response increased for samples with larger grain size. Higher thermal budgets also imposed higher levels of in-plane tensile stress on the perovskite layer; the imposed stress reduced the remanent polarization for the samples. Nonetheless, samples processed at higher temperatures showed larger average grain diameters and higher extrinsic contributions to the properties.

* Most of the chapter appears in F. Griggio and S. Trolier-McKinstry, J. Appl. Phys. **107**, 024105 (2010).

3.2 Introduction

Microelectromechanical systems (MEMS) are an active subject of study because of the continuing trend towards device miniaturization. The integration of functional electroceramic films into Si-based MEMS structures offers the ability to integrate large device arrays on a wafer; potential applications include inkjet printers, accelerometers, gyroscopes, and pressure sensors, among others.[100] Improvements in the sensor and actuator performance can be achieved through the use of optimized materials. Specifically for piezoelectric MEMS, the coefficient which should be maximized is, in many cases, the transverse piezoelectric response $e_{31,f}$.[101]

The most widely used ferroelectric thin films in these applications are based on lead zirconate titanate (PZT). Many factors influence the piezoelectric response in PZT, including composition, grain size and orientation. In terms of composition, the morphotropic phase boundary (MPB) between ferroelectric phases favors strong piezoelectric effects due to the large polarizability.[2,30] Grain size is also critical; it has been demonstrated for bulk PZT ceramics that as the grain size decreases below a few microns, the domain structure changes. This, in turn limits the extrinsic (e.g. domain-wall or phase boundary motion related) contributions to the dielectric constant and loss, piezoelectric coefficients and electromechanical coupling coefficients.[7] The property degradation can be partially recovered by increasing the amount of donor dopant in fine-grained PZT ceramics.

The relatively small grain sizes, mediocre crystal quality, compositional heterogeneity, and substrate clamping experienced by thin films limit the piezoelectric properties of thin films with respect to bulk ceramics.

Consequently, it becomes interesting to determine whether or not the properties of piezoelectric films could be increased by improving the structural quality and grain size, as has been shown for $BaTiO_3$ - based films.[63] One way to facilitate mass transport, in order to obtain

grain growth, would be to employ higher thermal budgets. However, this will come at the expenses of higher tensile stresses in the plane of the thin films on Si substrates,[102] which can lead to excessive curvature of released structures. Moreover, many Pt-coated Si substrates do not handle processing temperatures above ~ 800 °C gracefully.[103] Thus, while elevated temperatures should improve grain growth (and potentially properties), it is useful in MEMS applications to utilize comparatively modest processing temperatures.

As a means of approaching this problem, relaxor-based solid solutions with PZT were considered. Many of these materials show much easier single crystal growth than is characteristic of PZT.[49,104] As a model system, $Pb(Ni_{0.33}Nb_{0.67})O_3$ - $Pb(Zr_xTi_{1-x}O_3)$ (PNN-PZT) was chosen. It is anticipated that below the temperatures required for single crystal growth, the incorporation of NiO and excess PbO should also stimulate diffusion. For example, Hrovat *et al.* [105] extrapolated a eutectic at 875 ºC for the (1-x)PbO-xNiO system around x = 0.07. Shiratsuyu *et al.* were able to lower the sintering temperature of 0.6PZT-0.4PNN ceramics from 1100 to 800 ºC with excess NiO and PbO.[106] This offers the possibility of preparing larger grained piezoelectric thin films, in order to explore the relative importance of grain size in influencing the film properties. Moreover, many relaxor ferroelectric - PZT solid solutions exhibit superior dielectric and piezoelectric properties at room temperature; for example the piezoelectric coefficient d_{ijk} of PNN-PZT can be twice as large as that of pure PZT.[49] As reported by Kawakami *et al.* [107] thick films of PNN-PZT obtained via an aerosol deposition method had a transverse piezoelectric coefficient d_{31} of -164 pm/V.

This information motivated the study of PNN-PZT films. A chemical solution deposition process was developed for this system. Of particular interest was whether large grained films could be grown at comparable processing temperatures to those used for PZT piezoelectric films. The relative roles of grain size and tensile stress were then examined. Finally, the extrinsic properties of the films were investigated as a function of grain size.

3.3 Experimental Procedure

3.3.1 PNN-PZT Film Preparation

Thin (<300 nm) PNN-PZT films were prepared using a chemical solution deposition process derived from the procedure described by Budd, Dey and Payne for PZT.[35] Lead acetate trihydrate ($Pb(CH_3COO)_2 \cdot 3H_2O$) and Ni acetate tetrahydrate ($Ni(OCOCH_3)_2 \cdot 4H_2O$) were first added to 2-methoxyethanol (2-MOE) in a rotary evaporator flask under an Ar atmosphere. To favor the dissolution, the flask was placed in an oil bath and the temperature was gradually increased from 80 ºC to 120 ºC. The solution was then dehydrated under vacuum until a semidry powder remained. A mixture of zirconium n-propoxide ($Zr(OCH_2CH_2CH_3)_4$), titanium iso-propoxide ($Ti(OC_3H_7)_4$) and niobium ethoxide ($Nb(OCH_2CH_3)_5$) in 2-MOE at room temperature was added and the entire solution was refluxed for 2 h under Ar at 120 ºC. After refluxing, the solution was vacuum distilled and acetylacetone, ($CH_3COCH_2COCH_3$: 22.5 vol % as a chelating agent) and 2-MOE were added to reach the desired solution molarity as shown in Figure 3-1. The final solution was 0.25 M with 5 to 10 mol % Pb excess to compensate for high PbO volatility.[108]

Commercially manufactured (111) Pt/Ti/ SiO_2/Si wafers (Ramtron Int., Colorado Springs, CO) were used as substrates. The substrates were pre-annealed for 60 s at 500 ºC in O_2 immediately prior to solution deposition to remove organic surface contaminants and moisture.

To promote perovskite phase formation along with $\{001\}$ orientation for the PNN-PZT films, a 0.15 M $PbTiO_3$ solution was prepared with 40 % Pb excess. The template solution was deposited through a syringe with a 0.1 μm Whatman filter (Sigma-Aldrich, Milwaukee, WI) and the substrate was spun at 1500 rpm for 30 s using a PWM32 photoresist spinner (Headway

Research, Inc., Garland, TX). The deposited layer was pyrolyzed at 250 and 400 ºC for 1 min respectively and annealed at 580ºC for 1 min.

The PNN-PZT solution was then spun on to the substrate in the same manner as the seed layer. To facilitate a slow organic removal before the crystallization step, a 150 ºC hold for 5 min was used prior to the other pyrolysis steps. After this, the films were exposed successively to 300 and 430 ºC for 1 min each. The process was repeated to build up the desired thickness. The phase evolution was examined as a function of temperature, holding time and Pb excess concentration.

In order to study the microstructure evolution of oriented PNN-PZT films, samples were prepared using various crystallization conditions or Pb excess content. Details of the preparation conditions are given in Table 3-1. Series A samples were deposited from a solution containing 10 mol % Pb excess, and were crystallized at temperatures ranging from 650 – 800 °C using a ramp rate of 50 ºC/s. Series B samples were made by varying the amount of lead excess through the film depth. These samples were crystallized at 700 or 750 ºC using a ramp rate of 50 ºC/s. To further assess the importance of PNN fluxing on mass transport, the microstructures of the films were compared to a set of $PbZr_{0.45}Ti_{0.55}O_3$ (i.e. with the same Zr/Ti ratio as for the PNN-PZT films, but without the PNN) films (Series C). The PZT films were prepared from a solution containing 10 mol % Pb excess. These samples were spin coated, pyrolyzed and annealed following the same procedure used for PNN-PZT films.

Table **3-1**: Preparation conditions for the thin film samples characterized in this study.

Series	*Composition*	*Excess PbO (in solution)*	*Holding temperature and time*
A	$0.3PbNi_{0.33}Nb_{0.67}O_3$-$0.7PbZr_{0.45}Ti_{0.55}O_3$	10 mol%	650 ºC 10 min; 700, 750 and 800 ºC 1 min
B	$0.3PbNi_{0.33}Nb_{0.67}O_3$-$0.7PbZr_{0.45}Ti_{0.55}O_4$	10 mol% first and last layers, 5 mol% middle layers	700 ºC and 750 ºC 1 min
C	$PbZr_{0.45}Ti_{0.55}O_3$	10 mol%	650 ºC 10 min; 700, 750 and 800 ºC 1 min

Phase pure perovskite films with an average thickness of 245 nm were obtained within the detection limits of SEM and XRD analysis for all the PNN-PZT and PZT films prepared using the $PbTiO_3$ seed layer. The $\{100\}$-oriented seed layer promoted strong $\{001\}$-texture in all three series of films, with calculated Lotgering factors above 95% (Fig. 3-3 and 3-4).

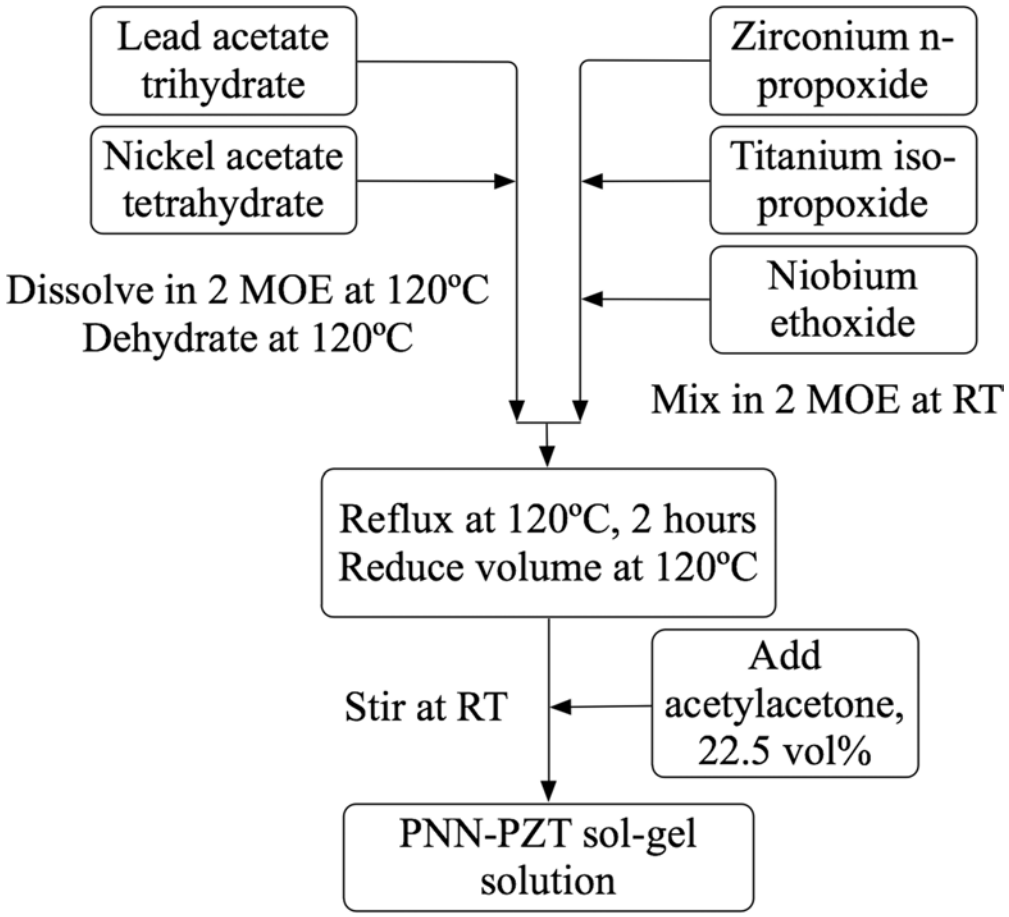

Figure **3-1**: Chemical solution process flow for PNN-PZT films prepared in this investigation.

3.3.2 Film Characterization

The orientation and crystal structure of the films were determined using a Philips Analytical x-ray diffractometer (PANalytical B. V., Almelo, The Netherlands). $Cu-K_{\alpha}$ radiation was used with a flat graphite monochromator; diffraction data were collected between 15 and 70º 2θ at a rate of 3.6° 2θ/min. A Scintag X2 (Scintag, Cupertino, CA) using $Cu-K_{\alpha}$ radiation on a $\theta-2\theta$ goniometer equipped with a Si(Li) Peltier detector in a grazing angle configuration was used to study the formation of second phases close to the surface. The data

reported were collected using a grazing angle of 2º. The degree of {001} texture on samples was estimated using the Lotgering factor;[109] the peak intensities from the films were compared to a randomly oriented crystallized PNN-PZT powder obtained from the same solution. For all estimates of the lattice parameter, the Si substrate was used as an internal standard.

Microstructural features were examined using a JEOL 6700 F field emission scanning electron microscope (FE-SEM) (JEOL Ltd., Tokyo, Japan). The grain diameters were analyzed by measuring 100 grains in the plan-view SEM images.

To enable electrical characterization, platinum top electrodes were sputter deposited using a CMS-18 deposition system (Kurt J. Lesker Company, Clairton, PA) through a shadow mask at a base pressure of 10^{-6} Torr. Circular electrodes with diameters ranging from 1.1 mm to 0.2 mm were prepared; the electrodes were annealed at 500 ºC for 1 min before performing the electrical characterization. Dielectric constant and loss at low field of the PNN-PZT films were determined from capacitance measurements using a HP 4192A LF impedance analyzer (Agilent Technology, Palo Alto, CA) at 10 kHz and an oscillating voltage of 30 mV_{rms}. Polarization-electric field hysteresis was measured using an RT 66A standard standardized ferroelectric test system (Radiant Technology Inc., Albuquerque, NM) in the virtual ground testing mode. When the voltage required for hysteresis loops exceeded the RT 66A tool's 20 V limit, a 10:1 voltage amplifier (AVC Instrumentation, Div. of PCB Piezotronics Inc., Depew, NY) was used. PUND (Positive-Up-Negative-Down) polarization hysteresis loops were measured using a TF Analyzer 2000 (aixACCT Systems GmbH, Aachen, Germany) as a function of temperature in an attempt to remove leakage effects from the hysteresis measurements at high temperature. The nonlinear dielectric measurements and the dielectric measurements as a function of temperature were performed using a HP 4284A precision LCR meter (Agilent Technology, Palo Alto, CA) on aged samples using a heated thin film stage. The measurements were acquired at 10 kHz; for the dielectric nonlinearity measurements the capacitance and loss tangent of the samples were

recorded sweeping from 30 mV to 1 V (rms values). To measure the transverse piezoelectric coefficient $e_{31,f}$ of the films, the wafer flexure technique was used.[110] Before the piezoelectric measurements, the films were poled at 5 times the coercive field for 20 min.

3.4 Results and Discussion

3.4.1 Perovskite Phase Development

$(0.3)Pb(Ni_{0.33}Nb_{0.67})O_3$ - $(0.7)Pb(Zr_{0.45}Ti_{0.55}O_3)$ was chosen as the base composition. This provides a $T_c > 200$ ºC[111] (which was confirmed for the films) and should be at the morphotropic phase boundary, as extrapolated from the phase diagram reported by Gilles.[112] Perovskite phase formation, crystal structure and lattice parameters for films of this composition were determined by XRD at room temperature as a function of the processing conditions.

It was found that when PNN-PZT films were deposited directly on platinized silicon substrates, formation of pyrochlore (or fluorite, here and elsewhere in the chapter) phase was likely. In an attempt to suppress the pyrochlore formation, different ramp rates for the crystallization anneal were tested (50, 80 and 100 ºC/s). It has been reported that fast ramp rates can minimize pyrochlore formation in lead-based perovskite films.[113] As seen in Figure 3.2, the ramp rate influenced the perovskite orientation somewhat, with higher levels of {001} orientation being observed for films annealed at higher ramp rates. However, pyrochlore was evident for all temperatures and ramp rates explored. The presence of a very fine-grained matrix and a rosette-like microstructure, analogous to those described by Tuttle *et al.*[114], was more sensitive than the diffraction patterns to the detection of the pyrochlore phase (See Fig. 3.4 a).

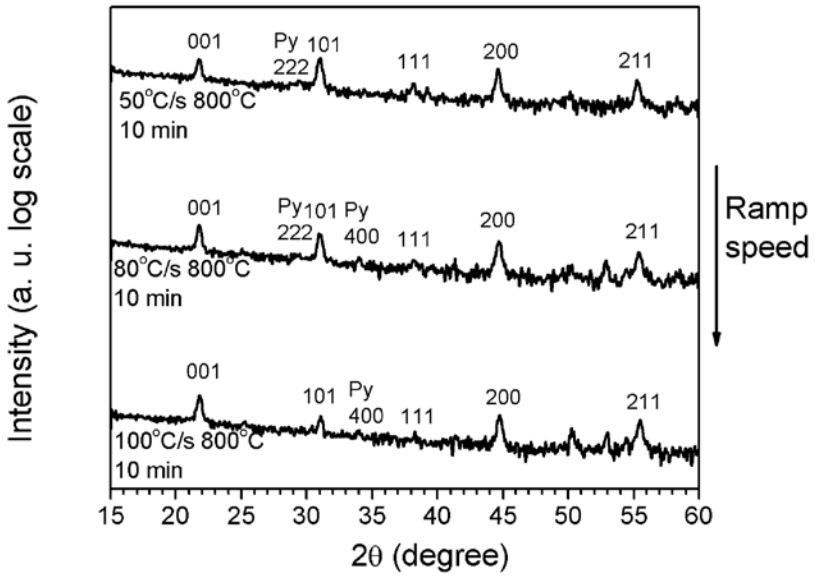

Figure **3-2**: XRD patterns (grazing angle ω=2º) of single layer 0.3PNN-0.7PZT films heat-treated at different ramp rates. The perovskite peaks are labeled in terms of pseudocubic indices. Pyrochlore peaks are denoted by Py.

A more effective means of suppressing pyrochlore formation was use of a perovskite buffer layer. For this purpose, a layer of {100} – oriented $PbTiO_3$ from 10 to 20 nm thick with 40 mol % Pb excess was used for all the films described in the chapter (unless otherwise specified). PNN-PZT samples deposited on such layers were pyrochlore-free and showed {001} – texture as shown in Figures 3-3 and 3-4. Here, as elsewhere in the chapter, pseudocubic indices are used to index the perovskite films.

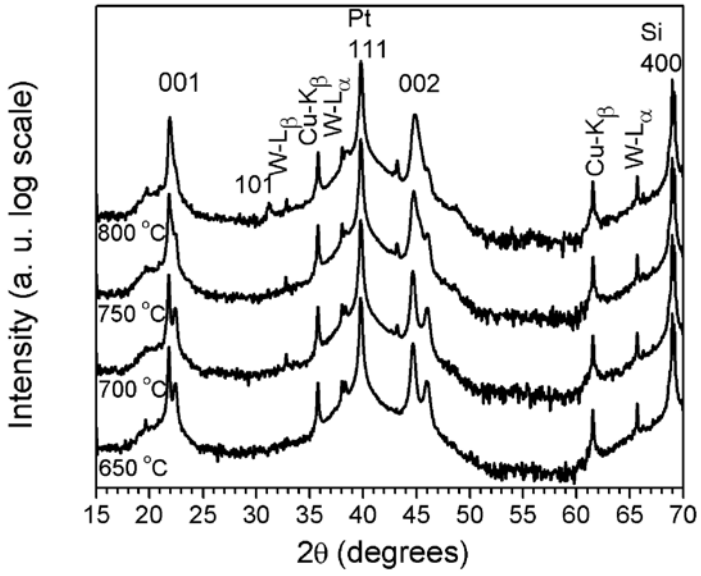

Figure **3-3**: XRD patterns of series A PNN-PZT thin films processed at different annealing temperatures. The perovskite peaks are labeled in terms of the pseudocubic indices. Platinum peaks are denoted by Pt. Peaks arising from other X-ray lines are denoted as $Cu-K_\beta$, $W-L_\alpha$ and $W-L_\beta$.

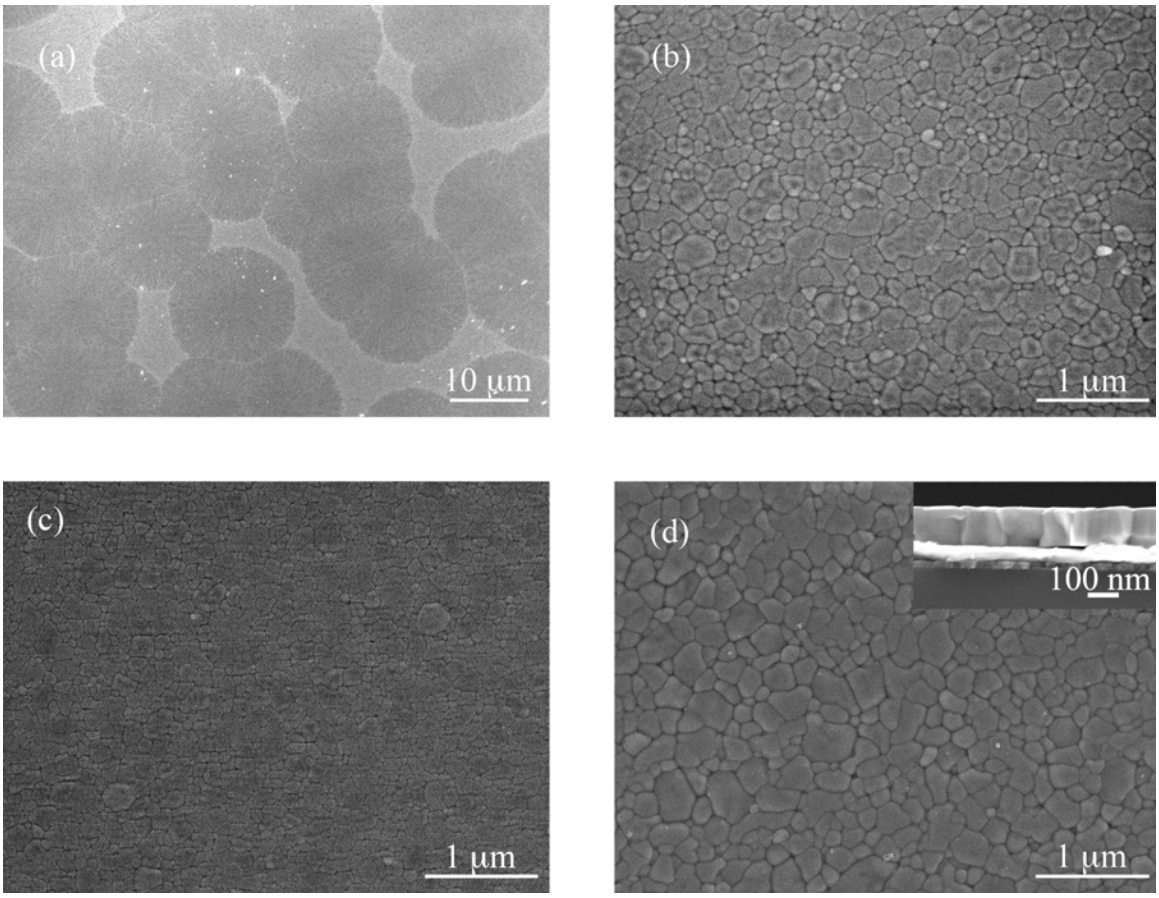

Figure **3-4**: (a) Single layer PNN-PZT film deposited without buffer layer (approximately 70 nm thick). The darker grey regions correspond to the perovskite phase, while the lighter grey areas are residual pyrochlore phase. PNN-PZT films from series A deposited on a $PbTiO_3$ buffer layer and heat-treated at (b) 700, (c) 750 and (d) 800 ºC for 1 min, respectively. The inset in (d) shows the cross-section indicating columnar growth.

3.4.2 Film Structure and Microstructure

FE-SEM images of the Series A films treated at different temperatures (with the $PbTiO_3$ buffer layer) are presented in Figure 3.4. Dense and crack free polycrystalline morphologies were obtained. The use of the perovskite buffer layer minimized the presence of the fine-grained pyrochlore phase visible at the film surface. The calculated average grain size and the standard deviation for these films for each of the treatment temperatures are shown in Fig. 3-5. The

average grain size of the PNN-PZT films processed on a $PbTiO_3$ buffer layer containing 10 mol % Pb excess increased with the annealing temperature, from 0.11 μm for the sample soaked for 10 min at 650 ºC to 0.21 μm for the sample treated at 800 ºC for 1 min. On the other hand, the average grain size for the PZT films (Series C) increased from 80 nm up to 120 nm on increasing the crystallization temperature from 650 to 800 ºC. It is clear that the presence of PNN enhances mass transport and promotes grain growth. Although not apparent at these magnifications, it is hypothesized that a small quantity of liquid phase manifests in the proximity of the 800 ºC RTA soak for the PNN-PZT films, assisting the coarsening process.

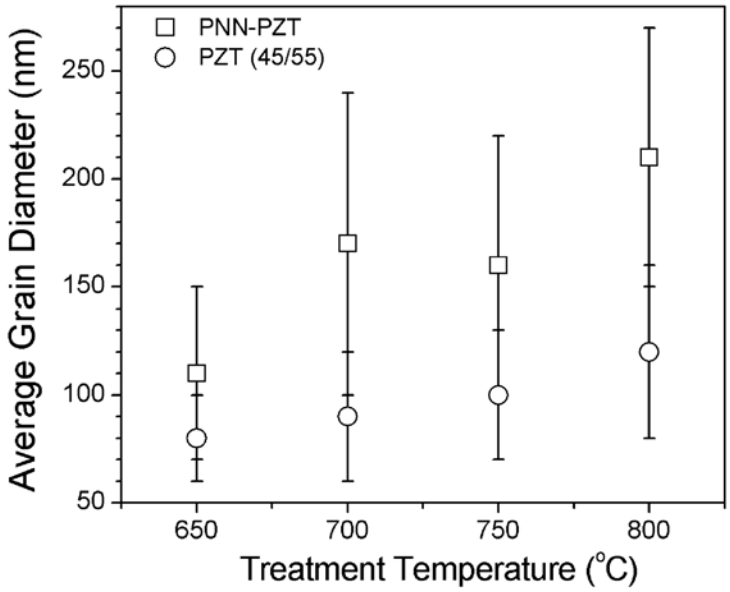

Figure **3-5**: The average grain diameter as a function of crystallization temperature for PNN-PZT and PZT thin films of the same thickness (series A).

In Series B samples, the concentration of Pb excess was varied through the film thickness and the annealing temperature was set at 700 or 750 ºC. For this set of films, the bottom and top layers contained 10 mol% Pb excess while the Pb excess level was set to 5 mol% for the 2 middle

layers. A higher lead content was chosen for the bottom layers to minimize potential problems associated with interdiffusion of lead into the Pt bottom electrode.[115]

In Figure 3-6, scanning electron micrographs reveal dense and large-grained microstructures for these films. Average grain sizes of 0.25 μm and 0.27 μm were calculated respectively for the sample treated at 700 and 750 ºC. It is believed that the larger grain sizes for series B samples if compared to series A are a consequence of a reduction in grain boundary drag associated with excess PbO at the grain boundaries.

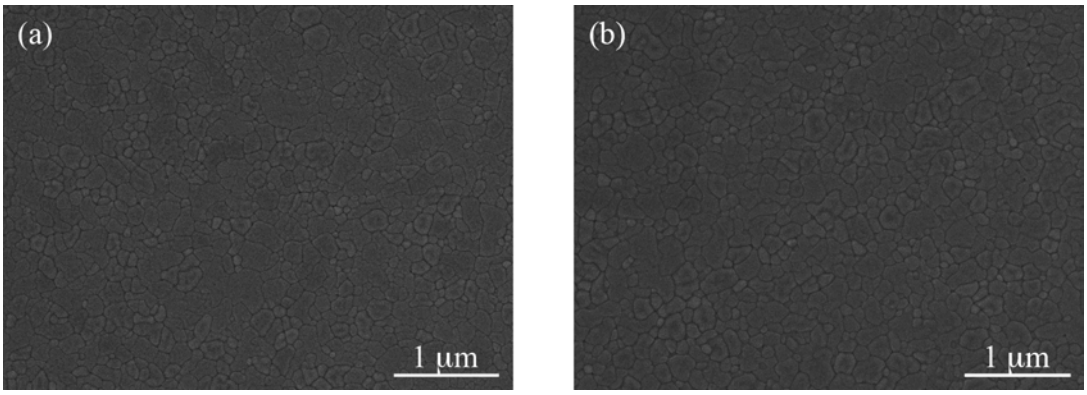

Figure **3-6**: PNN-PZT series B films deposited on $PbTiO_3$ buffer layer treated at (a) 700 ºC 1 min and (b) 750 ºC 1 min.

Figure 3-7 shows the {001} reflections for Series A samples processed using a PNN-PZT solution containing 10 mol% Pb excess as a function of the crystallization temperature. It can be observed that the 001 and 002 reflections shift to higher angles with the treatment temperature. In addition, there is a decrease in the intensity of the 100 and 200 reflections from the $PbTiO_3$ template layer as the crystallization temperature increases.

The pseudocubic lattice parameters for the PNN-PZT thin film samples (Series A) treated between 650 ºC and 800 ºC varied from 4.040±0.001 to 4.029 ±0.001 Å. The shift in the Bragg peaks from the PNN-PZT films to higher angles with crystallization temperature should originate, in part, from the stress on the ferroelectric film due to the mismatch in the thermal expansion

coefficient between the Si substrate and the film. The magnitude of the tensile stress in the PNN-PZT layer should increase as the crystallization temperature increases. The in-plane tensile stress leads to a contraction out-of-plane. For this reason, the measured diffraction peaks shift to higher angles as shown in Fig. 3-7. A second factor contributing to the change in lattice parameter could be $PbTiO_3$ interdiffusion into the PNN-PZT layer. Figure 3-7 shows a decrease of the $\{h00\}$ intensities relative to the $PbTiO_3$ and an increase of the FWHM for the $\{h00\}$ peaks relative to the PNN-PZT increasing the treatment temperature. These would be consistent with interdiffusion of the buffer layer into the PNN-PZT layer at higher crystallization temperatures. Since $PbTiO_3$ has a smaller pseudocubic lattice parameter than the PNN-PZT, this will also decrease the lattice parameter of the PNN-PZT film.

Series B samples showed a much weaker decrease of the $\{h00\}$ reflections relative to the $PbTiO_3$ and the calculated lattice parameters were 4.041±0.001 and 4.038 ±0.001 Å for the samples annealed at 700 and 750 ºC respectively.

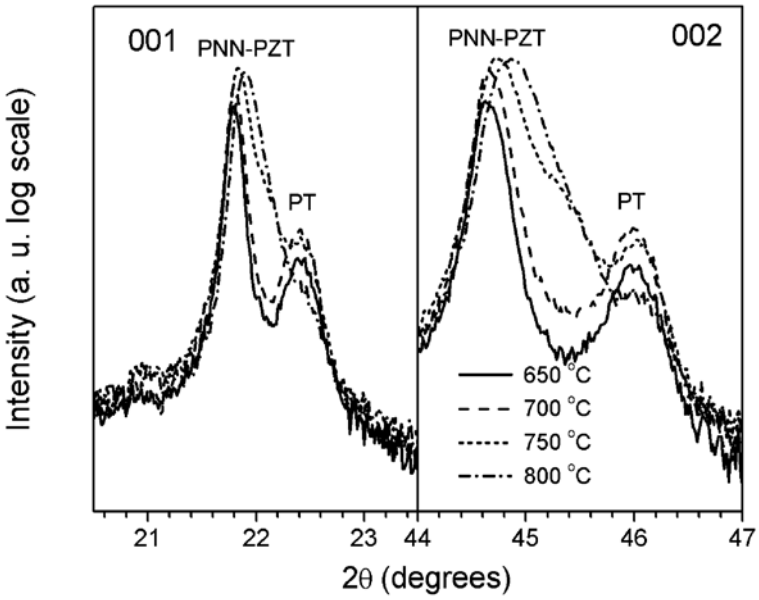

Figure **3-7**: XRD patterns of the $\{001\}$ family of peaks for the PNN- PZT layers and the $PbTiO_3$ seed layer. The samples were treated at 4 different temperatures in the interval 650-800 ºC. The $PbTiO_3$ peak is denoted by PT.

3.4.3 Transition Temperature Characterization

Figure 3-8 shows the temperature dependence of the dielectric response in PNN-PZT films with different levels of crystallographic texture. As shown in Fig. 3-8, two transition temperatures were observed in the films:

$T_1 \sim 140$ ºC

$T_2 \sim 260$ ºC

The T_{max} changed from T_1 to T_2 as the degree of $\{001\}$ texture decreased. It is speculated that the degree of $\{001\}$ orientation in the films can influence the domain patterns and therefore the extrinsic contributions to the dielectric permittivity. This in turn may affect the

relative height of the peaks associated with phase transitions as observed in the case of PMN-PT single crystals.[116] The dielectric constant varied from 1440 ± 50 to 1350 ± 45 going from 100 Hz to 100 kHz at room temperature. The calculated frequency dispersion of ~7% was lower than the one (~12%) calculated for the PNN-PZT epitaxial sample of the same composition (see section 5.3.4). The differences are in part related to the poorer crystal quality of polycrystalline samples processed on Si substrates and the much greater extrinsic contributions to the dielectric properties in the epitaxial sample. It is not known why no corresponding peaks in the loss tangent were observed, but possibilities include low crystal quality, a diffuse transition and/or interference from increased conduction for peaks at higher temperature.

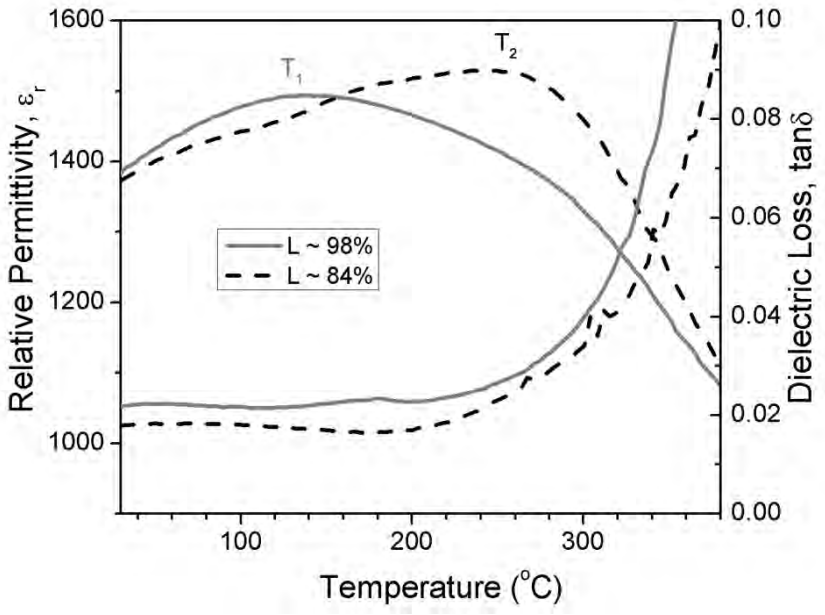

Figure **3-8**: Temperature dependence of permittivity for PNN-PZT thin films characterized by different levels of texture. "L" is the Lotgering factor.

To prove that the T_1 for the highly $\{001\}$ oriented sample is not associated with a ferroelectric to paraelectric phase transition, measurements of remanent polarization as a function of temperature on the same sample were performed using the positive up negative down (PUND)

technique, in order to separate between switching and non-switching contribution to the remanent polarization. This was particularly important for the high temperature measurements where the sample became more conductive. As seen in Figure 3-9, it was confirmed that the highly oriented sample transitioned to a paraelectric state at around 260 ºC. The smooth decay of the normalized remanent polarization may be related to a finite amount of relaxor character for the 0.3PNN-0.7PZT composition (see section 5.4.3).

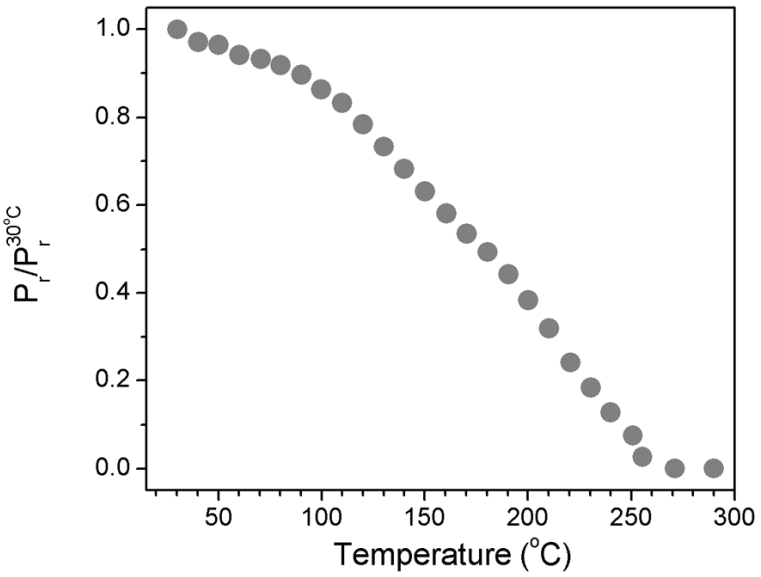

Figure **3-9**: Normalized remanent polarization measurements as a function of temperature for the highly {001} oriented sample measured using the PUND technique.

3.4.4 Effect of the In-plane Tensile Stress

The in-plane tensile stresses that develop on cooling from the crystallization temperature led to a reduction in the remanent polarization as the heat-treatment temperature increased. The net result, as shown in Figure 3-10, is that the hysteresis loops appear to rotate clockwise with increasing crystallization temperature. Ferroelastic domains in thin films change their configuration according to the imposed stress in order to minimize the elastic energy on cooling through the transition temperature.[117] In these {001} -textured films, the higher in-plane stresses that developed at higher treatment temperatures would be expected to pull the polarization closer to the plane of the substrate.[118] In many PZT films, once the polarization direction has been set at the phase transition, it is extremely difficult to generate switching of ferroelastic domains with an electric field.[65,119,120] Figure 3-10 shows how the remanent polarization decreased with the crystallization temperature. The remanent polarization, P_r, decreased from 21 to 17 $\mu C/cm^2$ for samples crystallized between 650 and 800 ºC, respectively (measured at a maximum electric field of 750 kV/cm).

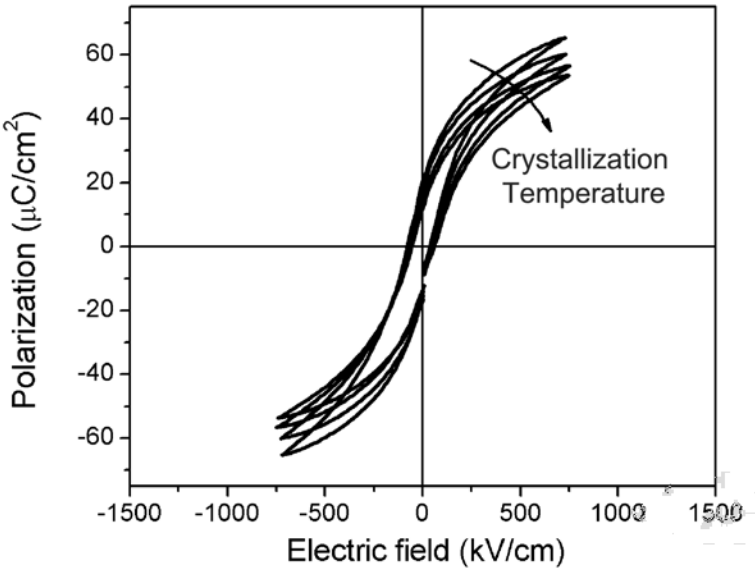

Figure **3-10**: Experimental hysteresis loops for 250 nm thick 0.3PNN-0.7PZT films heat treated at temperatures between 650 ºC to 800 ºC; the loops rotate clockwise as the annealing temperature increases from 650 ºC to 800 ºC.

3.4.5 Grain-size Effects

3.4.5.1 Dielectric Constant and Transverse Piezoelectric Coefficient

Figure 3-11 shows the dielectric constant and transverse piezoelectric response as a function of the average grain diameter for the films of this study. The plotted values are the average for 3 electrodes from each of the samples. It is clear that the dielectric and piezoelectric properties increased with grain size. This is true even when larger grain sizes were achieved with higher crystallization temperatures, despite the introduction of higher tensile stresses.

The room-temperature permittivity for PNN-PZT thin films increased by 13 % as the average grain size changes from 110 nm to 270 nm. This behavior is consistent with the observations of Ihlefeld *et al.*[63] on $BaTiO_3$ thin films. As will be shown below, at least part of the

increase in permittivity is associated with domain wall related contributions. Further work needs to be conducted to determine whether this is a function of an increase in the crystallinity with grain size or the introduction of a more complex domain pattern in larger-grained films.

In Fig. 3-11 (b), together with values of $e_{31,f}$ characterized from $\{001\}$ oriented films, the transverse response of a sample with a Lotgering factor of 84% is shown. This sample was crystallized at 800 ºC for 1 min on a poorly $\{001\}$ -textured $PbTiO_3$ buffer layer. Even this sample tracks the trend with grain size, suggesting that microstructure is an important determinant of the dielectric constant and piezoelectric properties. This is not discussed in previous reports by Tuttle *et al.*[121] and the group of Muralt.[4,122]

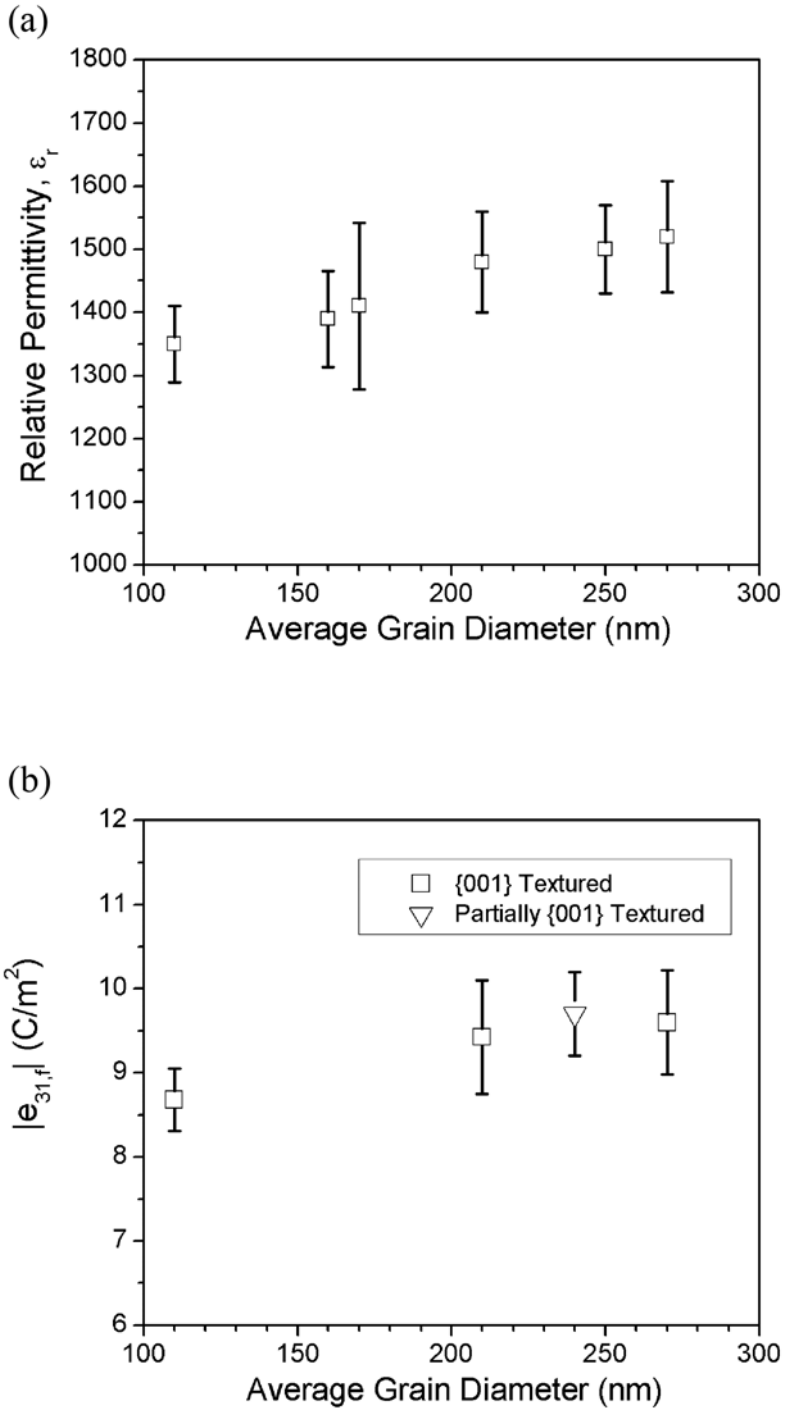

Figure **3-11**: (a) Relative permittivity at 20 ºC and (b) transverse piezoelectric coefficient $e_{31,f}$ plotted vs. the average grain diameter for films from this work. The {001} textured samples showed Lotgering factors higher than 95 %; the film shown as partially {001} textured had a Lotgering factor ~ 84 %.

3.4.5.2 Dielectric Nonlinearity

The AC electric field dependence of the dielectric properties was investigated for samples that showed a range of average grain sizes between 110 and 270 nm. Samples that did not show much $PbTiO_3$ interdiffusion from XRD analysis were chosen for this study; for this reason the series A sample annealed at 800 ºC was not included in the analysis. To isolate the grain size effect from the thickness dependence of nonlinear properties, all the samples had a thickness of approximately 0.245 μm.

The dielectric constant and loss are plotted as a function of AC electric field in Figure 3-12. No visible threshold field was noticeable in the explored AC field interval; a distinct region where ε' increases linearly with the applied AC electric field is visible for all the samples, followed by the onset of a sub-linear zone. The linear region was fitted to the Rayleigh relation expressed as:[58,60]

$$\varepsilon'(E_0) = \varepsilon'_{init} + \alpha' E_0 \qquad \text{Equation } \mathbf{3\text{-}1}$$

where α' is the irreversible Rayleigh coefficient and ε'_{init} represents a combination of the intrinsic dielectric response together with the contribution from reversible domain wall or phase boundary motion.

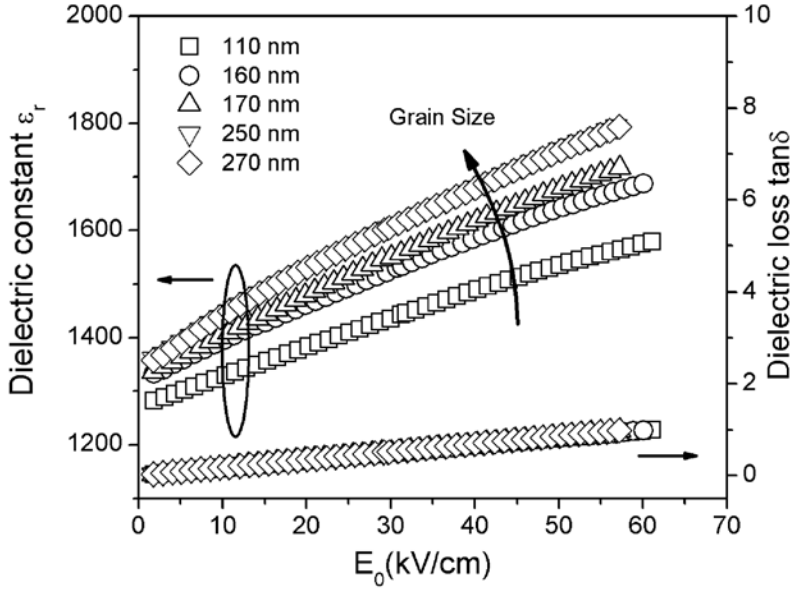

Figure **3-12**: Field dependence of the real dielectric permittivity and dielectric loss for PNN-PZT films of different average grain size and the same thickness.

Figure 3-13 shows α', ε'_{init} and $\alpha'/\varepsilon'_{init}$ for films of different grain size. It can be seen that an increase in average grain size is accompanied by larger reversible and irreversible contributions to the dielectric constant. As the average grain size increased from 110 nm to 270 nm, the Rayleigh coefficient α' increased by 100% (5.3 ± 0.02 and 10.6 ± 0.09 cm/kV, respectively) while ε'_{init} increased by 14% for the same grain size increase (1270 and 1470, respectively). The ratio $\alpha'/\varepsilon'_{init}$ increased by 79% over the same grain size interval (0.0042 and 0.0075 cm/kV, with standard deviations in the fifth decimal place), suggesting a considerable increase in the domain wall (extrinsic) contributions to the dielectric response with grain size. Such behavior was not observed for series C (PZT) samples, where α', ε'_{init} and $\alpha'/\varepsilon'_{init}$ did not show any significant change as a function of crystallization temperature. It should also be noted that the series C samples showed a clockwise rotation of the hysteresis loop similar to those of series A films (suggesting comparable residual stress levels), while the grain size depended only

weakly on the annealing temperature. These results suggest that the grain size, rather than a change in the residual stress level, dominates the domain wall mobility in the PNN-PZT samples.

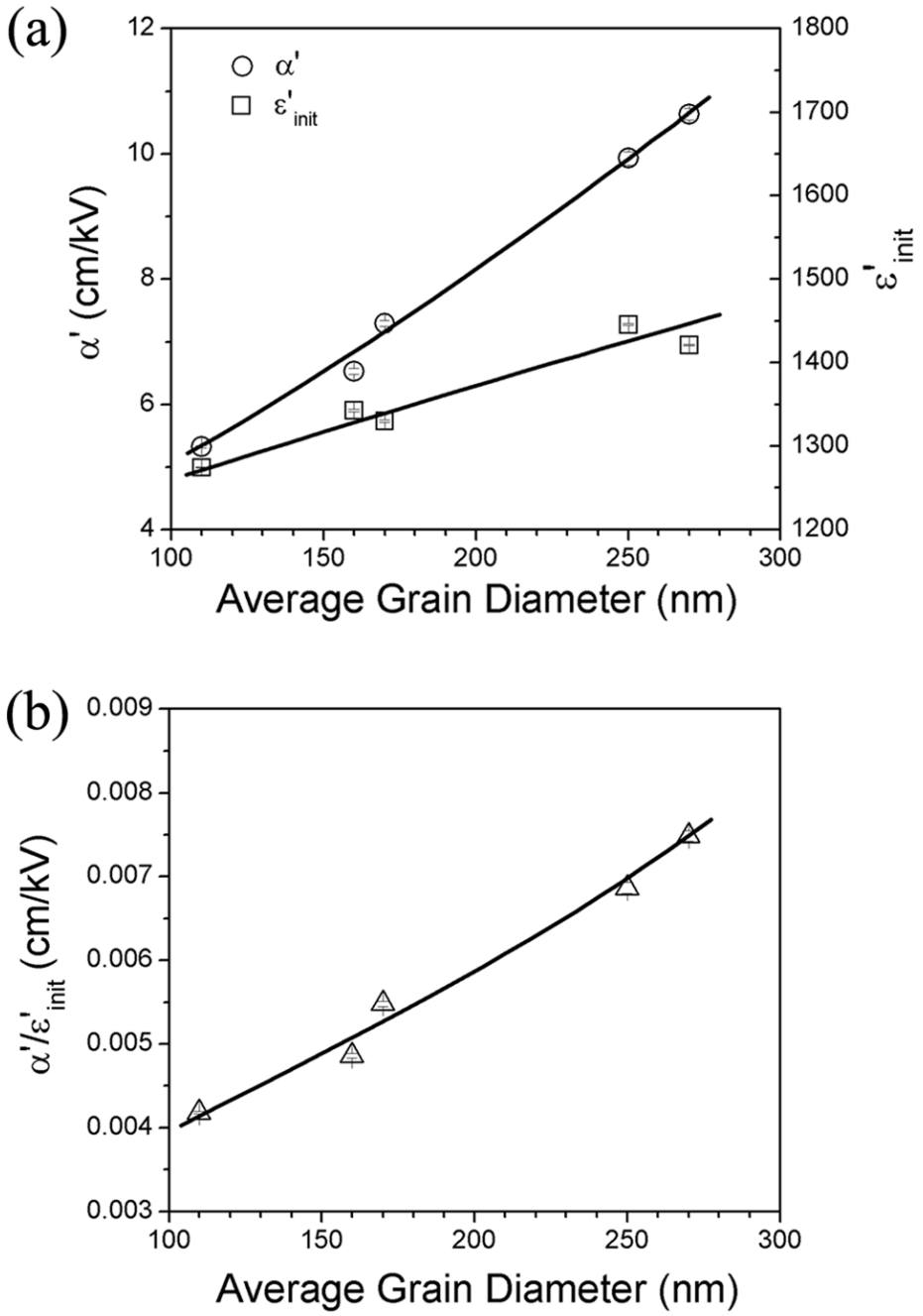

Figure **3-13**: (a) α' and ε'_{init} as a function of grain size and (b) α' / ε'_{init} ratio as a function of grain size. The error bars represent fitting errors.

To determine the origin of the differences in dielectric constant at low field, the AC field dependence of ε_r was measured at different dc biases. For all samples, the width of the Rayleigh region increased while α' decreased under increasing dc bias. This is expected, as the applied bias acts as a poling electric field that stabilizes the domain structure, hindering depoling and switching. Figure 3-14 shows the dc bias dependence of α', ε'_{init} and $\alpha'/\varepsilon'_{init}$. It can be observed that these parameters decrease monotonically with increasing DC bias and the data for all grain sizes largely converge at high DC biases, suggesting that the differences at low field are largely extrinsic in origin.

It was noticed that samples with smaller grain sizes converged more rapidly to values of α' lower than 0.3 cm/kV. For instance the 110 nm average grain size sample showed an extrapolated α' below 0.3 kV/cm at bias fields of 133 kV/cm and above, while bias fields of 222 kV/cm were necessary for the 270 nm average grain size sample to converge to α' values below 0.3 kV/cm. Conversely, the decay of the extrapolated ε'_{init} was slower and did not show a clear grain size dependence in the convergence.

It is speculated that the grain size effect on the field dependence of the irreversible Rayleigh parameter may be related to different levels of residual tensile stress for samples processed at different temperatures affecting the direction of the polarization with respect to the out of plane direction, and possibly differences in the field distribution for samples with different grain sizes.

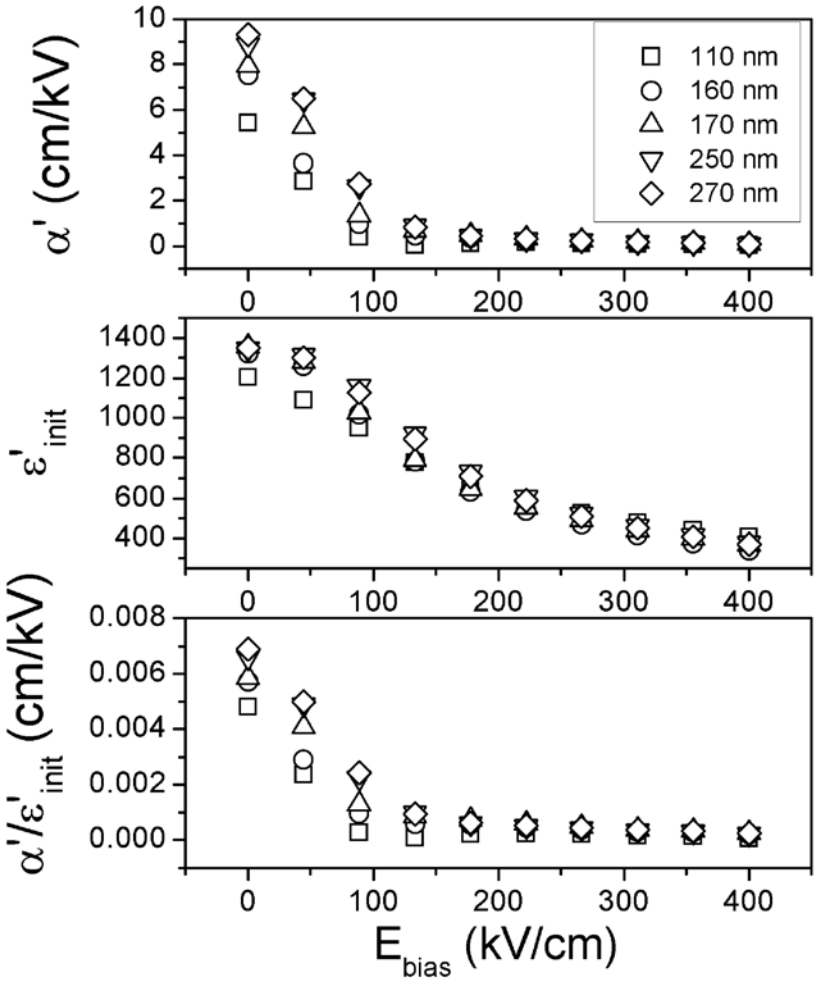

Figure **3-14**: The irreversible Rayleigh coefficient, α', the reversible Rayleigh coefficient ε'_{init} and the ratio $\alpha'/\varepsilon'_{init}$ for PNN-PZT samples of the same thickness but different grain sizes.

3.5 Conclusions

This chapter described the deposition of phase-pure PNN-PZT thin films of uniform thickness and composition with a range of grain sizes from 110 to 270 nm. PNN fluxing appeared to be effective at increasing diffusion. By controlling the amount of Pb excess in the solution and the thermal budget, large lateral grain sizes were achieved. Investigation of the dielectric and piezoelectric properties revealed a grain size dependence of the permittivity and the transverse piezoelectric response. It was also shown that an increase in grain size activated more extrinsic contributions to the dielectric constant. Control of grain size may offer the possibility of tailoring the piezoelectric response of thin ferroelectric films.

Chapter 4

Mapping Piezoelectric Nonlinearity in the Rayleigh Regime using Band Excitation Piezoresponse Force Microscopy [†]

4.1 Abstract

Band excitation piezoresponse force microscopy (BE-PFM) offers the possibility of investigating the nonlinear piezoelectric behavior of ferroelectric thin films *locally*. However, the presence of additional nonlinearity associated with a dynamic resonant response of the tip-surface junction can complicate the study of the material nonlinearity. Here, the relative importance of the two non-linearity sources was examined as a function of the excitation function. It was found that in order to minimize the effects of nonlinear tip-surface interactions but achieve good signal - noise level, an optimal excitation function with a specific energy density must be used.

[†] Most of this chapter appears in F. Griggio, S. Jesse, A. Kumar, D. Marincel, D. S. Tinberg, S. V. Kalinin, S. Trolier-McKinstry, Appl. Phys. Lett. **98**, 212901 (2011).

4.2 Introduction

Micromachined ferroelectric films are increasingly employed in a range of applications (for example sensing and actuating, data storage and tunability).[123] As such devices develop, the need for characterization tools capable of *local* probing of the response becomes fundamental. With the advent of piezo-response force microscopy (PFM), the investigation of nanoscale ferroelectric phenomena has become more accessible.[24,26,27] In particular, implementation of the band excitation method by Jesse *et al.*[124,125] allows resonance-enhanced PFM measurements unaffected by topographic cross-talk. Using this approach, Bintachitt *et al.*[89] demonstrated the existence of long range cooperative interaction among domain walls. The observed piezoelectric nonlinearity in the Rayleigh regime was described as a collective displacement within a specific interaction volume.

However, one key aspect of any SPM method is the fact that measured properties represent the convolution of intrinsic material responses and cantilever dynamics. In the nonlinearity measurements, the two primary sources of nonlinearity include the intrinsic piezoelectric nonlinearity of the ferroelectric and non-linear dynamics of the tip-surface junction. Here we develop an approach for quantitative *local* measurements of piezoelectric nonlinearity in the Rayleigh regime using piezoresponse force microscopy on model epitaxial ferroelectric capacitors.

Information on the *local* nonlinearities is obtained acquiring single-point measurements of the tip displacement as a function of the excitation voltage within the limits of the Rayleigh region. BE-PFM with an amplitude modulation was used to collect the piezoresponse of capacitor structures over a band of frequencies encompassing the resonance of the cantilever tip – surface system in order to amplify the signal to noise ratio.

4.3 Experimental Procedure

4.3.1 Measurement Setup

BE-PFM was implemented on a commercial Asylum Cypher system with an additional BE controller. A high voltage amplifier (F10A, FLC Electronics) was used to drive the ferroelectric capacitors in the subcoercive electric field regime. The top electrode and the conductive cantilever Olympus ACM240TM (Olympus, Corp., Tokyo, Japan) were driven with the same excitation function and the bottom electrode was grounded.

The measurements were performed on epitaxial (0.3) $Pb(Ni_{0.33}Nb_{0.67})O_3$ - (0.7) $Pb(Zr_xTi_{1-x}O_3)$ (PNN-PZT) thin films where x was chosen to be 0.2, 0.45 and 0.8 in order to sample different regions of the PNN-PZT phase diagram. The samples were prepared using a chemical solution deposition process described in chapter 3.[126] (100) $SrTiO_3$ single crystals (MTI Corp., Richmond, CA) were used as substrates. A $SrRuO_3$ bottom electrode layer was deposited via pulsed laser deposition (PLD) as described elsewhere.[127]

The PNN-PZT solution was spun on to the substrate and annealed every 4 pyrolyzed layers to achieve a thickness of about 1 μm. Proof of epitaxial growth on the $SrTiO_3$ substrates was given by the presence of 4 peaks of the 101 reflection of the PNN-PZT thin films in phi scans (as shown in Figure 5-1 (b)). The circular Pt top electrodes were sputter-deposited using a lift-off process and the diameters ranged from 10 to 200 μm. The top electrodes were connected directly to an external power source.

The *local* nonlinearities of the thin films were measured using global excitation of the capacitor with *local* displacement detection through the AFM cantilever.

In the imaging mode, the nonlinear BE-PFM measurements were acquired on a spatially resolved two-dimensional (2D) grid on the top electrode surface. This data acquisition gives rise

to a multi-dimensional data set of response as a function of frequency, excitation voltage and two spatial coordinates. The individual curves were fitted to a simple harmonic oscillator (SHO) equation to yield the amplitude at the resonance, A_{max}, the resonant frequency, ω_o and the mechanical quality factor, Q as a function of position and voltage, V_{ac}.

As described by Bintachitt *et al.*,[89] the amplitude is a nonlinear function of the applied voltage and can be described with a second order polynomial as in Equation 4-1. Differentiation with respect to the V_{ac} yields the Rayleigh law as in Equation 4-2.

$$A_{\max} = p_1 + p_2 V_{ac} + p_3 V_{ac}^2 \qquad A_{\max} = \xi h \qquad \text{Equation } \mathbf{4\text{-}1}$$

$$\xi d_{33,f} = \xi d_{33,init} + 2\xi \alpha_d V_{ac} \qquad \text{Equation } \mathbf{4\text{-}2}$$

where ξ is a parameter that accounts for the cantilever sensitivity, α_d is the Rayleigh coefficient associated with irreversible extrinsic contributions to $d_{33,f}$, the longitudinal piezoelectric coefficient and $d_{33,init}$ is the Rayleigh coefficient associated with the reversible extrinsic and intrinsic contributions to $d_{33,f}$.[54] The factor $2*p_3/p_2$ normalized for the sample's thickness, provides a *quantitative* and *local* ratio of the irreversible to reversible contributions to the converse piezoelectric coefficient $d_{33,f}$.

The presence of an additional nonlinearity associated with a dynamic resonant response complicated the measurements. An approach was developed to minimize this type of nonlinearities in order to discern the *local* piezoelectric nonlinearities of the samples. In particular, the excitation function used to probe the nonlinear response was amplitude modulated. Two subsequent excitation signals were sent in sequence with opposite frequency direction, first increasing and then decreasing in time. Comparison of these two signals provides information on the presence of additional dynamic nonlinearity.

4.3.2 Numerical Simulation Conditions

A numerical simulation of the cantilever dynamics was performed in order to investigate the interaction between BE signal type and nonlinearities in the tip-sample interaction. To this end, the cantilever behavior was simplified to a nonlinear simple harmonic oscillator (SHO) model (Figure 4-1 (b)) as in equation 4-3.

$$H(\omega) = \frac{Ae^{i\phi}}{\left(\frac{\omega}{\omega_o}\right)^2 + \frac{i\omega}{\omega_o Q} - 1} \qquad \text{Equation } \mathbf{4\text{-}3}$$

where ω is the angular frequency and ω_0 the resonance frequency, A is the amplitude and Q is the quality factor.

The effective mass and effective spring constant from the mode shapes of a cantilever were calculated with fixed boundary conditions at one end and a linear-spring at the opposite end (Fig. 4-1 (a)). By continuously varying the stiffness of the spring from 0 to infinity, one can tune the tip-surface interaction from that of a freely oscillating cantilever to one pinned to the surface, thereby allowing one to track cantilever behavior with respect to the sample's surface. The relationships between effective mass and effective spring constant as a function of tip-surface stiffness were calculated assuming the properties of an AC240 cantilever. Hertzian contact conditions between the tip and the surface were assumed so that the effective mass, spring constant and force could be expressed as a function of tip-surface separation distance (Figure 4-1(c) and (d)). These were used as inputs into the nonlinear SHO model.

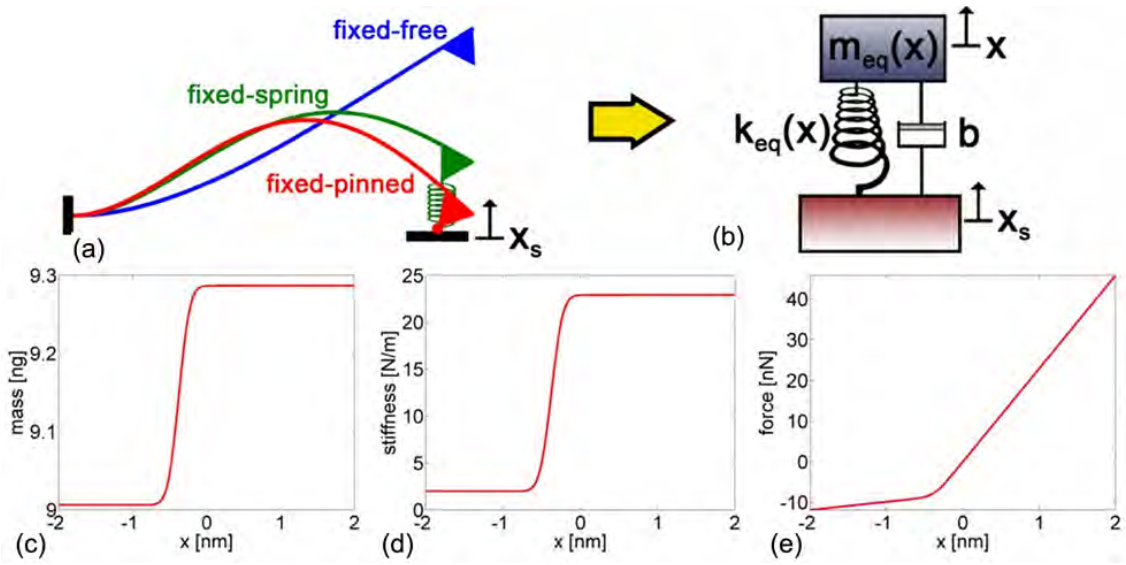

Figure **4-1**: Numerical simulation of BE driven cantilever dynamics with nonlinear tip-surface interactions. (a) Cantilever mode shapes determined for three different tip-surface stiffnesses; fixed free-zero stiffness corresponding to free oscillation, fixed spring-moderate stiffness, and fixed-pinned-infinite stiffness corresponding to a pinned cantilever. These mode shapes were used to calculate equivalent mass and spring values as a function of tip-surface separation for the nonlinear SHO model in (b). (c,d,e) equivalent mass, stiffness, and force as a function of tip surface separation respectively.

The simulations used the same excitation signals as those employed in experiments, whose amplitude and phase as expressed in the Fourier domain are:

$$Y_a(\omega) = \Omega \frac{A}{2} \sqrt{\frac{\tau|\beta|}{\omega_2 - \omega_1}} \left[erf\left(\frac{\omega - \omega_1 - 2\gamma}{\gamma} \right) - erf\left(\frac{\omega - \omega_2 + 2\gamma}{\gamma} \right) \right] \qquad \text{Equation } \mathbf{4\text{-}4}$$

$$Y_p(\omega) = -\left(\frac{\omega - \omega_1}{\omega_2 - \omega_1} \right)^2 \pi\beta\tau(\omega_2 - \omega_1) - \pi\tau(1 - \beta)\omega \qquad \text{Equation } \mathbf{4\text{-}5}$$

A is the amplitude of the signal, ω_1 and ω_2 are the lower and upper limits of the excitation band, and γ determines the sharpness of band edges. τ is the duration of the signal in the time domain and Ω is the sampling rate. β is the amount of phase variation ranging from -1 to 1, where $\beta = 1$ corresponds to an increasing frequency sweep with time or *chirp-up*, $\beta = -1$ to a decreasing

frequency sweep with time or *chirp-down*. The signal approaches a *sinc* function as β approaches 0. The energy contained in the band excitation signal is linearly proportional to $|\beta|$. These expressions are converted to the time domain using the inverse Fourier transform,

$$y(t) = iFFT(Y_a e^{iY_p}) \qquad \text{Equation } \mathbf{4\text{-}6}$$

4.4 Results and Discussion

4.4.1 Simulation Results

Simulations were carried out over a range of excitation amplitudes and energy. Figure 4-2 (a) compares the transfer functions resulting from excitation with $|\beta| = 1$ where for large amplitudes there are clearly distortions in the shape of the transfer function and these distortions are quite different for chirp-up and chirp-down. This contrasts significantly with the results in Figure 4-2 (b) which show that for $\beta = 0.03$ and -0.03 the transfer functions remain Lorentzian (linear) in shape across the range of excitation amplitudes. Figure 4.-2 (c) summarizes the simulations by plotting the difference in the integrated intensities of the magnitude of the transfer functions as compared to the response to perfectly linear oscillator. As expected, as $|\beta|$ gets smaller, the behavior of the systems becomes more linear. Therefore, measurements performed with BE signals with minimal phase content variation will be less susceptible to nonlinear interactions at the tip-surface junction. However, in practical measurements where noise becomes an important consideration, the countervailing trend is that as $|\beta|$ decreases, so does the signal-to-noise ratio. It is important therefore to find the proper value for signal energy to avoid non-linearities in tip dynamics but still retain sufficient response signal strength.

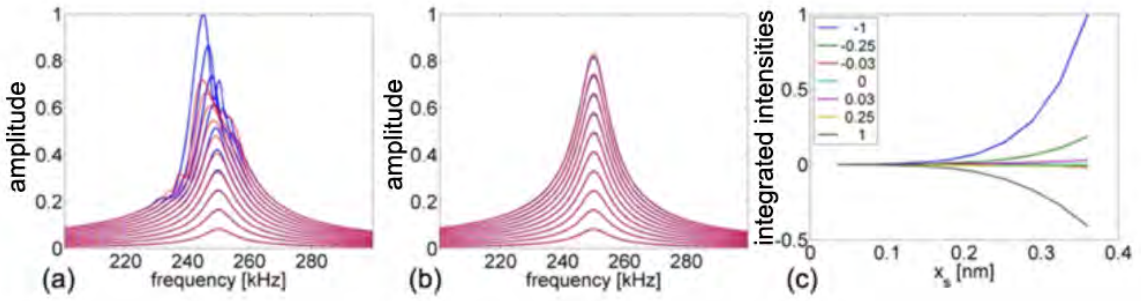

Figure **4-2**: (a) Transfer functions for $\beta = 1$ = chirp-up (red) and $\beta = -1$= chirp-down (blue) for excitation amplitudes corresponding to 0.1 to 1 V_{ac}. (b) Transfer functions for $\beta = 0.03$ (red) and $\beta = -0.03$ (blue) for excitation amplitudes corresponding to 0.1 to 1 V_{ac}. (c) Difference in integrated intensity of transfer functions as compared to a perfectly linear system for excitation amplitudes corresponding 0.1 to 1 V_{ac} and $|\beta| = \{0, 0.03, 0.25, 1\}$.

4.4.2 Local BE-PFM Nonlinear Piezoelectric Nonlinearity Maps

In order to study how the signal energy affects the dynamic nonlinearities measured on the response, the phase variation $|\beta|$ was altered from 3 to 100 % in absolute value during BE-PFM measurements on single locations of the sample. 100 datapoints were collected for each phase variation parameter $|\beta|$. Figure 4-3 illustrates the datapoints visualized in boxplots relative to $\alpha_d / d_{33,init}$ measurements on a single location for the sample. The boxplots show the median, the interquartile range (IQR), the whiskers that extend up to 1.5 IQR and outliers.

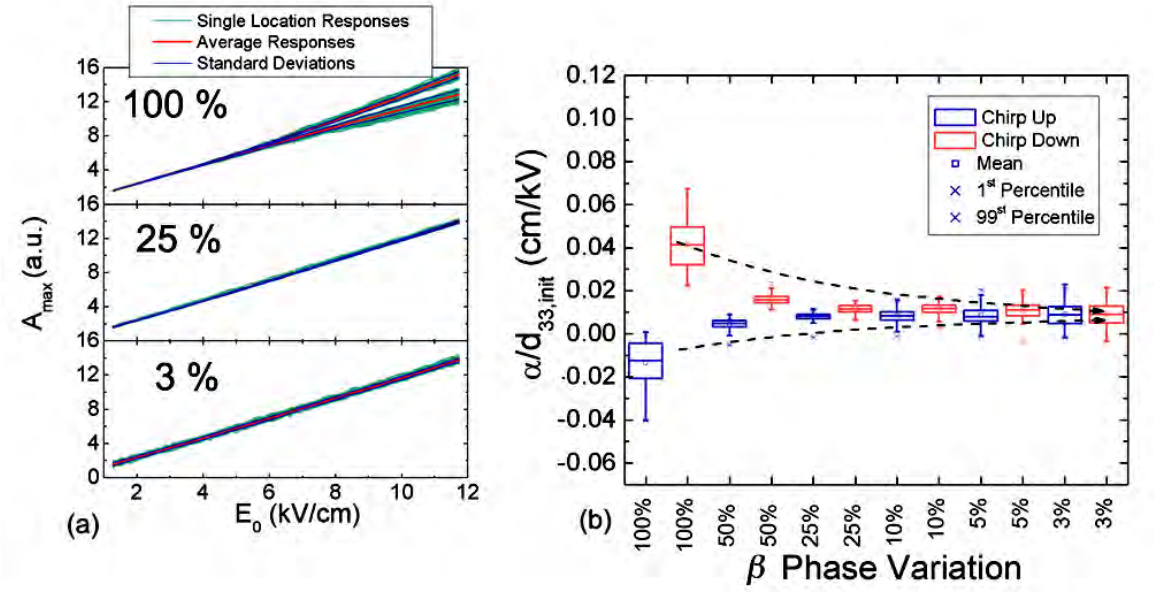

Figure **4-3**: (a) Amplitude responses from a single location; A_{max} is the maximum in amplitude extrapolated from fittings to the SHO equation. The plots represent 100 consecutive measurements (light blue lines) on sweeping up in frequency (suppressed amplitude for β = 100%) and 100 measurements on sweeping down (amplified amplitude for β = - 100%) in frequency. The dark blue and thick red lines represent the standard deviation and average for measurements for the two frequency sweeps. (b) ANOVA boxplots for different phase variation β. Each boxplot is representative of 100 measurements, the whiskers extend up to 1.5 times the interquartile range (IQR) and the average and 99th percentile are also represented.

It was found that the amplitude A_{max} is suppressed when the band excitation waveform sweeps up in frequency; it is amplified for the chirp down for $|\beta| \geq 50$ % due to dynamic nonlinearities. This is in good agreement with the numerical simulations of pure chirps.

It is clear that the cantilever dynamics are strongly dependent on the relative content of the chirp and sinc components of the signal. It is also critical to note that as the sinc character of the excitation is increased, the relative importance of the tip-cantilever nonlinearities is reduced, but that the signal becomes noisier. Thus, it is essential to determine an appropriate β parameter in order to limit the influence of dynamic nonlinearities on the overall response collected by the AFM tip. In practice, it was found that the relative content of the chirp and sinc components of the signal has to be tailored to the specific sample in order to increase the signal to noise ratio while suppressing the dynamic nonlinearities.

For instance the optimal β parameter was found to vary as a function of PNN-PZT composition as shown in Figure 4-4. A lower value, $|\beta| \sim 5\%$, was used for the Ti-rich PNN-PZT composition film in order to minimize the effects of dynamic nonlinearities while a relatively higher value, $|\beta| \sim 30\%$, had to be used for the Zr-rich PNN-PZT composition film to achieve a better signal to noise ratio in the collected data.

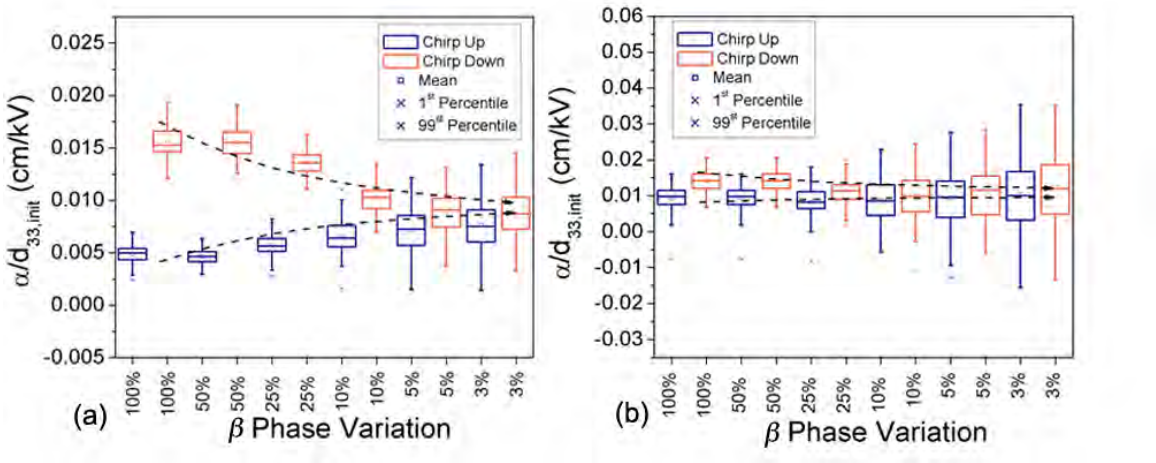

Figure **4-4**: ANOVA boxplots for different phase variations β for (a) an epitaxial $(0.3)Pb(Ni_{0.33}Nb_{0.67})O_3$ - $(0.7)Pb(Zr_{0.20}Ti_{0.80}O_3)$ (PNN-PZT) thin film and (b) an epitaxial $(0.3)Pb(Ni_{0.33}Nb_{0.67})O_3$ - $(0.7)Pb(Zr_{0.80}Ti_{0.20}O_3)$ (PNN-PZT) thin film.

To illustrate practical implementation of this approach, the spatial variability of the *local* piezoelectric nonlinearity in the ferroelectric capacitor was investigated. The topography on the top electrode, the *local* resonance frequency (averaged over the voltage V_{ac}) and the piezoelectric nonlinearity maps are shown in Fig. 4-5. Under the measurement conditions chosen: $|\beta| = 30$ %, 266 kHz center frequency and a bandwidth of 35 kHz, the contact resonance frequency is independent of V_{ac} (the standard deviation of the resonance is below 80 Hz for the scanned region compared to ~ 5 kHz peak width).

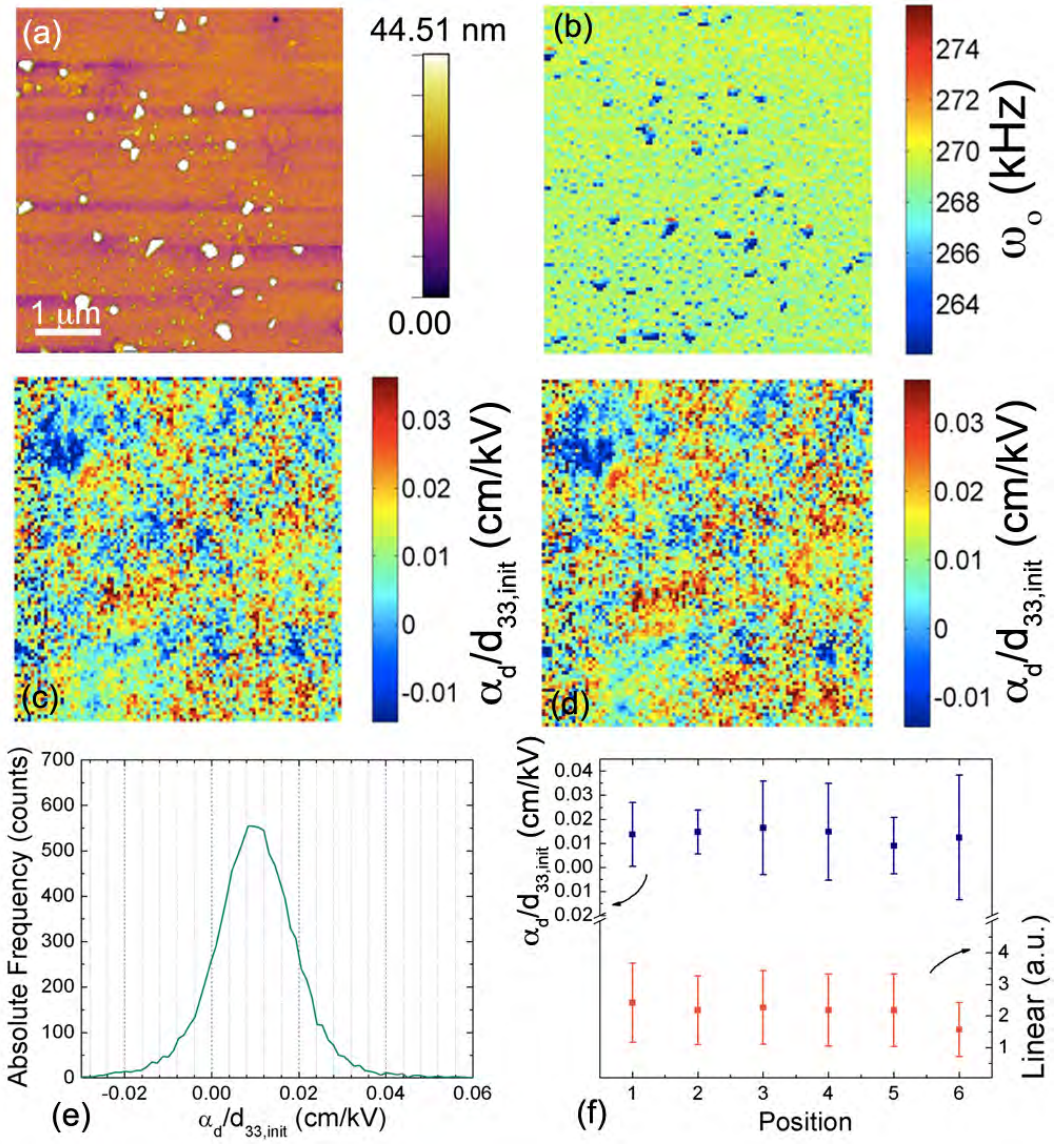

Figure **4-5**: (a) Topography on top electrode, (b) average resonance map for the measurements collected at $|\beta|$= 30% (c) and (d) $\alpha_d / d_{33,init}$ maps for positive and negative frequency sweeps, respectively, (e) absolute frequency histograms of the $\alpha_d / d_{33,init}$ values averaged for the 2 signals of opposite frequency sweep and $|\beta|$= 30%. Spatial averages of low resolution maps of $\alpha_d / d_{33,init}$ and linear component of the $A_{max}(V_{ac})$ response (a_2) values collected in 6 different locations equally spaced along the 200 μm diameter of the top electrode with $|\beta|$ = 25%.

This indicates that for the selected β value, the cantilever dynamics are nearly linear. In addition, the good agreement between the $\alpha_d / d_{33,init}$ maps obtained increasing (Fig. 4-5 (c)) and decreasing (Fig. 4-5 (d)) the frequency with time in the excitation signal testify to the absence of

additional nonlinearities. Thus, the observed nonlinearity in A_{max} as a function of V_{ac} is believed to stem from the piezoelectric response of the material.

The $\alpha_d / d_{33,init}$ maps show the presence of more strongly nonlinear features extending over a 1 μm-length scale as well as regions where the nonlinear piezoelectric response is suppressed. The observed clustering is a function both of the volume sampled during the measurement and the existence of cooperative domain wall motion in a medium of randomly distributed pinning sites.[89] The distribution of the local $\alpha_d / d_{33,init}$ values can be described with a broad Gaussian curve with a standard deviation of 9.8 cm/kV and an average of 10.1 cm/kV (Fig. 4-5 (e)). This result is indicative of a relatively large variation in response depending on the probed location in the 5 μm x 5 μm region analyzed. Further details will be the subject of chapter 5.[128]

In order to estimate the reproducibility of the measurement, low resolution maps (10 μm x 10 μm scans with 10 x 10 rows and columns) were acquired at equally spaced distances from the center to the edge (number 1 through 6 in Figure 4-5 (f)) of a 200 μm diameter electrode using $|\beta|$ = 25%. Figure 4-5 (f) illustrates the spatial averages at each location for the linear component of $A_{max}(V_{ac})$ response, and the spatial averages for the spatial averages of $\alpha_d / d_{33,init}$.

One-way analysis of variance (ANOVA) test was performed to assess the variability of $\alpha_d / d_{33,init}$ as a function of position on the electrode (Fig. 4-5 (f)).[129] For all of the locations, far from the electrode edge,[130] the averaged $\alpha_d / d_{33,init}$ values appeared to be independent of position.

4.5 Conclusions

Local measurements of the nonlinear converse piezoelectric response in model epitaxial ferroelectric capacitors were made using BE-PFM over a spatially resolved 2D grid. A method to

reduce the nonlinearities associated with a dynamic response from the cantilever – surface of the sample system was established. By ascertaining a phase variation parameter β that minimizes the dynamic nonlinearities without degrading the signal – noise ratio, it is possible to collect quantitative and *local* $\alpha_d / d_{33,init}$ maps independent of the particular location on the top electrode.

The advancements in characterization techniques capable of probing material responses at finer scales provides insight on the importance of particular factors related to the processing conditions (grain boundaries, stresses or defect dipoles to name a few) on the performance of thin films. Specifically, the knowledge gained from BE-PFM experiments will help to design processing routes that allow larger extrinsic contributions to the properties in ferroelectric thin films and enhance the piezoelectric response for microfabricated actuator applications.

Chapter 5

Composition Dependence of Local Piezoelectric Nonlinearity in $(0.3)Pb(Ni_{0.33}Nb_{0.67})O_3$-$(0.7)Pb(Zr_xTi_{1-x}O_3)$ Films [‡]

5.1 Abstract

The composition dependence of the dielectric and piezoelectric nonlinearities was characterized in epitaxially grown $(0.3)Pb(Ni_{0.33}Nb_{0.67})O_3$-$(0.7)Pb(Zr_xTi_{1-x}O_3)$ thin films deposited on $SrTiO_3$. Tetragonal, morphotropic phase boundary (MPB) and rhombohedral films were prepared by changing the Zr/Ti ratio. The relative dielectric permittivity ε_r and the converse piezoelectric coefficient $d_{33,f}$ were found to follow the Rayleigh law. The *local* piezoelectric nonlinearity map showed the formation of micron-sized clusters of higher nonlinear activity for the MPB and rhombohedral compositions. The ratios of the irreversible to the reversible Rayleigh constants $\alpha_\varepsilon / \varepsilon_{init}$ and spatially averaged $\alpha_d / d_{33,init}$ ratio were larger for the rhombohedral and MPB compositions compared to the tetragonal composition. The larger dielectric and piezoelectric nonlinearities observed for the rhombohedral sample are interpreted in terms of a higher domain wall mobility due to a smaller ferroelectric distortion and superior crystal quality.

[‡] Most of this chapter appears in F. Griggio, S. Jesse, W. Qu, A. Kumar, O. Ovchinnikov, D. S. Tinberg, S. V. Kalinin and S. Trolier-McKinstry, J. Appl. Phys., in press

5.2 Introduction

Piezoelectric thin films are currently being explored for a range of applications including actuators, medical ultrasound transducer arrays, energy scavengers and microwave devices.[12,21] Ferroelectric materials offer the advantage of higher strain energy density if compared to electromagnetic or electrostatic actuators, and have the potential for miniaturization and integration.[49,131-133] Progress in these applications necessitates maximization of the piezoelectric coefficient, in order to reduce the driving voltage or increase the sensitivity.[2] At the same time, an accurate description of the materials properties under cyclic electrical loading and under different geometries and elastic boundary conditions is essential to predict device behavior. This is particularly the case when ferroelectric films are employed, given the possibility for multiple polarization switching phenomena, aging, and domain wall pinning.

It is known that the dielectric, piezoelectric and elastic properties of ferroelectric materials stem from both the intrinsic response of the crystal and the extrinsic response of domain walls or phase boundaries to applied fields. Ferroelectric film devices, given their small thickness, often operate in the nonlinear regime. Therefore knowledge of the dielectric and piezoelectric nonlinearity is extremely valuable. The Rayleigh law, first developed for ferromagnetic materials,[55] describes the field dependence of the dielectric and piezoelectric properties of many ferroelectric materials as well.[56-60] The physical model is that of mobile interfaces (i.e. domain walls and phase boundaries) interacting with a distribution of pinning centers; the interaction energy as a function of domain wall position can be represented with a potential energy landscape where each well is controlled by the *local* distribution of elastic and electric fields. The assumption is that no correlation exists between the depth and shape of adjacent potential wells and that the probing field does not change the domain structure during

the measurement.[61] The Rayleigh relations (equations 2-5 and 2-6) can be used to quantify the irreversible extrinsic contributions to the dielectric properties of ferroelectrics.[60]

Measurements of the extrinsic contributions to the properties are generally macroscopic in character (see section 2.6, Impact of Composition on Extrinsic Contributions to the Properties), where domain walls are sampled collectively over large volumes of material. Thus, the nanoscale phenomena governing the extrinsic contributions through domain wall or phase boundary motion remain largely unknown. The chapter aims to compare the global dielectric nonlinearities and *local* electric-field-induced displacements using a band excitation PFM method in a series of perovskite films with different ferroelectric distortions. The measured changes in dielectric and *local* piezoelectric nonlinearity as a function of composition provide insight into the domain wall dynamics of piezoelectric thin films under subcoercive electric fields. The thin film samples in this study were epitaxially grown on $SrTiO_3$ substrate to eliminate the influence of large angle grain boundaries.

5.3 Experimental Procedure

5.3.1 Sample Preparation

(001) $SrTiO_3$ single crystals (MTI Corp., Richmond, CA) were used as substrates for the growth of epitaxial films. A $SrRuO_3$ bottom electrode was deposited via pulsed laser deposition (PLD) as described elsewhere.[127] $(0.3)Pb(Ni_{0.33}Nb_{0.67})O_3$ - $(0.7)Pb(Zr_xTi_{1-x})O_3$ films of approximately 1 μm in thickness were deposited on (001) $SrRuO_3/SrTiO_3$ using a solution deposition process. Solutions were prepared with zirconium to titanium ratios of x = 0.2, 0.45 and 0.8 with 10 mol % excess PbO in order to compensate for lead oxide volatility during the annealing steps. Details of the spin-coating and pyrolysis conditions are given elsewhere.[126] In

particular, every fourth layer, a solution with the same PNN-PZT composition but 20 mol% PbO excess was spun on. After this layer was pyrolyzed, the stack was crystallized at 800 ºC for 1 min with a ramp rate of 50 ºC/s using a rapid thermal annealer (Heatpulse 210, AG Associates, San Jose, CA or RTP 600, Modular Process Technology Corp., San Jose, CA). The deposition process was repeated 5 times to build up the desired thickness of ~ 1 μm for each sample.

5.3.2 Film Characterization

Out-of-plane lattice parameters were investigated using a Philips X'pert Pro MRD 4-circle diffractometer (PANalytical Inc., Tempe, AZ). Jade x-ray analysis software (Materials Data Inc., Livermore, CA) was used to extract *d*-spacings from the scans. These were fitted using the Nelson-Riley function to determine the out-of-plane lattice parameters.[134] For the in-plane lattice parameters, θ-2θ scans of the $\{101\}$ peaks were used. For all estimates of the lattice parameter, the STO substrate was used as an internal standard. ϕ scans were utilized to assess epitaxy.

To perform electrical and electromechanical characterization, an array of top electrodes was obtained by sputter-depositing 40 nm of Pt using a CMS-18 deposition system (Kurt J. Lesker Company, Clairton, PA) at a base pressure of 10^{-6} Torr. Circular electrodes with diameters ranging from 10 to 200 μm were patterned by the photolithography and lift-off process. To facilitate electrical access, several electrode dots on the top surface of the film were gold-wire-bonded (Kulicke & Soffa Industries Inc., Fort Washington, PA) to ceramic packages (Spectrum Semiconductor Materials Inc., San Jose, CA).

Dielectric constant and loss measurements of the PNN-PZT films were made using a HP 4192A LF impedance analyzer (Agilent Technology, Palo Alto, CA) at 10 kHz and an oscillating voltage of 30 mV_{rms}. Dielectric constant and loss were also measured as a function of

temperature and frequency using a HP 4284A precision LCR meter (Agilent Technology, Palo Alto, CA) on poled and thermally depoled samples with a computerized management and data acquisition software (Gadd and Vision, developed at PennState). The frequencies employed for the measurements went from 100 Hz to 1 MHz and an oscillating voltage of 30 mV (rms value). Measurements were made in an in-house designed multi-sample furnace from 30 ºC up to 500 ºC.

Polarization-electric field hysteresis was measured using an RT 66A standardized ferroelectric test system (Radiant Technology Inc., Albuquerque, NM) in the virtual ground mode. The nonlinear dielectric measurements were performed using a HP 4284A precision LCR meter (Agilent Technology, Palo Alto, CA) on aged samples. The measurements were performed at frequencies ranging from 50 Hz – 400 kHz and the capacitance and loss tangent of the samples were recorded sweeping from 5 mV (rms value) to approximately half of the coercive field.

Band excitation piezoresponse force microscopy (BE-PFM) was employed to characterize the *local* converse piezoresponse. In BE-PFM, the data acquisition is performed by exciting the cantilever with a signal with a specified amplitude and phase content in a defined frequency interval, rather than at a single frequency as in conventional PFM.[124] BE-PFM was implemented on a commercial Asylum MFP-3D system with a custom BE controller. A high voltage amplifier (F10A, FLC Electronics) was used to drive the capacitor structures. The top electrode and the conductive cantilever Olympus ACM240TM (Olympus, Corp., Tokyo, Japan) were driven with the same excitation function and the bottom electrode was grounded. Both dielectric and piezoelectric characterization measurements were performed after poling the ferroelectric capacitors for 20 min at 5 times the coercive field E_c and aging for at least 30 min.

For transmission electron microscopy (TEM), cross-sectional thin foils were prepared by conventional sample preparation techniques involving mechanical polishing and Ar-ion milling (Fischione 1010). The samples were characterized in a JEOL 2010 LaB_6 200 kV TEM operating at 200 kV using a Gatan 646 double tilt analytical holder.

5.4 Results

The (0.3)Pb($Ni_{0.33}Nb_{0.67}$)O_3-(0.7)Pb(Zr_xTi_{1-x})O_3 compositions were chosen to represent distinct regions of the PNN-PZT ternary phase diagram. The (0.3)Pb($Ni_{0.33}Nb_{0.67}$)O_3-(0.7)Pb($Zr_{0.45}Ti_{0.55}$)O_3 composition provides a $T_c \sim 200$ ºC [111] (which was confirmed for films of the same composition deposited on Si substrates, see section 3.4.3) and should be at the morphotropic phase boundary, as extrapolated from the phase diagram reported by Gilles.[112] The (0.3)Pb($Ni_{0.33}Nb_{0.67}$)O_3-(0.7)Pb($Zr_{0.20}Ti_{0.80}$)O_3 composition was chosen as the tetragonal member and the (0.3)Pb($Ni_{0.33}Nb_{0.67}$)O_3-(0.7)Pb($Zr_{0.80}Ti_{0.20}$)O_3 as the rhombohedral member of the series. The temperature dependence of the dielectric constant for the tetragonal sample evidenced a broad maximum, as well as a change in the slope of the temperature dependence when measurements where performed on thermally depoled samples. These characteristics suggest the possible presence of a normal to relaxor phase transition at temperatures lower than T_{max} for the Ti-rich sample.[135-137]

5.4.1 Crystallinity

Figure 5-1 (a) shows the θ-2θ scan profiles for the PNN-PZT films of different compositions. The full widths at half maximum (FWHM) for the X-ray rocking curves of the 002 peaks were 0.18º, 0.21º and 1.75º for the rhombohedral, MPB and tetragonal samples respectively (0.0018º being the resolution of the instrument). In these chemical solution deposited thin films, each layer nucleated epitaxially on the previous annealed layer.[138] No peaks from pyrochlore phases were recognized and only small peaks related to (110) and (222) misoriented grains were detected for the MPB and tetragonal samples.

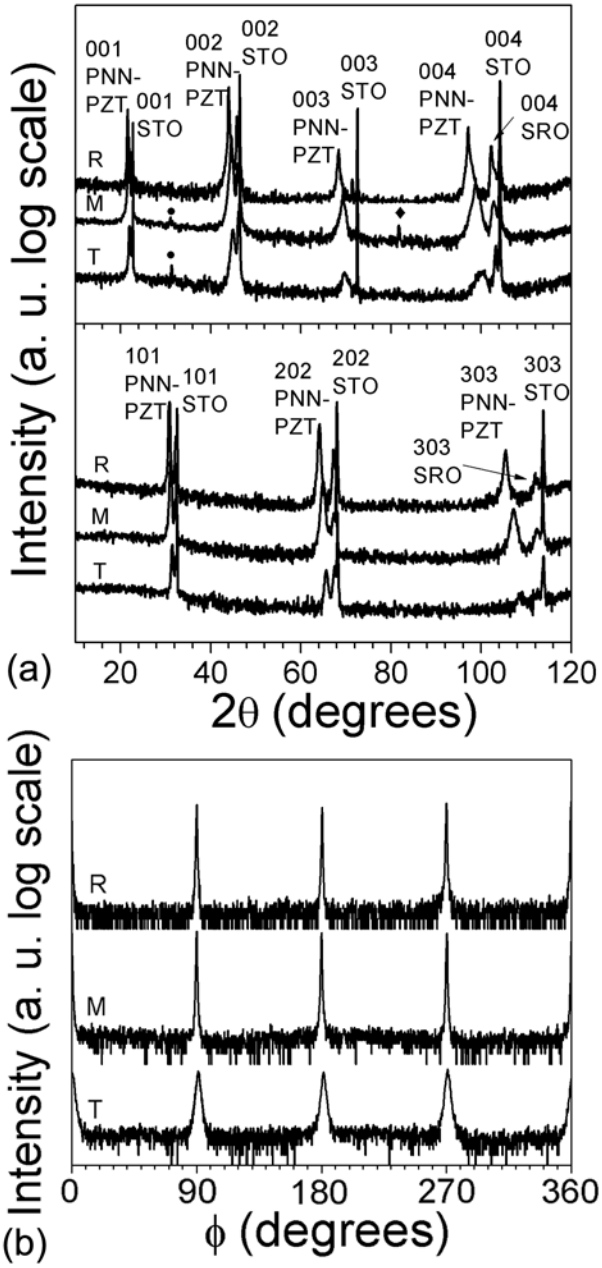

Figure **5-1**: (a) $\theta - 2\theta$ XRD patterns for the PNN-PZT films, R, M and T indicate Rhombohedral, MPB and Tetragonal compositions respectively, the ● and ◆ symbols mark 101 and 222 perovskite reflections respectively. (b) XRD Φ scans for the three compositions.

The out-of-plane pseudocubic lattice parameters for the samples were 4.036 ± 0.002 Å, 4.062 ± 0.002 Å and 4.112 ± 0.002 Å for the tetragonal, MPB and rhombohedral films,

respectively. The same values, within experimental errors, were obtained for the in-plane lattice parameters.

Figure 5-1 (b) presents the x-ray Φ-scan spectra of each film. The peaks occur at nearly the same azimuth Φ angles as the STO substrate reflections (not shown) and are separated by 90º. This indicates that the PNN-PZT films are epitaxially grown on the STO substrates.

5.4.2 Microstructural and Ferroelectric Domain Structures Analysis

As seen from the 4-circle XRD analysis, the PNN-PZT films were grown with an epitaxial relationship with respect to the STO substrate; TEM analysis further confirmed this by showing an epitaxial relationship between the PNN-PZT films and the underlying substrate diffraction patterns.

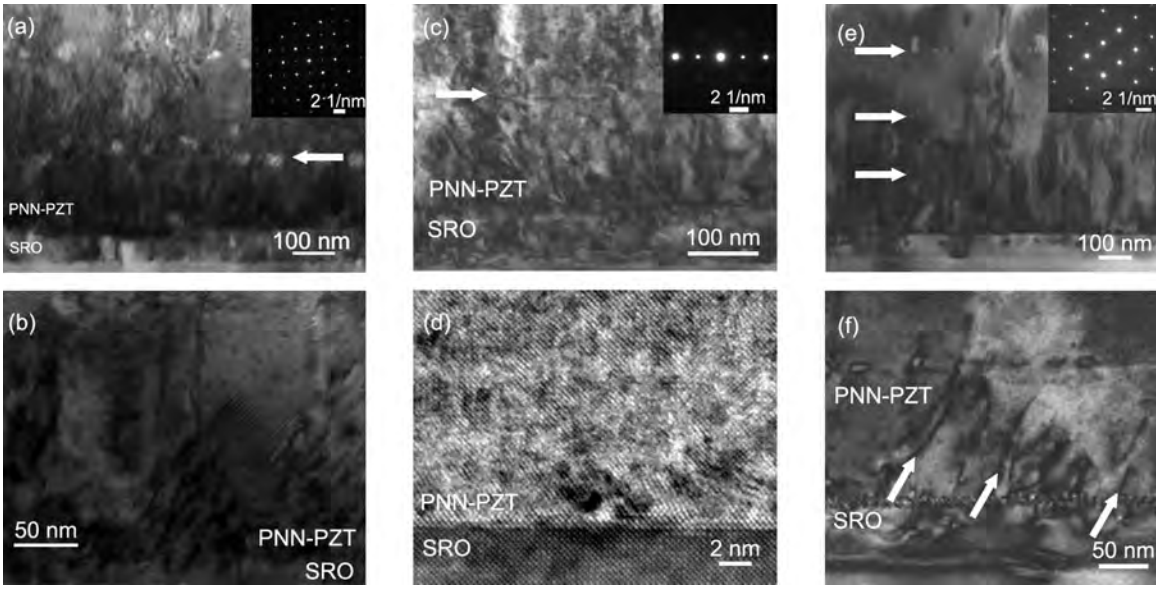

Figure **5-2**: (a) and (b) Cross-sectional dark-field $[1\,\bar{1}0]$ TEM images of the tetragonal PNN-PZT sample; the arrow points to planar defects. The inset in (a) shows the [001] zone axis electron diffraction pattern. The high angle peaks are elongated, indicative of small angle grain boundaries. (c) Cross-sectional dark-field [001] TEM image of the MPB PNN-PZT sample, showing the domain structure, the inset shows the diffraction pattern. (d) HR-TEM image of the MPB PNN-PZT/SRO boundary. (e) and (f) Cross-sectional [112] bright-field TEM images of the rhombohedral PNN-PZT sample. The horizontal arrow points at planar defects and the inclined arrows point at sheets of dislocations. The inset shows the diffraction pattern.

In Figure 5-2 cross-sectional TEM images of the three PNN-PZT/SRO/STO samples are reported. In the tetragonal sample, Figure 5-2 (a), a sharp PNN-PZT/SRO interface can be seen, suggesting negligible interdiffusion. However, planar defects parallel to the substrate surface were apparent as indicated by the arrow in Figure 5-2 (a). These defects are a consequence of repeated spin-coating/crystallization steps typical of chemical solution deposition processes. A clear coarse domain structure was not identified, probably due to a finite degree of relaxor ferroelectric character.[139]

The [001] zone axis diffraction pattern in the inset of Figure 2 (a) shows slight relative rotation of adjacent grains, indicative of the presence of small angle grain boundaries, consistent with the presence of Moiré patterns in the same region shown in Figure 5-2 (b).

Figure 5-2 (c) is a cross-sectional TEM image of the MPB PNN-PZT sample. The image shows a mottled type of contrast. The characteristic width of the identifiable features is ~ 10-30 nm, which is consistent with previous reports on irregular domains shapes of PZT thin films at the morphotropic phase boundary composition.[89,140,141]

Figure 5-2 (d) is a HR-TEM image of the MPB PNN-PZT/SRO boundary. The interface is clean with no presence of transition layers. The contrast in the PNN-PZT layer is attributed to the mottled domain structure.[89]

Figures 5-2 (e) and (f) were recorded with an electron beam parallel to the [112] zone axis and the PNN-PZT and electrode layers are indicated. Sheets of dislocations originating at the PNN-PZT/SRO interface and propagating through the several deposited layers of PNN-PZT, creating small angle grain boundaries, are visible in the cross-section in Figure 5-2 (e). The FWHM rocking curve value characterized for the out of plane 002 XRD reflection for the rhombohedral sample arises from this mosaicity.

5.4.3 Dielectric Characterization

Table 5-1 shows a summary of properties for the films in this study. The low field dielectric permittivity, ε_r, reached a maximum for the MPB composition sample with a ε_r of 2550 ± 90 while lower values of ε_r, 2250 ± 90 and 1180 ± 60 were found for the rhombohedral and tetragonal films, respectively. In general, maxima in piezoelectric and dielectric coefficients are observed in the vicinity of phase transitions.[3,4,142-144]

The observed trend in remanent polarization, P_r, is a function of at least two factors: differences in the Curie temperature, and the orientation dependence of the spontaneous polarization. The temperature at which the maximum permittivity was observed for the three PNN-PZT compositions studied is the highest for the tetragonal sample and the lowest for the rhombohedral sample. One would expect larger P_r along the polar axis for samples with higher transition temperatures. Secondly, while the polar direction is <001> for the tetragonal composition, the polarization lies along the <111> direction for the rhombohedral phase, at ~ 54.7º with respect to the normal to the (001) $SrTiO_3$ substrate.[49]

It is noted here that the ratio of the remanent polarization for the tetragonal and rhombohedral samples is 1.76, which is close to $\sqrt{3}$. The coercive fields increased with the degree of tetragonality as also reported by other authors.[3,78,145]

Table **5-1**: Dielectric properties for the films characterized in this study.

Sample composition	ε_r	$tan\delta$ (%)	P_r ($\mu C/cm^2$)	E_c (kV/cm)
Tetragonal	1180 ± 60	3.6	21	24
MPB	2550 ± 90	2.9	30	28
Rhombohedral	2250 ± 90	3.8	17	18

5.4.4 Temperature Dependence of Dielectric Properties

Temperature dependent permittivity measurements were performed on the samples in this study. Figure 5-3, 5-4 and 5-5 show the dielectric constant and loss temperature behavior for the rhombohedral, MPB and tetragonal films respectively.

Table **5-2**: Characterized T_{max} during heating and cooling at 10 kHz.

Composition	T_{max} *Ramp Up (ºC)*	T_{max} *Ramp Down (ºC)*
Rhombohedral	142 ± 1	130 ± 1
MPB	188 ± 1	172 ± 2
Tetragonal	275 ± 1	265 ± 1

The T_{max} reported in Table 5-2 are the temperature values that yield a null first derivative of a fifth order polynomial fit of the dielectric constant measured at 10 kHz. As shown in Table 5-2 a thermal hysteresis was noticed for the values of T_{max} characterized during ramp up and ramp down. Such behavior would be consistent with a first order ferroelectric to paraelectric transition.[146,147]

The temperature dependence of the dielectric constant in the paraelectric region of the rhombohedral sample was fitted to the Curie-Weiss law using equation 5-1

$$\varepsilon_r = \frac{C}{(T - T_0)} \qquad \text{Equation } \mathbf{5\text{-}1}$$

where C is the Curie-Weiss constant and T_0 is the Curie-Weiss temperature. A Curie-Weiss constant, C, of $1.7 \pm 0.007 * 10^5$ K was calculated for the ramp down set of data with correlation factors for linear regression, $R > 0.98$ for all fits. This value is on the same order of magnitude as other relaxor-ferroelectric solid solutions exhibiting displacive phase transitions and was found to be frequency independent.[148]

The ramp up set of data for the rhombohedral sample showed a similar Curie-Weiss constant, however some frequency dispersion was noticed in the 300 Hz – 1kHz frequency range, most likely due to non-negligible leakage mechanisms at temperatures above 200 ºC. It was not possible to perform similar fits for the MPB and tetragonal samples because of relatively higher leakage in the paraelectric temperature range.

The T_{max} measured for the MPB sample is lower than the transition temperature for films of this composition grown on Si substrates, based on the data on section 3.4.3. The T_{max} characterized in this study may correspond to the T_1 characterized for the highly {001} textured film deposited on Si.

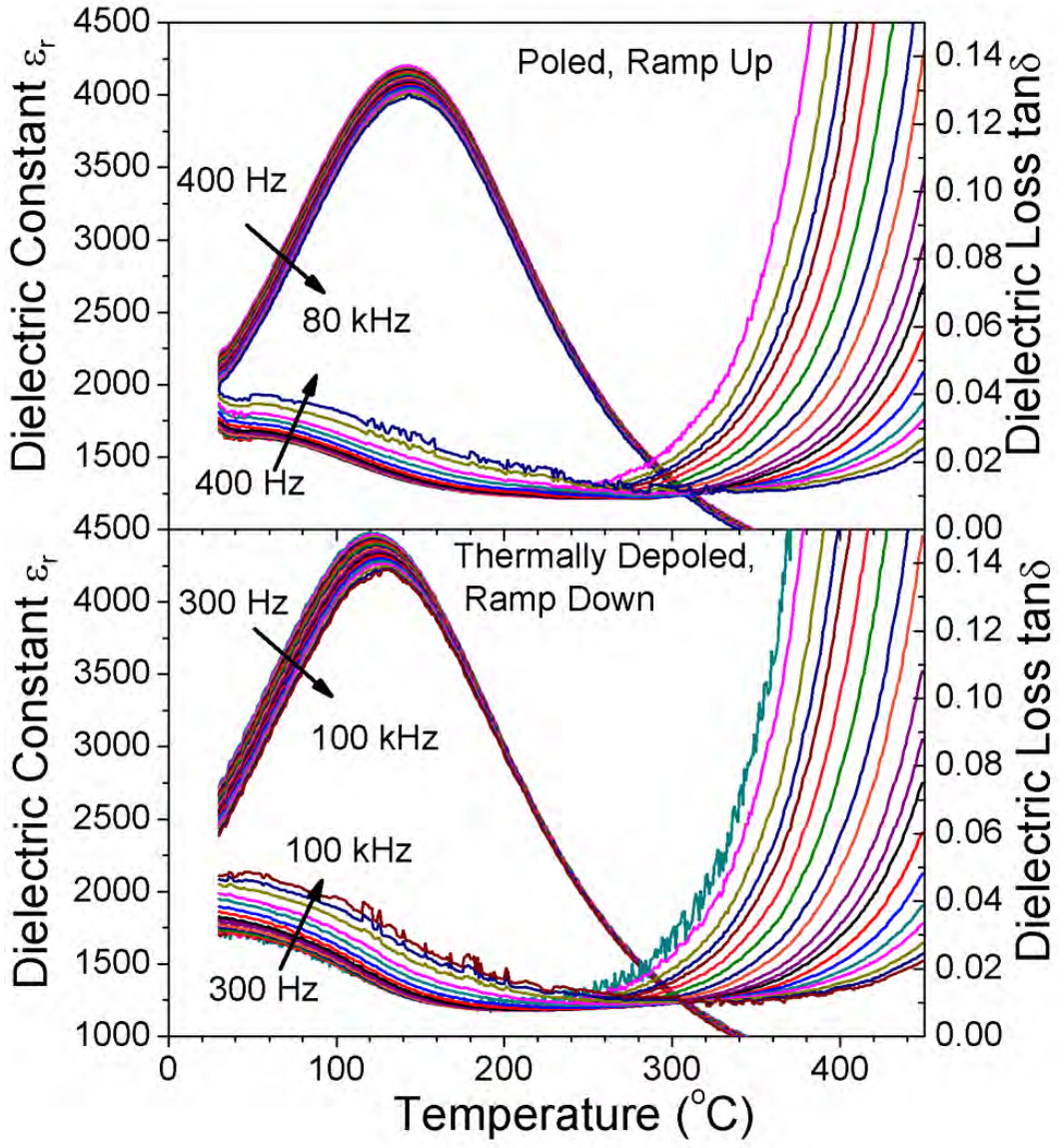

Figure **5-3**: Permittivity and dielectric loss curves for a poled (upper panel) and thermally depoled (bottom panel) rhombohedral PNN-PZT film.

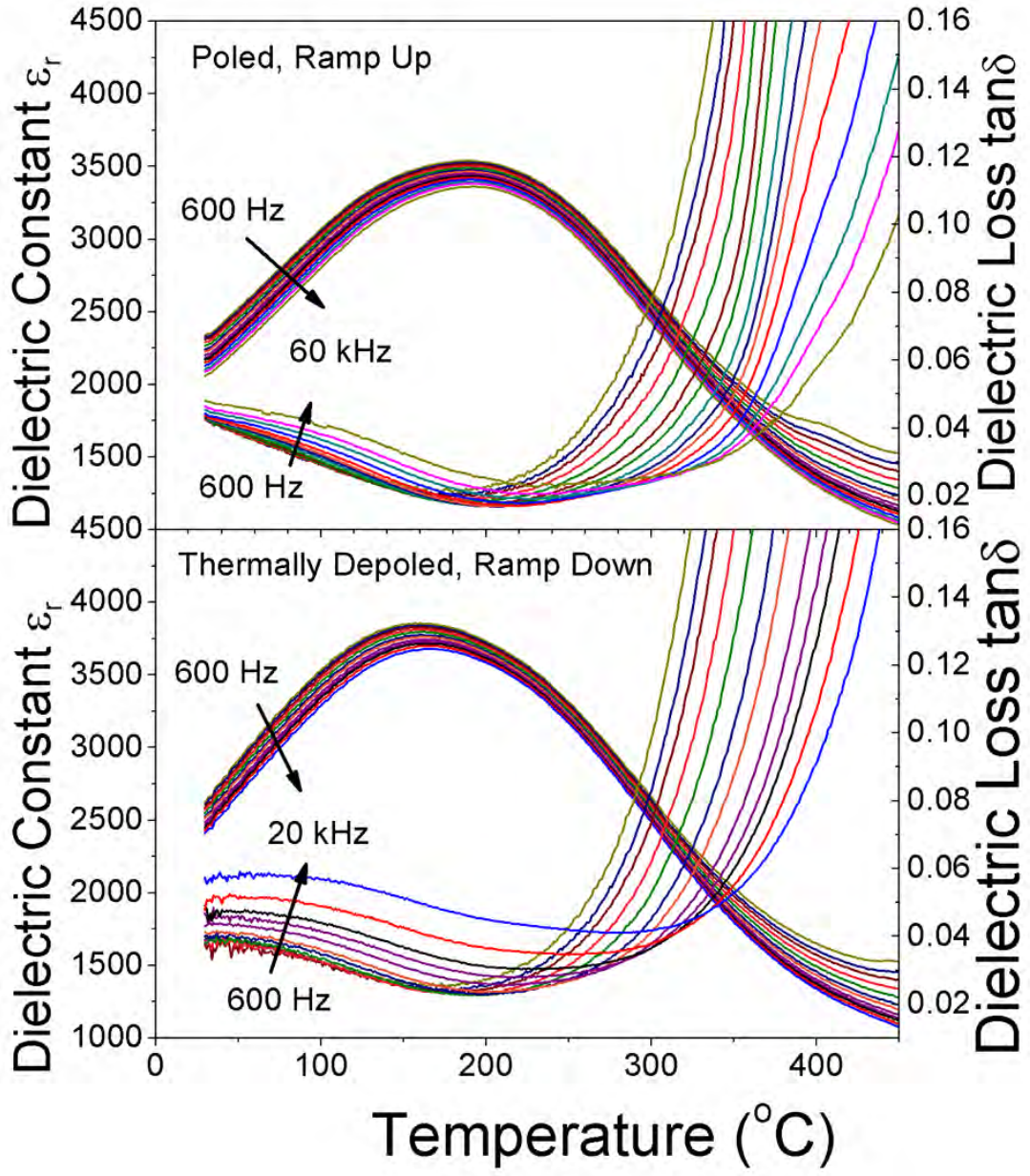

Figure **5-4**: Permittivity and dielectric loss curves for a poled (upper panel) and thermally depoled (bottom panel) MPB PNN-PZT film.

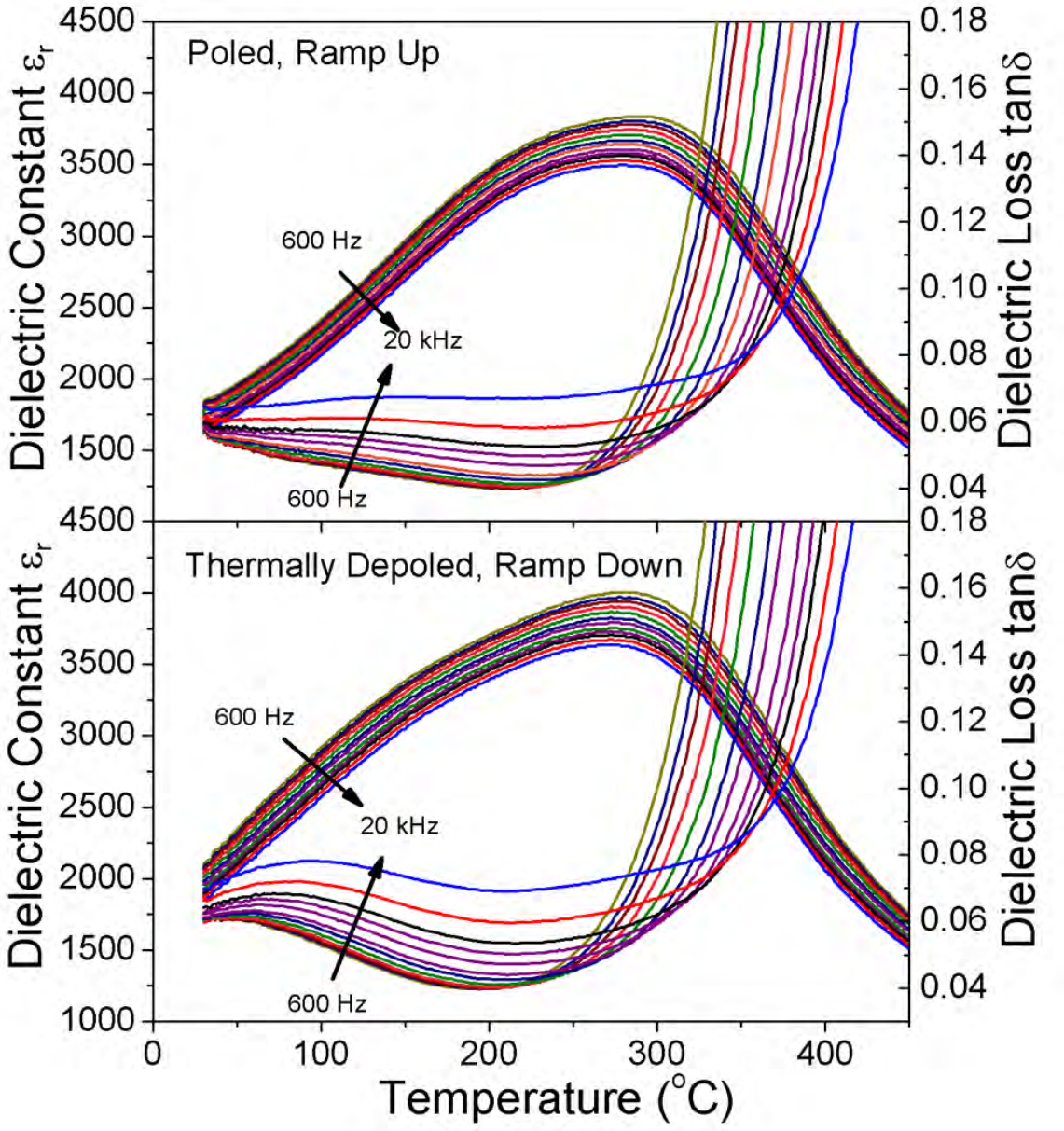

Figure **5-5**: Permittivity and dielectric loss curves for a poled (upper panel) and thermally depoled (bottom panel) tetragonal PNN-PZT film.

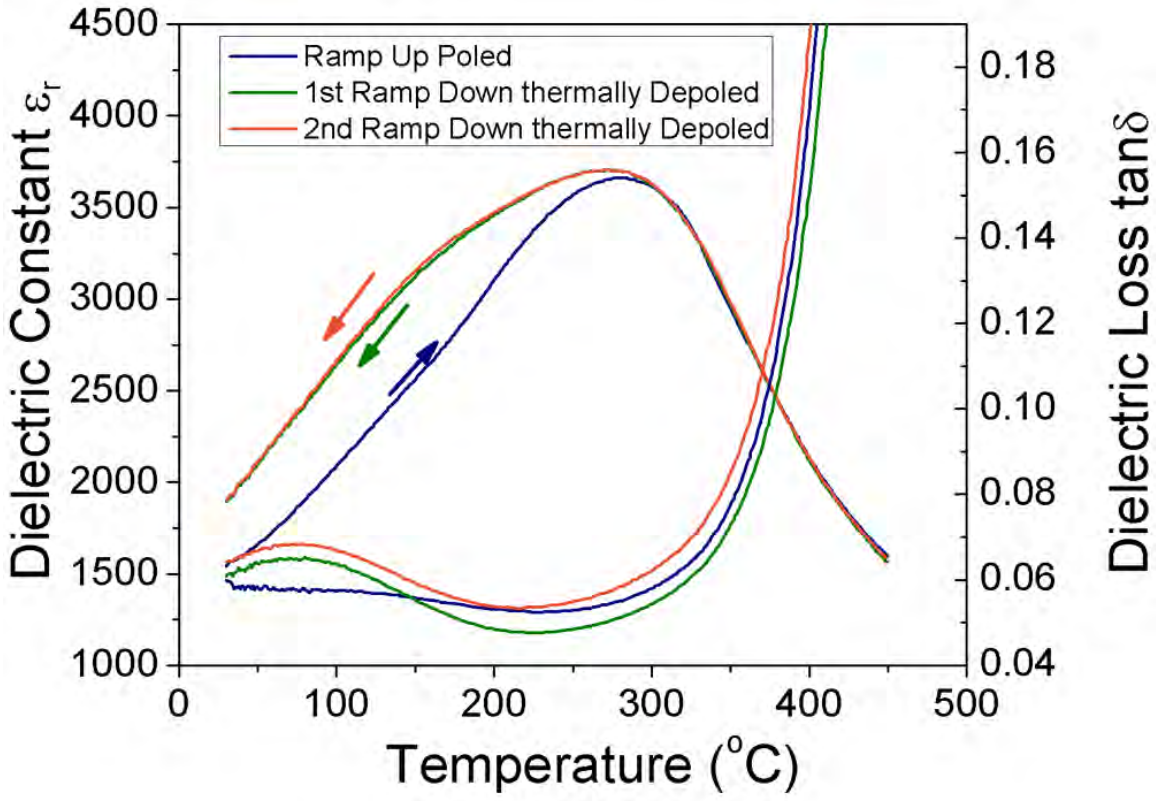

Figure **5-6**: Permittivity and dielectric loss curves for a poled and thermally depoled tetragonal PNN-PZT film at 10 kHz.

Finally, differences were noticed in the dielectric behavior in the ferroelectric temperature range for the tetragonal sample. In Figure 5-6, two curves obtained ramping down from a thermally depoled state are compared to the temperature dependence of the dielectric constant collected during heating of a poled sample. A clear, low-temperature shoulder on the permittivity peak is observed for the cooling data. It is possible that the shoulder visible on cooling is associated with a relaxor-normal ferroelectric phase transition similar to that reported by Stenger and Burggraaf for $Pb_{0.83}La_{0.17}Zr_{0.3}Ti_{0.7}O_3$.[136] Although a change in the frequency dispersion for T_{max} may not be noticeable because of the broad phase transition peak, it is

speculated that this phenomenon is associated with an induced phase transition from a relaxor phase to a long-range polar phase, i.e., from microdomain to macrodomain states.[146,149,150]

5.4.5 Dielectric Nonlinearity and Application of Rayleigh Law

The validity of the Rayleigh approach for these samples can be seen in Figure 5-7, where the Rayleigh parameters measured at 100 Hz were used to compare the extrapolated hysteresis minor loops using Equation 1b and the measured ones. The modeled behavior is very close to the experimental data for the three samples, suggesting that the Rayleigh formalism provides a good description of the dielectric properties.

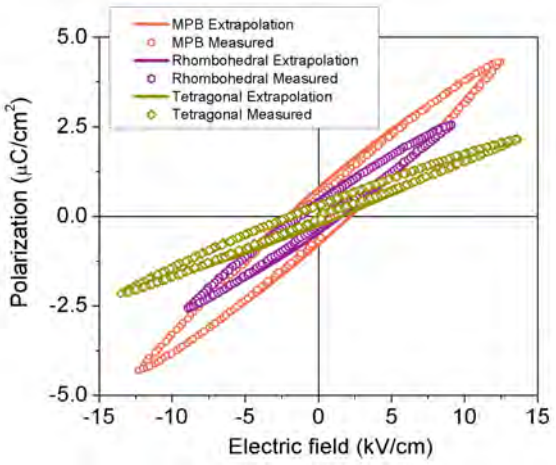

Figure **5-7**: The polarization, *P*, – electric field, *E*, sub-switching hysteresis loops for MPB, rhombohedral and tetragonal PNN-PZT. The measurements were performed at 100 Hz. Shown are both the experimental data and the loops calculated from the Rayleigh parameters.

Table **5-3**: Summary of dielectric nonlinearity characterization for the three compositions.

		Tetragonal	MPB	Rhombohedral
10 kHz	α_ε (cm/kV)	23.4 ± 0.1	89.2 ± 0.2	98.6 ± 0.03
	ε'_{init}	1275 ± 2	2334 ± 5	1941 ± 4
	$\alpha_\varepsilon / \varepsilon_{init}$ (cm/kV)	0.018 ± 0.0001	0.038 ± 0.0002	0.051 ± 0.0002
300 kHz	α_ε (cm/kV)	13.6 ± 0.1	61.1 ± 0.3	59.3 ± 0.3
	ε_{init}	1150 ± 1	2055 ± 2	1775 ± 2
	$\alpha_\varepsilon / \varepsilon_{init}$ (cm/kV)	0.012 ± 0.0001	0.029 ± 0.0003	0.033 ± 0.0003

The AC field dependence of the dielectric properties for the samples increased almost linearly with the applied field after a small threshold voltage (E_{th} < 0.2 kV/cm). The Rayleigh parameters for the dielectric response were calculated from fits to the linear portion of the data. The results are tabulated in Table 5-3. The reported errors were determined from the least squares analysis of the Rayleigh plots. The Rayleigh regions for the films extended up to half of the coercive field.

There is a clear dependence of the Rayleigh parameters on composition. At 10 kHz, the rhombohedral and MPB samples had the highest α_ε coefficients. The tetragonal sample showed α_ε values ~ 1/3 as large as those of the other samples. This indicates relatively smaller irreversible contributions to the dielectric properties in the tetragonal phase and is consistent with what observed by Eitel *et al.*[57], Damjanovic *et al.*[54] and Pramanick *et al.*[66] in bulk ferroelectric ceramic systems.

Damjanovic demonstrated a logarithmic frequency dependence of the direct piezoelectric coefficient for systems with properties governed by interface pinning.[151] The logarithmic frequency dependence of the extrinsic contributions to the properties is generally valid in random systems that have properties controlled by a normal distribution of restoring forces.[152,153] In Damjanovic's work, it was also shown that the logarithmic dependence held for the domain-wall pinning processes in ferroelastic-ferroelectric systems over a few orders of magnitude in frequency.[59]

For the PNN-PZT films, the frequency dependent Rayleigh parameters were fit to:

$$\varepsilon_{init}(\omega) = e_0 + e\ln\left(\frac{1}{\omega}\right) \qquad \text{Equation } \mathbf{5\text{-}1}$$

$$\alpha_{\varepsilon}(\omega) = a_0 + a\ln\left(\frac{1}{\omega}\right) \qquad \text{Equation } \mathbf{5\text{-}2}$$

where ω is the angular frequency. The data are shown in Figure 5-8 and the extrapolated values for e_0, e, a_0 and a and the fitting errors can be found in Table 5-4. The fit to the data using Equations 5-1 and 5-2 is good, with correlation factors for linear regression, $R > 0.98$ for all fits.

If the a/a_0 ratios are compared for the 3 compositions, the MPB sample has the weakest frequency dependence of the irreversible Rayleigh coefficient α_{ε} while the tetragonal exhibits the highest. As previously discussed by Bassiri-Gharb *et al.,*[154] frequency dependence of the Rayleigh parameters may be associated with the time constant distribution for domain wall motion. Thus, the stronger frequency dependence of the irreversible Rayleigh parameter α_{ε} in the tetragonal films may be associated with a larger fraction of the domain walls being slow-moving, so that their contribution to α_{ε} gradually freezes out with frequency. The weaker frequency dependence in the MPB and rhombohedral films may be associated with either uniformly more mobile domain walls, or a broader distribution of relaxation time constants for the domain walls.[155]

Differences were also noticed for the e/e_0 ratios, with the weakest frequency dependence in ε_{init} observed for the rhombohedral sample. Overall, these results indicate that the composition, and the associated domain structure and twin variants significantly impact the domain wall mobility.

Table **5-4**: Logarithmic frequency dependence of the dielectric Rayleigh parameters. The error bars shown are fitting errors for individual data sets

	Tetragonal	MPB	Rhombohedral
a_0	53 ± 0.4	168 ± 0.8	180 ± 0.9
a	2.6 ± 0.04	7.3 ± 0.1	8.3 ± 0.1
e_0	1664 ± 3	3017 ± 25	2458 ± 12
e	36 ± 0.3	66 ± 2.3	47 ± 1.1
a/a_0	0.049 ± 0.00084	0.043 ± 0.0005	0.046 ± 0.0005
e/e_0	0.021 ± 0.0002	0.022 ± 0.0008	0.019 ± 0.0005

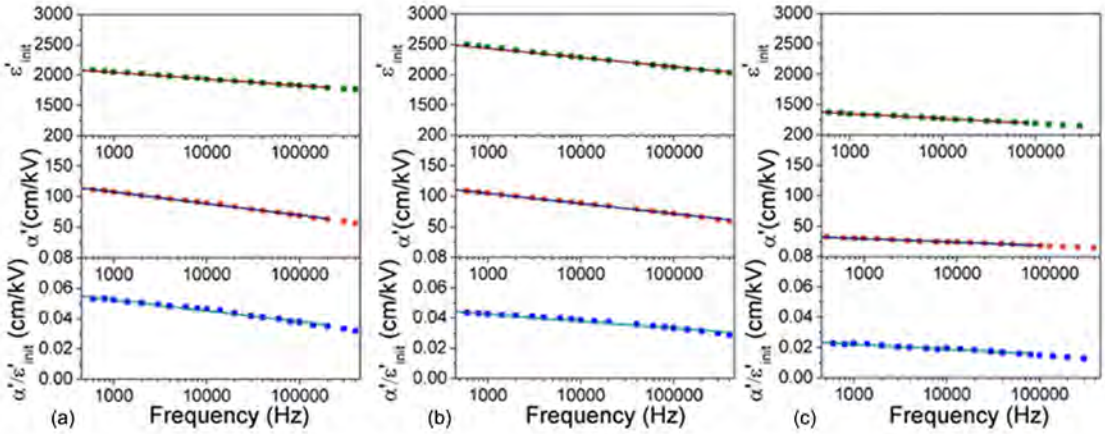

Figure **5-8**: Frequency dispersion of the Rayleigh parameters extrapolated from the AC field dependence of the dielectric constant. Part (a), (b) and (c) refer to the rhombohedral, MPB and tetragonal samples respectively.

5.4.6 Local Converse Piezoelectric Response Measurements by Band Excitation PFM

The piezoelectric response was collected using a band excitation signal with an amplitude modulation. The AC amplitude modulation covered the same field range as those used for the dielectric characterization; the frequency band was chosen to encompass the resonance of the cantilever tip in contact with the top electrode surface (around 270 kHz).

A simple harmonic oscillator model was used to approximate the dynamic behavior of the cantilever weakly interacting with the surface.[124] From the fit, *local* voltage-dependent maps of A_{max} i.e. the amplitude at the resonance, resonance frequency ω_0, the quality factor Q and the phase tan($\varphi(\omega)$) were extracted. All of these parameters were obtained as a function of the applied excitation voltage.

$$A(\omega) = \frac{A_{\max}\omega_0^2}{\sqrt{(\omega^2 - \omega_0^2)^2 + (\omega\omega_0/Q)^2}} \qquad \text{Equation } \mathbf{5\text{-}3}$$

$$\tan(\varphi(\omega)) = \frac{\omega\omega_0/Q}{\omega^2 - \omega_0^2}$$ Equation **5-4**

As described by Bintachitt *et al.,*[130] and reported in chapter 4, the amplitude is a nonlinear function of the applied voltage and can be described with a second order polynomial as in Equation 4-1. Differentiation with respect to V_{ac} yields the Rayleigh law as in Equation 4-2.

As shown by Kalinin *et al.,*[156] the anisotropy of the generated strain determines the interaction volume probed by the scanning cantilever tip in piezoelectric capacitors. By using Equations 5-5, 5-6 and 5-7 it is possible to estimate the sampled volume.

$$w(L,H) \cong s\left(\eta,\nu\frac{d_{31}}{d_{33}}\right)H + t\left(\eta,\nu\frac{d_{31}}{d_{33}}\right)L$$ Equation **5-5**

The coefficient *s* can be found as the solution of:

$$\arctan\left(\frac{s}{2}\right) + \frac{d_{33} + \nu d_{31}/2}{d_{33} + (1+2\nu)d_{31}}\ln\left(1 + \frac{4}{s^2}\right)\frac{s}{2} = \frac{\pi}{2}\eta$$ Equation **5-6**

where the coefficient *t* is

$$t = \eta\frac{\pi}{2}\frac{d_{33} + (1+2\nu)d_{31}}{d_{33} + \nu d_{31}/2}$$ Equation **5-7**

where w is the PFM lateral resolution determined as a bilinear function of the thickness of the ferroelectric film (H) and electrode thickness (L); d_{33} and d_{31} are the longitudinal and transverse piezoelectric coefficients, ν is Poisson's ratio and η is an arbitrary value that sets a saturation limit for the signal at the edge of the lateral resolution w.

In order to compare the lateral resolutions in capacitors of different compositions, w was estimated using $\eta = 0.76$, $\nu = -s_{12}^E/s_{11}^E$ calculated for each composition,[§] the film thicknesses (~ 1 μm) and the piezoelectric tensors for $PbZn_{1/3}Nb_{2/3}O_3$-$PbTiO_3$ (PZN-PT) and $PbMg_{1/3}Nb_{2/3}O_3$-

[§] $\nu = -s_{12}^E/s_{11}^E$ instead of $\nu = -s_{13}^E/s_{11}^E$ because of the large anisotropy in the compliance tensor for the MPB PMN-PT composition and the PZN-PT compositions. When the other Poisson's ratio was used, unphysical results were obtained.

$PbTiO_3$ (PMN-PT) single crystals.[157-161] Data for single crystals were utilized since the full property coefficient matrices are not known for any relaxor-based piezoelectric films. Because single crystal data have not been reported for PNN-PZT crystals, two different relaxor-PT families were examined as models.

The calculations show that the lateral resolutions depend upon composition as reported in Table 5-5 and 5-6. In PZN-PT single crystals, due to the strain anisotropy, the interaction volume for the rhombohedral and MPB compositions is 5 to 7 times smaller than for the tetragonal case. Similarly, in PMN-PT single crystals, the interaction volume for the rhombohedral and MPB compositions is 2 – 3 times smaller than for the tetragonal case.

Table **5-5**: Lateral resolution and sampled volume estimates for PZN-PT single crystals.

	Tetragonal	MPB	Rhombohedral
Composition and reference	PZN-12%PT Hentati *et al.*[157]	PZN-8%PT Jiang *et al.*[158]	PZN-4.5%PT Jiang *et al.*[158]
d_{31} (pC/N)	-207	-1450	-970
d_{33} (pC/N)	541	2900	2000
s	0.193	0.077	0.089
t	0.552	0.749	0.232
w (nm) lateral resolution	234	110	103
sampled volume (μm^3)	0.047	0.0100	0.009

Table **5-6**: Lateral resolution and sampled volume estimates for PMN-PT single crystals.

	Tetragonal	MPB	Rhombohedral
Composition and reference	PMN-38%PT Cao *et al.*[161]	PMN-33%PT Zhang *et al.*[159]	PMN-29%PT Zhang *et al.*[160]
d_{31} (pC/N)	-123	-1330	-699
d_{33} (pC/N)	300	2820	1540
s	0.162	0.099	0.118
t	0.501	0.435	0.157
w (nm) lateral resolution	198	121	128
sampled volume (μm^3)	0.0340	0.0121	0.0139

5.5 Discussion

Figure 5-9 shows the topography and $\alpha_d / d_{33,init}$ functional maps for the different samples. The spatial averages of $\alpha_d / d_{33,init}$ are reported in Table 5-7 along with the $\alpha_\varepsilon / \varepsilon_{init}$ values.

The averaged *local* piezoelectric nonlinearities for the MPB and rhombohedral sample show a large standard deviation representative of the clusters of enhanced extrinsic contributions as seen in Figure 5-9. A clear trend in the values of $\alpha_\varepsilon / \varepsilon_{init}$ for the 3 samples was detected with the highest value of 0.052 cm/kV collected for the rhombohedral sample and a lowest value of 0.02 cm/kV measured for the tetragonal one at 10 kHz. On the other hand the $\alpha_d / d_{33,init}$ spatial averages were comparable for the rhombohedral and MPB sample (with averages of 0.0115 and 0.0101 cm/kV, respectively) and smaller, 0.0044 cm/kV for the tetragonal sample. The

distributions for the *local* $\alpha_d / d_{33,init}$ characterized for the 3 samples appeared symmetric with median values coincident with the calculated spatial averages, after removing outliers higher than 0.1 cm/kV in absolute value.

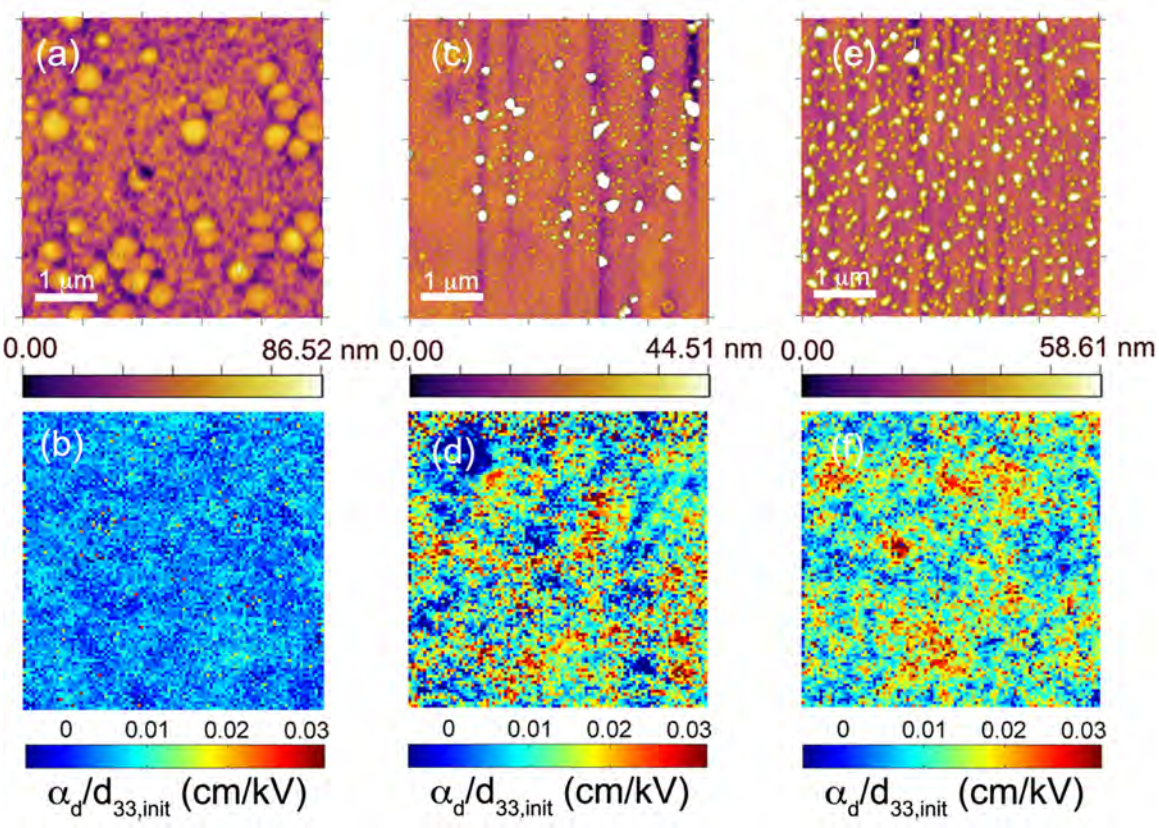

Figure **5-9**: Topography on top electrode and functional $\alpha_d / d_{33,init}$ maps for the (a) and (b) tetragonal, (c) and (d) MPB and (e) and (f) rhombohedral films.

The differences in the global dielectric and *local* piezoelectric nonlinearity measurements suggest that different populations of domain walls are contributing to the piezoelectric and dielectric irreversible contributions. This is in contrast with what observed in randomly oriented PZT[89] and {001} textured $0.5PbYb_{1/2}Nb_{1/2}O_3 - 0.5PbTiO_3$[154] thin films on silicon substrates. However the hierarchy in irreversible/reversible ratios is preserved, with relatively higher irreversible contributions to the properties observed for the rhombohedral and MPB samples.

Table **5-7**: Comparison of average $\alpha_\varepsilon / \varepsilon_{init}$ and $\alpha_d / d_{33,init}$.

	Tetragonal	*MPB*	*Rhombohedral*
$\alpha_\varepsilon / \varepsilon_{init} 10^{-3}$ (cm/kV)	14.3 ± 0.1	29.8 ± 0.3	33.4 ± 0.3
$\alpha_d / d_{33,init} 10^{-3}$ (cm/kV)	4.4 ± 3.8	10.1 ± 9.8	11.5 ± 5.6

There are several possible contributions to the observed composition dependence on the dielectric and piezoelectric nonlinearity. First, domain wall mobility may be favored for the rhombohedral sample because of a higher concentration of domain walls responding at the probing frequency band of BE-PFM. As discussed in the previous section, the rhombohedral sample showed a weaker frequency dependence of the reversible and irreversible dielectric Rayleigh parameters. Secondly, the number of spontaneous polarization directions (8) is larger in the rhombohedral phase as compared to the tetragonal phase (6). Thirdly, the smaller spontaneous strain in the rhombohedral and MPB samples relative to the tetragonal sample may increase the mobility of domain walls.[54,66,162] The elastic softening exhibited in compositions close to the MPB could also enhance domain wall motion by minimizing the associated stresses for the MPB sample.[143,163]

Finally, the tetragonal film shows more mosaicity than the rhombohedral and MPB samples, as evidenced by the larger FWHM in the XRD rocking curve. The lower values of $\alpha_\varepsilon / \varepsilon_{init}$ and $\alpha_d / d_{33,init}$ would be consistent with the denser network of small-angle grain boundaries in the tetragonal sample hindering the domain wall mobility.[126,164]

Statistical analysis of the distributions of the $\alpha_d / d_{33,init}$ values are shown in Figure 5-10 (a) and Table 5-7. The largest standard deviation of 9.8 10^{-3} cm/kV was characterized for the MPB sample; lower standard deviations, 5.6 10^{-3} and 4.4 10^{-3} cm/kV were characterized for the rhombohedral and tetragonal samples, respectively. These differences may be explained considering the different interaction volumes based on the strain anisotropy for samples of different compositions. As shown for the PZN-PT and PMN-PT single crystal systems in Tables 5-5 and 5-6, the estimated volume responding to the BE-PFM probing signal depends on the piezoelectric tensor. Similar trends are expected in the PNN-PZT system. The direct consequence is that for larger probed volumes, there is a higher likelihood of interacting with sites with high domain wall mobilities.[89] This would enable a more homogeneous nonlinear response to be collected and an overall smaller standard deviation for the $\alpha_d / d_{33,init}$ values. It is notable that the observed trend in standard deviations is consistent with the trend in interaction volume calculated for the PMN-PT and PZN-PT single crystal systems, with increasingly smaller values for the MPB, rhombohedral and tetragonal compositions respectively.

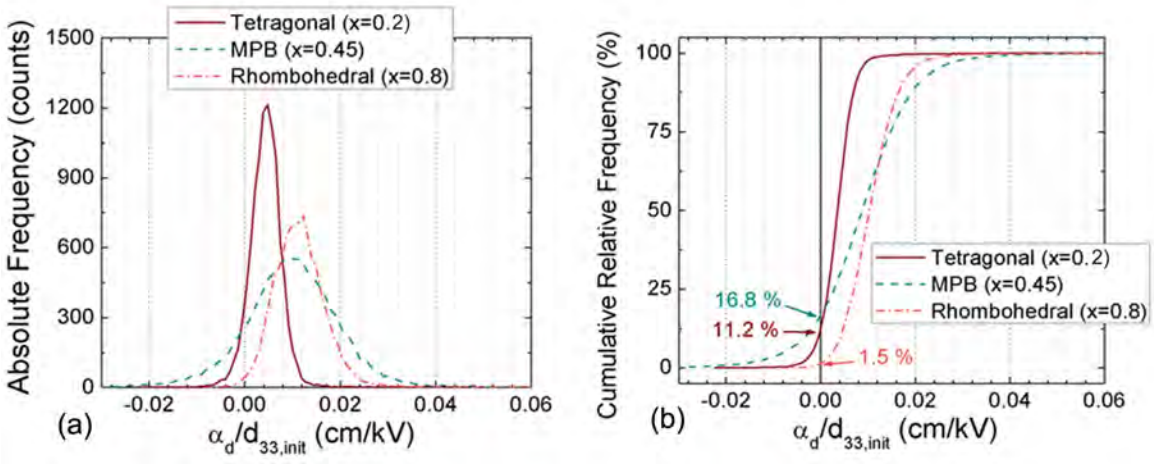

Figure **5-10**: Frequency histograms for the *local* nonlinear piezoelectric maps (a) absolute frequency count and (b) cumulative relative frequency.

As a final note, a non-negligible number of regions with negative $\alpha / d_{33,init}$ values were observed. From the cumulative relative frequency plot (Fig. 5-10 (b)) the negative regions accounted for 16.8 %, 11.2 % and 1.5 % of the maps in order for the MPB, tetragonal and rhombohedral. Arlt *et al*.[165] and Damjanovic *et al*.[54] predicted and reported respectively on the reduced mobility of domain walls in systems with closely spaced domain walls. The observed negative regions may be associated with hard *local* behavior. More substantive discussions of this will be the subject of chapter 6.

5.6 Conclusions

The dielectric and piezoelectric nonlinearities of model ferroelectric capacitors of tetragonal, MPB and rhombohedral PNN-PZT compositions were investigated through the application of the Rayleigh-like model to describe the collective dynamics of domain wall motion. A clear dependence of the degree of nonlinearity was observed in large dielectric measurements and in *local* piezoelectric measurements using BE-PFM.

The irreversible Rayleigh constants for the tetragonal composition α_ε were ~ 1/3 as large as those observed for the rhombohedral and MPB compositions. Similar behavior was observed for the piezoelectric Rayleigh coefficients. This correlates with the presence of more small-angle grain boundaries acting as pinning sites, and a larger fraction of slow-moving domain walls, as seen in the frequency dependence of the irreversible Rayleigh parameters.

In contrast, the rhombohedral and MPB samples showed the formation of clusters of higher nonlinear activity in a weakly nonlinear matrix as well as larger average $\alpha_\varepsilon / \varepsilon_{init}$ and $\alpha_d / d_{33,init}$ values. The higher nonlinearity of the rhombohedral and MPB thin film samples is believed to be related to the higher number of spontaneous polarization directions and the smaller

spontaneous strain associated with the rhombohedral and MPB distortions. The broader spatial distribution of $\alpha_d / d_{33,init}$ values collected *locally* for the MPB sample is consistent with a smaller probed volume around this composition as expected from strain anisotropy.

Chapter 6

Grain Size and Substrate Clamping Effects on Local Piezoelectric Nonlinearity in Lead Zirconate Titanate Thin Films[**]

6.1 Abstract

The properties of a broad range of functional thin film materials are controlled by the dynamics of domain or phase boundary motion. Changes in the microstructure and the mechanical boundary conditions of ferroelectric thin films would be expected to influence both the global dielectric properties and the local length scale over which domain walls interact. It was found that when the residual in-plane tensile stresses in PZT thin films on Si are relieved, a dramatic increase in the global dielectric nonlinearity is observed.

BE-PFM was applied to locally map the nonlinearities in the converse piezoelectric response due to domain wall activity. Nonlinear piezoelectric maps of PZT films released from the Si substrate showed a distinct change in the correlation length associated with the coupling of domain wall motion, with respect to clamped regions. In particular, it was no longer possible to detect significant clustering in the nonlinear behavior after release, and the spatial average ratio of $\alpha_d / d_{33,init}$ increased from 0.002 ± 0.010 cm/kV to 0.013 ± 0.006 cm/kV. Furthermore, when the average residual stress state was released by fracturing diaphragms, the dielectric nonlinearities approached those of bulk PZT ceramics. Using a parallel capacitor model, the irreversible Rayleigh coefficient increased from 11.7 ± 0.04 cm/kV to 147.7 ± 4.4 cm/kV for the clamped and

[**] Parts of this chapter appear in F. Griggio, S. Jesse, A. Kumar, O. Ovchinnikov, H. Kim, T. N. Jackson, S. V. Kalinin, S. Trolier-McKinstry (to be submitted)

released case respectively. These results suggest that both the local and the global mechanical boundary conditions strongly influence the domain wall dynamics.

6.2 Introduction

The design of microelectromechanical systems (MEMS) utilizing sensors and actuators, sometimes in combination with Si-based integrated circuits, in miniaturized devices is today a well established area in microelectronics.[21] Ferroelectric thin films with the perovskite crystal structure close to a morphotropic phase boundary such as lead zirconate titanate ($PbZr_{0.52}Ti_{0.48}O_3$, PZT) are of interest for MEMS applications because of their large piezoelectric coefficients.[2] Over the last decade, it has been demonstrated that the transverse piezoelectric coefficient $e_{31,f}$ can be increased significantly if high levels of $\{001\}$ crystallographic texture,[4] large grain sizes,[126] and small composition gradients[122] are achieved in dense films. One way of increasing the properties is by enhancing the extrinsic contributions arising from domain wall motion. In spite of this, the piezoelectric response in thin films is observed to be much smaller than in bulk materials of the same composition.[75,166]

As explained in chapters 2 and 3, both residual stresses and grain boundaries acting as pinning sites can severely affect the domain wall mobility and the extrinsic contributions to the dielectric and piezoelectric properties. It was demonstrated in chapter 4 that BE-PFM enables improved mapping of the local nonlinear piezoelectric response in ferroelectric capacitors. In this chapter, PFM was utilized to investigate the nonlinear piezoelectric response locally so that the interactions between domain wall or phase boundary motion and local defect structures could be investigated. The purpose of this chapter is to analyze the influence of grain boundaries and mechanical clamping on piezoelectric nonlinearities measured locally using BE-PFM.

6.3 Experimental Procedure

6.3.1 PZT Film Preparation

Thin $Pb(Zr_{0.52}Ti_{0.48})O_3$ films with a thickness ranging from 1.04 to 1.3 μm were prepared using a chemical solution process derived from the procedure originally developed by Budd, Dey and Payne[35] as described in Wolf and Trolier-McKinstry.[6] The solution was 0.25 M with 10 to 20 mol % Pb excess to compensate for high PbO volatility. Commercially manufactured (111) $Pt/Ti/SiO_2/Si$ wafers (Ramtron Int., Colorado Springs, CO) were used as substrates. The substrates were pre-annealed for 60 s at 500 ºC immediately prior to solution deposition.

For all films, a 0.15 M template solution of $PbTiO_3$ containing 40 mol % Pb excess was used to promote $\{001\}$ orientation for the PZT films and a 0.25 M solution of $(0.3)Pb(Ni_{0.33}Nb_{0.67})O_3 - (0.7)Pb(Zr_{0.45}Ti_{0.55})O_3$ containing 20 mol % Pb excess was used in some cases to template large grained microstructures in the PZT thin films. The procedures for the solution preparation and deposition for the $PbTiO_3$ and PNN-PZT layers are described elsewhere.[126]

After the seed and template layer deposition, the PZT solution was spun on the substrate at 1500 rpm for 30 s using a PWM32 photoresist spinner (Headway Research, Inc., Garland, TX). The deposited layers were pyrolyzed at 250 and 400 ºC for 1 min respectively. Every four pyrolyzed layers, the film was annealed at 700 ºC for 1 min at a ramp rate of 50 ºC/s. The process was repeated to build up the desired thickness.

The three PZT samples investigated in this work were processed according to the conditions described in Table 6-1. Sample A was obtained depositing a ~ 15 nm thick seed layer of $\{001\}$ $PbTiO_3$, a templating layer of PNN-PZT roughly 60 nm thick and using one PZT solution containing 20 mol% Pb excess. Sample B was deposited on the same seed layers, using a

lower content of lead excess (10 mol% Pb excess) for the first 3 pyrolyzed layers and higher content of lead excess for the 4th layer of PZT prior to each anneal step. Sample C was prepared similarly to sample B without the PNN-PZT template layer. For all samples, a total of 20 layers were deposited and anneals were repeated every 4 pyrolysis steps. A 40 nm thick platinum was sputter deposited using a CMS-18 deposition system (Kurt J. Lesker Company, Clairton, PA) at a base pressure of 10^{-6} Torr and patterned using lift off process in case of sample A and B to obtain circular electrodes with diameters ranging from 0.2 to 1.1 mm.

Table **6-1**: Preparation conditions for PZT films with different grain sizes for BE-PFM studies.

Sample name	*Template layers*	*Excess PbO in PZT layers*	*Thickness*
A	{001} $PbTiO_3$, PNN-PZT	20 mol % through entire stack	1.3 μm
B	{001} $PbTiO_3$, PNN-PZT	10 mol % for the first 3 pyrolyzed layers and 20 mol % for the last pyrolyzed layer before anneal	1.3 μm
C	{001} $PbTiO_3$	10 mol % for the first 3 pyrolyzed layers and 20 mol % for the last pyrolyzed layer before anneal	1.04 μm

6.3.2 Released PZT Films

In order to release the PZT film from the underlying substrate, diaphragm structures were fabricated from sample C according to the process flow in Figure 6-1. The final structures were obtained using 3 photolithography masks. The first mask was used to pattern the desired

geometry for the Pt top electrode as in Figure 6-1 (e). Eight element arrays were obtained by dry etching the Pt top electrode using Cl_2 and Ar gases (Tegal 6540 plasma etch, Tegal Corp. Petaluma, CA). A second mask was used to pattern the opening to the Pt/Ti bottom electrode via dry etch using Ar, CF_4 and Cl_2. The third patterning step was used to dry etch the 10 μm diameter openings in the middle of the circular features down to the Si layer as in Figure 6-1 (b). The dry etch step for the 400 nm thick SiO_2 layer was performed using CF_4 (Versalock ICP, Plasma Therm Inc., N. St. Petersburg, FL). Etch rates of ~ 80, 110 and 50 nm/min were characterized for the Pt, PZT and SiO_2 layers respectively. Finally, the Si under the circular hole was etched by XeF_2 gas from the top-side (e1 Series Xetch, Xactix, Inc., Pittsburg, PA) as shown in Figure 6-1 (c) and (d). This yielded a spherical cavity with a diameter of 70 μm. Details on the processing steps will be provided in chapter 7.

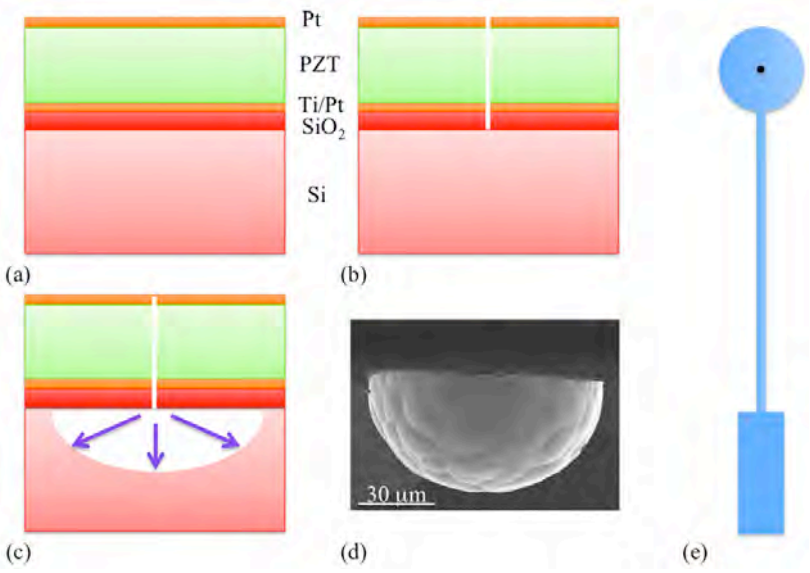

Figure **6-1**: Fabrication process of the diaphragm structures. (a) First two dry-etch steps define the top electrode features and openings for the bottom electrode (b) Third dry-etch step, opening down to Si (c) isotropic etch step using XeF_2 to release the actuator, (d) image of a cross section of fabricated device and (e) plan-view schematic of top electrode, with the released region underneath the top circular feature.

6.3.3 Film Characterization

The orientation and crystal structure of the films were determined using a Philips Analytical x-ray diffractometer (PANalytical B. V., Almelo, The Netherlands). $Cu-K_{\alpha}$ radiation was used with a flat graphite monochromator; diffraction data were collected between 15 and 70º 2θ at a rate of 3.6° 2θ/min. The degree of $\{001\}$ texture on samples was estimated using the Lotgering factor;[109] the peak intensities from the films were compared to a randomly oriented crystallized PZT powder obtained from the same solution. For all estimates of the lattice parameter, the Si substrate was used as an internal standard.

Microstructural features were examined using a Leo 1530 field emission scanning electron microscope (FE-SEM) (Leo Electronic Microscopy, Inc., Thornwood, NY). The grain diameters were analyzed by measuring 100 grains in the plan-view SEM images.

To facilitate electrical contacts for electrical and piezoelectric characterization, several top electrodes were gold-wire-bonded (Kulicke & Soffa Industries Inc., Fort Washington, PA) to ceramic packages (Spectrum Semiconductor Materials Inc., San Jose, CA). Connections to the measurement equipment were then made via the package to avoid damaging the film.

The dielectric characterization was performed using a HP 4284A precision LCR meter (Agilent Technology, Palo Alto, CA). The dielectric nonlinearity was measured from 100 Hz to 1 MHz on sweeping the voltage from 5 mV (rms value) to 24 kV/cm, approximately half of the coercive field. Polarization-electric field hysteresis was measured using an RT 66A standardized ferroelectric test system (Radiant Technology Inc., Albuquerque, NM) in the virtual ground testing mode. To measure the transverse piezoelectric coefficient $e_{31,f}$ of the films, the wafer flexure technique was used.[110]

Band excitation piezoresponse force microscopy (BE-PFM) was employed to characterize the *local* converse piezoelectric response. In BE-PFM, the data acquisition is

performed by exciting the cantilever with a signal with a specified amplitude and phase content in a defined frequency interval, rather than at a single frequency as in conventional PFM.[124] BE-PFM was implemented on a commercial Asylum MFP-3D system with a custom BE controller (including a custom developed MATLAB/ LABVIEW data acquisition and control system). A high voltage amplifier (FLC 10-A) was used to drive the capacitor structures. The top electrode and the conductive cantilever Olympus ACM240TM (Olympus, Corp., Tokyo, Japan) were driven with the same excitation function and the bottom electrode was grounded. While the converse piezoelectric nonlinearity was probed using amplitude modulation, minor piezoelectric hysteresis loops were collected using the field sweep depicted in Figure 6-11(d). A slow (~1 Hz) triangular wave defined the envelope of the waveform (here, two identical hysteresis loops). The wave was modulated by higher frequency band excitation rectangular pulses (~ 2-4 ms) that read-out the polarization state. The minor loops were then plotted adjusting for the vertical offset. Both dielectric and piezoelectric characterization measurements were performed after poling the ferroelectric capacitors for 20 min at 5 times the coercive field E_c and aging for at least 30 min. Piezoelectric and sometimes dielectric measurements on released PZT samples were performed on capacitors poled at the coercive field to prevent breaking the structures.

6.4 Results and Discussion

6.4.1 Microstructure and Perovskite Phase Characterization

FE-SEM images of the samples in this study are presented in Figure 6-2. Dense and crack-free polycrystalline morphologies were achieved. The calculated average grain sizes and standard deviations were 360 ± 170 nm, 140 ± 45 nm and 135 ± 70 nm for samples A, B and C respectively. An average grain size of 190 ± 70 nm was calculated for the PNN-PZT template

layer used for samples A and B. While the PNN-PZT template layer successfully enhanced grain growth for sample A, the same effect was not detected for sample B. The higher Pb excess content in sample A may have facilitated the mass transport with respect to sample B and C.

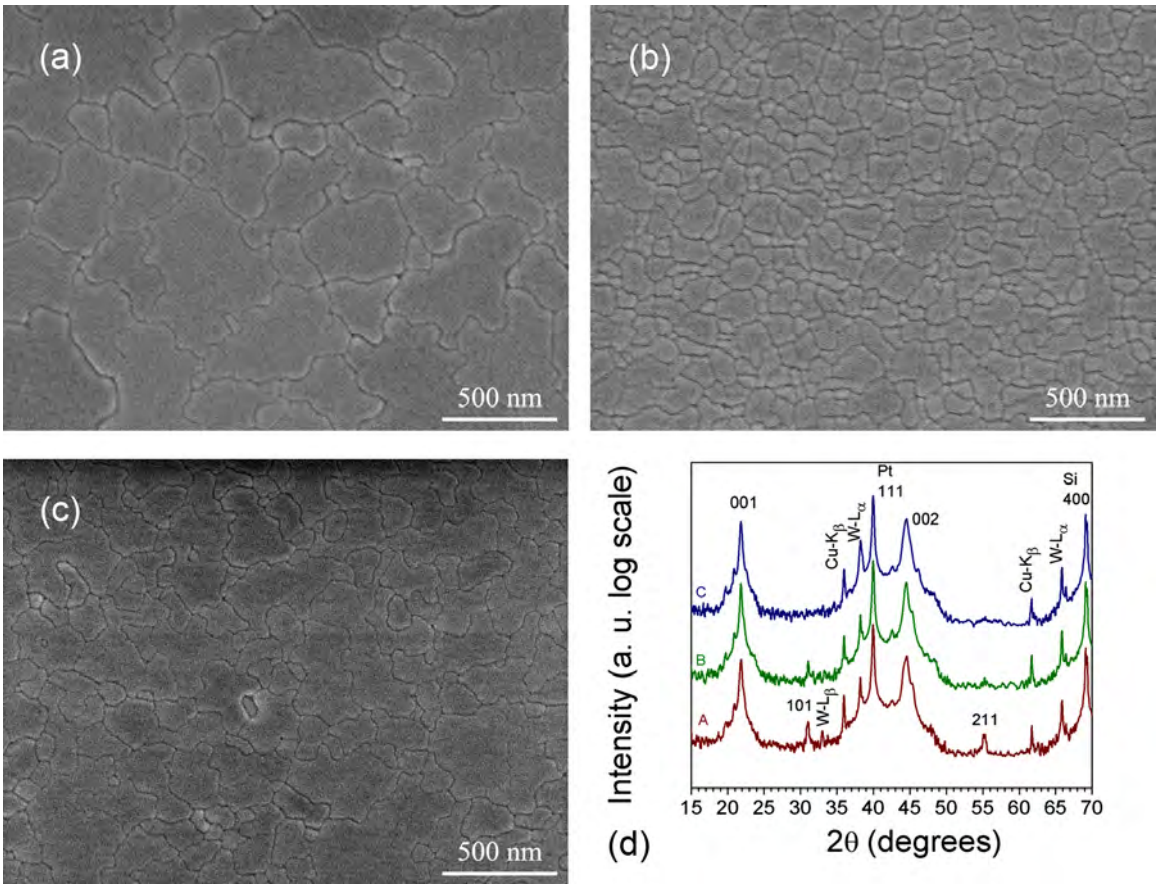

Figure **6-2**: Plan-view micrographs of (a) sample A, (b) sample B and (c) sample C. (d) XRD patterns relative to sample A, B and C.

The XRD patterns indexed using pseudocubic indices are shown in Figure 6-2 (d). Phase pure perovskite films were obtained within the detection limits of SEM and XRD analyses for these films. The {100} $PbTiO_3$ seed layer promoted a strong {001} texture, with calculated Lotgering factors higher than 98 % for all three samples.

6.4.2 High Field and Low Field Dielectric Characterization

The low field dielectric constant, loss tangent, hysteresis loops and transverse piezoelectric coefficient $e_{31,f}$ are reported in Figure 6-2; the values shown are an average for three electrodes from each of the samples. A 15% increase in low field dielectric permittivity was observed for sample A with respect to sample B and C. This is consistent with observations on $BaTiO_3$ and PNN-PZT thin films, where the properties increased with grain size.[63,64,126] The smaller grain size may be responsible for the slightly lower values of remanent polarization characterized for sample B and C (32 and 31 $\mu C/cm^2$ respectively) with respect to sample A (34 $\mu C/cm^2$).[4,121] The higher remanent polarization value for sample A was confirmed using the PUND technique. Substantial interactions between domain structures and grain boundaries have previously been reported;[167,168] an enhancement in dielectric and piezoelectric properties is reasonable in thin films with larger grain sizes, where the domain structure may have more twin variants, as well as higher domain wall mobilities.

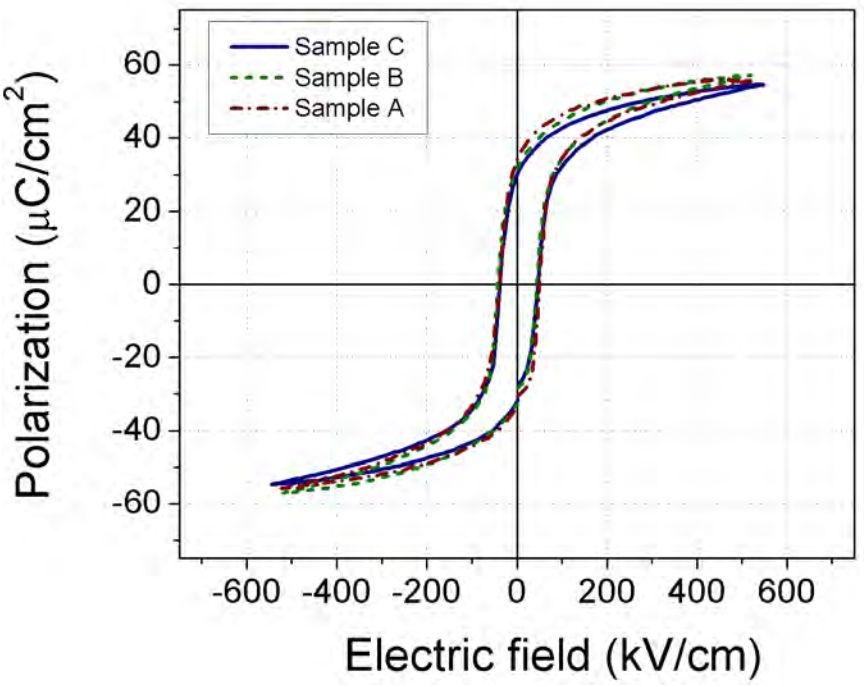

Figure **6-3**: Hysteresis loops for samples A, B and C.

Transverse piezoelectric response $e_{31,f}$ values of -12.1 and -12.2 C/m^2 were characterized for samples B and C respectively while a value of – 9.7 C/m^2 was measured for sample A. Formation of voids most likely associated with PbO volatility during subsequent annealing steps resulted in a less dense microstructure for sample A with respect to sample B and C, which may lower the piezoelectric response.

Table **6-2**: Summary of dielectric and piezoelectric characterization properties for PZT films A, B and C with different grain sizes.

Sample	*Average grain size (nm)*	ε_r	*tanδ (%)*	P_r *(μC/cm²)*	E_c *(kV/cm)*	$e_{31,f}$ *(C/m²)*
A	360 ± 170	1297 ± 3	2.6	34	44	- 9.7 ± 1.0
B	140 ± 45	1130 ± 3	2.0	32	43	- 12.1 ± 0.8
C	135 ± 70	1140 ± 15	1.8	31	44	- 12.2 ± 0.7

The ac electric field dependence of the dielectric properties was investigated for clamped capacitors of samples A, B and C. Measurements were also conducted on electroded regions of sample C that included a 11.4 % area where the PZT had been released from the underlying Si substrate (Fig. 6-1 (e)). The shape of the hole that allowed access to the Si substrate for XeF_2 isotropic etch was designed to provide stress concentration points, so that when the diaphragms were cycled through ac fields greater than 5 times E_c, the formation of 3 radial cracks 120 º apart was common. This enabled the in-plane lateral clamping to be completely relieved.

Nonlinearity measurements were performed on poled and aged samples. Figure 6-4 illustrates the permittivity and polarization versus the amplitude of the ac field (E_0). In the sub-coercive field region, the dependence of the dielectric constant ε_r and polarization P can be expressed using the Rayleigh relations (equations 2-5 and 2-6) modified for ferroelectric materials shown in Chapter 2.[55,56]

The Rayleigh parameters for the dielectric response were calculated from fits to the linear portion of the data. The results are given in Table 6-3; the reported errors were determined from the least squares analysis of the Rayleigh fits.

As expected,[60,126] the irreversible Rayleigh parameter α_ε increased by 104 % as a function of grain size and thickness from a value of 11.7 ± 0.04 cm/kV for sample C to a value of 23.9 ± 0.1 cm/kV for sample A. A 22 % increase was also measured for the reversible Rayleigh parameter from a value of 1005.0 ± 0.3 for sample C to a value of 1224.4 ± 0.8 for sample A. Overall the ratio of $\alpha_\varepsilon / \varepsilon_{init}$ increased by 68 % going from 11.7 ± 0.04 10^{-3} cm/kV of sample C to a 19.6 ± 0.07 10^{-3} cm/kV of sample A. The α_ε and ε_{init} values measured at 100 Hz were used to calculate the minor hysteresis loops using Equations 2-5 and 2-6. The good agreement between the calculated and measured loops as seen in Figure 6-4(b) suggests that the nonlinear dielectric behavior can be well described by a Rayleigh-like mechanism.

A higher threshold field E_{th} was characterized for sample C with respect to samples A and B. Defining E_{th} as the amplitude of the field at which a 1% increase in ε_r was observed, values of ~ 1.5 kV/cm were characterized for sample A and B while a value of ~ 3.5 kV/cm was observed for sample C both in capacitor and released structures. Nonetheless the extrapolated ε_{init} was within 2 % of ε_r at 0 ac field and the influence in subsequent fittings was negligible. The presence of a threshold field indicates that the potential barrier heights associated with pinning centers are not uniformly distributed all the way to zero field. By increasing E_0, domain walls may move away from stronger pinning centers and experience a uniform distribution of barrier heights.

The mechanical boundary conditions can significantly alter the functional properties in ferroelectric thin films.[65,87] In bulk PZT ceramics, domain wall motion contributes up to 55% of the dielectric and piezoelectric properties at room temperature.[57,66] However the extrinsic contributions to the piezoelectric response in ferroelectric thin films can be severely limited by substrate clamping, among other factors.[60]

To quantify the importance of the mechanical boundary conditions without changing the remainder of the pinning sites, in Figure 6-4 (c) and (d) the electric field dependence of ε_r and the minor hysteresis loops for diaphragm structures are reported before and after cracking the diaphragms. When the diaphragms were broken, the three sections of the diaphragm curled up by 430 nm due to the release of the tensile stress in the PZT layer over 11.4% of the measured capacitor area. As a result, the irreversible Rayleigh coefficient α_ε increased by 114 %, going from 12.7 ± 0.04 cm/kV up to 27.2 ± 0.07 cm/kV. Using a parallel capacitor model, the Rayleigh constants of the fully and partially clamped film were utilized to determine α_ε for a PZT thin film that is completely mechanically decoupled from the underlying Si substrate (released/broken row in Table 6-3) and a PZT thin film only released from the Si substrate (released row in Table 6-3). Both fitting errors for the Rayleigh parameters and errors in released area were accounted for in the error propagation. It was found that α_ε of the released and broken area was 147.7 ± 4.4 cm/kV, which is comparable to that of polycrystalline undoped MPB PZT bulk (131.6 ± 0.26 cm/kV) but smaller than a donor doped MPB PZT ceramic (as high as 394 ± 1.03 cm/kV for 1% Nb doped PZT).[72] Likewise the reversible Rayleigh constant increased to 1426 ± 210. This confirms that one of the most critical factors limiting extrinsic contributions to the properties of ferroelectric films is mechanical clamping. For the PZT diaphragm which was released from the Si substrate but not broken, α_ε increased by 75 % going from 11.7 ± 0.04 to 20.5 ± 2.5 cm/kV relative to the fully clamped film, while ε_{init} increased by 86 % going from 1005.0 ± 0.6 to 1865 ± 215 (See Fig. 6-4). The origin of these differences is discussed below.

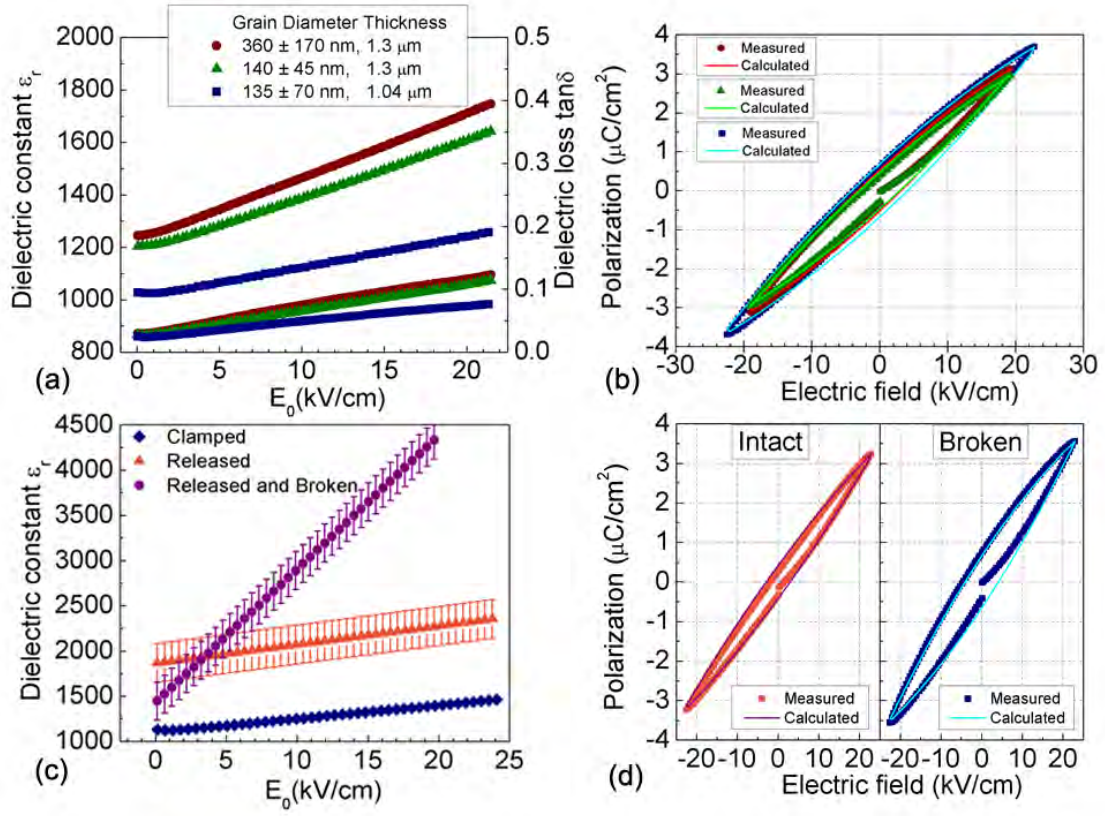

Figure **6-4**: (a) Field dependence of the real dielectric permittivity and dielectric loss for samples A, B and C and (b) calculated and measured minor hysteresis loops. (c) Field dependence of the real dielectric permittivity for the fully clamped PZT capacitor, for the fully released PZT and for the fully released and broken PZT capacitor. The orange and violet data points were obtained by normalizing for the released region using a parallel capacitor model. (d) calculated and measured minor hysteresis loops (uncorrected for the area fraction which was released).

Table **6-3**: Summary of the dielectric nonlinearity for samples A, B and C. * Normalized with respect to the released area.

	α_ε (cm/kV)	ε_{init}	$\alpha_\varepsilon / \varepsilon_{init} x\ 10^3$ (kV/cm)
Sample A	23.9 ± 0.1	1224.4 ± 0.8	19.6 ± 0.07
Sample B	21.3 ± 0.02	1173.9 ± 0.3	18.1 ± 0.01
Sample C	11.7 ± 0.04	1005.0 ± 0.6	11.7 ± 0.04
Sample C released	12.7 ± 0.04	1103.0 ± 0.6	11.5 ± 0.03
Sample C released/broken	27.2 ± 0.07	1053.0 ± 0.9	25.8 ± 0.05
Sample C released/broken, normalized*	147.7 ± 4.4	1426 ± 210	103.6 ± 15.6
Sample C released, normalized*	20.5 ± 2.5	1865 ± 215	11.0 ± 1.8

Differences in the dielectric nonlinearities for sample C fully clamped capacitors and capacitors that had been partially released from the Si substrate but not broken, were assessed by measuring the frequency dispersion of the Rayleigh parameters. Although the $\alpha_\varepsilon / \varepsilon_{init}$ values characterized at 10 kHz for the fully clamped, 11.7 ± 0.04 10^{-3} cm/kV and a partially clamped capacitor, 11.5 ± 0.004 10^{-3} cm/kV were very close in value, partially released capacitors showed higher reversible Rayleigh parameters in the investigated 800 Hz – 1 MHz frequency range as seen in Figure 6-5.

Although the Rayleigh model by itself does not have any time dependence, in random systems that have properties controlled by a normal distribution of restoring forces, the extrinsic contributions often obey a logarithmic frequency dependence as in equations 5-1 and 5-2.[54,169,170]

It was found that when the a/a_0 ratios are compared for the completely clamped and partially released capacitors, the latter have a weaker frequency dependence of the irreversible Rayleigh parameter α_ε with a decrease of 120 % of the a/a_0 ratio over the 800 Hz – 1 MHz frequency range. As previously described by Bassiri-Gharb *et al.* the stronger frequency dependence for the completely clamped capacitors may be associated with a narrower distribution of the relaxation time constants for the domain walls, with the net result of a larger number of domains freezing out at higher frequencies.[154] Interestingly enough, a different trend was observed for the extrinsic reversible contribution to the dielectric constant, with a slower decay of e/e_0 with frequency for the completely clamped samples. This could be due to a larger population of domain walls contributing reversibly in the clamped films up to higher frequencies. This observation would be consistent with the assumption that the barrier heights associated with specific pinning centers rise under increasing in-plane stress.

A few key points should be considered in interpreting these results. First, the concentration of microstructure-based pinning sites is comparable between the released and clamped capacitors (since they come from the same film). Moreover, on undercutting the Si, the *average* residual stress in the PZT film changes only a small amount, as the diaphragm stays taut, with only small vertical deflections observed near the central hole. Thus, the observed differences in the Rayleigh response on releasing the sample from the underlying substrate are likely to be related, at least in part, to a change in the *local* stresses in the PZT film. It is believed that these local stresses develop at the film/substrate interface, and might arise from the development of the film domain structure on cooling through the ferroelectric transition temperature. That is, the ferroelastic strains associated with domain formation couple to the substrate, which in turn, imposes mechanical constraints on the position and mobility of adjacent domain walls. This will be discussed further below.

Secondly, it is clear that the dielectric nonlinearities change substantially when both the local and the average residual stresses are eliminated in the film when the released diaphragm is broken. Again, there is no change in microstructure-based pinning sites; the grain sizes and point defect concentrations will not be changed by fracture. The large irreversible Rayleigh constant observed in this case is comparable to those of bulk ceramics, and exceeds those of the clamped film by an order of magnitude. This points to the fact that one of the most significant factors reducing the irreversible motion of domain walls in PZT films on Si is residual stress.

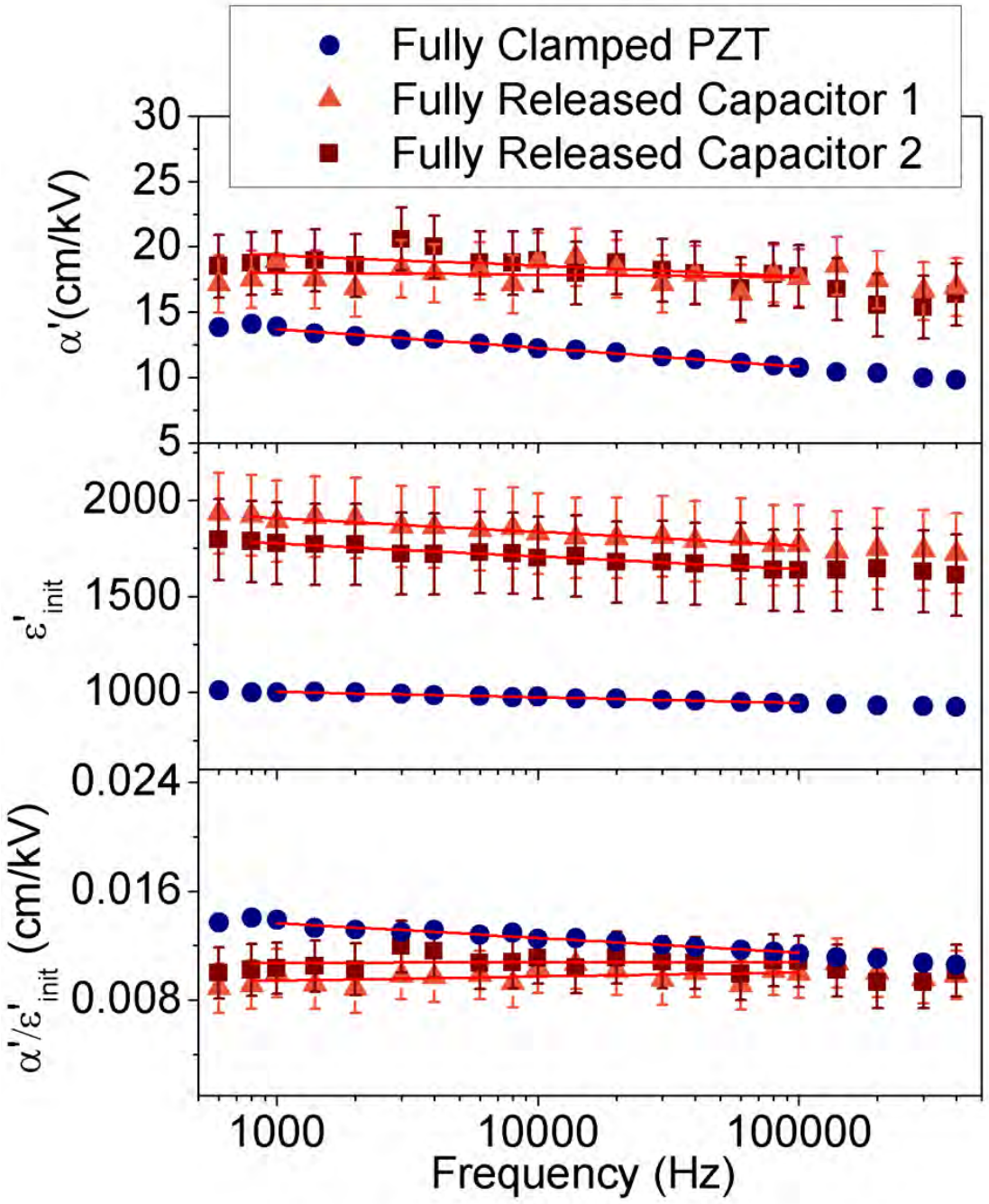

Figure **6-5**: Frequency dispersion of the Rayleigh parameters extrapolated from the AC field dependence of the dielectric constant for clamped capacitors and partially released but still intact electrode of sample C. The square and triangle data points are normalized Rayleigh parameters from 11.4 and 14 % released areas using a parallel capacitor model. The error bars take into account errors from the area and Rayleigh parameters fittings.

Table **6-4**: Logarithmic Frequency Dependence Parameters for the Permittivity. Values extrapolated from a PZT capacitors released for * 11.4 % and ** 14 % of the total area. The errors refer to fitting errors.

	Clamped	*Fully Released**	*Fully Released***
a_0	19.4 ±0.1	18.7 ± 1.4	22.5 ± 1.2
a	0.65 ± 0.01	0.08 ± 0.12	0.36 ± 0.11
e_0	1100 ± 6	2181 ± 24	2035 ± 20
e	11.6 ± 0.5	31.1 ± 2.2	29.54 ± 1.8
a/a_0	0.033 ± 0.0004	0.004 ± 0.0004	0.015 ± 0.004
e/e_0	0.010 ± 0.0004	0.014 ± 0.007	0.015 ± 0.0007

6.4.3 Local Converse Piezoelectric Response Measurements by Band Excitation PFM

The *local* converse piezoelectric nonlinearities of the thin films were measured by driving the entire electroded region, with local displacement detection through the AFM cantilever. In order to minimize the effects of nonlinear tip-surface interactions on the measurement, the energy of excitation functions was tailored as explained in Chapter 4.[171] The probing signals utilized were combined chirp-sinc hybrid functions; sweeps in opposite frequency directions were measured at each position. The material nonlinearity is independent of frequency sweep direction. Thus, the quality of the measurements was assessed based upon the agreement between the maps generated from signals of reverse frequency sweeps.

An amplitude modulated band excitation signal was used to characterize the electromechanical response as a function of frequency and the amplitude of the applied voltage, V_{ac}. The individual curves of displacement as a function of frequency were fitted to a simple harmonic oscillator (SHO) model to yield the amplitude at the resonance, A_{max}, the resonant frequency, ω_o and the mechanical quality factor, Q as a function of position and voltage, V_{ac}.[124] As explained in Chapter 4,[89] A_{max} is a nonlinear function of the driving force. It was well fit by a second-order polynomial $A_{max} = a_1 + a_2 V_{ac} + a_3 V^2_{ac}$. By differentiation, the Rayleigh law is obtained: $\xi d_{33,f} = \xi d_{33,init} + 2\xi\alpha_d V_{ac}$, where ξ is a parameter that accounts for the cantilever sensitivity, α_d is the Rayleigh coefficient associated with irreversible extrinsic contributions to $d_{33,f}$, the longitudinal piezoelectric coefficient and $d_{33,init}$ is the Rayleigh coefficient associated with the intrinsic and reversible extrinsic contributions to $d_{33,f}$.[54]

6.4.3.1 Clamped Piezoelectric Capacitors

As has been reported previously, maps of $\alpha_d / d_{33,init}$ show clusters of high values embedded in a matrix of material with lower $\alpha_d / d_{33,init}$. Correlation function analysis of images was performed on a map 20 μm on a side in order to extract quantitative information on the cluster size for sample A. The resolution in this large scan was determined by the acquisition time, and a pixel size of 200 nm was chosen. A MATLAB code was developed to low-pass filter the linear, quadratic and $\alpha_d / d_{33,init}$ maps. The clusters were then defined using a threshold value of half a standard deviation above the spatial average of the maps. After transforming the maps into binary images, statistics were extracted on the equivalent diameter of the clusters. The results are reported in Figure 6-5.

Average equivalent cluster diameters and standard deviations of 1.05 ± 0.64 μm, 1.12 ± 0.77 μm and 1.03 ± 0.83 μm were determined for the linear a_2, quadratic a_3 and α_d / $d_{33,init}$ maps (Fig. 6-6 (d)). As already reported,[89] the characteristic length scale of these clusters is much larger than the average grain diameter of sample A (360 ± 170 nm). The distributions of equivalent diameters of the clusters show a very asymmetric character, with positive skews of 0.73, 1.14 and 1.87 μm for the linear a_2, quadratic a_3 and α_d / $d_{33,init}$ of the maps in Fig.6-6. Despite the limits in resolution due to the pixel size of 200 nm, it can be seen that there is some overlap between the quadratic and linear maps. In many cases, regions showing larger linear coefficients also show large quadratic coefficients. However, the position and shape of the clusters differ for the linear and quadratic maps. Furthermore, the maxima in the linear map do not always correspond to relative maxima in the quadratic map. This would suggest that high piezoresponse regions are not necessarily the only nucleation sites for higher amounts of irreversible domain wall motion.

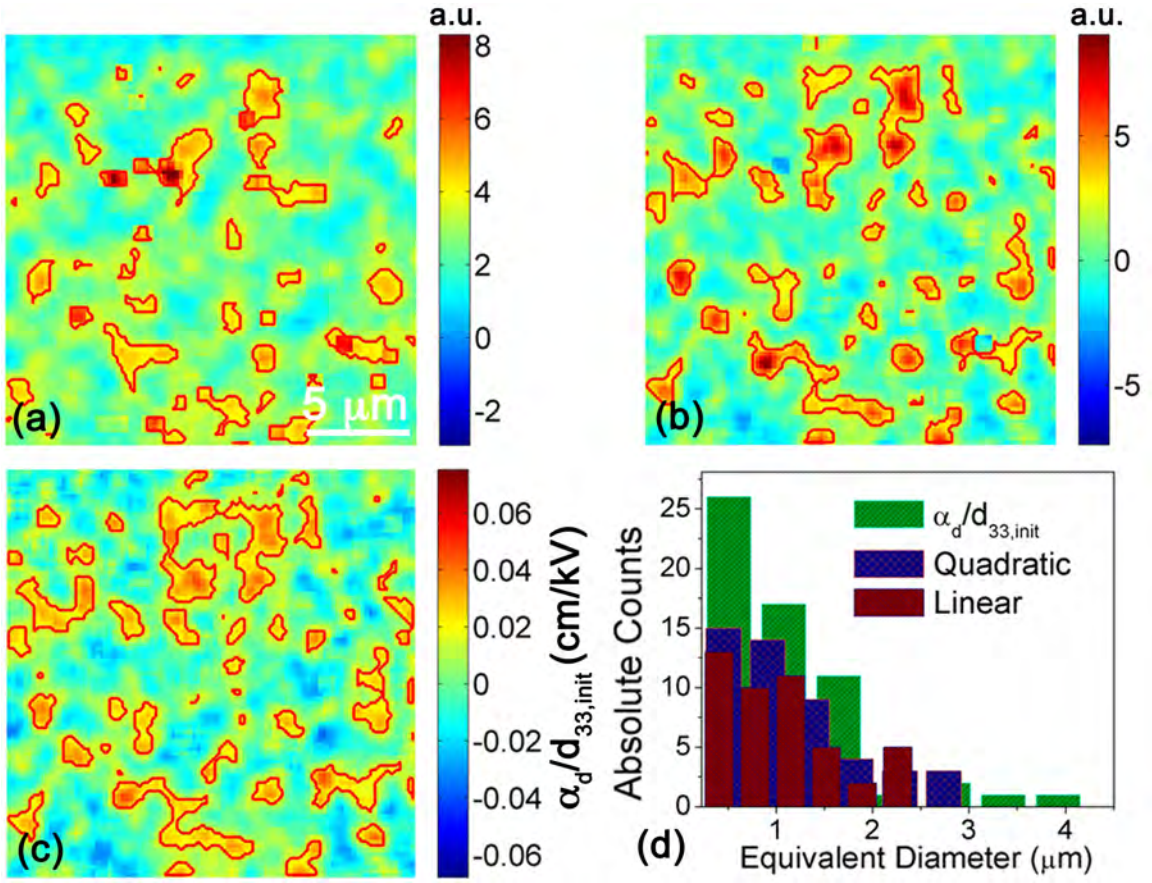

Figure **6-6**: Low-pass filtered maps of (a) linear, (b) quadratic component of $A_{max}(V_{ac})$, (c) $\alpha_d/d_{33,init}$ and (d) histogram of the equivalent diameters of the regions marked in the maps. The red outline defines threshold values at half standard deviation above the spatial average of the maps, and were used for the statistical analysis.

Higher resolution maps of topography, resonance frequency, linear and quadratic component of $A_{max}(V_{ac})$ are shown in Figure 6-7, 6-8 and 6-9 for samples A, B and C, respectively. The resonance maps (panel b of Figures 6-7, 6-8 and 6-9) exhibit some line-to-line drift consistent with the raster direction and a number of frequency shifts at contamination spots. The linear and quadratic component maps are presented in panels c and d of these figures. Both are plotted on color scales spanning 4 standard deviations. A comparison between the topography and the functional maps shows that cross-talk due to roughness or contaminants on the surface of the samples was negligible.

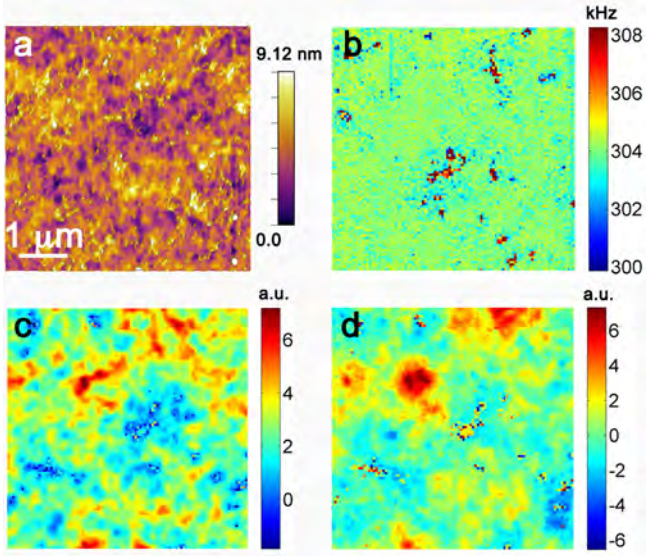

Figure **6-7**: Nonlinearity imaging of sample A. (a) Surface topography, (b) resonance frequency map, and maps of nonlinear fitting coefficients (c) slope, a_2, (proportional to $d_{33,init}$) and (d) quadratic coefficient, a_3 (proportional to α_d)

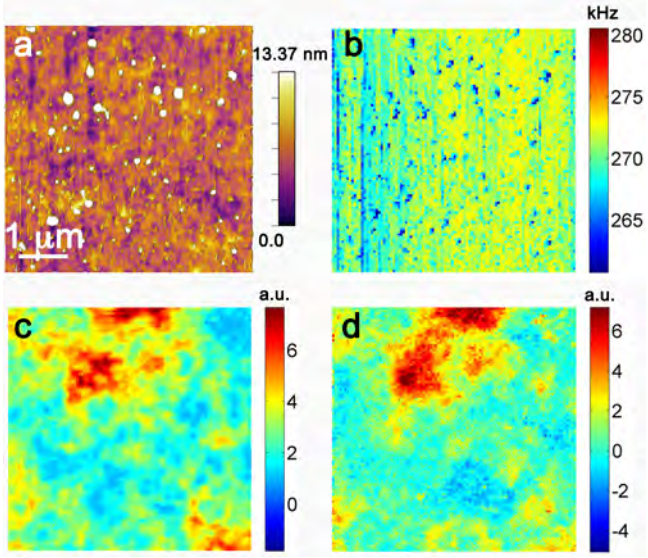

Figure **6-8**: Nonlinearity imaging of sample B. (a) Surface topography, (b) resonance frequency map, and maps of nonlinear fitting coefficients (c) slope, a_2, (proportional to $d_{33,init}$) and (d) quadratic coefficient, a_3 (proportional to α_d).

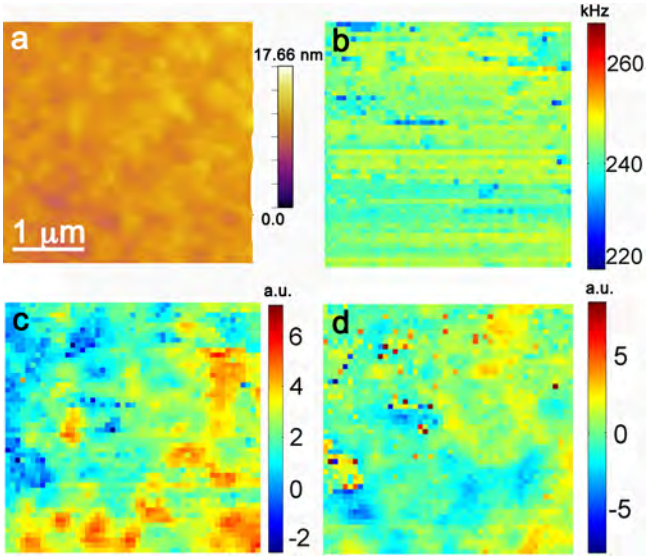

Figure **6-9**: Nonlinearity imaging of sample C. (a) Surface topography, (b) resonance frequency map, and maps of nonlinear fitting coefficients (c) slope, a_2, (proportional to $d_{33,init}$) and (d) quadratic coefficient, a_3 (proportional to α_d).

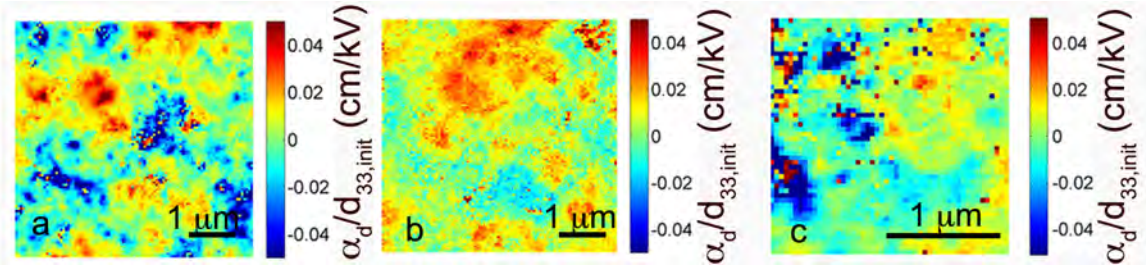

Figure **6-10**: Maps of $\alpha_d / d_{33,init}$ ratio for (a) sample A, (b) sample B and (c) sample C.

As previously observed, both the linear and quadratic components maps show clusters with higher values.[89] The clustering appears to have different correlation lengths for the linear and quadratic maps; typically clusters of smaller size are observed for the linear, a_2 component over a 5 µm × 5 µm window. On the other hand the quadratic, a_3 maps show larger and more sparse aggregations over the same area. Also the $\alpha_d / d_{33,init}$ maps (Fig. 6-10) show clusters that appear to be only partly correlated to the a_2 maps. The pixel size in these 2.5 µm × 2.5 µm maps is 50 nm. This confirms the observation on the larger area, lower resolution map of sample A; the

irreversible domain wall motion contribution to the converse piezoelectric response is often, but not always highest in regions where the reversible contribution is also higher.

The histograms of nonlinear response $\alpha_d / d_{33,init}$ are shown in Figure 6-11. The area utilized for sample C is the one highlighted in orange in Figure 6-15 (a). The distributions are approximately symmetric with respect to the center frequency. The calculated averages and standard deviations of $\alpha_d / d_{33,init}$ for samples A, B and C were respectively 0.001 ± 0.016, 0.008 ± 0.011 and 0.002 ± 0.011 cm/kV while the corresponding medians were 0.002, 0.007 and 0.002 cm/kV.

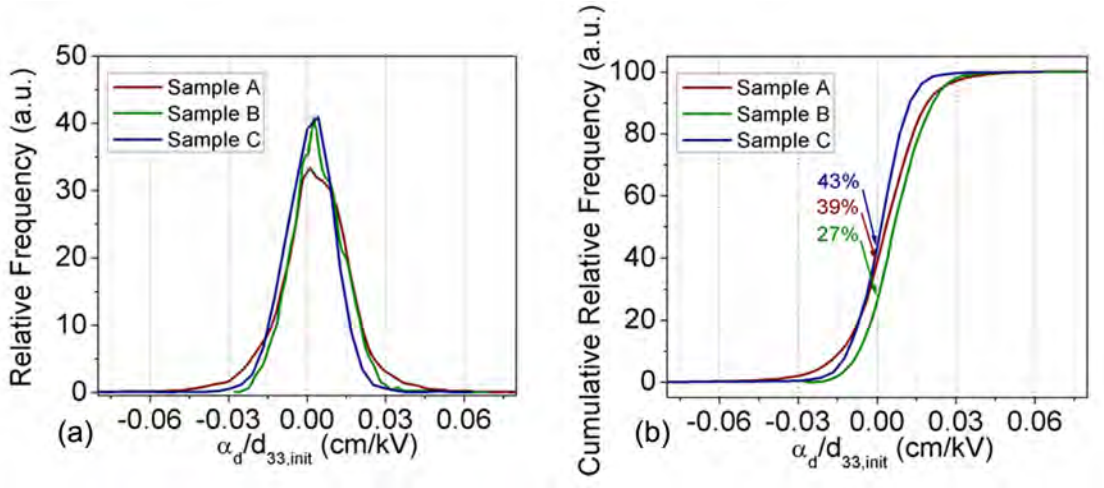

Figure **6-11**: (a) Relative frequency distribution and (b) cumulative frequency distribution histograms for local values of $\alpha_d / d_{33,init}$ of sample A, B and C.

For all three samples, there are regions in the maps with negative $\alpha_d / d_{33,init}$ values. These regions are clearly not Rayleigh-like in character. From the cumulative distribution plot (Fig. 6-11 b) the fractional area with negative $\alpha_d / d_{33,init}$ values were 39, 27 and 43 % for samples A, B and C respectively.

There are several possible origins of this behavior. First, similar to what is observed here, Shvartsman *et al.* previously reported that the effective d_{33} (measured locally using a conventional lock-in PFM without a top electrode) decreased with increasing ac field

amplitude.[172] They attributed this to the presence of two oppositely polarized layers in the depth of the film. At small driving voltages, the pinned domain wall separating the two layers experiences only limited field-induced displacement. However, an abrupt change in the electric field dependence of the effective $d_{33,f}$ was reported at a threshold field; the characterized threshold field of 160 kV/cm, well above the Rayleigh regime, was described as being responsible for depinning the boundary, inducing polarization reversal under the tip.

There are a number of differences between Shvartsman work and the work in the present thesis. Here, the measurements on ferroelectric capacitors enable sampling of a much larger population of domain walls than in the work by Shvartsman *et al.* Moreover, the nonlinearities were not probed beyond the Rayleigh region for our films. Nonetheless depinning of domain walls could contribute to the negative $\alpha_d / d_{33,init}$ regions observed here.

Alternatively, the presence of negative α_d regions could be related to a *local* hard behavior in the films, such that the distribution of restoring forces for the domain walls can no longer be treated as Gaussian, and the response is no longer Rayleigh-like in character. [72] This could occur, for example, due to a higher concentration of randomly oriented defect dipoles in certain regions of the material.[173] To assess the likelihood of this, minor piezoelectric hysteresis loops were collected using the same V_{ac} interval for the voltage steps and frequency bandwidth used for the Rayleigh measurements. A systematic difference was observed between loops collected from regions associated with a negative and positive quadratic coefficients a_3 (Figure 6-12). In particular, regions with negative curvature of the field dependence of the displacement were substantially more hysteretic in their small signal response. It is speculated that this is related to a *pinched* character of the local ferroelectric hysteresis. As a result, the material does not retain a remanent polarization well. The large, but hysteretic response would then be due to realignment of the polarization during the course of the measurement.

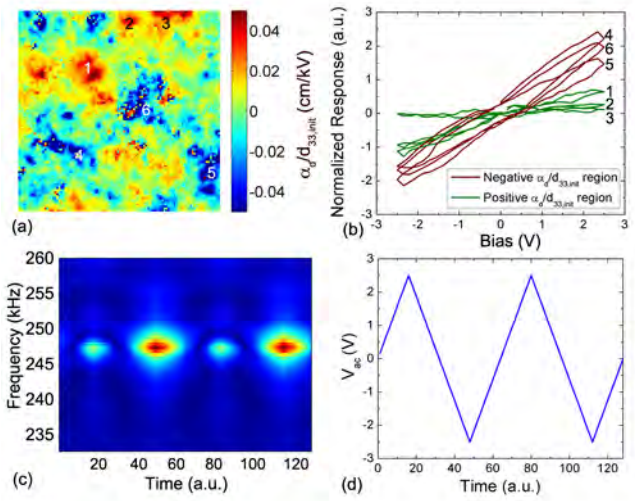

Figure **6-12**: (a) α_d / $d_{33,init}$ map for sample A and (b) minor piezoelectric response loops for different regions as indicated in the map. (c) 2D spectrogram of piezoresponse as a function of time and frequency, (d) two consecutive voltage cycles were used to calculate the normalized piezoresponse in (b).

6.4.3.2 Partially Released Ferroelectric Capacitors

Piezoelectric nonlinear maps were collected on areas of sample C where the PZT thin film had been released from the substrate. There was little topographic indication of the boundary between the clamped and released regions. It was found that the easiest way to identify the boundary was through lock-in PFM maps. When the sample was probed at a frequency just below the cantilever resonance, the phase of the response was found to change by 180° at the boundary as shown in Figure 6-13. At this time, it is believed that this phase change may be related to a contribution from a pitching mode of the actuated diaphragm. Furthermore, a phase change was detected in BE-PFM maps of the same area average over the V_{ac} excitation range, but it did not show an apparent correlation with the clamped – released boundary. However, it was observed in Figure 6-15 (b) that the resonance frequency for the BE-PFM data extracted from the same region did not change among released and clamped areas of the map.

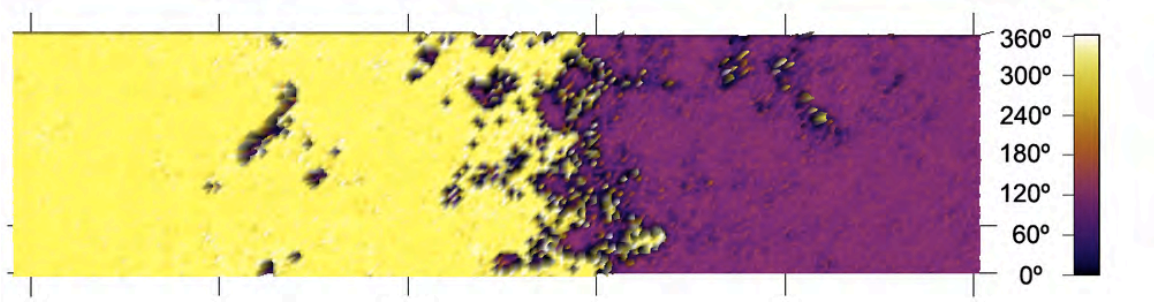

Figure **6-13**: Phase map for the same region reported in Figures 6-14, 6-15 and 6-16. The map was collected at a single frequency just below the resonance. The phase change is associated with a slope change of the surface of the film in the released region. The vertical side of the image is 2.5 μm long.

It was found that the piezoelectric response was much larger on the released areas, which necessitated optimizing the BE-PFM excitation conditions separately for the released and clamped areas.

As described in detail elsewhere,[171] the energy of the excitation signal E_s during the BE-PFM measurements can be tailored by varying a phase variation parameter β (eq. 5).

$$E_s = \int |S(\omega)|^2 d\omega = CA^2\beta \qquad \text{Equation } \mathbf{6\text{-}1}$$

where $S(\omega)$ is the spectrum of the excitation function, β is the phase variation parameter, A is the voltage amplitude and C is a constant.

For $\beta = 0$ the magnitude and phase of the spectrum are

$$Y_a = erf\left(\frac{\omega - \omega_1 - 2\gamma}{\gamma}\right) - erf\left(\frac{\omega - \omega_2 + 2\gamma}{\gamma}\right) \qquad \text{Equation } \mathbf{6\text{-}2}$$

$$Y_p = -\pi\tau\omega \qquad \text{Equation } \mathbf{6\text{-}3}$$

where ω_1 and ω_2 are the lower and upper limits of the excitation band, γ determines the sharpness of the band edges and τ is the duration of the signal in the time domain. The corresponding signal in the time domain is then normalized for the desired amplitude. The magnitude of β determines

the amount of energy contained in the band excitation of the signal and the sign of β controls the direction of frequency sweep in the time domain.

It was found that when a phase variation β of 50% was used, a good signal to noise ratio was obtained over the clamped region of the sample. Furthermore, this yielded good agreement between maps taken with different frequency sweep directions. However, using the same excitation function, the response collected over the released region of the sample was dominated by the softening of the cantilever tip-surface mechanics.

If instead a sinc function was used ($\beta = 0$), the dynamic nonlinearities in the released region could be minimized at the expenses of a low signal to noise ratio in the clamped region. These results can be seen qualitatively in Figure 6-14, where the maps obtained for a $|\beta| = 50$ % and sinc excitation function are compared. In Figure 6-14 (a) the spectra, averaged over the selected regions, show a good agreement between excitation functions with opposite frequency sweeps over the clamped PZT region, indicative of negligible dynamic nonlinearities. However a dramatic softening was noticed over the released PZT region. In this case, the resonance frequency ω_0 strongly depends on the position, and the excitation voltage and the overall response in amplified for the chirp down as typically observed in systems where dynamic nonlinearities are present.[171] In contrast, in Figure 6-14 (b) the spatial average of the response in the released PZT region is not affected by dynamic nonlinearities, however a poor signal to noise ratio prevents the characterization of the clamped PZT region.

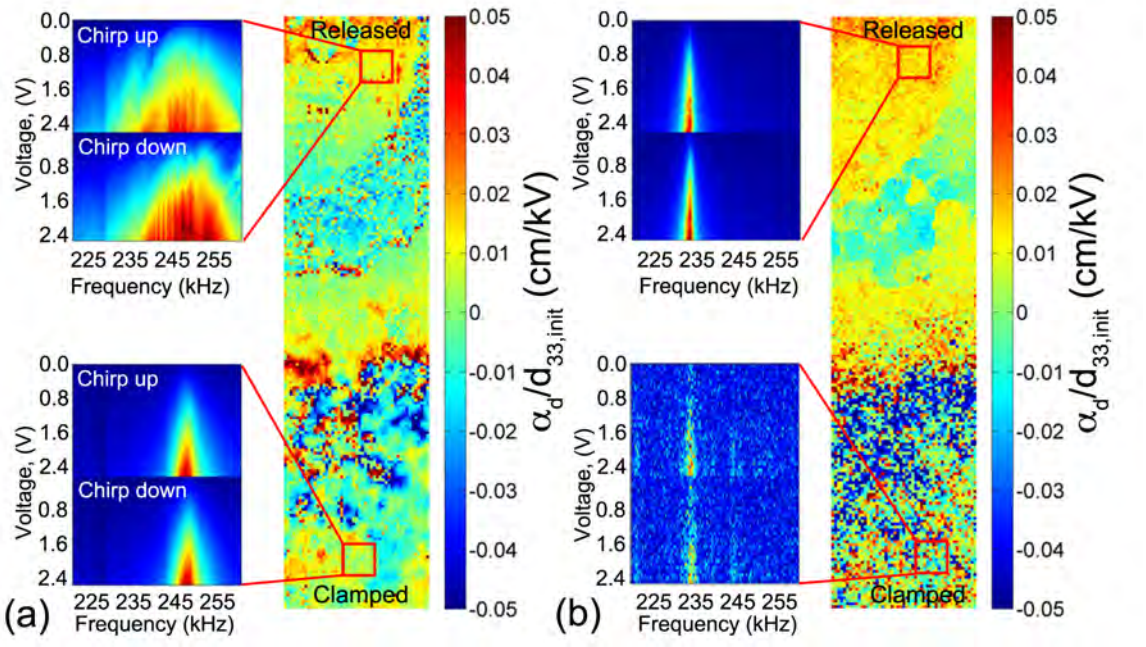

Figure **6-14**: α_d / $d_{33,init}$ maps of the same region collected using different excitation functions. (a) Map collected using a higher energy excitation signal, increasing (chirp up) and decreasing (chirp down) the frequency with time; (b) map collected using a lower energy excitation signal, in this case all of the frequencies are sent simultaneously.

To minimize artifacts, a composite map was constructed using a $|\beta|$ = 50% excitation function for the clamped half and a sinc function for the released half. Figure 6-15 shows the spatially resolved maps of topography, resonance frequency ω_0, the standard deviation of the resonance frequency as a function of V_{ac} and the α_d / $d_{33,init}$ ratio. The structure visible in the resonance frequency map in the released PZT region does not correlate with topography. The changes in resonance can be as high as 15 kHz and are not a result of dynamic nonlinearities, since no softening was observed in standard deviation of $\omega_0(V_{ac})$ map reported in Figure 6-15 (c). It is speculated that this may be due to local variations in the mechanical boundary conditions, perhaps from an incompletely circular membrane, or residual Si on the back of some of the diaphragm. It should also be noted that the relative constant resonant frequency across the map (including the released regions) is consistent with the idea that the release process did not make large changes in the average stress state of the PZT in the diaphragm region.

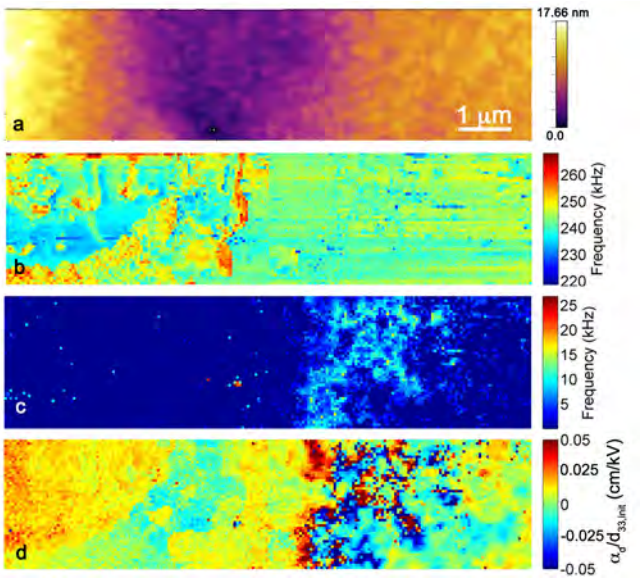

Figure **6-15**: (a) Topography map (b) resonance frequency ω_0 map, (c) standard deviation of $\omega_0(V_{ac})$ and (d) α_d / $d_{33,init}$ ratio map.

The standard deviation of $\omega_0(V_{ac})$ map is below 200 Hz for most of the map, which is an indication of negligible dynamic nonlinearities, considering that the peak width at the maximum V_{ac} is 5 kHz; however regions showing softening of the resonance peak as a function of the applied excitation voltage are apparent in the clamped half of the explored area. The local dynamic nonlinearities present in those regions increased the noise in the α_d / $d_{33,init}$ map and prevented a quantitative characterization. The following statistical analysis on local α_d / $d_{33,init}$ values did not include those areas.

In Figure 6-16 (b) and (c), the histograms of nonlinear response relative to clamped and released regions are compared; spatial averages of 0.002 ± 0.010 cm/kV and 0.013 ± 0.006 cm/kV were characterized for the clamped and released regions, the latter being very close to the dielectric nonlinearity value characterized on completely clamped capacitors of sample C. This would indicate that the same population of domain walls responding to the exciting field globally

in dielectric measurements can be probed at much smaller volumes (~0.022 μm^3) when the diaphragms are released.[65,89]

Possible contributions to the changes in the mobility of domain walls observed between the clamped and released regions are:

- A partial release of the average residual in-plane tensile stress due to the thermal expansion coefficient mismatch between the PZT and the Si substrate. This was manifested by the small amount of vertical deflection observed after release.
- Deformation strains associated with formation of domains could couple mechanically to the underlying substrate. This, in turn, could produce local stresses at the PZT-Pt interface which may differ from the average residual stress. Such local mechanical stresses may influence the configuration and mobility of domain walls at the PZT-Pt interface.

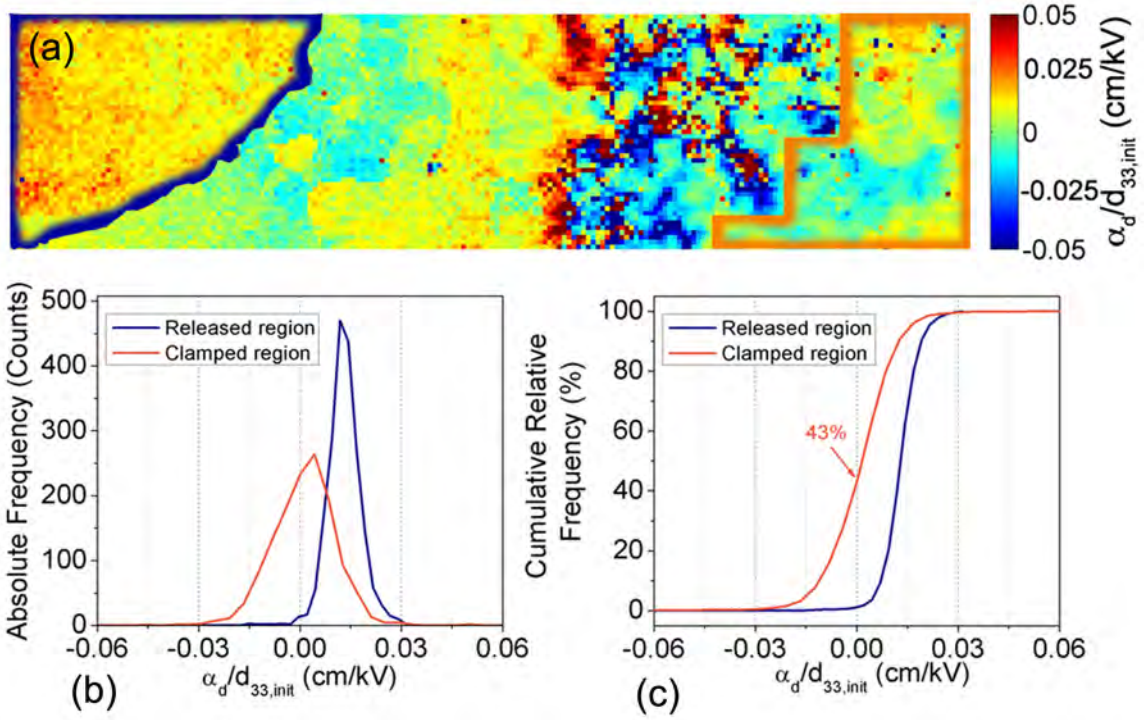

Figure **6-16**: Mechanical boundary condition dependence of nonlinearity. (a) α_d / $d_{33,init}$ ratio map highlighting the released (blue) and clamped (orange) regions used for (b) the absolute frequency and (c) cumulative relative frequency histograms.

The local piezoelectric nonlinearity data suggest that a larger fraction of domain walls is contributing irreversibly to the piezoelectric properties in the released (but not broken) region of the PZT. This is consistent with the measured frequency dispersion of the dielectric Rayleigh parameters.

It is also critical to note that the length scale over which correlated motion of domain walls is observed increases substantially as the diaphragm is released. Thus, while strong clustering of the α_d / $d_{33,init}$ ratio is observed in the clamped region, this clustering largely disappears in the released portion of the sample. This observation was borne out on larger areas of the released portion of the sample, as shown in Fig. 6-16. The histogram of the α_d / $d_{33,init}$ ratio

on this portion of the sample shows a much tighter distribution than is characteristic of the clamped regions.

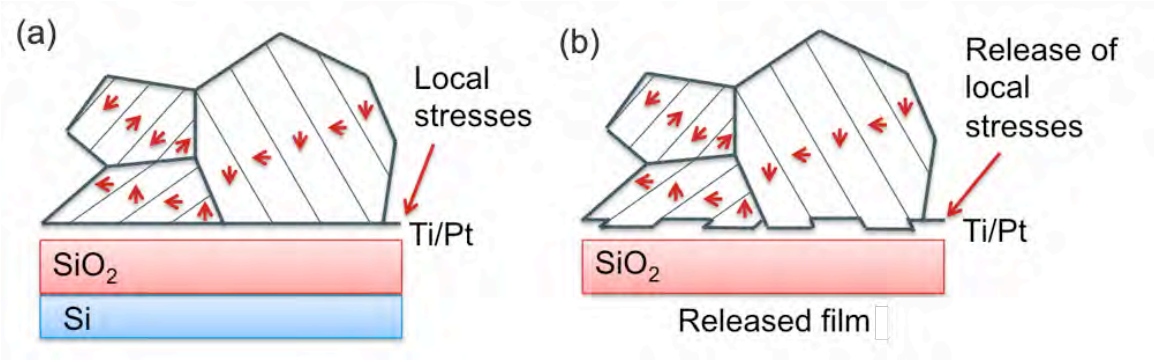

Figure **6-17**: Deformation strains associated with formation of domains could couple mechanically to the underlying substrate. (a) Local stresses develop at the PZT – bottom electrode interface which may differ from the average residual stress and influence the domain wall mobility. (b) Removal of mechanical constraints imposed by the Si substrate at the PZT – bottom electrode interface allows the domain walls to respond to the electric field more freely.

The microstructural pinning site concentration can be assumed to be the same for the clamped and released areas of the film, and the stress state is not completely relaxed, since no macroscopic cracks were induced before the *local* BE-PFM measurements. It is possible, as speculated above, that the elimination of the substrate allows local deflections out of the film plane, so that the local mechanical boundary conditions differ for the released and clamped portions of the film, even though the average residual in-plane stress does not change dramatically.

It cannot be excluded that a resonating mode of the diaphragm structure may influence the local response collected by the AFM cantilever. It is hypothesized that in this scenario the structure nonlinearity would add an offset, but would preserve the same clustering characterized in the clamped capacitors. However, the spatial distributions observed for the clamped and released regions (Fig. 6-16 (b)) showed a significant change, with a much narrower distribution of $\alpha_d / d_{33,init}$ values characterized in the released region.

Thus, it is believed that the observed increase in the dielectric $\alpha_\varepsilon / \varepsilon_{init}$ is related to the larger volume of film over which correlated motion of domain walls can occur. This, in turn, is believed to result from the fact that reduction of local stresses on removal of the substrate may eliminate pinning centers at the film/electrode interface as illustrated in Figure 6-17. Therefore, this description is consistent with the piezoelectric nonlinearity being a function of the dynamic coupling between domain walls and the length-scale of the interaction being influenced dramatically by *local* stresses.

6.5 Conclusions

The influence of microstructure and mechanical boundary conditions was analyzed in morphotropic phase boundary PZT thin films on Si substrates. By creating cavities beneath the PZT capacitors, the mechanical boundary conditions were altered and the domain wall motion contributions were probed dielectrically and piezoelectrically as a function of the mechanical boundary conditions.

A grain size dependence was observed in the global $\alpha_\varepsilon / \varepsilon_{init}$ ratios. However, maps of local converse piezoelectric nonlinearity evidenced cluster of larger $\alpha_d / d_{33,init}$ values which were of similar size for clamped films with different grain sizes.

When the piezoelectric nonlinear measurements were performed on released regions of PZT, a remarkable difference in the length scale of cooperative interaction was observed. This change was consistent with a smaller dispersion of the irreversible contributions to the dielectric constant in partially released samples. These results offer evidence for a significant influence of substrate clamping on the extrinsic contributions to the dielectric and piezoelectric properties. It is worth noting that substrate clamping and mobile interfaces interaction is a cross-cutting

phenomenon, of interest in other physical system such as ferromagnetic and ferroelastic materials and systems undergoing martensitic transformations.

While the work in this chapter pointed to a few key factors influencing the behavior of domain walls in ferroelectric thin films, the results point to a number of unanswered questions that should be addressed in future work. These include:

- What is the potential depth associated with any pinning center?
- What concentration of defects is required to pin a domain wall?
- How do particular defect types influence the volume of material participating in a domain wall cascade?
- How do macroscopic nonlinearities develop from local responses?
- How many domain walls are required to move in order to see Rayleigh-like behavior?
- What is the nature of the local strains at the film/substrate interface that leads to clustering in the $\alpha_d / d_{33,init}$ values?
- What is the origin of the non-Rayleigh regions seen in some maps?

Chapter 7

Fabrication of MEMS Diaphragm Transducer Arrays Using {001} Textured PZT Thin Films

7.1 Abstract

A piezoelectric ultrasound system on a Si substrate was fabricated using a diaphragm geometry transducer with PZT films. A 1-D array of 8 elements was designed and fabricated using 4 photolithography steps. Cavities under the resonating elements were obtained by XeF_2 etching from the top-side of the wafer. Capacitance and admittance spectra showed a resonance at ~ 42 MHz for the fabricated structures with a quality factor of 2.1, this resonance was higher than the one predicted by the natural frequency equation for circular plate. Catch- and pitch-mode tests were performed in water. Sensing and actuating functionalities were demonstrated for the fabricated devices, with collected signals of 40 mV peak-to-peak at a distance of 7.2 mm during the catch-mode test and amplitudes as high as 15 mV peak-to-peak at a distance of 7.4 mm during the pitch-mode test. A bandwidth of 83 % was calculated during pitch-mode test.

7.2 Introduction

Significant progress towards implementation of piezoelectric thin films in MEMS devices has taken place over the past 15 years. Piezoelectric thin films have been employed in several applications including fluid transport systems,[15] accelerometers[174] and ultrasonic transducers[45,175] to name a few. The design approach in all of these applications includes a piezoelectric film deposited on a passive elastic layer with a well-defined geometry, commonly a cantilever beam or a membrane. By applying an electric field to the film, the resulting strain (due to the converse piezoelectric effect) causes the structure to bend, and thus, perform useful work.

In medical ultrasound systems both sensing and actuating capabilities are needed, in bulk ceramic systems, better sensing performance is obtained by optimizing the materials constants. However, in thin film systems the sensitivity is also influenced by the structure response, in particular by the fact that out-of-plane stresses produced amplified in-plane stresses. Furthermore, the geometry of the substrate defines the working resonance frequency of the device and the compliance of the substrate structure improves the acoustical impedance match with the medium. A large piezoelectric coefficient is also important for the actuating capabilities of transducers, by reducing the driving voltage and enabling potential integration with complementary metal oxide semiconductors (CMOS).[2]

High-resolution, two-dimensional or three-dimensional ultrasonic imaging requires the transducer arrays including multiple transducer elements. In order to achieve directivity and focusing of the ultrasound beam, the timing on the array firing needs to be properly synchronized. Moreover, the elements should be spaced at no more than the half the acoustic wavelength. Recent advancements in device miniaturization enable higher operational frequencies and hence an increase in the axial and lateral resolution. Microfabrication techniques bypass some of the limitations of conventional bulk ceramic processing and constitute an efficient approach to make

transducer arrays with compact design, high precision in the definition of the resonating features and reproducibility. At the same time, the use of bending elements decreases the acoustic impedance mismatch between the stiff piezoelectric layer and water, as is the case for C-MUT devices.

Because of the versatility of microfabrication techniques, piezoelectric micromachined ultrasound transducers (PMUT) have recently been explored by many research groups.[98,99,176-180] In particular the bending mode, in which a layer of piezoelectric material is supported by a passive substrate, is the most common design for PMUTs and it has been exploited in cantilever-type[45,181,182] and diaphragm type designs.[16,17,98]

This chapter describes the fabrication and testing of a miniaturized high sensitivity ultrasound transducer array using $\{001\}$ textured PZT deposited on (111) Pt/Ti/ SiO_2/Si wafers. To define the resonating features, micromachining techniques including reactive ion etching and xenon difluoride, XeF_2 silicon etching were used. Thicknesses on the order of one micrometer of the PZT layer allow the structures to be driven at CMOS compatible voltage levels. The resonance of the fabricated structures was experimentally measured from admittance spectra and the sensitivity of 80 μm diameter diaphragms was characterized in water.

7.3 Experimental Procedure

7.3.1 Design of One Dimensional Transducer Array and Process Overview

The small thickness of the piezoelectric material in a micromachined structure would lead to a thickness resonance mode which is typically in the GHz range, too high for significant penetration depth of the ultrasound beam in human tissue. To lower the resonance frequency, thin films on larger resonating structures can be employed. This, in turn, allows bending modes

to be used for stress amplification in the receive mode, as well as displacement amplification on send. Consequently, it is of interest to be able to prepare released resonating elements for this application.

Figure 7-1 (a) illustrates schematically the structure of one of the transducer elements in many MEMS diaphragm arrays. Two general approaches can be illustrated: surface micromachining, or deep Si etching from the back-side of the Si substrate. [15,16,17]

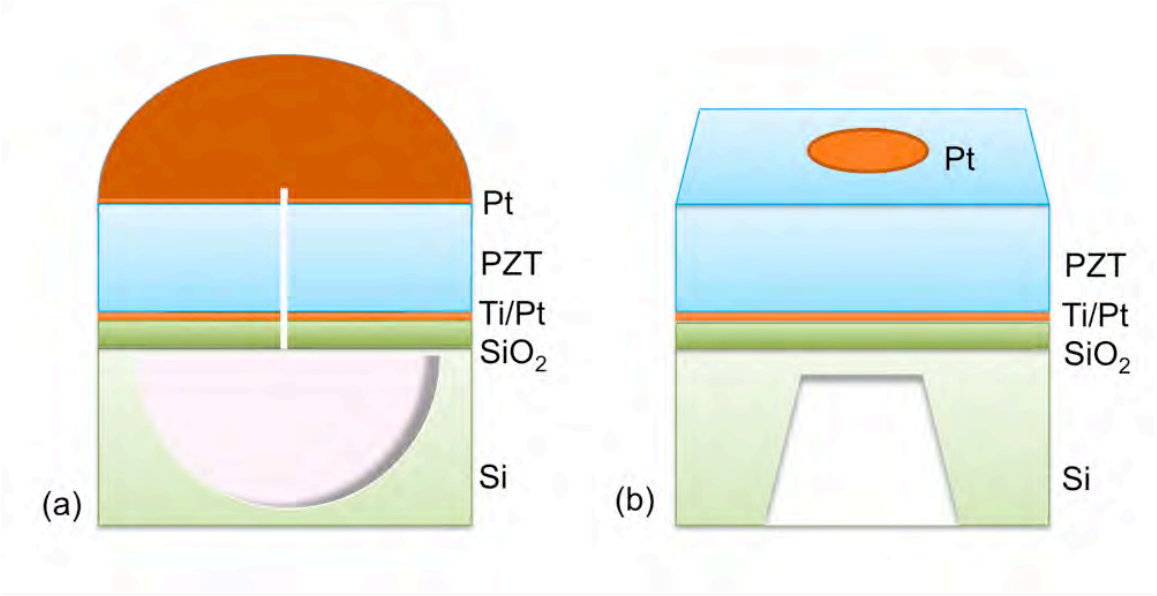

Figure **7-1**: Schematic illustrations for the transducer geometry adopted in this work (a) and adopted by other groups (b)[15-17]. The cavity diameter is not drawn to scale.

In this work, the processing method for the diaphragm structures adopted a surface micromachining approach, by releasing the PZT film via a hole from the top-side of the wafer using a XeF_2 isotropic etch. The diaphragm structures were fabricated according to the process flow in Figure 7-3. The one-dimensional transducer array was patterned using three photolithography masks. A fourth photolithography mask was used to expose a protective MX5000C^{TM} (DuPont, Wilmington, DE) acrylic polymer film for MEMS applications.

First, an overview of the fabrication process will be given; this is followed by details on the individual processing steps. The process began with deposition of the piezoelectric/electrode stack on an SiO_2-coated Si wafer. The cavities for the resonating elements were 80 ± 8 μm in diameter and the minimum feature size in the pattern was 10 μm. Given the relatively large sizes of the transducer elements explored here, contact alignment was used for all lithography steps. The first mask was used to pattern the Pt top electrode as in Figure 7-3 (b). One-dimensional arrays of 8 identical features were obtained by dry etching the Pt top electrode using Cl_2 and Ar gases. A second mask was used to pattern the opening to the Pt/Ti bottom electrode via dry etch using Ar, CF_4 and Cl_2. The third patterning step was used to dry etch the 10 μm diameter openings in the middle of the circular features down to the Si layer as in Figure 7-3 (c). The dry etch step for the 400 nm thick SiO_2 layer was performed using CF_4. A XeF_2 etch was adopted to open circular cavities by undercutting the Si beneath the PZT as in Figure 7-3 (d). The obtained diaphragm arrays were then protected with a polymeric protective layer as in Figures 7-3 (e) and (f).

7.3.2 PZT Film and Top Metal Electrode Deposition

Thin $Pb(Zr_{0.52}Ti_{0.48})O_3$ films with a thickness 1.74 μm were prepared using a chemical solution deposition process described in chapter 6. Larger displacement is expected from films thicker than 500 nm. Commercially manufactured (111) Pt/Ti/ SiO_2/Si wafers (Ramtron Int., Colorado Springs, CO) were used as substrates. In this work PZT films were used rather than PNN-PZT, because it enabled larger thicknesses on Si without cracking. The thickness for all the layers is given in Table 7-1. The neutral axis for the fabricated plates was calculated to be at 2.64 μm using the bottom surface of the SiO_2 layer as the origin.[183] The neutral axis, indicated as a function of the SiO_2 thickness in Figure 7-2, was evaluated using the method of equivalent areas

and elastic moduli of 179, 77, 101 and 3.2 GPa were used respectively for Ti/Pt, SiO_2, PZT and the MX500C^{TM} layers.[184-187] Given that the sum of the SiO_2 and Ti/Pt bottom electrode is 0.5 μm, the neutral axis was located inside the MX5000C^{TM} layer. A thickness of 1.0 μm and higher for the SiO_2 would bring the neutral axis inside the PZT layer, therefore decreasing the sensitivity of the transducer.

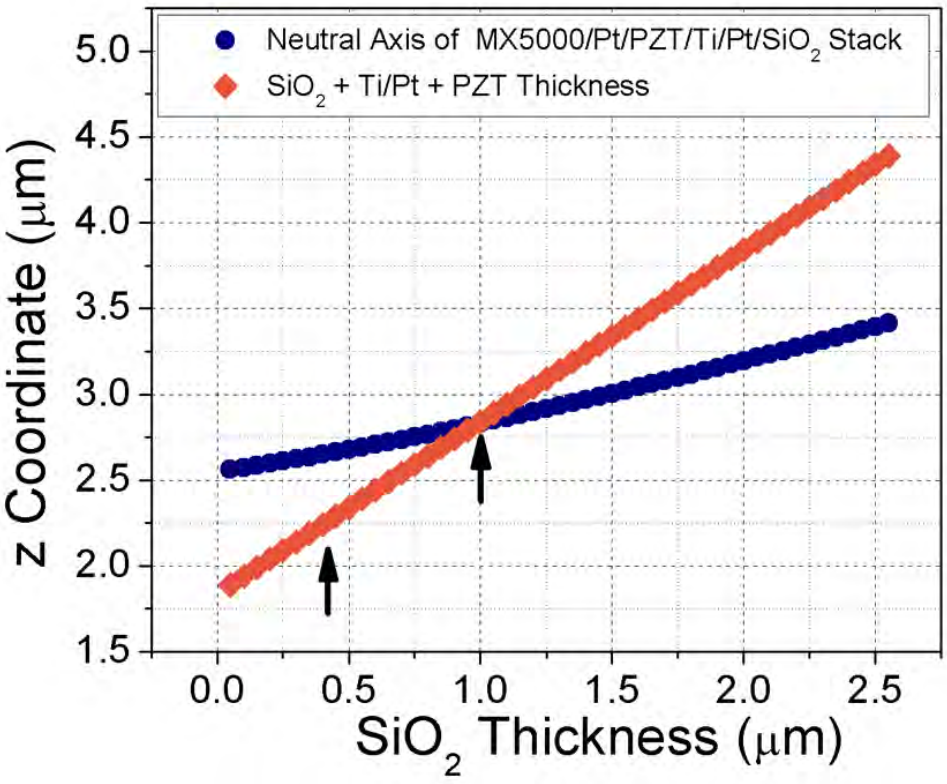

Figure **7-2**: SiO_2 thickness dependence of the position of the neutral axis for the PZT/Ti/Pt/SiO_2 stack. The z coordinate has the origin on the bottom surface of the SiO_2 layer. The left arrow indicates the position of the neutral axis for a 400 nm thick layer of SiO_2. The right arrow indicates that for a 1.0 μm thick SiO_2 layer or thicker, the neutral axis would be located within the PZT layer.

Table **7-1**: Thickness of the layers in the MEMS transducer.

Layer	*Thickness*
Si	500 μm
SiO_2	400 nm
Ti/Pt bottom electrode	100 nm
PZT	1.74 μm
Pt top electrode	40 nm

The substrates were pre-annealed for 60 s at 500 ºC immediately prior to solution deposition. A 0.15 M solution of $PbTiO_3$ containing 40 mol % Pb excess was used to create a seed layer which promoted {001} orientation for the PZT films as described in section 3.3.1. After the seed and template layer deposition, the PZT solution was spun on the substrate at 1500 rpm for 30 s using a PWM32 photoresist spinner (Headway Research, Inc., Garland, TX). The deposited layers were pyrolyzed at 250 and 400 ºC for 1 min respectively. Two MPB PZT solutions were used: a lower content of lead excess (15 mol% Pb excess) for the first 3 pyrolyzed layers and higher content of lead excess (20 mol% Pb excess) for the 4^{th} layer of PZT prior to each anneal step. Every four pyrolyzed layers, the film was annealed at 700 ºC for 1 min at a ramp rate of 50 ºC/s. The process was repeated to build up the desired thickness of 1.74 μm.

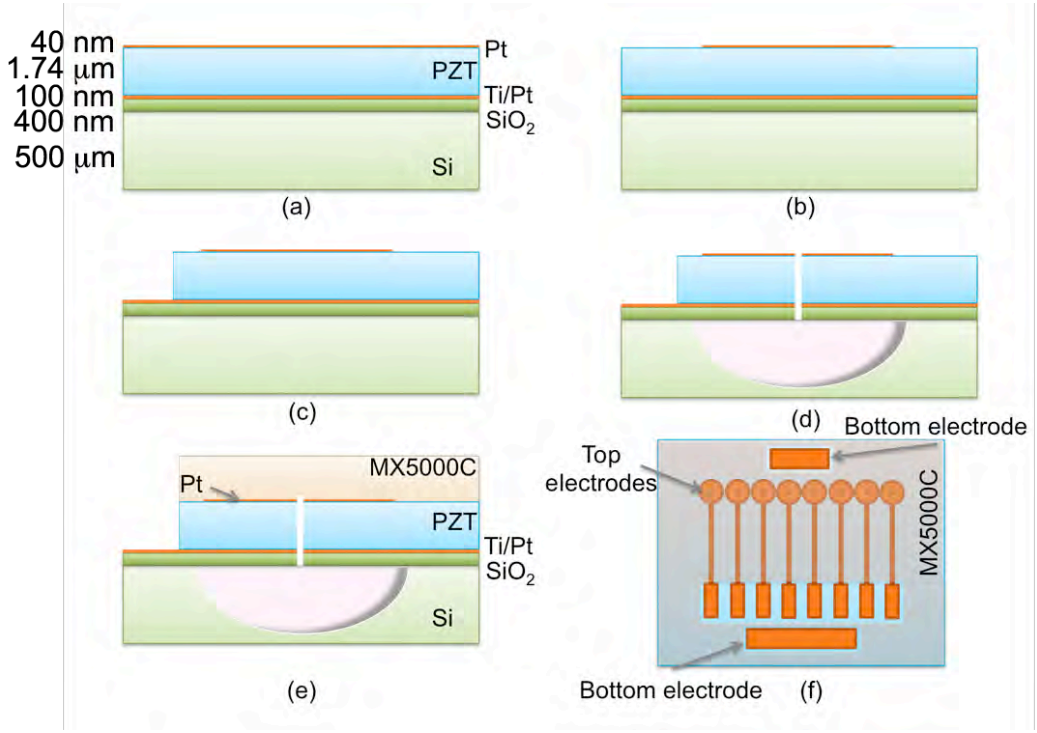

Figure **7-3**: Fabrication process of the diaphragm transducer array. (a) Cross-section of the initial Pt/PZT/Pt/Ti/SiO_2/Si stack, (b) reactive ion etch of the Pt top layer to define the transducer elements, (c) reactive ion etch of the PZT layer to open the bottom electrode contacts, (d) reactive ion etch of the Pt/PZT/Pt/Ti/ SiO_2 layers and subsequent isotropic XeF_2 etch of the Si underneath the transducer, (e) hot lamination of MX5000C^{TM} on the fabricated MEMS to close the hole created during step (d), (f) top view of the array structure. Images not drawn to scale.

A 40 nm thick platinum was sputter deposited using a CMS-18 deposition system (Kurt J. Lesker Company, Clairton, PA) at a base pressure of 2.5 mTorr in Ar atmosphere as the top electrode. A sputtering time of 150 s at a dc power of 200 W was required to reach the desired thickness. The target to substrate distance was 120 mm.

7.3.3 Reactive Ion Etch Steps

A ~ 7 μm thick photoresist (SPR 220, Shipley Company, L.L.C., Marlborough, MA) was exposed and developed as a mask for the dry etching steps, as summarized in Table 7-2.

Table **7-2**: Photolithography process conditions from the transducer dry etch step.

Photoresist Recipe: Shipley SPR 220	
Wafer preparation	Vapor priming of the surface using hexamethyldisilazane (HDMS)
Spin of photoresist	4000 rpm for 45 s
Bake steps sequence	95 ºC 90 s, 115 ºC 90 s, 95 ºC 90 s
Exposure sequence	10 s exposure, 10 s wait, repeated 5 times at 8 mW/cm^2 30 min wait before develop
Develop	CD26 2 min

First, after a dehydration step at 100 ºC for 1 min, the surface of the wafer was prepared using vapor priming. Surface moisture is one of the major factors that could reduce resist adhesion, inducing pattern lifting or unwanted lateral etching. Vapor priming of hexamethyldisilazane was performed in order to increase the liquid contact angle of the photoresist by making the surface of the wafer more hydrophobic.

Following manufacturer specifications for a ~7 μm thickness,[188] the photoresist was spun at 4000 rpm for 45 s and 3 subsequent soft bake steps at 95, 115, and 95 °C were performed to avoid crack formation. The film was then exposed with a 5 step cycle by alternating 10 s of exposure at 8 mW/cm^2 and 10 s of wait time using a MA6 contact aligner (SUSS MicroTec Inc. Sunnyvale, CA) with a mixed exposure wavelength of 365/405 nm. After a 30 min wait, the photoresist was developed in CD26 (Rohm and Haas Electronic Materials LLC, Marlborough, MA).

Etch of the top and bottom metal layers and the PZT were performed with a high-density plasma etch tool Tegal 6540 (Tegal Corp. Petaluma, CA). The tool generated an electromagnetic

field at a power level of 310 or 615 W at 13.56 MHz depending on the etching step. The procedures and etch rates for the metal layers and PZT are reported in Table 7-3. The etch of the SiO_2 layer was performed with a Versalock ICP 700 (Plasma Therm Inc., N. St. Petersburg, FL).

Table **7-3**: Etch recipes and rates for metal, PZT and SiO_2 layers.

Layer	*Gas*	*Flow (sccm)*	*Pressure (mTorr)*	*Power (W)*	*Frequency (MHz)*	*Etch rates (nm/min)*
Pt, Pt/Ti	Cl_2	20	5	310	13.56	80
	Ar	40				
	CF_4	28		310		
PZT	Cl_2	7	5	615	13.56	110
	Ar	45		310		
SiO_2	CF_4	155	5	310	13.56	180

For PZT dry etching, there is not a known gas that forms volatile compounds with Pb, Zr, and Ti at the same rate to stoichiometrically remove the PZT layer. For this reason, both CF_4 and Cl_2 were used in the dry etch recipe for PZT to provide a residue-free removal of the layer. Chlorine plasmas are generally used because of higher volatility of metal chlorides than metal fluorides (e.g. $PbCl_3$, PbF_4).[189] However, CF_4 ion bombardment is known to be more selective with respect to the platinum electrodes.[190] Also, the volatility of the reactive ion etch by-products of Pb, Zr and Ti is limited,[191] energetic ion bombardment of Ar was adopted to assist the complete removal of the PZT layer.

The calculated PZT etch rate of 110 nm/min is relatively high.[192] The etching was performed with consecutive steps 30 s long alternated with 60 s in Ar atmosphere to allow the

wafer to cool down. This method was adopted to preserve the stability of the photoresist. Figure 7-4 illustrates side walls after a Pt/PZT/Pt/Ti etch.

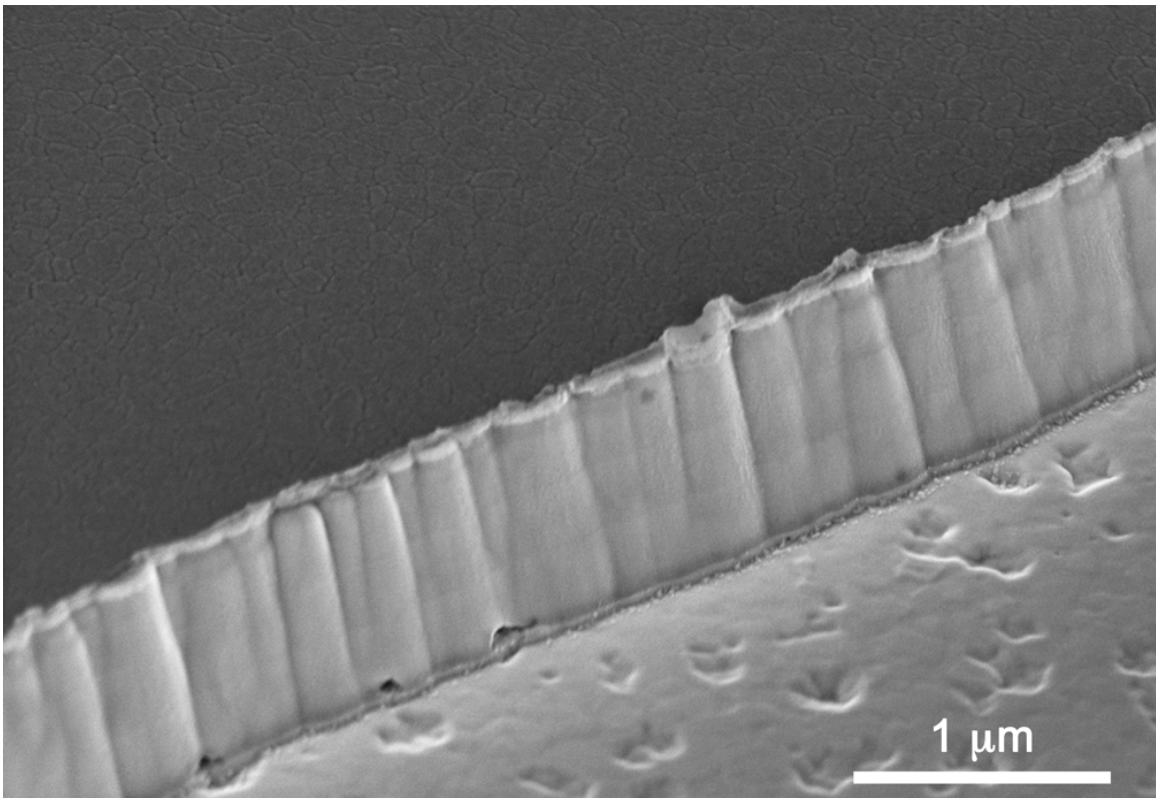

Figure **7-4**: FE-SEM image of Pt/PZT on SiO_2 after dry etching. Almost vertical side-walls were obtained with the processing conditions of Table 7-3. The 40 nm thick Pt top metal layer conforms to the PZT microstructure.

7.3.4 Xenon Difluoride Silicon Etching

The Si under the circular transducer elements was isotropically etched with xenon difluoride (XeF_2) gas from the topside of the wafer to obtain diaphragms using an e1 Series Xetch tool (Xactix, Inc., Pittsburg, PA). This etching process generated a spherical cavity with diameters of approximately 80 μm under the Pt/PZT/Pt/Ti/SiO_2 layers. The selectivity of XeF_2 versus SiO_2 and photoresist is higher than 1000:1.[193,194] The XeF_2 etching reaction is:

$$2XeF_{2(g)} + Si_{(s)} \rightarrow 2Xe_{(g)} + SiF_{4(g)}$$ Equation **7-1**

Gaseous XeF_2 adsorbs on the silicon surface and dissociates to form fluorine. Fluorine then reacts with Si in an exothermic reaction to form gaseous SiF_4.

XeF_2 is a white crystalline solid with a vapor pressure at room temperature of ~ 4.5 Torr.[195] Consequently, XeF_2 can be introduced into a vacuum system by opening a control valve which isolates the XeF_2 from the processing chamber under vacuum. The tool has two expansion chambers, one of which is the etching chamber. Repeated cycles of XeF_2 expansion and by-product removal were performed to obtain the desired cavity diameters.

The benefits of using XeF_2 versus other etching techniques are:[196]

- The very high selectivity to silicon with respect to silicon dioxide, metals and crystalline PZT
- Absence of release stiction, no drying is needed to avoid sticking issues that often afflict wet etch release processes
- Delicate and complicated structures can be safely released even after wire-bonding
- Negligible interaction with crystallized PZT

Table **7-4**: XeF_2 etch conditions.

XeF_2 pressure (Torr)	*N_2 pressure*	*Etch time/cycle*	*Etch rate (μm/min)*
3	0	60 s	0.63 ± 0.04

The etch rate was calculated using a Si wafer with a 100 nm thick layer of SiO_2 for the hard mask. After creating approximately circular openings to the Si, the wafer was etched isotropically using XeF_2; the transparent layer of SiO_2 allowed the etch rates to be calculated as the ratio of the cavity radius to the total etching time. Ten cavities were measured to assess the etching rate. Since the XeF_2 etching tool was located in a different building than the other etching tools, the wafers were transported under vacuum between the two cleanrooms to minimize the formation of native SiO_2 surface layer, which could affect the initial XeF_2 etching rates.

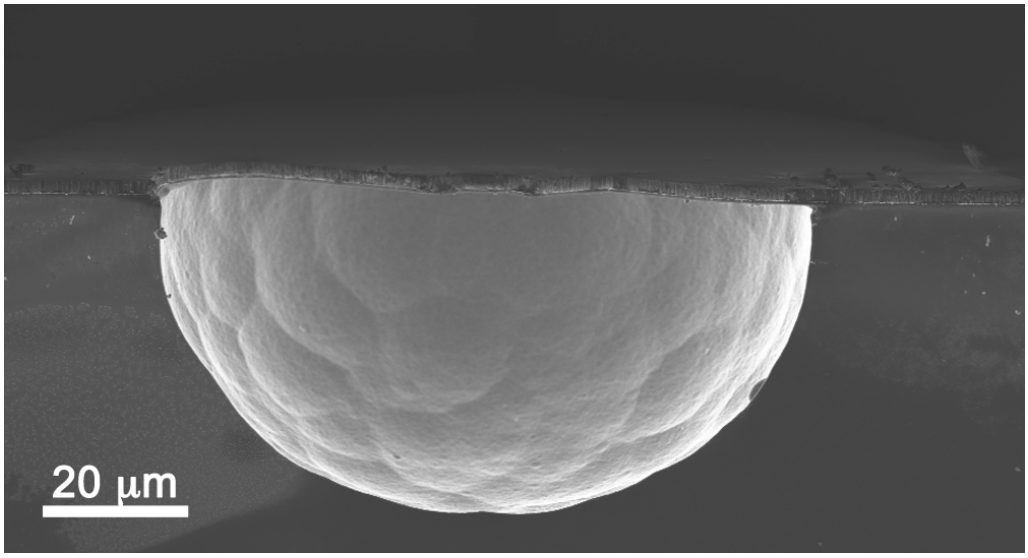

Figure **7-5**: FE- SEM image of cross-section of fabricated diaphragm, the cavity was ~ 80 μm in diameter.

7.3.5 Dry Film Resist Lamination

It was important to cover the hole introduced at the center of the diaphragm structure in order not to compromise the sound pressure output of the resonating structures. Spin coating or physical deposition were difficult to implement for this purpose; a negative dry photosensitive film based on acrylic monomer chemistry was used instead. 15 μm thick films of Dupont MX5000C™ were vacuum laminated on the fabricated structures, followed by exposure using the conditions reported in Table 7-5. The Dupont product has two protective layers, one of them needs to be removed before lamination, and the other one must be removed before alignment and UV exposure. It was critical not to bring the laminated wafer in contact with the mask, or the MX5000C™ delaminated upon contact, often damaging the underlying structures. This protective layer may also have improved the acoustical impedance match between water and the diaphragm structure.[197,198]

Table **7-5**: Etch recipes and rates for metal, PZT and SiO_2 layers.

Dry Film Resist Recipe: DuPont™ MX5000C™	
Lamination	1 min, top surface 100 ºC, bottom surface 100 ºC, 100 s dwell pressure, 100 s dwell vacuum
Pre-exposure bake	100 ºC 45 s
Exposure	8 mW/cm^2 5 min
Post-exposure bake	100 ºC 45 s
Develop	0.75 wt% Na_2CO_3 1 min

7.3.6 Parylene Layer Deposition

Before in-water test of the fabricated structures, a 1.5 μm parylene C layer was deposited on the surface of packaged devices using a thermal evaporator (PDS 2010, Labcoater, SCS, Inc., Indianapolis, IN). The dimer is first vaporized at 150 ºC and 1.0 Torr atmosphere. After pyrolysis at 680 ºC and 0.5 Torr, the monomer is deposited at 25 ºC at 0.1 Torr. A cold trap in the final stage collects the excess monomer. Parylene C provides greater moisture vapor resistance than parylene N and D.[199] The parylene C has a chlorine atom on the benzene ring, and this variation offers superior breakdown resistance than parylene N at smaller thicknesses.[200]

Due to the low surface energy of the parylene, a surface treatment was required to improve the surface wettability of the packaged devices for in-water testing. The devices were treated in an oxygen plasma (45 sccm) for 5 sec at 100 W (150 V) using a PlasmaTherm 720 (PlasmaTherm, LLC., St. Petersburg, FL). After the treatment, the device surface was hydrophilic. Figure 7-6 illustrates an optical image of a device wire-bonded to a 16-pin ceramic package.

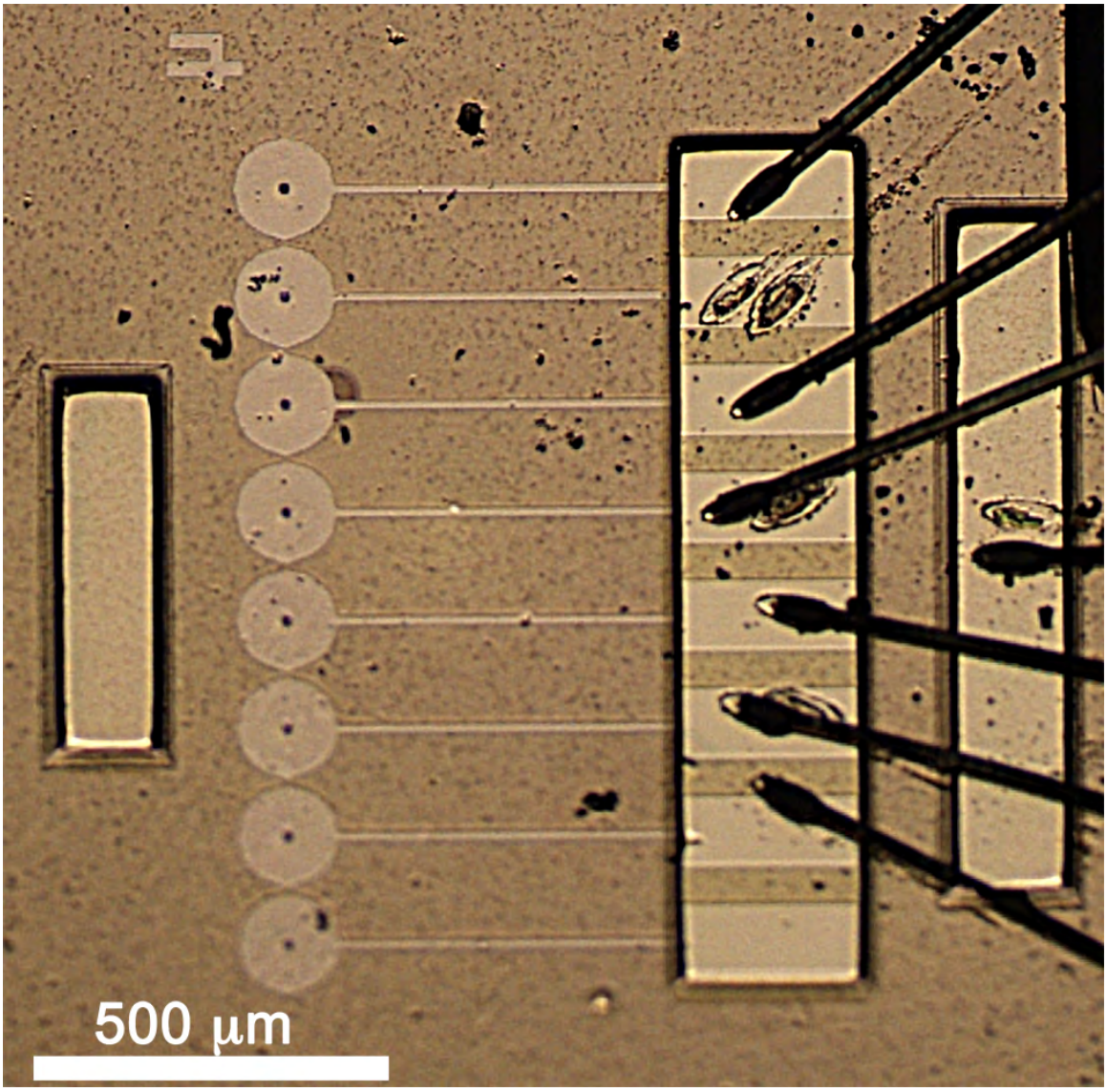

Figure **7-6**: Optical image of packaged 1 D array of diaphragm transducers.

7.3.7 Dielectric Characterization of the Fabricated Devices

Dielectric characterization before and after a temperature treatment (done before packaging) was performed to assess the recovery of the fabricated devices, using a HP 4284A precision LCR meter (Agilent Technology, Palo Alto, CA). Impedance, admittance and capacitance sweeps up to frequencies of 100 MHz were performed using a HP 4294A impedance

analyzer (Agilent Technology, Palo Alto, CA). For the impedance, admittance and capacitance sweeps as well as for the in-water tests the fabricated devices were first poled at the coercive field for 30 min and aged for at least 30 min.

7.3.8 In-water Test Setup

In water functionalities were examined in both transmit and receive modes. In both cases, the transducer arrays were dipped in de-ionized water. For the pitch mode tests, the fabricated transducers were excited using an external pulser; the signal was received using a commercial transducer. Catch-mode tests were conducted by receiving an ultrasound pulse from a commercial transducer. Figure 7-7 illustrates the schematic for the tests. The measurement conditions have been described in more detail elsewhere.[175,198]

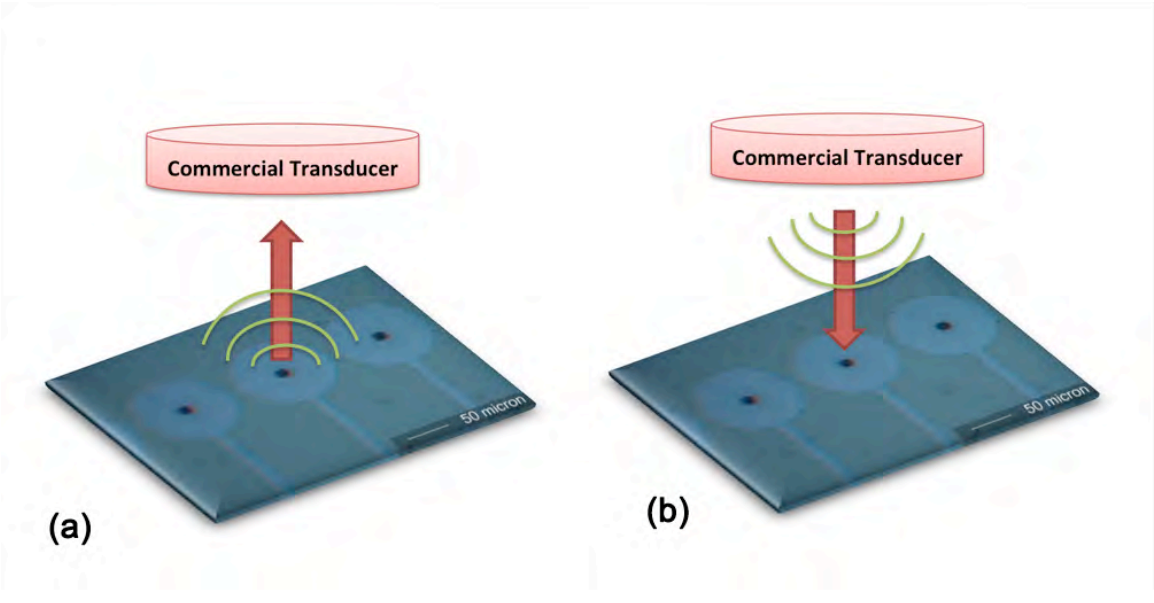

Figure **7-7**: In-water (a) pitch and (b) catch mode test.

7.3.8.1 Catch-test Measurement Setup

For this configuration, the test device and a commercial transducer M316 (Olympus, Japan) with a center frequency of 20 MHz, were immersed in a water tank.[201] A printed circuit board was used for the test with a socket to house the 16-pin ceramic package containing the fabricated transducer array. A six-axis positioner, nanomax 17MAX603/R (Melles Griot, Bensheim, Germany) was used to align the MEMS transducers with respect to the M316. A pulser/receiver, PR5900 (Olympus, Japan), was used to excite the M316 and collect the pulse with the test device. The collected signal was fed to an Infinium high precision oscilloscope (Agilent Technologies, Inc., Santa Clara CA).

Table **7-6**: PR5900 Excitation parameters for M316 transducer.

Mode	*Through*
Pulse Energy	1 μJ
Damping	50 Ω
Pulse Repetition Frequency	200 Hz
High Pass Filter	1 MHz
Low Pass Filter	100 MHz
Receiver Gain	26 dB

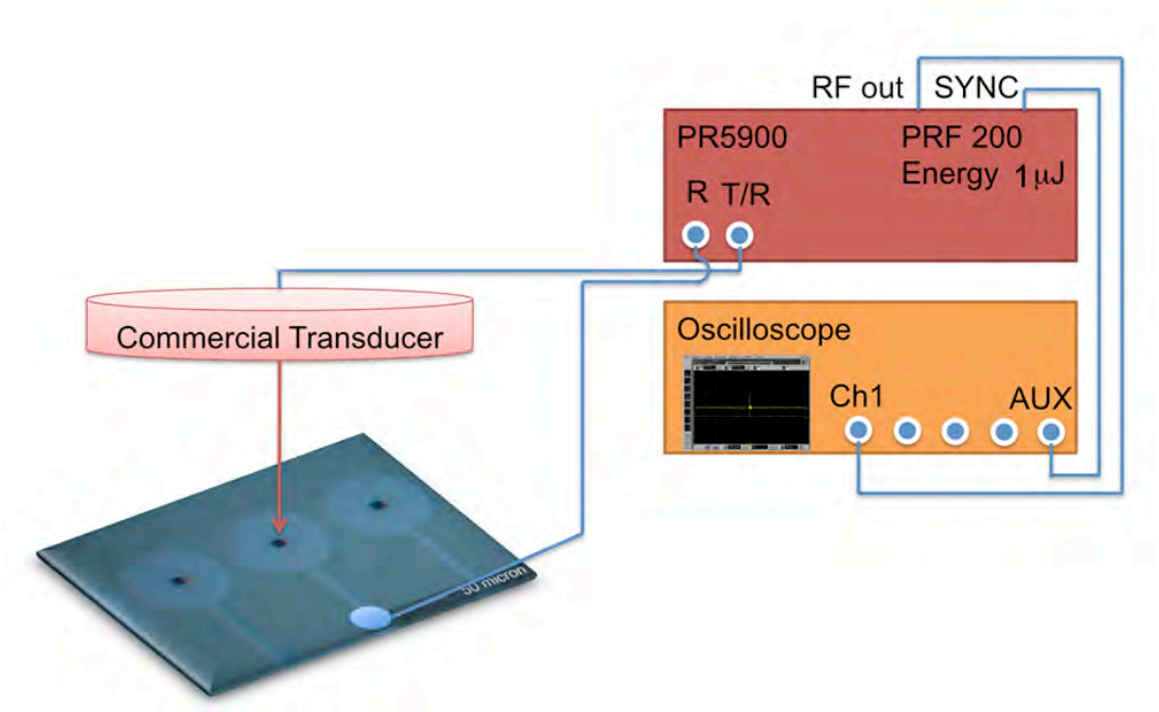

Figure **7-8**: Catch-mode test setup. RF out refers to the channel that is fed to the oscilloscope to monitor the sent and received signals. SYNC refers to the channel containing the synchronization signal using sync pulses. R and T/R are respectively the receiving and transmit and receiving channels of the pulser and receiver PR 5900. PRF 200 refers to the pulse repetition frequency.

7.3.8.2 Pitch-test Measurement Setup

In the pitch-mode, the test device and the commercial transducers were immersed in water and aligned using a six-axis positioner. For this test however, the test device was excited using an external pulse generator HP8011A (Agilent Technologies, Inc., Santa Clara CA). Unipolar pulses of 14 V (80 kV/cm) were used to excite single elements. The generated waves from the MEMS transducer were amplified with the receiver gain set at 26 dB.

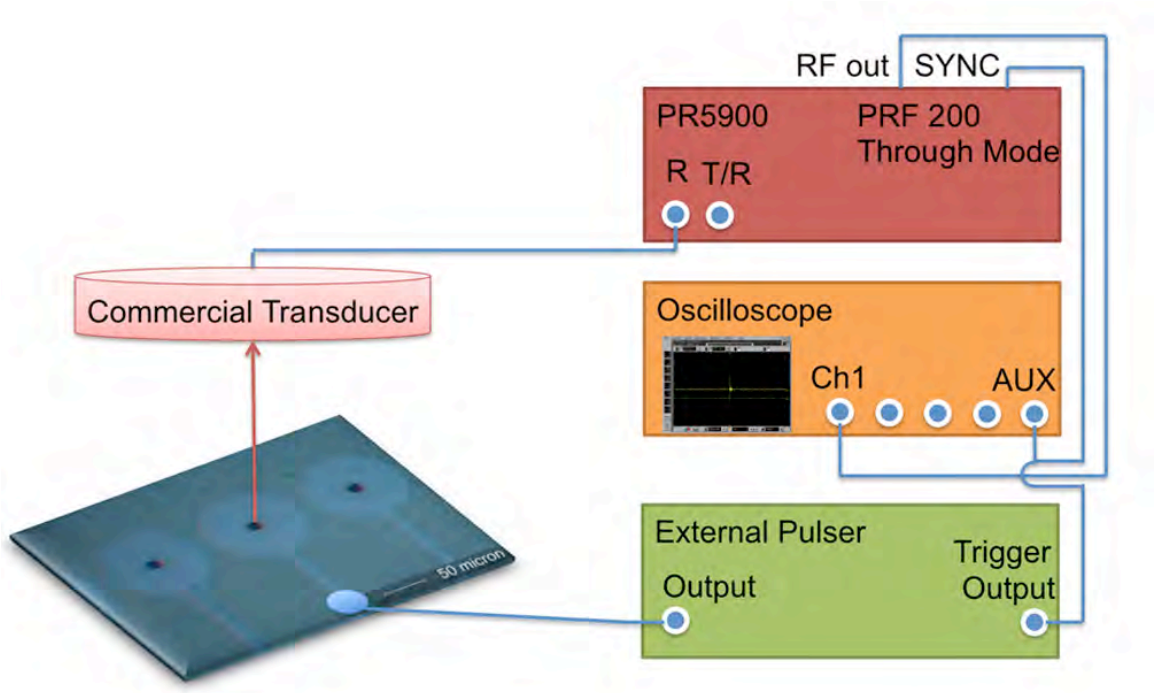

Figure **7-9**: Pitch-mode test setup. The pulse generator (green) HP8011A excites the MEMS transducer. The received signal is amplified through the pulser and receiver PR5900 and then fed to the oscilloscope. The trigger output of the external pulser provides the sync pulses to the oscilloscope.

7.4 Results and Discussion

7.4.1 Dielectric Characterization

After the dry etch steps of the fabricated diaphragm structures, the devices were heat-treated at 250 ºC for 12 h in a box furnace. It was found that treatments in an RTA or at higher temperature were likely to induce cracks, due to the inherent brittleness of the structures and small angles at the holes in the center of the diaphragm acting as stress concentration points. Cracks could also be induced by driving the fabricated structures at three times the coercive field with 100 ms cycles or lower. Figure 7-10 illustrates the typical crack formation. In order not to damage the structures, the transducers were poled the coercive field for 30 min.

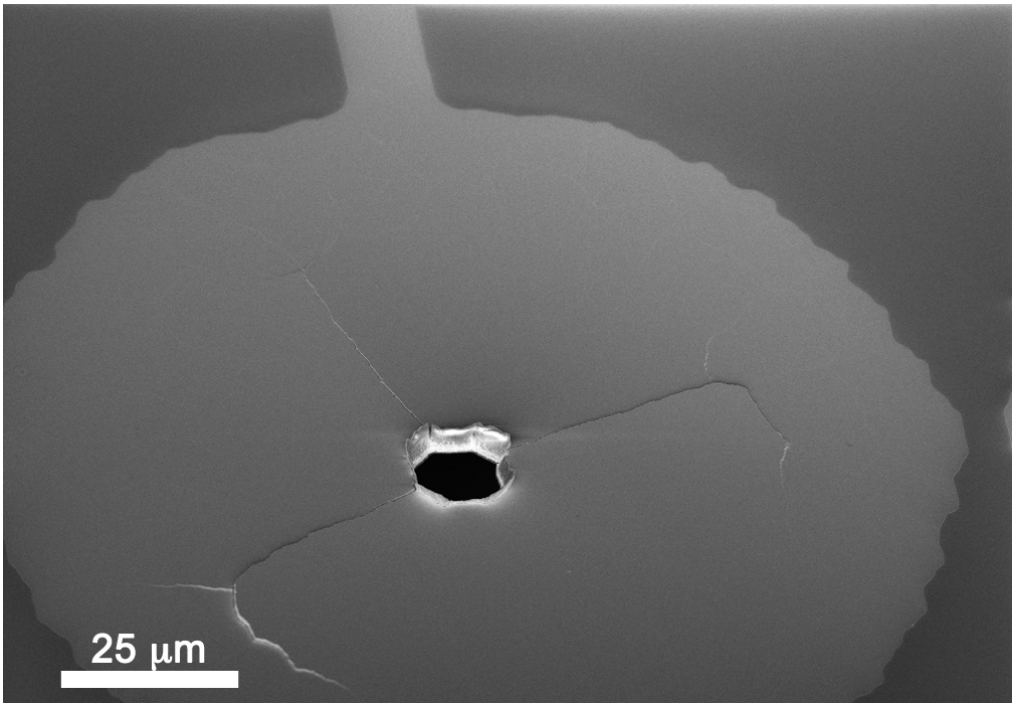

Figure **7-10**: Radial cracks developed on a diaphragm structure after applying an electric field of three times the coercive field. The rough edge of the electrode pattern is due to the method used to manufacture the photolithography masks; the circles were the result of finite rotation steps of rectangular features. The radial cracks appear to terminate at the cavity edge.

Figure 7-11 shows the frequency dependence of the dielectric constant for the fabricated diaphragms before and after a thermal anneal at 250 ºC for 12 hours. As previously reported, dry etch steps can induce formation of randomly oriented defect dipoles.[202] However, for the present work, no pinching was detected in minor polarization hysteresis loops and negligible differences in the frequency dependence of the dielectric constant were noticed when measurements were performed after the etching steps. The properties are comparable to sample C used in chapter 6.

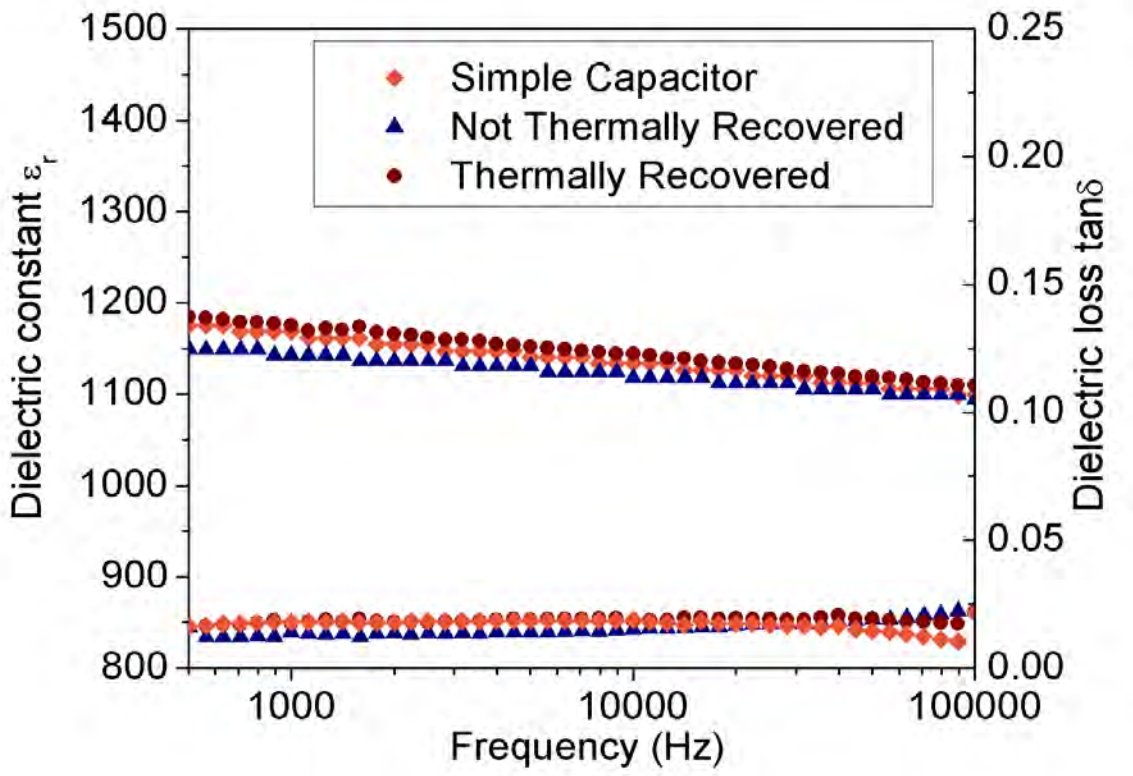

Figure **7-11**: Comparison of the frequency dependence of the dielectric constant for devices before and after the thermal recovery and a sample capacitor from the same PZT film. "Simple capacitor" refers to a capacitor of the same film that was not exposed to microfabrication steps.

7.4.2 Resonance Measurements

7.4.2.1 Natural Frequency Prediction

In the case of an edge-clamped circular plate of a material with a uniform cross-section (in material composition and thickness), the natural frequencies are given by:[203-205]

$$f = \frac{\alpha}{2\pi R^2}\sqrt{\frac{D_E}{\rho h}} \qquad \text{Equation } \mathbf{7\text{-}1}$$

$$D_E = \frac{Eh^3}{12(1-\nu^2)} \qquad \text{Equation } \mathbf{7\text{-}2}$$

where f is the resonance frequency, α is a constant determined by the vibration mode, R is the radius of the diaphragm, h is the diaphragm thickness, ρ is the diaphragm density, D_E is the flexural rigidity of the diaphragm, E is the Young's modulus and Poisson's ratio of the diaphragm.

By using reported values for MX5000C^{TM}, PZT 4 and SiO_2 [19,187,206] for the Young's modulus, density and Poisson's ratio, the expected natural frequencies were calculated as a function of the cavity diameter and different vibration modes. It was predicted that the fundamental natural frequencies of fully clamped 80 μm diameter diaphragm transducers without a hole in the center should lie between 1 and 4 MHz as shown in Figure 7-12, depending on the resonance mode.

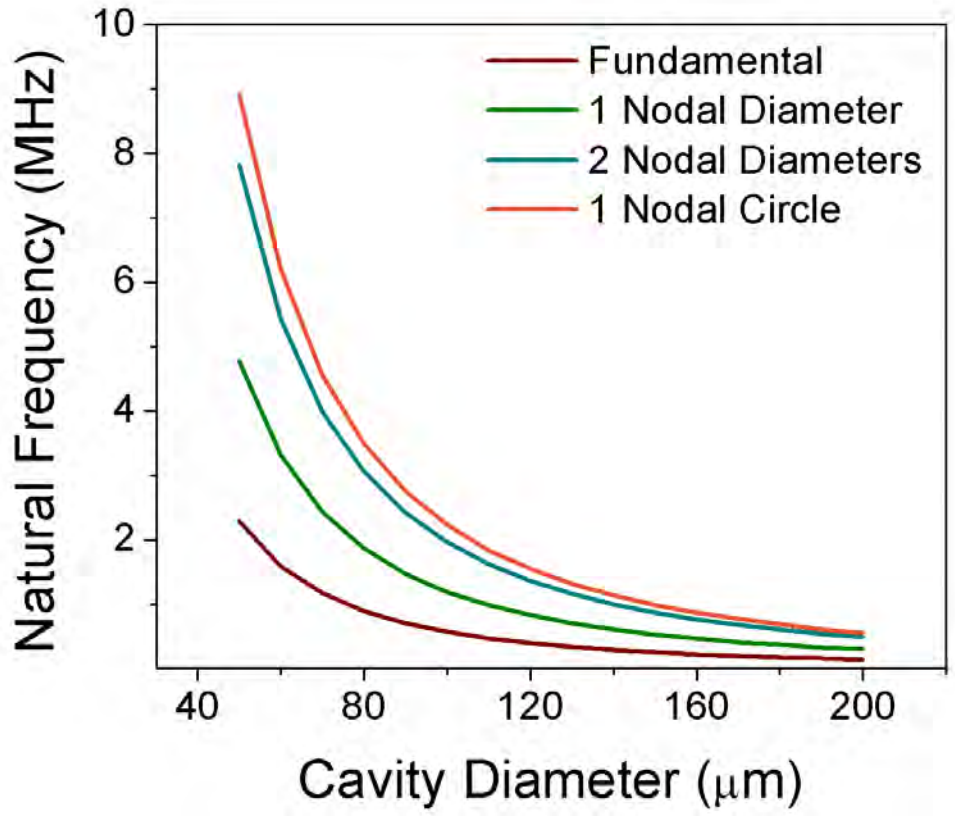

Figure **7-12**: Predicted natural frequencies of diaphragm structures as a function of the diameter, using the vibrating plate equation.

7.4.2.2 Finite Element Analysis

Finite element analysis was performed to predict the conductance spectra, the resonance frequency and related mode for the diaphragm structures tested in this study. The properties of PZT 4 as indicated in Table 7-7 were used to simulate the behavior of the plate.

Table **7-7**: PZT 4 properties used in finite element model.[19, 20]

Property	*PZT 4*
Young's Modulus (N/m^2)	$6.3 * 10^{10}$
Shear Modulus (N/m^2)	$2.84 * 10^{10}$
Poisson's Ratio	0.43
Density (kg/cm^2)	$7.5 * 10^3$
Transverse Piezoelectric Coefficient d_{31} (pm/V)	-123
Quality Factor	500

For geometric parameters, a cavity diameter of 80 μm and a hole diameter of 12 μm at the center of the plate were considered. The PZT thickness was 1.74 μm. In this analysis the PZT was modeled imposing clamped external edges, an underlying layer 400 nm thick of SiO_2 and the 15 μm thick sealing polymeric layer. An elastic modulus of 77 GPa, a Poisson's ratio of 0.17 and a density of 2,200 kg/m^3 were utilized for the SiO_2.[206] An elastic modulus of 3.2 GPa, a Poisson's ratio of 0.45 and a density of 1,100 kg/m^3 were used for the MX5000™ layer.[207]

The electric field was applied with a positive polarity on the top surface and the bottom surface was grounded. The mesh grid used for the model is shown in Figure 7-13.

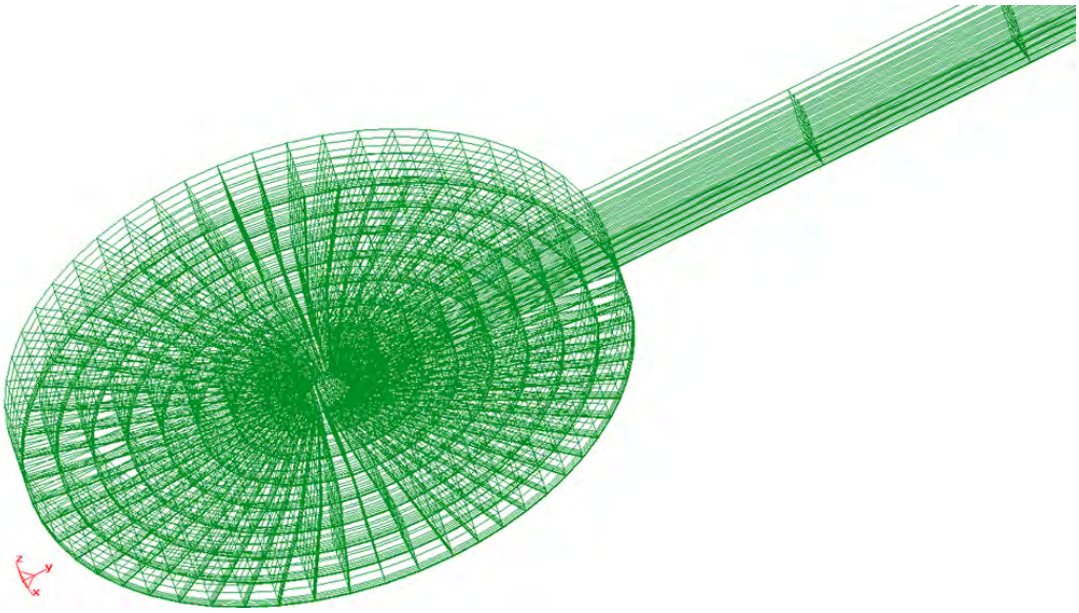

Figure **7-13**: Mesh grid of a unimorph PZT plate with a hole in the center, the simulation included a 15 μm thick acrylic polymer film covering the top electrode layer.

First, resonance mode analysis was performed and a relative maximum in the coupling mode was found at ~ 38.2 MHz. The conductance and susceptance spectra were then calculated for the modeled PZT structure and the results are shown in Figure 7-14. Only the conductance spectrum showed a detectable resonance.

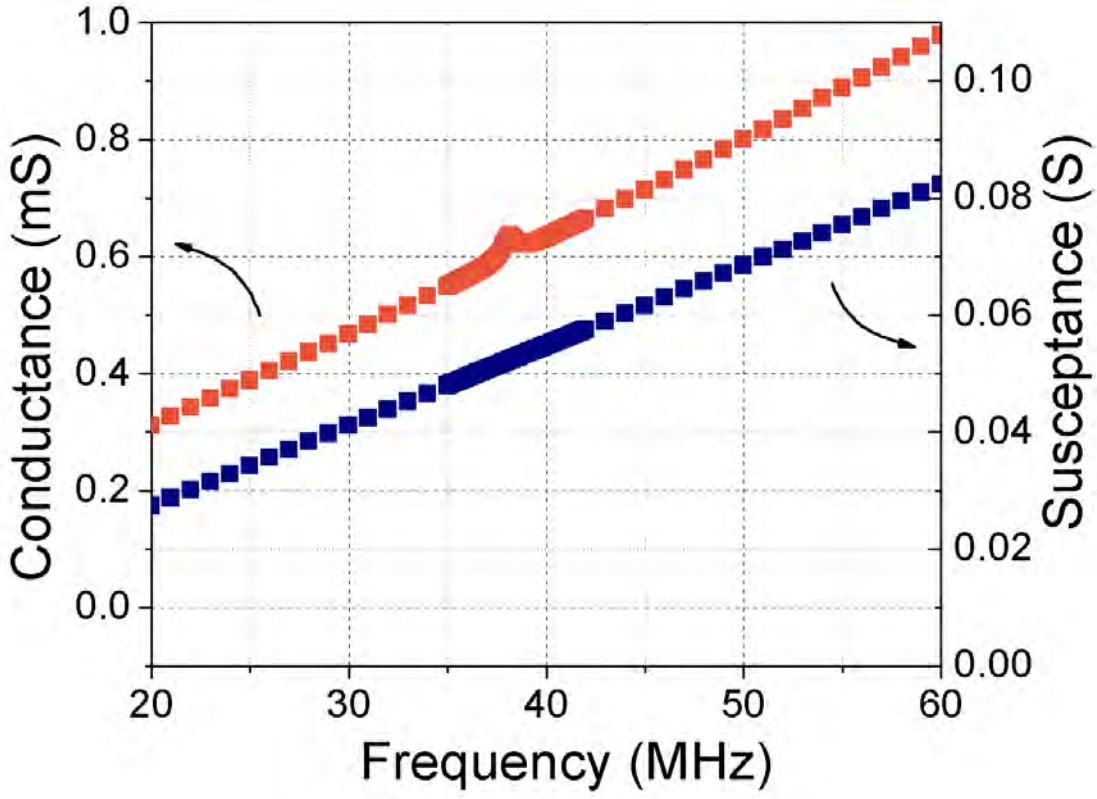

Figure **7-14**: Calculated conductance and susceptance versus frequency for the modeled diaphragm structure.

7.4.2.3 Capacitance and Conductance Spectra

Values of Capacitance and Conductance were collected as a function of frequency for packaged devices with a cavity diameter of 80 μm and a PZT thickness of 1.74 μm. The results are shown in Figures 7-15 and 7-16.

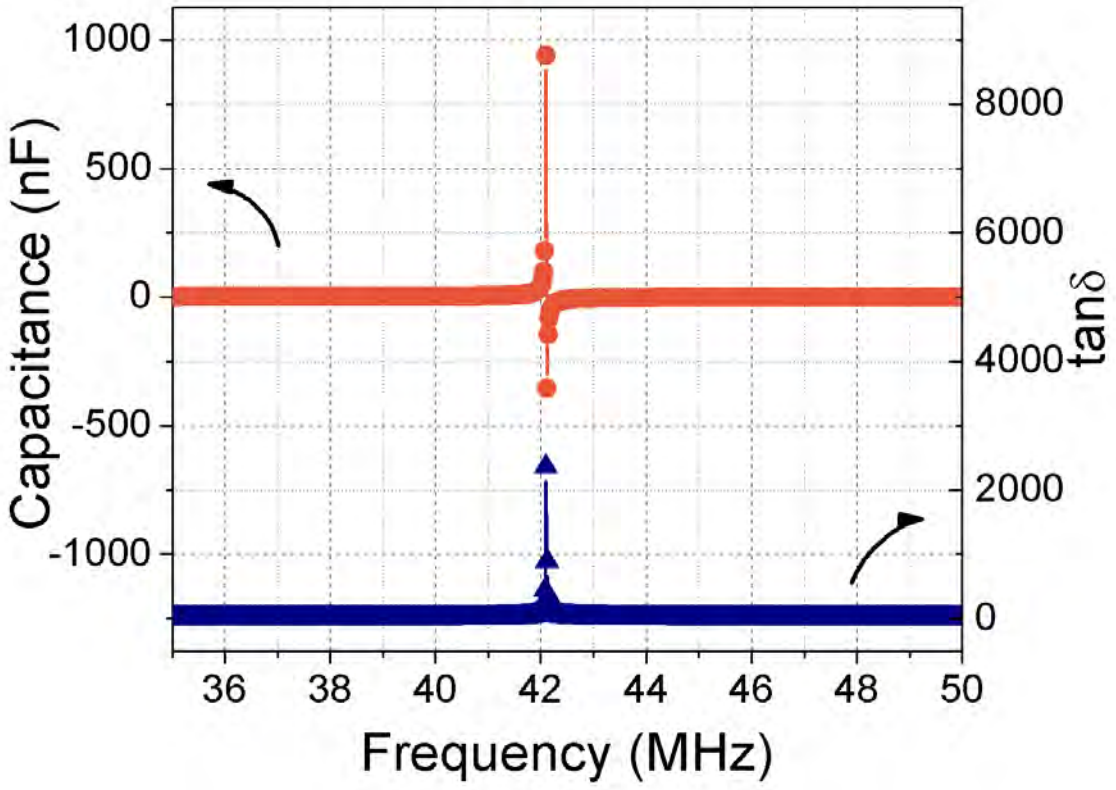

Figure **7-15**: Capacitance and *tanδ* as a function of frequency for a fabricated device.

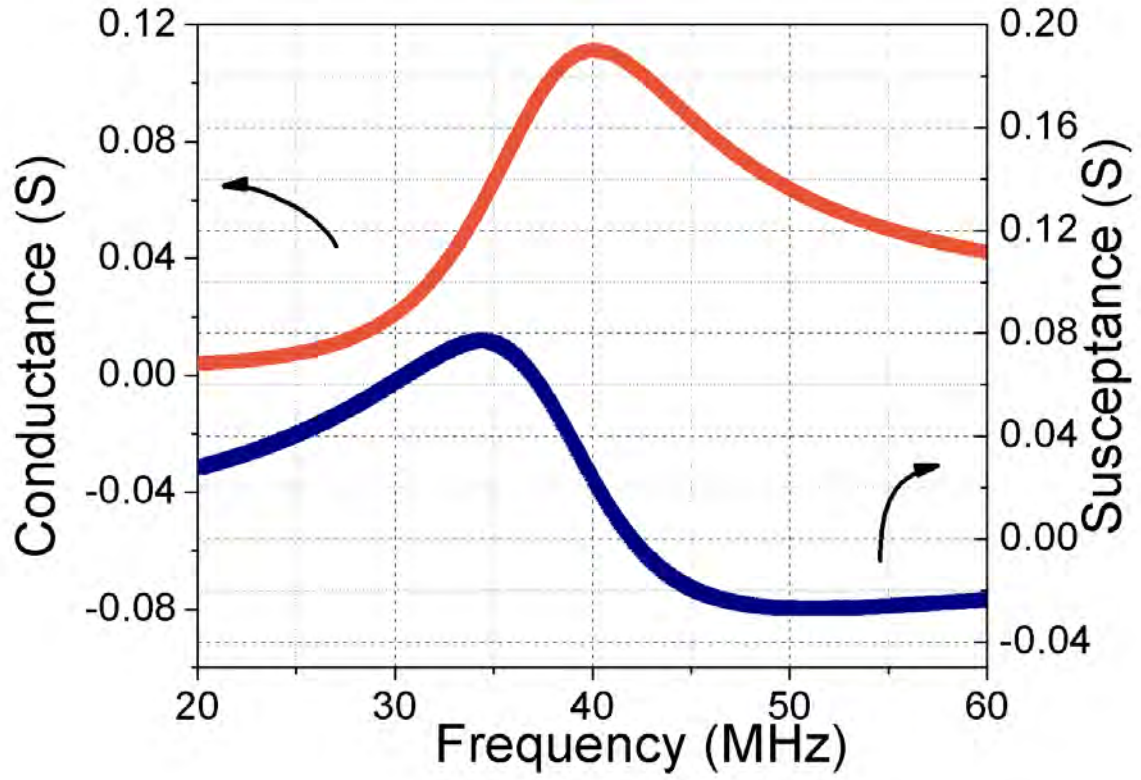

Figure **7-16**: Conductance and susceptance as a function of frequency for a fabricated device.

A resonance in the conductance spectrum was detected at ~ 40 MHz and a quality factor of ~ 2.1 was calculated from the admittance plot using the following formula:[208]

$$Q = \frac{f_r}{f_H - f_L} \qquad \text{Equation } \mathbf{7\text{-}3}$$

where f_r is the conductance resonance frequency and f_L and f_H are the frequencies at – 6 dB below the peak value; their difference represents the width of the conductance peak at its half height. A clear impedance peak was not detectable, probably because of the large area of the capacitor that was not released (e.g. in the traces and contact pads)..

There are multiple reasons for the disagreement between the resonance characterized dielectrically and the resonance calculated using Equation 7-1. These include the significant

oversimplifications used in the modeling, the residual tensile stresses in the plane of the film generated during the crystallization steps, and the possibility of detecting a higher order harmonic response.[65]

It would be expected that residual stresses would stiffen the structure, therefore increasing the resonance frequency.[206] In order to account for the residual stress state of the diaphragm the following equation should be used:[15]

$$f = \frac{\alpha}{2\pi R}\sqrt{\frac{T}{\rho h}} \qquad \text{Equation } \mathbf{7\text{-}4}$$

where f is the resonance frequency of the diaphragm, α is a vibration mode constant, R is the radius of the diaphragm, h the diaphragm thickness, ρ the diaphragm density and T the initial tension of the diaphragm. Given the different dependence on the radius of equation 7-4 and 7-1, if diaphragms of different diameters were fabricated it would be possible to identify the correct relation describing the geometry dependence of the natural frequency.

7.4.3 In-water Tests

7.4.3.1 Catch-mode Test

During these tests, the MEMS transducer was positioned on the bottom of the water tank facing the M316 transducer. After aligning the two transducers with respect to each other and finding the focal distance, the detected transmitted acoustic signal by the MEMS transducer was recorded and the results are shown in Figure 7-17 for the catch test.

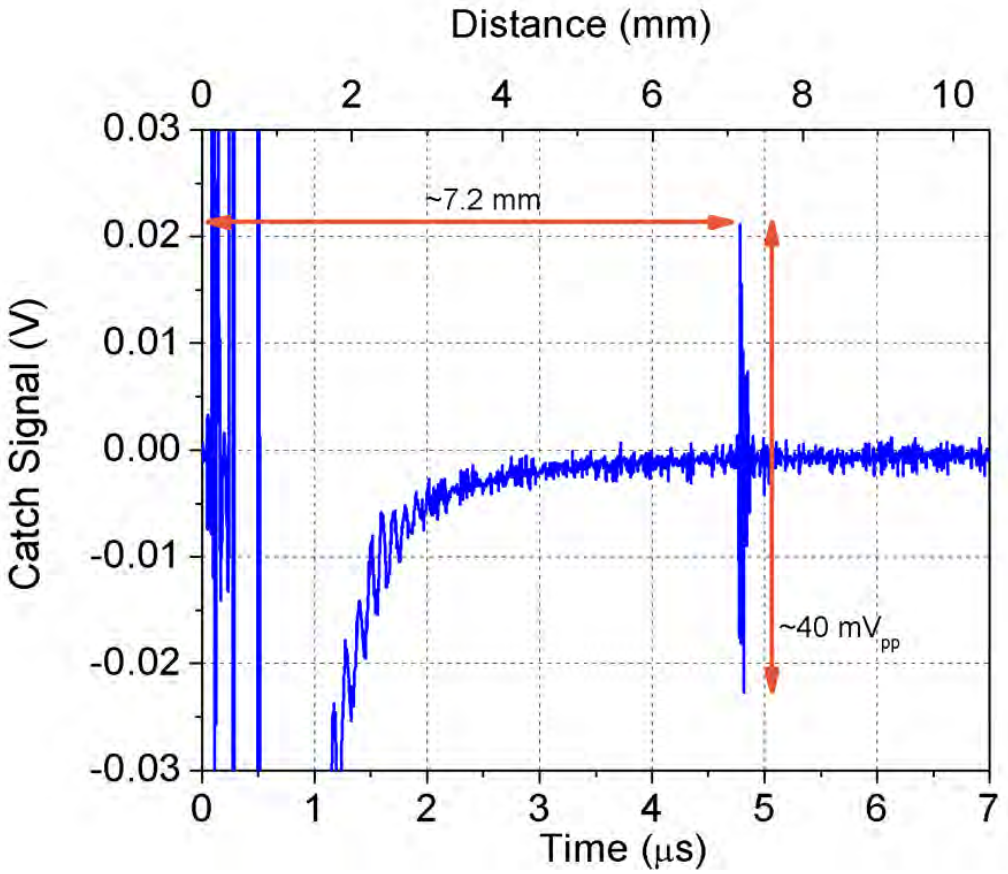

Figure **7-17**: Received signal in catch mode using the fabricated diaphragm transducer.

The received amplified signal in the catch mode was observed at ~ 4.8 μs with a peak-to-peak amplitude of 40 mV (2 mV raw signal). This signal was on the same order of magnitude of the one received with fully released PZT xylophone transducer, 38 mV peak-to-peak, but smaller than the one characterized with partially released PZT xylophone bar transducers, 200 mV peak-to-peak.[198]

7.4.3.2 Pitch-mode Test

In this experiment an external pulse generator was added to the setup to excite the MEMS transducer with ~ 14 V unipolar pulses. The pulse used in the experiment is reported in Figure

7-16. An impedance of 10 Ω was characterized for the tested device at 40 MHz. The impedance mismatch with the front-end electronics will degrade the energy transfer between the source and the load.

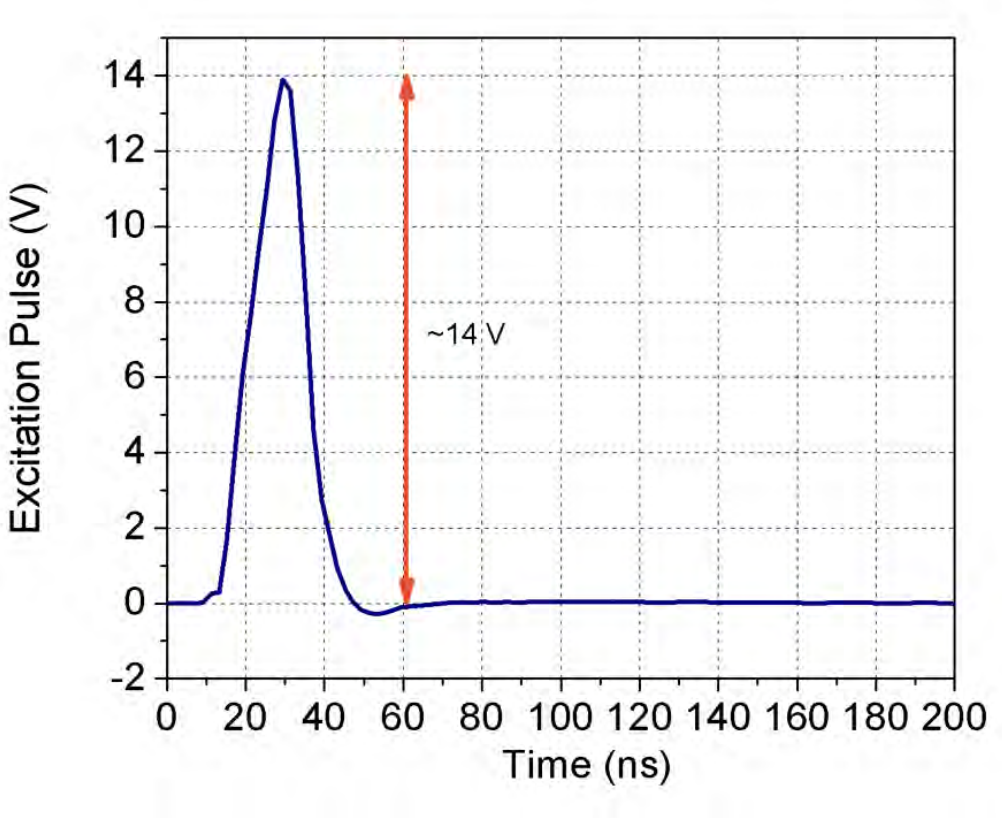

Figure **7-18**: Unipolar excitation pulse generated by the external pulser to excite the MEMS transducer.

The fabricated diaphragm transducers generated sound waves and Figure 7-19 shows the received pitch-mode signal collected by the M316 transducer. The collected signal was received after 4.9 μs with a maximum peak-to-peak amplitude of 15 mV (0.75 mV raw signal). The bandwidth of the collected signal was 83 % at – 6 dB as shown in Figure 7-20. The amplitude of this diaphragm transducer's pitch mode signal was greater than those received by PZT

transducers using a xylophone geometry (5 and 13 mV peak-to-peak received signals for the fully and partially released structures respectively).[198]

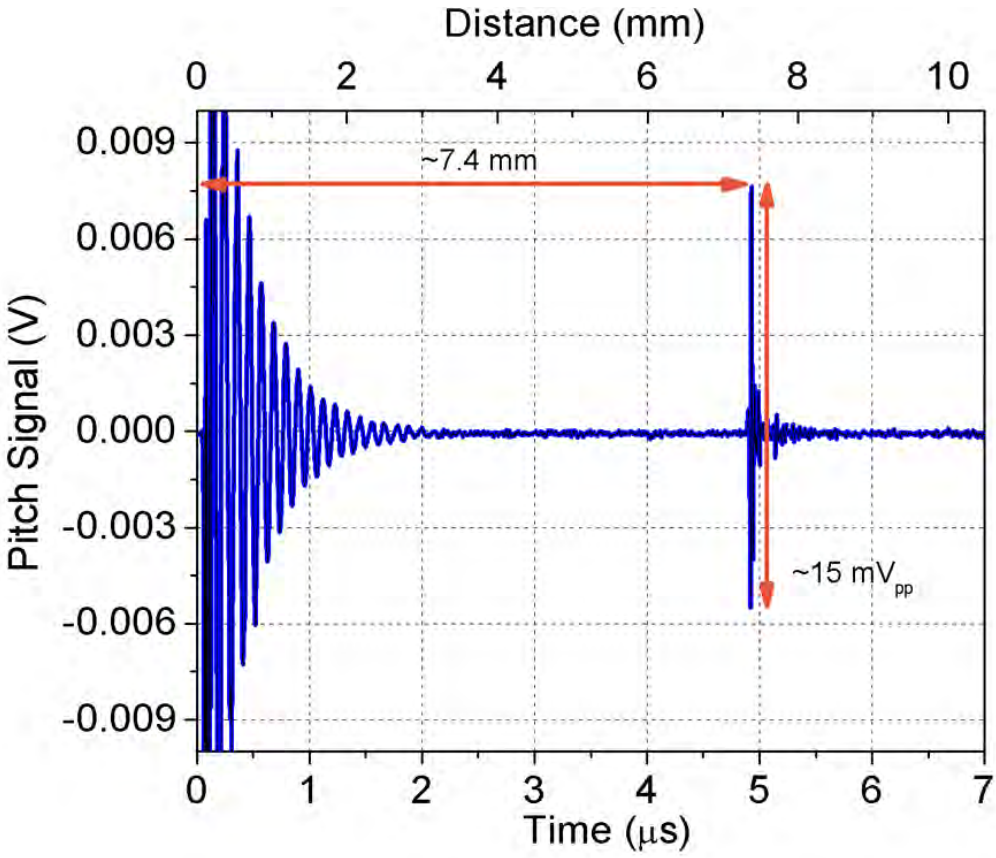

Figure **7-19**: Signal sent by the MEMS transducer and collected by the commercial transducer.

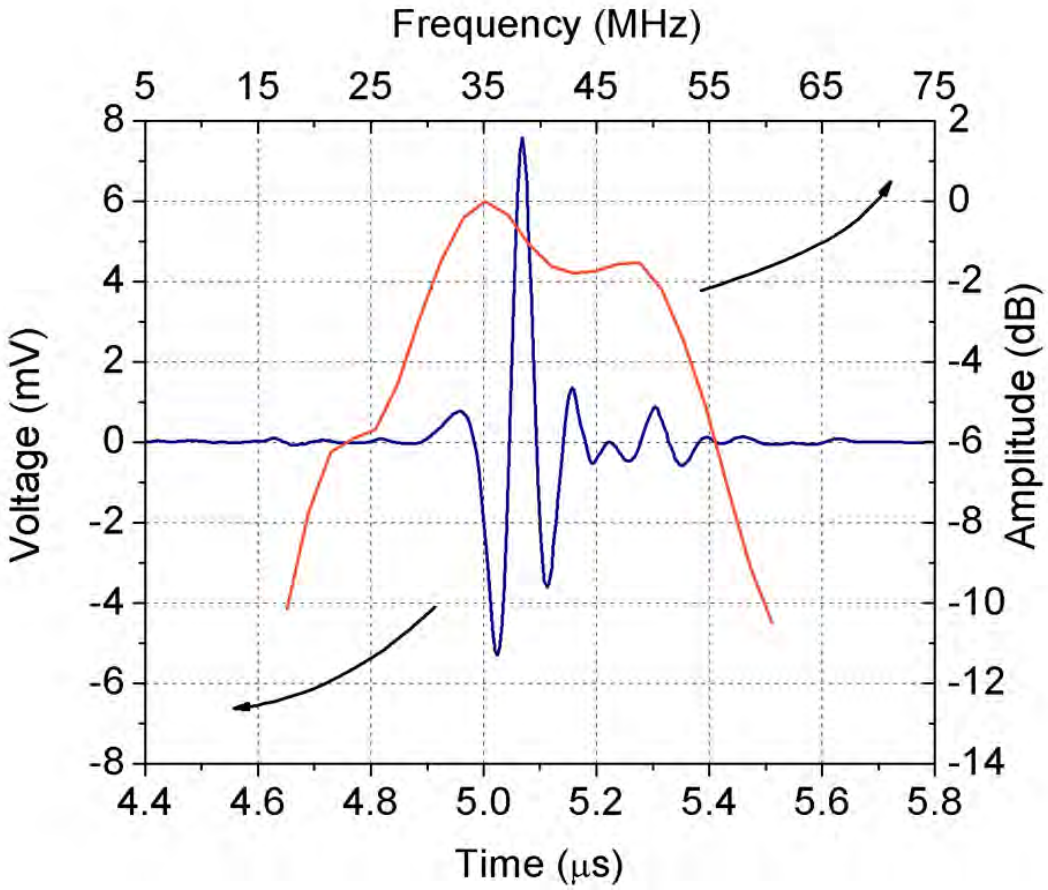

Figure **7-20**: Measured pitch-mode signal and frequency spectrum for the fabricated diaphragm transducer.

The calculated bandwidth of 32.4 MHz for a center frequency of 39.3 MHz represents the band of frequencies in which the output acoustic amplitude is within 6 dB of its peak value at resonance, when a constant voltage (independent of frequency) is applied to the transducer.

Previous work from Kim *et al.* showed that MEMS transducer with a xylophone geometry had bandwidths of 60 % in pitch and pitch-catch mode test when optimal device alignment was achieved between the transducer and the target.[175,198] Those devices had an output sound pressure per voltage of 0.6 kPa/V, which is relatively small if compared to MEMS transducers operating in the d_{33} mode.[13]

The geometry investigated in this work should enable a more efficient sound projection because of the larger actuating area if compared to the xylophone design. Therefore higher values of sound pressure output are expected. In the future, optimized geometries should be employed to maximize the projected sound and the receive sensitivity. In addition, timed excitation of the array should be used to amplify and steer the acoustic signal.

7.5 Conclusions

An ultrasonic hydrophone transducer array with a diaphragm geometry was designed and fabricated. The fabrication approach included a top-down etch of the Si using XeF_2 to generate cavities beneath the active area. Admittance spectra showed a resonance at 42 MHz with a quality factor Q of 2.1. In-water test demonstrated the functionality of the fabricated structures with signals received after 7.4 mm in water launched by a commercial transducer in catch-mode test and a transmitted signal collected by a commercial transducer with a peak-to-peak amplitude of 15 mV and a bandwidth of 83 %.

Chapter 8

Conclusions and Future Work

8.1 Conclusions

This thesis intended to study the effects of crystalline quality, grain size and mechanical boundaries on the dielectric and piezoelectric properties of PZT-based thin films across length scales. The knowledge gained from the characterization helped to define processing routes to optimize the properties of PZT based thin films for MEMS applications. Ultimately, the functionality of a diaphragm high frequency transducer array was demonstrated in water using {001} textured PZT thin films.

8.1.1 Synthesis and Properties of Lead Nickel Niobate – Lead Zirconate Titanate Thin Films

The large transverse piezoelectric coefficient, high dielectric constant and relatively high T_{max} (~200 ºC) make $(0.3)Pb(Ni_{0.33}Nb_{0.67})O_3$-$(0.7)Pb(Zr_{0.45}Ti_{0.55})O_3$ a candidate for applications in MEMS sensors and actuators. In this work it was shown that fluxing of PNN enhances the mass transport and grain growth. It was proven that larger average grain sizes enable larger extrinsic contributions to the dielectric properties and higher transverse piezoelectric coefficient $e_{31,f}$. This suggests that grain boundaries can act as pinning sites, hindering the domain wall mobility. Since many PZT-based thin films have grain sizes in the 50 – 200 nm range, they can be particularly susceptible to a reduction of the extrinsic contributions to the properties. Improved control of nucleation in PZT-based films could ultimately increase the domain wall mobility and so increase the piezoelectric response for actuators applications.

8.1.2 Mapping Piezoelectric Nonlinearity Regime Using Band Excitation Piezoresponce Force Microscopy

The majority of nonlinearity measurements of dielectric and piezoelectric response probe the interaction of domain walls or phase boundary motion at a macroscopic scale. The need for a technique capable of distinguishing the impact of different factors influencing the domain wall mobility (grain boundaries, dislocations or stresses just to name a few) motivated the optimization of band excitation piezoresponse force microscopy (BE-PFM) to map *locally* the piezoelectric nonlinearity. It was found that nonlinear surface-cantilever tip interactions (called dynamic nonlinearities) interfere with quantification of the material nonlinearity. In order to minimize the dynamic nonlinearities, a mix of chirp – sinc excitation signal tailored specifically for different samples had to be used.

8.1.3 Composition Dependence of Local Piezoelectric Nonlinearities in $(0.3)Pb(Ni_{0.33}Nb_{0.67})O_3$-$(0.7)Pb(Zr_xTi_{1-x}O_3)$ Films

The PNN-PZT composition ceramics belong to the relaxor-normal ferroelectric ceramic family and are often the material of choice for bulk ceramic piezoelectrics. *Local* probing of nonlinearities in a model ferroelectric system was made possible by epitaxial growth of PNN-PZT thin films on $SrTiO_3$ substrates to eliminate the influence of large-angle grain boundaries. By varying the Zr/Ti ratio, three compositions from representative regions of the PNN-PZT phase diagram (tetragonal, MPB and rhombohedral) were studied.

A clear composition dependence on the degree of nonlinearity was observed in global dielectric and *local* piezoelectric measurements. In particular, the irreversible dielectric Rayleigh coefficient α_ε for the tetragonal sample was 1/3 as large as those observed for the rhombohedral and MPB samples. A similar trend was observed for the piezoelectric nonlinearity.

A logarithmic frequency dependence of the dielectric Rayleigh parameters was observed. Progressively larger frequency dispersion was observed for the MPB, rhombohedral, and tetragonal samples. This suggests that a larger population of domain walls may respond at higher frequencies to the exciting field in MPB and rhombohedral samples with respect to the tetragonal. *Local* piezoelectric nonlinearity maps showed the formation of clusters with higher nonlinear activity in the MPB and rhombohedral samples.

The higher nonlinearity of the rhombohedral and MPB samples was interpreted in terms of the higher number of spontaneous polarization directions and smaller spontaneous strain associated with the ferroelectric distortion. The broader distribution of $\alpha_d / d_{33,init}$ collected *locally* on these two samples (relative to the tetragonal sample) was consistent with a smaller volume of material generating the collected information, as expected from strain anisotropy.

8.1.4 Grain Size and Substrate Clamping Effects on Local Piezoelectric Nonlinearity in Lead Zirconate Titanate Thin Films

Global dielectric and *local* piezoelectric nonlinearities were analyzed as a function of grain size and mechanical boundary conditions in ~ 1 μm thick $\{001\}$ oriented MPB PZT films. As expected, a grain size effect was noticed in the global Rayleigh coefficients characterized dielectrically, with a 68 % change in $\alpha_\varepsilon / \varepsilon_{init}$ when the grain size and thickness increased. However, the global dielectric changes did not correlate with obvious differences in the scale of correlated motion of domain walls in maps of *local* nonlinear piezoelectric response collected using BE-PFM.

A larger frequency dispersion of the irreversible dielectric Rayleigh parameters was noticed for fully clamped PZT capacitors. In contrast, higher α_ε values were characterized at high frequency for the partially released capacitors, suggesting that a larger population of domain

walls can contribute at higher frequencies when the PZT is partially released from the Si substrate.

A more dramatic change in the Rayleigh parameters was observed when the in-plane stresses were removed by inducing the formation of radial cracks. A six fold increase in α_ε was calculated going from 20.5 ± 2.5 cm/kV up to 147.7 ± 4.4 cm/kV for the intact and broken structures respectively.

A remarkable difference in the length scale of domain wall motion was observed in the regions of the film released from the Si substrate, with a greater spatial average and narrower standard deviation for the *locally* collected $\alpha_d / d_{33,init}$ values compared to the clamped region. These results offer a quantitative evaluation of the effect of substrate clamping both on the frequency dispersion of extrinsic contributions to the properties and the *local* piezoelectric nonlinearities. More generally, the conclusions from this study could be extended to other systems where ferroelastic domains are present, such as ferromagnetic, shape-memory alloys and martensites.

8.1.5 Fabrication of MEMS Diaphragm Transducer Arrays Using {001} Textured PZT Thin Films

MEMS diaphragm high frequency transducer prototypes were fabricated using surface micromachining techniques. The approach chosen involved the release of the Si beneath the diaphragms from the top-side of the wafer using a XeF_2 isotropic etch. The hole that allowed access to the Si substrate from the top of Pt/PZT/Pt/Ti/SiO_2/Si stack was subsequently sealed with a protective dry resist film, Dupont MX5000C^{TM}.

The functionality of the MEMS transducer was demonstrated by performing pitch and catch-mode tests in water. In the catch-mode test, the signal was generated by a commercial

transducer and it was received by the MEMS transducer at a distance of 7.2 mm with a peak-to-peak amplitude of 40 mV with a 26 dB gain. In the pitch-mode test a transmitted signal launched by the MEMS device was collected after 7.4 mm by a commercial transducer with a peak-to-peak amplitude of 15 mV and a bandwidth of 83 %.

8.2 Recommendations for Future Work

BE-PFM is a valuable tool that significantly expanded the capabilities to explore nonlinearities in piezoelectric thin films. The technique allows one to probe the extent of domain wall motion for several piezoelectric samples with good spatial resolution. Some of the recommendations for future work describe possible improvements to the experiments and additional investigations exploiting the potential of BE-PFM to confirm or further the theories proposed in this thesis.

The sample geometry analyzed using BE-PFM in this work is that of a capacitor structure. Having demonstrated that quantitative nonlinearity measurements are possible, it is now appropriate to consider experiments on model capacitor structures, including those probe specific tilt boundaries or regions were the PZT had been released from the underlying substrate. Ideas on how to improve the signal detection will be discussed.

Recommendations on an improved design of the diaphragm transducer prototype will follow.

8.2.1 Discriminating the Influence of Specific Defects on Collective Domain Wall Dynamics

Many defects influence the domain wall mobility. Given the potential of BE-PFM to spatially map the piezoelectric nonlinearities, experiments were designed to quantify the role of

specific defects on the nonlinearities. Initial experiments along these lines were conducted to probe domain wall motion across isolated grain boundaries. For this purpose, epitaxial MPB PNN-PZT and PZT films were prepared on commercially available {001} $SrTiO_3$ single crystals and bi-crystal substrates (MTI Corp. Richmond, CA). The samples were prepared via sol-gel and PLD deposition. The non-linear behavior as function of the degree of tilt across the single and well-defined "grain boundary" was probed for samples deposited on 7º, 15º and 24º tilt boundaries.

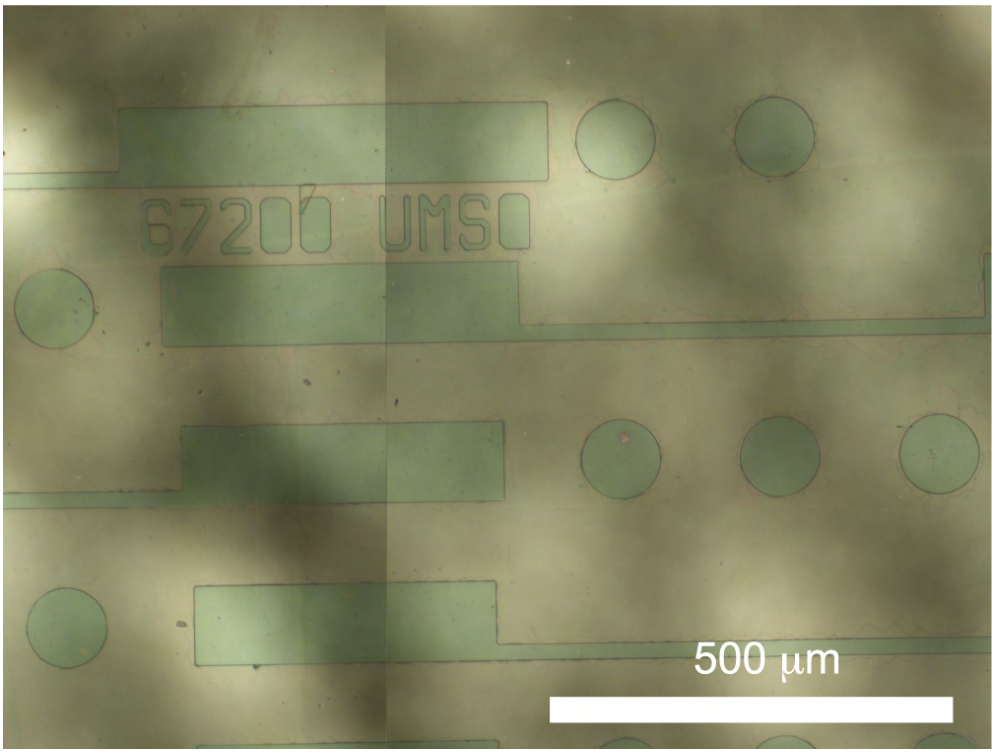

Figure **8-1**: Optical microscopy image using polarized lenses of the bicrystal boundary and patterned photoresist, before sputtering the Pt top electrode. The lighter regions are the PZT surface.

Pt electrodes designed for this set of experiments were deposited on the surface of the samples via photolithography lift-off method as in Figure 8-1. The electrodes allowed easy

access to the tilt boundary for the PFM cantilever and a large pad to facilitate wire-bonding. The collected data did not show meaningful differences in the tilt boundary area. It is speculated that the topographic roughness complicated the detection of small changes in the piezoresponse amplitude at the boundary. Also the small domain sizes for the MPB PNN-PZT samples complicated the task. One way to minimize the artifacts associated with surface roughness would be to perform a chemical mechanical polish of the surface of the deposited films.

If the conditions of a sufficiently smooth surface to decouple topographic cross-talk are met, BE-PFM maps of nonlinearity could be correlated with maps of amplitude of the piezoresponse. Such an experiment could possibly shed light on the interaction of specific angle grain boundary and domain wall cascade. It is recommended that experiments of this type be conducted on thin films with well-defined domain structures.

8.2.2 Local Nonlinearity on Released PZT Thin Films

The geometry utilized to probe the *local* nonlinearity on PZT thin films released from the substrate was a diaphragm with a circular hole in the center. It would be of interest to add a mathematical description to the observed phenomena. To simplify the boundary conditions for the model, it would be beneficial to collect maps of *local* nonlinear piezoelectric response on a simple structure, where the natural frequencies can be predicted with more precision. An example could be a beam clamped to the Si substrates at both ends. Such a geometry could be fabricated adopting a similar top-down approach as the one used to release the diaphragms. By choosing a specific aspect ratio, it should be possible to identify the resonance modes and account for the possible contributions during the BE PFM measurements

8.2.3 Additional Characterization Using Band Excitation Method

By applying the same amplitude modulation to the conducting probing tip and the top electrode layer, it is possible to minimize electrostatic forces and obtain a homogenous electric field in the ferroelectric capacitor. This enables a quantitative analysis of the field dependence of the piezoelectric response. *Local* measurements of domain wall dynamics in the Rayleigh regime provide valuable information on the influence of *local* defect structures and mechanical boundary conditions on the piezoelectric nonlinearity. It would be of great interest to couple other applications of the band excitation method to study related phenomena as described below.

8.2.3.1 BE Switching Spectroscopy PFM

The information collected using an amplitude modulation of the excitation function to obtain *local* piezoelectric nonlinearity maps could be correlated to maps of the same region using a switching waveform (Figure 8-2, where the voltage scales extends to voltages higher than the coercive field). In this case information on the initial piezoresponse, imprint, work of switching and switchable polarization could be correlated to the domain wall mobility at low field to see if regions of the material that show a large domain wall activity in the sub-switching regime can act as nucleation sites for the nucleation and growth of domains.

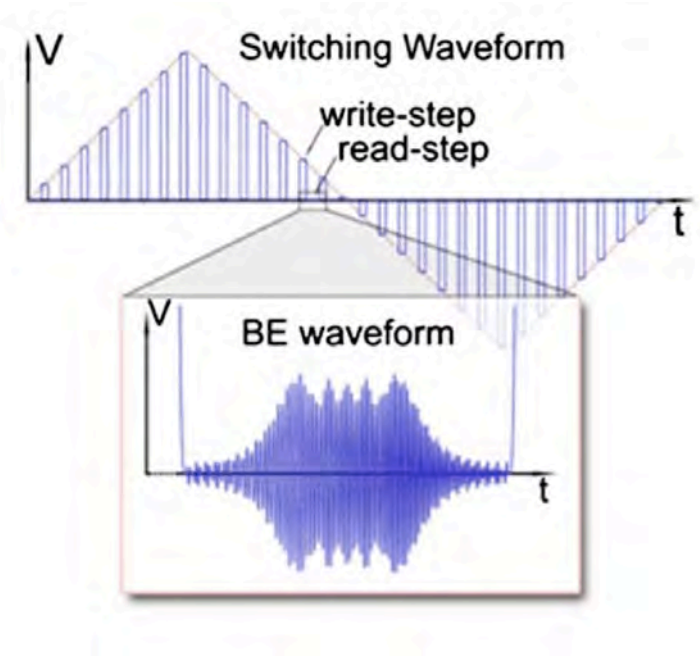

Figure **8-2**: Schematic of typical train of DC and BE pulses in BE switching spectroscopy PFM.[18]

8.2.3.2 Fatigue, Minor Loops and Piezoelectric Nonlinearity

Preliminary analysis using on-pulse reading of piezoresponse evidenced the presence of fat minor loops in regions with lower $\alpha_d / d_{33,init}$ as shown in section 6.4.3.1. It would be of interest to further investigate the origin of such behavior. A possible experiment would involve cycling the ferroelectric capacitors through polarization reversal cycles (< 10^5 cycles) using short pulses at voltage levels higher than the coercive field. This is a typical treatment for rejuvenation of imprinted capacitors.[209] Collecting another high resolution map of piezoelectric nonlinearity after the application of the cycles could enable the detection of changes in the position and shape of higher nonlinear $\alpha_d / d_{33,init}$ regions and *local* minor loop shape related to the distribution of randomly oriented defect dipoles.

8.2.3.3 Dynamic PFM

Another possible set of measurements that switching spectroscopy coupled to BE PFM can enable is the study of aging at a *local* scale in ferroelectric capacitors. This technique is referred to as dynamic switching spectroscopy piezoresponse force microscopy.[210] Preliminary work was done on cracked ferroelectric capacitors, in which cracks propagated perpendicular to the substrate surface without causing the capacitors to short. By collecting multiple piezoelectric hysteresis loops as a function of the delay time, it is possible to study the kinetics of relaxation mechanisms from the piezoresponse loops. It would be useful to develop an understanding of how aging correlates with specific mechanical boundary conditions.

8.2.4 Transducer Design Implementation and Characterization

The prototype 1-D transducer array design for this research did not include an insulating layer between the wire-bond contact pads and the resonating regions. This prevented the clear observation of a resonance peak in the impedance sweeps (due to the large parasitic capacitance). By adding an extra silicon nitride deposition and patterning step after the dry etch patterning of the top electrode features, it could be possible to reduce the contributions generated by the clamped region of the PZT.

After the deposition and patterning of silicon nitride, fan-out wiring connecting the PZT top electrode and the contact pads could be sputter deposited using Cr-Au, which provides a better adhesion for wire-bonding.

The design of efficient high frequency transducers requires careful matching of the electrical impedance of the transducer to that of the driving and receiving circuitry. The insertion loss over the bandwidth of transducer operation should be characterized.

Appendix A

MATLAB Code for PFM Data Interpretation

The following is a collection of MATLAB code for the interpretation of PFM data. A brief description of the code will be provided at the beginning of each section

A.1 Code to Plot Quadratic, Linear and Offset Maps from $A_{max}(x,y,\omega,V_{ac})$

The following is a general code that perform a second order polynomial fit on the values of A_{max} obtained from the SHO fit of raw data (see section 4.3.1). The code can be easily applied to any data fitted using the BEPS graphic user interface (GUI) provided by CNMS to obtain SHO fits from values of amplitude and phase as a function of frequency and position. The suffix _1 refers to positive frequency sweeps and the suffix _2 refers to negative frequency sweeps.

```
clear all

file_path =
'F:\Flavio1210\FGEPIPNNPZT_09\5mic_highres_2Vsetpoint_5%pv_0001_d';
file_name = '5mic_highres_2Vsetpoint_5%pv_0001';
fit_suffix = 'SHO_fit';

load([ file_path '\' file_name ])
load([ file_path '\' file_name '_' fit_suffix ])
[num_rows,num_cols,num_steps,num_coefs] = size(coef_mat4);

amp_mat3 = coef_mat4(:,:,:,1);

% include_vec is the voltage modulation for a single frequency sweep

include_vec = 1 : num_steps/2;

for k1 = 1 : num_rows
```

```
for k2 = 1 : num_cols

amp_vec_1 = squeeze(amp_mat3(k1,k2,1:num_steps/2));
amp_vec_2 = squeeze(amp_mat3(k1,k2,num_steps/2+1:end));
Vac_1 = dc_amp_vec_full(1:num_steps/2);
Vac_2 = dc_amp_vec_full(num_steps/2+1:end);

p_1(k1,k2,:) = polyfit(Vac_1(include_vec),amp_vec_1(include_vec)',2);
p_2(k1,k2,:) = polyfit(Vac_2(include_vec),amp_vec_2(include_vec)',2);

end
end

title_cell = { 'quadratic' ; 'linear' ; 'offset' };
figure(1)
clf

% The following plots the quadratic, linear and offset components

for k1 = 1 : 3

p_mean1 = mean(p_1(:,:,k1));
p_mean2 = mean(p_2(:,:,k1));

p_std1 = std(p_1(:,:,k1),1,1);
p_std2 = std(p_2(:,:,k1),1,1);

caxis_min = min([ p_mean1- 1*p_std1 p_mean2- 1*p_std2 ]);
caxis_max = max([ p_mean1+ 1*p_std1 p_mean2+ 1*p_std2 ]);

subplot(3,2,k1*2-1)
imagesc(p_1(:,:,k1))
colorbar
axis off
title([ title_cell{k1} ' 1' ])
caxis([caxis_min caxis_max]);

subplot(3,2,k1*2)
imagesc(p_2(:,:,k1))
colorbar
axis off
title([ title_cell{k1} ' 2' ])
caxis([caxis_min caxis_max]);

end

m1 = p_1(2:end,:,1)./p_1(2:end,:,2)/10*thickness*2;
m_mean1 = mean(mean(m1))
m_std1 = std(reshape(m1,numel(m1),1));

m2 = p_2(2:end,:,1)./p_2(2:end,:,2)/10*thickness*2;
m_mean2 = mean(mean(m2))
```

```
m_std2 = std(reshape(m2,numel(m2),1));


caxis_min = min([ m_mean1-2*m_std1 m_mean2-2*m_std2 ]);
caxis_max = max([ m_mean1+2*m_std1 m_mean2+2*m_std2 ]);


% The following plots alpha/d33,init maps

figure(2)
clf
imagesc(m1)
axis off
title([texlabel('alpha')'/d_3_3_,_i_n_i_t 1,mean = 'num2str(m_mean1)])
caxis([ caxis_min caxis_max ])
colormap(jet)
colorbar
axis image


figure(3)
clf
imagesc(m2)
axis off
title([texlabel('alpha')'/d_3_3_,_i_n_i_t 1,mean = 'num2str(m_mean2)])
caxis([ caxis_min caxis_max ])
colormap(jet)
colorbar
axis image


% The following is frequency histogram of the spatial alpha/d33,init

m = (m1 + m2)/2;


figure(4)

m1D = reshape(m,numel(m),1);
for k1 = 1 : 100

inc = (max(m1D)- min (m1D))/100;
edges (k1,:) = min(m1D) + (k1-1)*inc;
edgesc = edges';

end

hist(m1D,edgesc)
[N,X] = hist(m1D,edgesc);
N = N';
X = X';
h = findobj(gca,'Type','patch');
set(h,'FaceColor','r','EdgeColor','b')
```

```
title( ['Frequency Histogram' ])
ylabel('Absolute Frequency');
xlabel([ texlabel('alpha') '/d_3_3_,_i_n_i_t']);
```

A.2 Code to Plot Resonance Frequency ω_o, Quality Factor and Standard Deviation of $\omega_o(V_{ac})$

The following code plots the resonance frequency, quality factor and standard deviation of the resonance frequency as a function of voltage. The latter is useful to quickly identify influences of dynamic nonlinearities to the measurement (see chapter 4).

```
res_mat3 = coef_mat4 (:,:,:,2);
q_mat3 = coef_mat4 (:,:,:,3);


for k1 = 1 :num_rows
for k2 = 1 : num_cols

res_vec_1 = squeeze(res_mat3(k1,k2,1:num_steps/2));
res_vec_2 = squeeze(res_mat3(k1,k2,num_steps/2+1:end));
mean_res_1(k1,k2) = mean(res_vec_1);
mean_res_2(k1,k2) = mean(res_vec_2);
std_res_1(k1,k2) = std(reshape(res_vec_1,1,numel(res_vec_1)));
std_res_2(k1,k2) = std(reshape(res_vec_2,1,numel(res_vec_2)));
end
end

for k1 = 1 :num_rows
for k2 = 1 : num_cols

q_vec_1 = squeeze(q_mat3(k1,k2,1:num_steps/2));
q_vec_2 = squeeze(q_mat3(k1,k2,num_steps/2+1:end));
q_res_1(k1,k2) = mean(q_vec_1);
q_res_2(k1,k2) = mean(q_vec_2);
q_res_1(k1,k2) = std(reshape(q_vec_1,1,numel(q_vec_1)));
q_res_2(k1,k2) = std(reshape(q_vec_2,1,numel(q_vec_2)));
end
end

m_mean_res_1 = mean(mean(mean_res_1));
std_mean_res_1 = std(reshape(mean_res_1,numel(mean_res_1),1));
m_mean_res_2 = mean(mean(mean_res_2));
std_mean_res_2 = std(reshape(mean_res_2,numel(mean_res_2),1));


caxis_min = min([ m_mean_res_1- 5*std_mean_res_1 m_mean_res_2-
5*std_mean_res_2 ]);
```

```
caxis_max = max([ m_mean_res_1+ 5*std_mean_res_1 m_mean_res_2+
5*std_mean_res_2 ]);

figure(1)
clf
imagesc(mean_res_1*1000)
colorbar
set(colorbar,'fontsize',20);
title('Resonance Map 1, Colorbar in kHz');
caxis([caxis_min*1000 caxis_max*1000])
axis image
axis off

figure(2)
clf
imagesc(q_res_1)
colorbar
set(colorbar,'fontsize',20);
title('Quality Factor 1');
axis off

figure(3)
clf
imagesc(mean_res_2*1000)
colorbar
set(colorbar,'fontsize',20);
title('Resonance Map 2, Colorbar in kHz');
caxis([caxis_min*1000 caxis_max*1000])
axis image
axis off

figure(4)
clf
imagesc(q_res_2)
colorbar
set(colorbar,'fontsize',20);
title('Quality Factor 1');
axis off

figure(5)
clf
imagesc(std_res_1)
axis off
title('Resonance Map 1, Standard Deviation')
colormap(jet)
colorbar
axis off

figure(6)
clf
imagesc(std_res_2)
axis off
title('Resonance Map 2, Standard Deviation')
colormap(jet)
```

```
colorbar
axis off
```

A.3 Graphic User Interface to Extract Descriptive Statistic Data on Spatial Distributions of $\alpha_d / d_{33,init}$

This code generates a GUI to select specific area of a map and plot the average $A_{max}(V_{ac})$, $\omega_0(V_{ac})$ and frequency histograms of $\alpha_d / d_{33,init}$ over the selected area. Quadratic, linear and offset fits are from the code in section A.1 are required as input. They can be saved in the file 'data.mat' by using the following line at the end of the code in section A.1.

```
save([ file_path '\data.mat'],'Vac_1','Vac_2','amp_mat3','p_1','p_2');
```

The following is the code that generates the GUI

```
function nl_viewer

clear all
close all

global filter_index

load_nl_data

if filter_index

    make_figure
    make_panel
    make_buttons
    make_caxis_cont
    plot_on_axis
end

end

function load_nl_data

global p_1 p_2 error_mat1 error_mat2 amp_mat3 Vac_1 Vac_2...
    load_dir load_name filter_index res_mat3

[load_name_temp, load_dir_temp, filter_index] =
uigetfile({'*.mat'},'load non linear fit results',load_dir);
```

```
if filter_index
    load_name=load_name_temp;
    load_dir=load_dir_temp;

    load(fullfile(load_dir,load_name))

end

end

function make_figure

global figure_main

sr_dim=get(0,'ScreenSize');

figure_main = figure(1);
clf(figure_main);

mx_siz = min(sr_dim(3:4));
mx_ind = find(sr_dim(3:4)==min(sr_dim(3:4)),1);

if mx_ind==3
    pos_vec=[mx_siz*.1 (sr_dim(4)-(mx_siz))/2 mx_siz*.8 mx_siz];
else
    pos_vec=[(sr_dim(3)-(mx_siz))/2 mx_siz*.1 mx_siz mx_siz*.8];
end

set(figure_main,'Position',pos_vec)

end

function make_panel

global figure_main cont_panel ax_panel ax_main cax_panel

%% control panel

cont_wid=.2;

cont_panel = uipanel('parent',figure_main,...
    'units','normalized',...
    'position',[0 0 cont_wid 1]);
%% caxis control

cax_h=.05;

cax_panel = uipanel('parent',figure_main,...
    'units','normalized',...
    'position',[cont_wid 0 1-cont_wid cax_h]);
```

```
%% axes panel
ax_panel = uipanel('parent',figure_main,...
    'units','normalized',...
    'position',[cont_wid cax_h 1-cont_wid 1-cax_h]);

ax_main=axes('parent',ax_panel,...
    'units','normalized',...
    'position',[0 0 1 1]);



end

function make_buttons

global cont_panel thickness cur_plot name_vec

but_h=.025;
but_off=.025;
thickness=1;
cur_plot=1;
name_vec={'\alpha/d_{33,init}','quadratic/linear 1','quadratic/linear
2','quadratic 1','linear 1','offset 1','quadratic 2','linear 2','offset
2'};

k=1;

uicontrol('parent',cont_panel,...
    'style','push',...
    'string','load_new_data',...
    'units','normalized',...
    'position',[.1 1-k*(but_h+but_off) .8 but_h],...
    'callback',@load_new_nl_data,...
    'visible','on')

k=k+1;

uicontrol('parent',cont_panel,...
    'style','popupmenu',...
    'string',name_vec,...
    'units','normalized',...
    'position',[.1 1-k*(but_h+but_off) .8 but_h],...
    'callback',@change_plot,...
    'visible','on')

k=k+1;

uicontrol('parent',cont_panel,...
    'style','push',...
    'string','select points',...
    'units','normalized',...
    'position',[.1 1-k*(but_h+but_off) .8 but_h],...
```

```
    'callback',@select_points,...
    'visible','on')

k=k+1;

uicontrol('parent',cont_panel,...
    'style','push',...
    'string','select_area',...
    'units','normalized',...
    'position',[.1 1-k*(but_h+but_off) .8 but_h],...
    'callback',@select_area,...
    'visible','on')

k=k+1;

uicontrol('parent',cont_panel,...
    'style','text',...
    'string','thickness',...
    'units','normalized',...
    'position',[.1 1-k*(but_h+but_off) .8 but_h],...
    'visible','on')

k=k+1;

uicontrol('parent',cont_panel,...
    'style','edit',...
    'string',num2str(thickness),...
    'units','normalized',...
    'position',[.1 1-k*(but_h+but_off) .8 but_h],...
    'callback',@change_thickness,...
    'visible','on')


end

function make_caxis_cont

global cax_panel main_caxis

uicontrol('parent',cax_panel,...
    'style','slider',...
    'units','normalized',...
    'position',[0 .5 1 .5],...
    'min',-1,...
    'max',1,...
    'value',1,...
    'userdata',2,...
    'callback',@caxis_cont_move,...
    'visible','on')

uicontrol('parent',cax_panel,...
    'style','slider',...
```

```
    'units','normalized',...
    'position',[0 0 1 .5],...
    'min',-1,...
    'max',1,...
    'value',-1,...
    'userdata',1,...
    'callback',@caxis_cont_move,...
    'visible','on')

main_caxis=[-1,1];

end

function load_new_nl_data(source_info,event_info)

global p_1 p_2 error_mat1 error_mat2 amp_mat3 Vac_1 Vac_2...
    load_dir load_name filter_index res_mat3

[load_name_temp, load_dir_temp, filter_index] =
uigetfile({'*.mat'},'load non linear fit results',load_dir);

if filter_index
    load_name=load_name_temp;
    load_dir=load_dir_temp;

    load(fullfile(load_dir,load_name))
    plot_data_in
end

end

function select_points(sourcee_info,event_info)

global ax_main figure_main


set(figure_main,'pointer','fullcrosshair');
hold(ax_main,'on')
pl=get(ax_main,'children');
c_data=get(pl(end),'CData');

xy_corr=[];
but_out=1;
while but_out~=3;
    waitforbuttonpress
    temp=get(ax_main,'currentpoint');

    button = get(figure_main, 'SelectionType');
    if strmatch(button,'alt')
        but_out = 3;
    else
        but_out = 1;
```

```
    end

    if but_out~=3;
        if temp(1,3)==1
            point_out(2)=temp(1,2);
            point_out(1)=temp(1,1);

            xy_corr(:,end+1)=point_out;


plot(temp(1,1),temp(1,2),'kx','markersize',10,'linewidth',2,'parent',ax
_main);
        end

    end
end

set(figure_main,'pointer','arrow')
hold(ax_main,'off')
cla(ax_main);
imagesc(c_data,'parent',ax_main)
recaxis_main

make_view_plot(xy_corr)

end

function select_area(sourcee_info,event_info)

global ax_main figure_main


set(figure_main,'pointer','fullcrosshair');
hold(ax_main,'on')
pl=get(ax_main,'children');
c_data=get(pl(end),'CData');

xy_area=[];
but_out=1;
while but_out~=3;
    waitforbuttonpress
    temp=get(ax_main,'currentpoint');

    button = get(figure_main, 'SelectionType');
    if strmatch(button,'alt')
        but_out = 3;
    else
        but_out = 1;
    end

    if but_out~=3;
        if temp(1,3)==1
```

```
            point_out(2)=temp(1,2);
            point_out(1)=temp(1,1);

            xy_area(:,end+1)=point_out;


plot(xy_area(1,:),xy_area(2,:),'k','linewidth',2,'parent',ax_main);
        end

    end
end


[x_mat,y_mat]=meshgrid(floor(min(xy_area(1,:))):ceil(max(xy_area(1,:)))
,floor(min(xy_area(2,:))):ceil(max(xy_area(2,:))));


x_mat=reshape(x_mat,1,numel(x_mat));
y_mat=reshape(y_mat,1,numel(y_mat));

atoms_in_area = inpolygon(x_mat,y_mat,xy_area(1,:),xy_area(2,:));


temp=x_mat(atoms_in_area);
xy_corr(1,1:numel(temp))=temp;
temp=y_mat(atoms_in_area);
xy_corr(2,1:numel(temp))=temp;


set(figure_main,'pointer','arrow')
hold(ax_main,'off')
cla(ax_main);

imagesc(c_data,'parent',ax_main)
recaxis_main

make_view_plot(xy_corr)
end

function change_thickness(source_info,event_info)

global thickness cur_plot

cur_thick=str2double(get(source_info,'string'));

if ~isnan(cur_thick)
    thickness=cur_thick;
    if cur_plot<4
        plot_on_axis
    end
else
```

```
    set(source_info,'string',num2str(thickness));
end

end

function change_plot(source_info,event_info)

global cur_plot
cur_plot=get(source_info,'value');

plot_on_axis

end

function plot_on_axis

global cur_plot ax_main  p_1 p_2 thickness


switch cur_plot
    case 1
        m1=(p_1(:,:,1)./p_1(:,:,2))/10*thickness*2;
        m2=(p_2(:,:,1)./p_2(:,:,2))/10*thickness*2;
        m=(m1 + m2)/2;
    case 2
        m=(p_1(:,:,1)./p_1(:,:,2))/10*thickness*2;
    case 3
        m=(p_2(:,:,1)./p_2(:,:,2))/10*thickness*2;
    case 4
        m=p_1(:,:,1);
    case 5
        m=p_1(:,:,2);
    case 6
        m=p_1(:,:,3);
    case 7
        m=p_2(:,:,1);
    case 8
        m=p_2(:,:,2);
    case 9
        m=p_2(:,:,3);
end
imagesc(m,'parent',ax_main);
recaxis_main

end

function caxis_cont_move(source_info,event_info)

global main_caxis


val=get(source_info,'userdata');
```

```
val2=(abs(val-3));
temp=get(source_info,'value');

if val==1 && temp>main_caxis(val2)
    temp=main_caxis(val2)-.0001;
end

if val==2 && temp<main_caxis(val2)
    temp=main_caxis(val2)+.0001;

end

set(source_info,'value',temp);
main_caxis(val)=temp;

recaxis_main
end

function recaxis_main

global main_caxis ax_main


pl=get(ax_main,'children');
c_data=get(pl(end),'CData');

mx=max(max(c_data));
mn=min(min(c_data));

mn_2=(mx+mn)/2;
mx=mx-mn_2;
mn=mn-mn_2;

mx=mx*main_caxis(2);
mn=mn*-main_caxis(1);

mx=mx+mn_2;
mn=mn+mn_2;

caxis(ax_main,[mn mx]);
end

function make_view_plot(xy_points)

global ax_main cur_plot Vac_1 Vac_2 p_1 p_2 amp_mat3 main_caxis
thickness...
    name_vec load_dir res_mat3


switch cur_plot
    case 1
```

```
        m1=(p_1(:,:,1)./p_1(:,:,2))/10*thickness*2;
        m2=(p_2(:,:,1)./p_2(:,:,2))/10*thickness*2;
        m=(m1 + m2)/2;
        threshold = find(abs(m)>.1);
        m(threshold) = 0;
        m_mean = mean(mean(m));
        m_std = std(reshape(m,numel(m),1));
    case 2
        m=(p_1(:,:,1)./p_1(:,:,2))/10*thickness*2;
    case 3
        m=(p_2(:,:,1)./p_2(:,:,2))/10*thickness*2;
    case 4
        m=p_1(:,:,1);
    case 5
        m=p_1(:,:,2);
    case 6
        m=p_1(:,:,3);
    case 7
        m=p_2(:,:,1);
    case 8
        m=p_2(:,:,2);
    case 9
        m=p_2(:,:,3);
end

fig=figure;

pl=get(ax_main,'children');
c_data=get(pl(end),'CData');

mx=max(max(c_data));
mn=min(min(c_data));

mn_2=(mx+mn)/2;
mx=mx-mn_2;
mn=mn-mn_2;

mx=mx*main_caxis(2);
mn=mn*-main_caxis(1);

mx=mx+mn_2;
mn=mn+mn_2;

ax_1=subplot(3,3,1,'parent',fig,'yticklabel',[],'xticklabel',[]);
imagesc(m,'parent',ax_1)
hold(ax_1,'on')
plot(xy_points(1,:),xy_points(2,:),'kx','markersize',8,'linewidth',2,'p
arent',ax_1);
axis(ax_1,'off')
axis image
caxis([ m_mean-.5*m_std m_mean+.5*m_std ]);
% caxis(ax_1,[mn mx]);
title(ax_1,'area selected','fontsize',20)
```

```
xy_points=ceil(xy_points);

amp_vec_mean_1=[];
fit_res_mean_1=[];
res_vec_mean_1=[];
amp_vec_mean_2=[];
fit_res_mean_2=[];
res_vec_mean_2=[];
data_vec=[];

for k=1:size(xy_points,2)

    num_steps=numel(Vac_1);

    amp_vec =
squeeze(amp_mat3(xy_points(2,k),xy_points(1,k),1:num_steps));
    fit_res =
polyval(squeeze(p_1(xy_points(2,k),xy_points(1,k),:)),Vac_1);
    res_vec =
squeeze(res_mat3(xy_points(2,k),xy_points(1,k),1:num_steps));

    amp_vec_mean_1(:,end+1)=amp_vec;
    fit_res_mean_1(:,end+1)=fit_res;
    res_vec_mean_1(:,end+1)=res_vec;

    amp_vec =
squeeze(amp_mat3(xy_points(2,k),xy_points(1,k),num_steps+1:end));
    fit_res =
polyval(squeeze(p_2(xy_points(2,k),xy_points(1,k),:)),Vac_2);
    res_vec =
squeeze(res_mat3(xy_points(2,k),xy_points(1,k),num_steps+1:end));

    amp_vec_mean_2(:,end+1)=amp_vec;
    fit_res_mean_2(:,end+1)=fit_res;
    res_vec_mean_2(:,end+1)=res_vec;

    data_vec(end+1)=m(xy_points(2,k),xy_points(1,k));

end

ax_2=subplot(3,3,4,'parent',fig);
cla(ax_2)
hold(ax_2,'on')
plot(Vac_1,mean(amp_vec_mean_1,2),'b','parent',ax_2);
plot(Vac_1,mean(fit_res_mean_1,2),'r--','parent',ax_2);
axis(ax_2,'tight')
% set(ax_2,'yticklabel',[],'xticklabel',[])
title(ax_2,{'average amplitude';'sweep up'},'fontsize',16)

ax_3=subplot(3,3,7,'parent',fig);
hold(ax_3,'on')
```

```
plot(Vac_2,mean(amp_vec_mean_2,2),'b','parent',ax_3);
plot(Vac_2,mean(fit_res_mean_2,2),'r--','parent',ax_3);
axis(ax_3,'tight')
% set(ax_3,'yticklabel',[],'xticklabel',[])
title(ax_3,{'average amplitude'; 'sweep down'},'fontsize',16)


ax_5=subplot(3,3,2,'parent',fig);
hold(ax_5,'on')
plot(Vac_1,mean(res_vec_mean_1,2),'b','parent',ax_5);
axis(ax_5,'tight')
% set(ax_5,'yticklabel',[],'xticklabel',[])
title(ax_5,{'resonance frequency'; 'sweep up'},'fontsize',16)

ax_6=subplot(3,3,3,'parent',fig);
hold(ax_6,'on')
plot(Vac_2,mean(res_vec_mean_2,2),'b','parent',ax_6);
axis(ax_6,'tight')
% set(ax_6,'yticklabel',[],'xticklabel',[])
title(ax_6,{'resonance frequency'; 'sweep down'},'fontsize',16)

ax_4=subplot(3,3,[5,6,8,9],'parent',fig);
cla(ax_4)
hold(ax_4,'on')
% if abs(std(data_vec))>0.1
%     hist(data_vec,ceil(numel(data_vec)/5),'parent',ax_4);
% else
%     hist(data_vec,ceil(sqrt(numel(data_vec))),'parent',ax_4);
% end

% if numel(data_vec)>50                     % original from Oleg
%     h_data_y=hist(data_vec,ceil(numel(data_vec)/5),'parent',ax_4);
%     hist(data_vec,ceil(numel(data_vec)/5),'parent',ax_4);
% else

if numel(data_vec)>50
    h_data_y=hist(data_vec,ceil(sqrt(numel(data_vec))),'parent',ax_4);
    hist(data_vec,ceil(sqrt(numel(data_vec))),'parent',ax_4);
else

    h_data_y=hist(data_vec,10,'parent',ax_4);
    hist(data_vec,10,'parent',ax_4);
end
% h_data_x=min(data_vec):(max(data_vec)-
min(data_vec))/(numel(h_data_y)-1): max(data_vec); % original from Oleg
for k1 = 1 : sqrt(numel(data_vec))          % I made the following for
the bins

    inc = (max(data_vec)- min (data_vec))/sqrt(numel(data_vec));
    edges (k1,:) = min(data_vec) + (k1-1)*inc;
    h_data_x = edges';

end
```

```
alphad_mean = mean(data_vec);
alphad_median = median(data_vec);
alphad_std = std(data_vec);
title(ax_4,['hist of area selected in ',name_vec{cur_plot},' Average =
',num2str(alphad_mean),' ± ',num2str(alphad_std)],'FontSize',20)
set(gca,'fontsize',20);

% axis([alphad_mean-3*alphad_std alphad_mean+3*alphad_std ymin ymax]);
% set(h,'FaceColor','r','EdgeColor','w');



%
temp(:,1)=vac;temp(:,2)=mean(amp_vec_mean,2);temp(:,3)=mean(amp_vec_mea
n,2);
%
% temp;


mean_amp_vec_1=mean(amp_vec_mean_1,2);
mean_amp_vec_2=mean(amp_vec_mean_2,2);
mean_fit_res_1=mean(fit_res_mean_1,2);
mean_fit_res_2=mean(fit_res_mean_2,2);

k9=0;
temp=fopen(fullfile(load_dir,'hist_data.mat'));
if temp<0;

save(fullfile(load_dir,'hist_data.mat'),'h_data_x','h_data_y','Vac_1','
Vac_2','mean_amp_vec_1','mean_amp_vec_2','mean_fit_res_1','mean_fit_res
_2','xy_points','m');
else
    while temp>0
        fclose(temp);
        k9=k9+1;

temp=fopen(fullfile(load_dir,['hist_data_',num2str(k9),'_.mat']));
    end

save(fullfile(load_dir,['hist_data_',num2str(k9),'_.mat']),'h_data_x','
h_data_y','Vac_1','Vac_2','mean_amp_vec_1','mean_amp_vec_2','mean_fit_r
es_1','mean_fit_res_2','xy_points','m','alphad_median');
end


end
```

Appendix B

MATLAB Code for Bandwidth Analysis of Signal Amplitude in Transducer Tests

B.1 Loading and Plotting the Received Signal

One-dimension arrays containing the amplitude of the signals recorded using the oscilloscope and the sampling rates are required as input.

```
close all;
clear all;
clc;

load pitchcatch_june23

% ts is the sampling rate

ts = 1.000000000E-08;
fs = 1/ts;
intFactor = 4;
offset =  -1.0000000000000E-05;

time = 0:ts:(ts*length(pitchcatch_june23));
time = time(1:length(pitchcatch_june23)) + offset;

figure(1);
plot(time,pitchcatch_june23);
grid;xlabel('time','fontsize',20);ylabel('voltage','fontsize',20);set(g
ca,'FontSize',16)
title('Original Data Set','fontsize',20);
```

B.2 Bandwidth Calculation

The following code Fourier transforms the collected signal and calculates the bandwidth by letting the user select manually the upper and lower bounds for the amplitude at -6 dB.

```
VoltageBuffer = pitchcatch_june23(2531:2650);
VoltageBufferI = resample(VoltageBuffer,intFactor,1);
TimeBufferI = 0:ts*intFactor:length(VoltageBufferI)*ts*intFactor;
TimeBufferI = TimeBufferI(1:length(VoltageBufferI));
MeanVoltage = mean(VoltageBufferI);
VoltageBufferI = VoltageBufferI - MeanVoltage;
w1 = window(@hamming,length(VoltageBufferI));
VoltageBufferI = VoltageBufferI.*w1;

Figure(2);
plot(TimeBufferI,VoltageBufferI);
grid;xlabel('time','fontsize',20);ylabel('voltage','fontsize',20);
title('Interpolated Data Set','fontsize',20);

L = length(VoltageBufferI);
NFFT = 2^nextpow2(L); % Next power of 2 from length of y
Y = fft(VoltageBufferI,NFFT)/L;
f = (intFactor*fs)/2*linspace(0,1,NFFT/2+1);

SingleSidedSpectrum = 2*abs(Y(1:NFFT/2+1));
MaxSingleSidedSpectrum = max(SingleSidedSpectrum);
SingleSidedSpectrum =
20*log10(SingleSidedSpectrum./MaxSingleSidedSpectrum);

% Plot single-sided amplitude spectrum.
Figure(3);
plot(f./1e6,2*abs(Y(1:NFFT/2+1)));
title('Single-Sided Amplitude Spectrum of y(t)','fontsize',20)
xlabel('Frequency (MHz)','fontsize',20)
ylabel('|Y(f)|','fontsize',20)
grid;

figure(4);
plot(f./1e6,SingleSidedSpectrum);
title('Single-Sided Amplitude Spectrum of y(t)','fontsize',20)
xlabel('Frequency (MHz)','fontsize',20)
ylabel('dB','fontsize',20)
grid;

[ymaxMagnitude, xmaxFrequency] = max(SingleSidedSpectrum);
MagnitudePointer = find(SingleSidedSpectrum > (ymaxMagnitude - 10));
MagnitudeBuffer = SingleSidedSpectrum(MagnitudePointer);
FrequencyBuffer = f(MagnitudePointer);

Figure(5);
plot(FrequencyBuffer./1e6,MagnitudeBuffer);
```

```
title('Single-Sided Amplitude Spectrum of y(t)','fontsize',20)
xlabel('Frequency (MHz)','fontsize',20)
ylabel('dB','fontsize',20)
grid;

%%%%%%%%%%%%%%%%%%%%%%%%%%%%%%%%%%%%%%%%%%%%%%%%%%%%%%%%%%%%%%%%%%%%%%%
% Select Center Peak of Resonance
% This will do the following:
% 1.  Calculates the Magnitude of the Peak in dB by clicking
%     mouse on peak of selected resonance
% 2.  Finds the -6dB down points
% 3.  Remaps the cropped image in Magnitude and Frequency
%%%%%%%%%%%%%%%%%%%%%%%%%%%%%%%%%%%%%%%%%%%%%%%%%%%%%%%%%%%%%%%%%%%%%%%

[minPeak maxPeak] = ginput(1);
MagnitudePointer = find(SingleSidedSpectrum > (maxPeak - 6));
MagnitudeBuffer = SingleSidedSpectrum(MagnitudePointer);
FrequencyBuffer = f(MagnitudePointer);

plot(FrequencyBuffer./1e6,MagnitudeBuffer);
title('Single-Sided Amplitude Spectrum of y(t)','fontsize',20)
xlabel('Frequency (MHz)','fontsize',20)
ylabel('dB','fontsize',20)
grid;

%%%%%%%%%%%%%%%%%%%%%%%%%%%%%%%%%%%%%%%%%%%%%%%%%%%%%%%%%%%%%%%%%%%%%%%
% Select the -6dB down points with mouse
% This will do the following:
% 1.  Calculates the Magnitude of the Peak in dB
% 2.  Finds the -6dB down points by clicking once with the mouse
%     on the lower frequency and then clicking on the higher frequency
% 3.  Remaps the cropped image in Magnitude and Frequency
%%%%%%%%%%%%%%%%%%%%%%%%%%%%%%%%%%%%%%%%%%%%%%%%%%%%%%%%%%%%%%%%%%%%%%%

[minFreq maxFreq] = ginput(2);
Bandwidth = minFreq(2) - minFreq(1);

fo = minFreq(1) + Bandwidth/2;

PercentBandwidth = (Bandwidth/fo)*100;

string1 = ['Bandwidth = ' num2str(Bandwidth) ' MHz'];
string2 = ['fo = ' num2str(fo) ' MHz'];
string3 = ['% Bandwidth = ' num2str(PercentBandwidth) '%'];

zoom on;

plot(FrequencyBuffer./1e6,MagnitudeBuffer);
title('Single-Sided Amplitude Spectrum of y(t)','fontsize',20)
xlabel('Frequency (MHz)','fontsize',20)
ylabel('dB','fontsize',20)
grid;
```

```
%%%%%%%%%%%%%%%%%%%%%%%%%%%%%%%%%%%%%%%%%%%%%%%%%%%%%%%%%%%%%%%%%%%%%%%%
% After you have zoomed into the correct resonance
% Hit the return key to continue
%%%%%%%%%%%%%%%%%%%%%%%%%%%%%%%%%%%%%%%%%%%%%%%%%%%%%%%%%%%%%%%%%%%%%%%%

pause;

%%%%%%%%%%%%%%%%%%%%%%%%%%%%%%%%%%%%%%%%%%%%%%%%%%%%%%%%%%%%%%%%%%%%%%%%
% This will print out the following on the plot:
% 1.  Use the mouse to select the (x,y) position
% 2.  Then click the mouse once and it will display
%     information
%     a.  Bandwidth
%     b.  Center Frequency
%     c.  Bandwidth
%%%%%%%%%%%%%%%%%%%%%%%%%%%%%%%%%%%%%%%%%%%%%%%%%%%%%%%%%%%%%%%%%%%%%%%%

gtext({string1,string2,string3});
```

References

[1] D. I. Woodward, J. Knudsen, and I. M. Reaney, Phys. Rev. B: Condens. Matter **72,** 104110 (2005).

[2] S. Trolier-McKinstry and P. Muralt, J. Electroceram. **12,** 7 (2004).

[3] H. D. Chen, K. R. Udayakumar, C. J. Gaskey, and L. E. Cross, Appl. Phys. Lett. **67,** 3411 (1995).

[4] N. Ledermann, P. Muralt, J. Baborowski, S. Gentil, K. Mukati, M. Cantoni, A. Seifert, and N. Setter, Sens. Actuators, A **105,** 162 (2003).

[5] F. Xu, R. A. Wolf, T. Yoshimura, and S. Trolier-McKinstry, Proc. 11th International Symposium on Electrets (ISE 11)**,** 386 (2002).

[6] R. A. Wolf and S. Trolier-McKinstry, J. Appl. Phys. **95,** 1397 (2004).

[7] C. A. Randall, N. Kim, J. P. Kucera, W. W. Cao, and T. R. Shrout, J. Am. Ceram. Soc. **81,** 677 (1998).

[8] K. K. Park, H. J. Lee, M. Kupnik, O. Oralkan, and B. T. Khuri-Yakub, Proc. 21st IEEE MEMS Conference**,** 339 (2008).

[9] G. G. Yaralioglu, A. S. Ergun, B. Bayram, E. Haeggstrom, and B. T. Khuri-Yakub, IEEE Trans. Ultrason. Ferroelectr. Freq. Control **50,** 449 (2003).

[10] S. E. Park and T. R. Shrout, IEEE Trans. Ultrason. Ferroelectr. Freq. Control **44,** 1140 (1997).

[11] B. Belgacem, F. Calame, and P. Muralt, J. Electroceram. **19,** 369 (2007).

[12] N. Yamauchi, T. Shirai, T. Yoshihara, Y. Hayasaki, T. Ueda, T. Matsushima, K. Wasa, I. Kanno, and H. Kotera, Appl. Phys. Lett. **94,** 172903 (2009).

[13] M. Klee, H. Boots, B. Kumar, C. Van Heesch, R. Mauczok, W. Keur, M. De Wild, H. Van Esch, A. L. Roest, K. Reimann, L. Van Leuken, O. Wunnicke, J. Zhao, G. Schmitz, M. Mienkina, M. Mleczko, and M. Tiggelman, IOP Conference Series: Materials Science and Engineering **8,** 012008 (2010).

[14] M. A. Dubois and P. Muralt, IEEE Trans. Ultrason. Ferroelectr. Freq. Control **45,** 1169 (1998).

[15] E. Hong, S. V. Krishnaswamy, C. B. Freidhoff, and S. Trolier-McKinstry, Sens. Actuators, A **119,** 521 (2005).

[16] M. Lebedev, J. Akedo, and Y. Akiyama, Jpn. J. Appl. Phys., Part 1 **39,** 5600 (2000).

[17] T. Iijima and K. Kunii, Jpn. J. Appl. Phys., Part 1 **40,** 5740 (2001).

[18] S. Guo, O. S. Ovchinnikov, M. E. Curtis, M. B. Johnson, S. Jesse, and S. V. Kalinin, J. Appl. Phys. **108,** 084103 (2010).

[19] Y. B. Jeon, R. Sood, J. H. Jeong, and S. G. Kim, Sens. Actuators, A **122,** 16 (2005).

[20] Q. M. M. Zhang and J. Z. Zhao, IEEE Trans. Ultrason. Ferroelectr. Freq. Control **46,** 1518 (1999).

[21] P. Muralt, R. G. Polcawich, and S. Trolier-McKinstry, MRS Bull. **34,** 658 (2009).

[22] D. W. Wu, Q. F. Zhou, X. C. Geng, C. G. Liu, F. Djuth, and K. K. Shung, IEEE Trans. Ultrason. Ferroelectr. Freq. Control **56,** 2304 (2009).

[23] S. Tadigadapa and K. Mateti, Meas. Sci. Technol. **20,** 30 (2009).

[24] A. Gruverman, H. Tokumoto, A. S. Prakash, S. Aggarwal, B. Yang, M. Wuttig, R. Ramesh, O. Auciello, and T. Venkatesan, Appl. Phys. Lett. **71,** 3492 (1997).

[25] S. Hong, J. Woo, H. Shin, J. U. Jeon, Y. E. Pak, E. L. Colla, N. Setter, E. Kim, and K. No, J. Appl. Phys. **89,** 1377 (2001).

[26] S. V. Kalinin and D. A. Bonnell, Phys. Rev. B: Condens. Matter **63,** 10419 (2001).

[27] A. Gruverman, A. Kholkin, A. Kingon, and H. Tokumoto, Appl. Phys. Lett. **78,** 2751 (2001).

[28] C. Durkan, M. E. Welland, D. P. Chu, and P. Migliorato, Phys. Rev. B: Condens. Matter **60,** 16198 (1999).

[29] M. E. Lines and A. M. Glass, *Principles and Applications of Ferroelectrics and Related Materials* (Oxford: Pergomon Press, New York, 1977).

[30] B. Jaffe, W. R. Cook, and H. L. Jaffe, *Piezoelectric Ceramics* (Academic Press, London, 1971).

[31] D. W. Chapman, J. Appl. Phys. **40,** 2381 (1969).

[32] B. S. Sharma, S. F. Vogel, and P. I. Prentky, Ferroelectrics **5,** 69 (1973).

[33] J. F. Scott, C. A. Araujo, H. B. Meadows, L. D. McMillan, and A. Shawabkeh, J. Appl. Phys. **66,** 1444 (1989).

[34] J. F. Scott and C. A. P. Dearaujo, Science **246,** 1400 (1989).

[35] K. D. Budd, S. K. Dey, and D. A. Payne, Brit. Ceram. Proc. **36,** 107 (1985).

[36] S. K. Dey, K. D. Budd, and D. A. Payne, IEEE Trans. Ultrason. Ferroelectr. Freq. Control **35,** 80 (1988).

[37] R. Takayama, Y. Tomita, K. Iijima, and I. Ueda, J. Appl. Phys. **61,** 411 (1987).

[38] M. Okuyama and Y. Hamakawa, Ferroelectrics **63,** 243 (1985).

[39] M. Okuyama, K. Ohtani, T. Ueda, and Y. Hamakawa, Int. J. Infrared Millimeter Waves **6,** 71 (1985).

[40] D. L. Polta, Microelectronic Engineering **29,** 51 (1995).

[41] D. L. Polla and L. F. Francis, Annu. Rev. Mater. Sci. **28,** 563 (1998).

[42] D. L. Polla and P. J. Schiller, Integrated Ferroelectrics **7,** 359 (1995).

[43] H. D. Chen, K. R. Udayakumar, C. J. Gaskey, L. E. Cross, J. J. Bernstein, and L. C. Niles, J. Am. Ceram. Soc. **79,** 2189 (1996).

[44] C. R. Cho, L. F. Francis, and M. S. Jang, Jpn. J. Appl. Phys. Pt 2-Lett. **38,** L751 (1999).

[45] I. G. Mina, H. Kim, I. Kim, S. Kyu, K. Choi, T. N. Jackson, R. L. Tutwiler, and S. Trolier-McKinstry, IEEE Trans. Ultrason. Ferroelectr. Freq. Control **54,** 2422 (2007).

[46] M. Goel, Ceram. Int. **30,** 1147 (2004).

[47] P. Muralt, Journal of Nanoscience and Nanotechnology **8,** 2560 (2008).

[48] Y. Nemirovsky, A. Nemirovsky, P. Muralt, and N. Setter, Sens. Actuators, A **56,** 239 (1996).

[49] S. E. Park and T. R. Shrout, J. Appl. Phys. **82,** 1804 (1997).

[50] Z. Kighelman, D. Damjanovic, and N. Setter, J. Appl. Phys. **90,** 4682 (2001).

[51] J. P. Maria, W. Hackenberger, and S. Trolier-McKinstry, J. Appl. Phys. **84,** 5147 (1998).

[52] J. H. Park, F. Xu, and S. Trolier-McKinstry, J. Appl. Phys. **89,** 568 (2001).

[53] IEEE Trans. Ultrason. Ferroelectr. Freq. Control **50,** 1613 (2003).

[54] D. Damjanovic and M. Demartin, J. Phys. Condens. Matter **9,** 4943 (1997).

[55] J. W. Lord Rayleigh, Phil. Mag. **5,** 225 (1887).

[56] D. V. Taylor and D. Damjanovic, J. Appl. Phys. **82,** 1973 (1997).

[57] R. E. Eitel, T. R. Shrout, and C. A. Randall, J. Appl. Phys. **99,** 7 (2006).

[58] D. A. Hall, J. Mater. Sci. **36,** 4575 (2001).

[59] D. Damjanovic, J. Appl. Phys. **82,** 1788 (1997).

[60] N. Bassiri-Gharb, I. Fujii, E. Hong, S. Trolier-McKinstry, D. V. Taylor, and D. Damjanovic, J. Electroceram. **19,** 47 (2007).

[61] O. Boser, J. Appl. Phys. **62,** 1344 (1987).

[62] B. A. Tuttle, T. J. Garino, J. A. Voigt, T. J. Headley, D. Dimos, and M. O. Eatough, in *Science and Technology of Electroceramic Thin Films*, edited by O. Auciello and R. Waser (Kluver Academy Publisher, The Nederlands, 1995), p. 117.

[63] J. F. Ihlefeld, W. J. Borland, and J. P. Maria, Adv. Funct. Mater. **17,** 1199 (2007).

[64] J. F. Ihlefeld, A. M. Vodnick, S. P. Baker, W. J. Borland, and J. P. Maria, J. Appl. Phys. **103,** 074112 (2008).

[65] B. A. Tuttle, J. A. Voigt, T. J. Garino, D. C. Goodnow, R. W. Schwartz, D. L. Lamppa, T. J. Headley, and M. O. Eatough, Proc. IEEE Int. Symp. Appl. Ferroelectr.**,** 344 (1992).

[66] A. Pramanick, D. Damjanovic, J. C. Nino, and J. L. Jones, J. Am. Ceram. Soc. **92,** 2291 (2009).

[67] A. Pramanick, J. E. Daniels, and J. L. Jones, J. Am. Ceram. Soc. **92,** 2300 (2009).

[68] F. Li, S. J. Zhang, Z. Xu, X. Y. Wei, J. Luo, and T. R. Shrout, J. Appl. Phys. **108,** 034106 (2010).

[69] Y. M. Jin, Y. U. Wang, A. G. Khachaturyan, J. F. Li, and D. Viehland, Phys. Rev. Lett. **91,** 197601 (2003).

[70] Y. U. Wang, Phys. Rev. B: Condens. Matter **73,** 014113 (2006).

[71] J. E. Garcia, R. Perez, and A. Albareda, J. Phys. D: Appl. Phys. **34,** 3279 (2001).

[72] M. Morozov, D. Damjanovic, and N. Setter, J. European Ceram. Soc. **25,** 2483 (2005).

[73] S. Li, W. Cao, and L. E. Cross, J. Appl. Phys. **69,** 7219 (1991).

[74] D. V. Taylor and D. Damjanovic, Appl. Phys. Lett. **73,** 2045 (1998).

[75] F. Xu, F. Chu, and S. Trolier-McKinstry, J. Appl. Phys. **86,** 588 (1999).

[76] T. Ogawa, A. Senda, and T. Kasanami, Jpn. J. Appl. Phys., Part 1 **30,** 2145 (1991).

[77] T. Miyoshi, M. Nakajima, and H. Funakubo, Jpn. J. Appl. Phys. **48,** 09KD09 (2009).

[78] S. Yokoyama, Y. Honda, H. Morioka, S. Okamoto, H. Funakubo, T. Iijima, H. Matsuda, K. Saito, T. Yamamoto, H. Okino, O. Sakata, and S. Kimura, J. Appl. Phys. **98,** 094106 (2005).

[79] S. Utsugi, T. Fujisawa, Y. Ehara, T. Yamada, S. Yasui, M. T. Chentir, H. Morioka, T. Iijima, and H. Funakubo, J. Ceram. Soc. Jpn. **118,** 627 (2010).

[80] A. L. Kholkin, E. K. Akdogan, A. Safari, P. F. Chauvy, and N. Setter, J. Appl. Phys. **89,** 8066 (2001).

[81] J. F. Li, D. D. Viehland, T. Tani, C. D. E. Lakeman, and D. A. Payne, J. Appl. Phys. **75,** 442 (1994).

[82] L. Lian and N. R. Sottos, J. Appl. Phys. **95,** 629 (2004).

[83] S. Trolier-McKinstry, J. F. Shepard, J. L. Lacey, T. Su, G. Zavala, and J. Fendler, Ferroelectrics **206,** 381 (1998).

[84] M. B. Kelman, P. C. McIntyre, B. C. Hendrix, S. M. Bilodeau, and J. F. Roeder, J. Appl. Phys. **93,** 9231 (2003).

[85] A. L. Roytburd, S. P. Alpay, V. Nagarajan, C. S. Ganpule, S. Aggarwal, E. D. Williams, and R. Ramesh, Phys. Rev. Lett. **85,** 190 (2000).

[86] V. Nagarajan, A. Stanishevsky, L. Chen, T. Zhao, B. T. Liu, J. Melngailis, A. L. Roytburd, R. Ramesh, J. Finder, Z. Yu, R. Droopad, and K. Eisenbeiser, Appl. Phys. Lett. **81,** 4215 (2002).

[87] V. Nagarajan, A. Roytburd, A. Stanishevsky, S. Prasertchoung, T. Zhao, L. Chen, J. Melngailis, O. Auciello, and R. Ramesh, Nat. Mater. **2,** 43 (2003).

[88] S. Buhlmann, B. Dwir, J. Baborowski, and P. Muralt, Appl. Phys. Lett. **80,** 3195 (2002).

[89] P. Bintachitt, S. Jesse, D. Damjanovic, Y. Han, I. M. Reaney, S. Trolier-McKinstry, and S. V. Kalinin, Proc. Nat. Acad. Sci. **107,** 7219 (2010).

[90] H. R. Chabok, J. M. Cannata, H. H. Kim, J. A. Williams, J. Park, and K. K. Shung, IEEE Trans. Ultrason. Ferroelectr. Freq. Control **58,** 206 (2011).

[91] P. Sun, G. F. Wang, D. W. Wu, B. P. Zhu, C. H. Hu, C. G. Liu, F. T. Djuth, Q. F. Zhou, and K. K. Shung, Ferroelectrics **408,** 120 (2010).

[92] T. A. Ritter, T. R. Shrout, R. Tutwiler, and K. K. Shung, IEEE Trans. Ultrason. Ferroelectr. Freq. Control **49,** 217 (2002).

[93] K. K. Park, H. J. Lee, M. Kupnik, and B. T. Khuri-Yakub, J. Microelectromech. Syst. **20,** 95 (2011).

[94] G. Caliano, F. Galanello, A. Caronti, R. Carotenuto, M. Pappalardo, V. Foglietti, and N. Lamberti, Ultrasonics Symposium, 2000 IEEE **1,** 963 (2000).

[95] A. S. Ergun, G. G. Yaralioglu, and B. T. Khuri-Yakub, Journal of Aerospace Engineering **16,** 76 (2003).

[96] J. Johnson, O. Oralkan, U. Demirci, S. Ergun, M. Karaman, and P. Khuri-Yakub, Ultrasonics **40,** 471 (2002).

[97] D. M. Mills, Ultrasonics Symposium, 2004 IEEE **1,** 384 (2004).

[98] P. Muralt and J. Baborowski, J. Electroceram. **12,** 101 (2004).

[99] J. J. Bernstein, J. Bottari, K. Houston, G. Kirkos, R. Miller, B. Xu, Y. Ye, and L. E. Cross, Proc. Ultrasonics Symposium **2,** 1145 (1999).

[100] N. Setter, *Electroceramic-based MEMS fabrication-technology and applications* (Springer Science, New York, 2005).

[101] M. A. Dubois and P. Muralt, Sens. Actuators, A **77,** 106 (1999).

[102] J. F. Shepard, Ph.D. Thesis, Pennsylvania State University, 1998.

[103] W. Chen, Z. H. Wang, C. Ke, W. Zhu, and O. K. Tan, Mater. Sci. Eng., B **162,** 47 (2009).

[104] Z. G. Ye, P. Tissot, and H. Schmid, Mater. Res. Bull. **25,** 739 (1990).

[105] M. Hrovat, J. Holc, and D. Kolar, J. Mater. Sci. Lett. **13,** 1406 (1994).

[106] K. Shiratsuyu, K. Hayashi, A. Ando, and Y. Sakabe, Jpn. J. Appl. Phys., Part 1 **39,** 5609 (2000).

[107] Y. Kawakami, S. Aisawa, and J. Akedo, Jpn. J. Appl. Phys., Part 1 **44,** 6934 (2005).

[108] D. Dimos, R. W. Schwartz, and S. J. Lockwood, J. Am. Ceram. Soc. **77,** 3000 (1994).

[109] F. K. Lotgering, J. Inorg. Nucl. Chem. **9,** 113 (1959).

[110] J. F. Shepard, P. J. Moses, and S. Trolier-McKinstry, Sens. Actuators, A **71,** 133 (1998).

[111] N. Vittayakorn, G. Rujijanagul, X. Tan, M. A. Marquardt, and D. P. Cann, J. Appl. Phys. **96,** 5103 (2004).

[112] R. Gilles, Ph.D. Thesis, EPFL, 2001.

[113] L. F. Francis and D. A. Payne, J. Am. Ceram. Soc. **74,** 3000 (1991).

[114] B. A. Tuttle, T. J. Headley, B. C. Bunker, R. W. Schwartz, T. J. Zender, C. L. Hernandez, D. C. Goodnow, R. J. Tissot, J. Michael, and A. H. Carim, J. Mater. Res. **7,** 1876 (1992).

[115] L. Sagalowicz, P. Muralt, S. Hiboux, T. Maeder, K. Brooks, Z. Kighelman, and N. Setter, Mater. Res. Soc. Symp. Proc. **596,** 265 (1999).

[116] Z. Y. Feng, X. Y. Zhao, and H. S. Luo, J. Appl. Phys. **100,** 024104 (2006).

[117] A. L. Roitburd, Phys. Status Solidi A **37,** 329 (1976).

[118] P. Muralt, J. Am. Ceram. Soc. **91,** 1385 (2008).

[119] P. Muralt, A. Kholkin, M. Kohli, and T. Maeder, Sens. Actuators, A **53,** 398 (1996).

[120] F. Xu, S. Trolier-McKinstry, W. Ren, B. M. Xu, Z. L. Xie, and K. J. Hemker, J. Appl. Phys. **89,** 1336 (2001).

[121] B. A. Tuttle, J. A. Voigt, D. C. Goodnow, D. L. Lamppa, T. J. Headley, M. O. Eatough, G. Zender, R. D. Nasby, and S. M. Rodgers, J. Am. Ceram. Soc. **76,** 1537 (1993).

[122] F. Calame and P. Muralt, Appl. Phys. Lett. **90,** 062907 (2007).

[123] N. Setter, D. Damjanovic, L. Eng, G. Fox, S. Gevorgian, S. Hong, A. Kingon, H. Kohlstedt, N. Y. Park, G. B. Stephenson, I. Stolitchnov, A. K. Taganstev, D. V. Taylor, T. Yamada, and S. Streiffer, J. Appl. Phys. **100,** 051606 (2006).

[124] S. Jesse, S. V. Kalinin, R. Proksch, A. P. Baddorf, and B. J. Rodriguez, Nanotechnology **18,** 435503 (2007).

[125] S. Jesse, P. Maksymovych, and S. V. Kalinin, Appl. Phys. Lett. **93,** 112903 (2008).

[126] F. Griggio and S. Trolier-McKinstry, J. Appl. Phys. **107,** 024105 (2010).

[127] J. P. Maria, H. L. McKinstry, and S. Trolier-McKinstry, Appl. Phys. Lett. **76,** 3382 (2000).

[128] F. Griggio, S. Jesse, A. Kumar, O. S. Ovchinnikov, W. Qu, D. S. Tinberg, S. V. Kalinin, and S. Trolier-McKinstry, Journal of Applied Physics (in press).

[129] H. R. Lindman, *Analysis of Variance in Experimental Design* (Springer-Verlag, New York, N.Y., USA, 1992).

[130] P. Bintachitt, S. Trolier-McKinstry, K. Seal, S. Jesse, and S. V. Kalinin, Appl. Phys. Lett. **94,** 042906 (2009).

[131] V. Giurgiuntiu, Z. Chandhry, and C. A. Rogers, "Energy-based Comparison of Solid-State Actuators," Report No. CIMSS 95-101, Virginia Polytechnic Institute and State University (1995).

[132] V. Giurgiutiu and C. A. Rogers, Journal of Intelligent Material Systems and Structures **8,** 738 (1997).

[133] Y. Liao and H. A. Sodano, Journal of Intelligent Material Systems and Structures **20,** 505 (2009).

[134] J. B. Nelson and D. P. Riley, Proc. Phys. Soc. **57,** 160 (1945).

[135] C. G. F. Stenger and A. J. Burggraaf, J. Phys. Chem. Solids **41,** 17 (1980).

[136] C. G. F. Stenger and A. J. Burggraaf, J. Phys. Chem. Solids **41,** 31 (1980).

[137] C. G. F. Stenger and A. J. Burggraaf, J. Phys. Chem. Solids **41,** 25 (1980).

[138] P. Muralt, J. Appl. Phys. **100,** 051605 (2006).

[139] A. Feteira, D. C. Sinclair, and J. Kreisel, J. Am. Ceram. Soc. **93,** 4174 (2010).

[140] I. M. Reaney, K. Brooks, R. Klissurska, C. Pawlaczyk, and N. Setter, J. Am. Ceram. Soc. **77,** 1209 (1994).

[141] R. D. Klissurska, K. G. Brooks, I. M. Reaney, C. Pawlaczyk, M. Kosec, and N. Setter, J. Am. Ceram. Soc. **78,** 1513 (1995).

[142] G. A. Rossetti, J. P. Cline, Y. M. Chiang, and A. Navrotsky, J. Phys. Condens. Matter **14,** 8131 (2002).

[143] G. A. Rossetti, G. Popov, E. Zlotnikov, and N. Yao, Mater. Sci. Eng., A **433,** 124 (2006).

[144] K. A. Schönau, L. A. Schmitt, M. Knapp, H. Fuess, R. Eichel, H. Kungl, and M. J. Hoffmann, Phys. Rev. B: Condens. Matter **75,** 184117 (2007).

[145] C. M. Foster, G. R. Bai, R. Csencsits, J. Vetrone, R. Jammy, L. A. Wills, E. Carr, and J. Amano, J. Appl. Phys. **81,** 2349 (1997).

[146] J. Han and W. Cao, Phys. Rev. B: Condens. Matter **68,** 134102 (2003).

[147] R. Wang, R. J. Xie, K. Hanada, K. Matsusaki, H. Bando, and M. Itoh, physica status solidi (a) **202,** R57 (2005).

[148] *IEEE Standard on Piezoelectricity,* , Vol. 176 (ANSI/IEEE Std., 1987).

[149] G. C. Deng, A. L. Ding, G. R. Li, X. S. Zheng, W. X. Cheng, P. S. Qiu, and Q. R. Yin, J. Appl. Phys. **98,** 094103 (2005).

[150] X. Zeng, A. L. Ding, G. C. Deng, T. Liu, X. S. Zheng, and W. X. Cheng, Journal of Physics D-Applied Physics **38,** 3572 (2005).

[151] D. Damjanovic, Phys. Rev. B: Condens. Matter **55,** R649 (1997).

[152] V. N. Smelyanskiy, M. I. Dykman, H. Rabitz, and B. E. Vugmeister, Phys. Rev. Lett. **79,** 3113 (1997).

[153] J. Lehmann, P. Reimann, and P. Hänggi, Phys. Rev. Lett. **84,** 1639 (2000).

[154] N. B. Gharb, S. Trolier-McKinstry, and D. Damjanovic, J. Appl. Phys. **100,** 044107 (2006).

[155] M. Ozgul, E. Furman, S. Trolier-McKinstry, and C. A. Randall, J. Appl. Phys. **95,** 2631 (2004).

[156] S. V. Kalinin, B. J. Rodriguez, S. H. Kim, S. K. Hong, A. Gruverman, and E. A. Eliseev, Appl. Phys. Lett. **92,** 152906 (2008).

[157] M. A. Hentati, M. Guennou, H. Dammak, H. Khemakhem, and M. P. Thi, J. Appl. Phys. **107,** 064108 (2010).

[158] W. H. Jiang, R. Zhang, B. Jiang, and W. W. Cao, Ultrasonics **41,** 55 (2003).

[159] R. Zhang, B. Jiang, and W. W. Cao, Appl. Phys. Lett. **82,** 3737 (2003).

[160] S. J. Zhang, S. M. Lee, D. H. Kim, H. Y. Lee, and T. R. Shrout, J. Am. Ceram. Soc. **91,** 683 (2008).

[161] H. Cao and H. Luo, Ferroelectrics **274,** 309 (2002).

[162] A. Pramanick and J. L. Jones, IEEE Trans. Ultrason. Ferroelectr. Freq. Control **56,** 1546 (2009).

[163] A. K. Singh, S. K. Mishra, Ragini, D. Pandey, S. Yoon, S. Baik, and N. Shin, Appl. Phys. Lett. **92,** 022910 (2008).

[164] A. Gruverman, O. Auciello, and H. Tokumoto, Integrated Ferroelectrics **19,** 49 (1998).

[165] G. Arlt and N. A. Pertsev, J. Appl. Phys. **70,** 2283 (1991).

[166] J. K. Lee, T. Y. Kim, I. Chung, and S. B. Desu, Appl. Phys. Lett. **75,** 334 (1999).

[167] S. Tsurekawa, K. Ibaraki, K. Kawahara, and T. Watanabe, Scripta Mater. **56,** 577 (2007).

[168] H. Takahashi, Y. Numamoto, J. Tani, and S. Tsurekawa, Jpn. J. Appl. Phys. **46,** 7044 (2007).

[169] M. I. Tsindlekht, G. I. Leviev, V. M. Genkin, I. Felner, Y. B. Paderno, and V. B. Filippov, Phys. Rev. B: Condens. Matter **73,** 104507 (2006).

[170] X. B. Wang and P. Ryan, J. Appl. Phys. **108,** 083913 (2010).

[171] F. Griggio, S. Jesse, A. Kumar, D. M. Marincel, D. S. Tinberg, S. V. Kalinin, and S. Trolier-McKinstry, Appl. Phys. Lett. **98,** 212901 (2011).

[172] V. V. Shvartsman, A. L. Kholkin, and N. A. Pertsev, Appl. Phys. Lett. **81,** 3025 (2002).

[173] D. Dimos, W. L. Warren, M. B. Sinclair, B. A. Tuttle, and R. W. Schwartz, J. Appl. Phys. **76,** 4305 (1994).

[174] L. P. Wang, R. A. Wolf, Y. Wang, K. K. Deng, L. C. Zou, R. J. Davis, and S. Trolier-McKinstry, J. Microelectromech. Syst. **12,** 433 (2003).

[175] I. Kim, H. Kim, F. Griggio, R. L. Tutwiler, T. N. Jackson, S. Trolier-McKinstry, and K. Choi, IEEE Transactions on Biomedical Circuits and Systems **3,** 293 (2009).

[176] J. J. Bernstein, S. L. Finberg, K. Houston, L. C. Niles, H. D. Chen, L. E. Cross, K. K. Li, and K. Udayakumar, IEEE Trans. Ultrason. Ferroelectr. Freq. Control **44,** 960 (1997).

[177] B. M. Xu, L. E. Cross, and J. J. Bernstein, Thin Solid Films **377,** 712 (2000).

[178] K. Yamashita, H. Katata, M. Okuyama, H. Miyoshi, G. Kato, S. Aoyagi, and Y. Suzuki, Sens. Actuators, A **97-8,** 302 (2002).

[179] G. Percin and B. T. Khuri-Yakub, IEEE Trans. Ultrason. Ferroelectr. Freq. Control **49,** 573 (2002).

[180] G. Percin and B. T. Khuri-Yakub, IEEE Trans. Ultrason. Ferroelectr. Freq. Control **49,** 585 (2002).

[181] H. J. Nam, Y. S. Kim, S. M. Cho, C. S. Lee, J. U. Bu, J. W. Hong, and Z. G. Khim, Jpn. J. Appl. Phys., Part 1 **41,** 7153 (2002).

[182] T. L. Ren, L. T. Zhang, H. S. Liu, L. T. Liu, and Z. H. Li, Microelectronic Engineering **66,** 683 (2003).

[183] J. M. Gere and B. J. Goodno, *Mechanics of materials*, 7th ed. (Cengage Learning, Mason, OH, 2009).

[184] J.-H. Zhao, T. Ryan, P. S. Ho, A. J. McKerrow, and W.-Y. Shih, J. Appl. Phys. **85,** 6421 (1999).

[185] T. Tuchiya, T. Itoh, G. Sasaki, and T. Suga, J. Ceram. Soc. Jpn. **104,** 159 (1996).

[186] J. Mencik, D. Munz, E. Quandt, E. R. Weppelmann, and M. V. Swain, J. Mater. Res. **12,** 2475 (1997).

[187] Acrylic Polymer Properties. Available at: http://www.goodfellow.com/A/Polymethylmethacrylate.html.

[188] SPR 220 Specifications. Available at: http://www.microresist.de/download_en/distriproducts_p1_09050805.pdf.

[189] D. R. Lide and H. V. Kehiaian, *CRC handbook of thermophysical and thermochemical data* (CRC Press, Boca Raton, 1994).

[190] J. Baborowski, J. Electroceram. **12,** 33 (2004).

[191] H. Mace, H. Achard, and L. Peccoud, Microelectronic Engineering **29,** 45 (1995).

[192] G. McLane, R. Polcawich, J. Pulskamp, B. Piekarski, M. Dubey, E. Zakar, J. Conrad, R. Piekarz, M. Ervin, and M. Wood, Integrated Ferroelectrics **37,** 397 (2001).

[193] T. Zhu, P. Argyrakis, E. Mastropaolo, K. K. Lee, and R. Cheung, Journal of Vacuum Science & Technology B **25,** 2553 (2007).

[194] N. H. Tea, V. Milanovic, C. A. Zincke, J. S. Suehle, M. Gaitan, M. E. Zaghloul, and J. Geist, J. Microelectromech. Syst. **6,** 363 (1997).

[195] H. F. Winters and J. W. Coburn, Appl. Phys. Lett. **34,** 70 (1979).

[196] K. R. Williams and R. S. Muller, Microelectromechanical Systems, Journal of **5,** 256 (1996).

[197] Plastic Material's Acoustic Properties. Available at: http://www.ndt.net/links/proper.htm.

[198] H. Kim, PhD Thesis, The Pennsylvania State University, 2010.

[199] X. Yong, J. Fukang, L. Qiao, J. Clendenen, S. Tung, and T. Yu-Chong, in *The Fifteenth IEEE International Conference on Micro Electro Mechanical Systems* (2002), p. 340.

[200] Y.-Y. Lin, R. D. Evans, E. Welch, B.-N. Hsu, A. C. Madison, and R. B. Fair, Sensors and Actuators B: Chemical **150,** 465 (2010).

[201] Olympus M316 transducer. Available at: http://www.olympus-ims.com/en/panametrics-ndt-ultrasonic/immersion/.

[202] S. J. Gross, Q. Zhang, S. Tadigadapa, S. Trolier-McKinstry, T. N. Jackson, and F. T. Djuth, Proc. SPIE **4558,** 72 (2001).

[203] R. Jones, Journal of Sound and Vibration **38,** 503 (1975).

[204] S. Timoshenko and S. Woinowsky-Krieger, *Theory of plates and shells*, 2nd ed. (McGraw-Hill, New York, 1959).

[205] W. C. Young, R. G. Budynas, and R. J. Roark, 7th ed. (McGraw-Hill, New York, 2002).

[206] O. Al-Hattamleh, J. Cho, R. F. Richards, D. F. Bahr, and C. D. Richards, J. Microelectromech. Syst. **15,** 1715 (2006).

[207] M. Motomatsu, T. Takahashi, H.-Y. Nie, W. Mizutani, and H. Tokumoto, Polymer **38,** 177 (1997).

[208] K. Shibata, K. Shoji, and K. Sakata, Jpn. J. Appl. Phys., Part 1 **40,** 5719 (2001).

[209] A. Gruverman, B. J. Rodriguez, A. I. Kingon, R. J. Nemanich, J. S. Cross, and M. Tsukada, Appl. Phys. Lett. **82,** 3071 (2003).

[210] A. Kumar, O. S. Ovchinnikov, H. Funakubo, S. Jesse, and S. V. Kalinin, Appl. Phys. Lett. **98,** 202903 (2011).

VITA

Flavio Griggio

Flavio Griggio was born in Venice, Italy on April 13th 1982. He received his Bachelor's and Master's degrees in Materials Science and Engineering from University of Padova, Italy in 2004 and 2007 respectively. While pursuing his Master's degree, Flavio had the opportunity to spend one year at University of California, Irvine and three months at the Pennsylvania State University. It was while at PennState that he concluded his Master's research on synthesis and templating studies of mullite under the guidance of Prof. Paolo Colombo and in collaboration with Prof. Gary Messing. In the summer of 2007 he came back to the Pennsylvania State University and began his doctorate degree in Materials Science and Engineering.